The Dissertation Committee for Dylan Whitney Meyer Certifies that this is the approved version of the following dissertation:

DYNAMICS OF GAS FLOW AND HYDRATE FORMATION WITHIN THE HYDRATE STABILITY ZONE

Committee:

Peter B. Flemings, Supervisor

David DiCarlo

Timothy J. Kneafsey

Sean S. Gulick

Richard A. Ketcham

DYNAMICS OF GAS FLOW AND HYDRATE FORMATION WITHIN THE HYDRATE STABILITY ZONE

by

Dylan Whitney Meyer

Dissertation

Presented to the Faculty of the Graduate School of

The University of Texas at Austin

in Partial Fulfillment

of the Requirements

for the Degree of

Doctor of Philosophy

The University of Texas at Austin

August 2018

Acknowledgements

In retrospect, when considering graduate school in 2011, I believe that I neither truly understood the investment of time and energy required to pursue a doctoral degree nor could I have understood. Even during my graduate career, while immersed in my research, the momentous continuum of daily research activities tended to overwhelm any attempt at personal reflection. It has only been recently, as I wrote this dissertation, that I have come to appreciate the magnitude of the opportunities I have enjoyed while pursuing my doctorate. My transformation into a doctor, which I hope emanates from the pages that follow, would have been impossible without the dedicated support and mentorship of a multitude of individuals in my life. I would like to take the following paragraphs to express my deepest gratitude to them all.

I thank my loving girlfriend, Gaëlle, who entered the scene during the last, and most trying, two years of my doctorate. She was a source of unwavering support and advice, gladly sacrificing her own time and energy in my pursuit of my degree. She kept me positive and focused on the future, which was essential to my continual forward progress.

I thank my parents, who raised me on tales of traveling the world with the Ocean Drilling Program and the wonders of the Earth sciences. They both continue to be the sources of inspiration and motivation that are essential to cultivating my academic growth. I am blessed to have such a dedicated, knowledgeable, and supportive pair of people behind me.

I extend the most profound gratitude to my advisor, Peter Flemings, who was the cornerstone of my personal development into a scientist. Over the years, Peter has put countless hours into guiding, critiquing, and supporting my research to help make my stories more complete and my communication clearer. He pushed me beyond my limits, showed me what I am capable of accomplishing, and imbued me with an appreciation for what it means to grasp a concept from all angles. I am truly grateful that I met Peter at the American Geophysical Union in 2011 and that I was able to have him as my graduate advisor. I am a better scientist, thinker, and person as a result.

I have benefitted greatly from a research team and dissertation committee with a broad range of expertise, including high-pressure laboratory techniques, computed-tomography analysis, sedimentology and hydrology of marine environments, thermodynamics, and fluid flow. I thank David DiCarlo and Timothy Kneafsey, who provided me guidance in developing my experimental method and in analyzing the results. I truly appreciate my lab managers, Peter Polito and Josh O'Connell, who helped me troubleshoot all the issues that emerged during that process. Finally, I thank my project managers, Tessa Green and Jac Erengil, who answered my innumerable questions with a smile on their face and care in their hearts.

I thank my friends, both at UT Austin and from other aspects of my life. They have provided me with an enormous amount of support during my doctorate and I am so grateful to them all. In addition, I appreciate the support of the fellow graduate students and department research scientists who provided me with important critical feedback and

community support. In particular, I thank Peter Carlson, Kimmy McCormack, Michael O'Connor, Kehua You, Steve Phillips, Kris Darnell, and Baiyuan Gao.

Finally, I thank the following monetary support: the U.S. Department of Energy, the Institute for Geophysics Ewing-Worzel and Gale White Fellowships, the Jackson School of Geosciences Graduate Fellowship and Energy Geosciences SEED Grant, and the Chevron Graduate Student Fellowship.

DYNAMICS OF GAS FLOW AND HYDRATE FORMATION WITHIN THE HYDRATE STABILITY ZONE

by

Dylan Whitney Meyer, Ph.D.
The University of Texas at Austin, 2018

Supervisor: Peter B. Flemings

Methane hydrate comprises a significant piece of the global carbon cycle and is an important potential energy resource. Thick marine sands around the world contain free gas beneath and high concentrations of methane hydrate far above the base of the hydrate stability zone. The mechanisms controlling gas transport and hydrate formation within the region where hydrate is stable remains an important research question.

I developed a new experimental method to investigate the fundamental behaviors associated with hydrate formation during gas flow into the hydrate stability zone. First, I performed a set of experiments at the same experimental conditions, to determine the repeatability of this behavior. I compared these results to those from an experiment performed outside the hydrate stability zone to elucidate the change in intrinsic gas flow behavior due to hydrate formation. Second, I performed additional experiments at a range of flow rates as well as several shut-in experiments, where I observed long-term hydrate

formation after flow took place. I analyzed the bulk and core-scale behaviors of these experiments using a combination of mass balance and computed-tomography analyses.

I found that many of my experimentally observed behaviors are not accurately described by previous models and that the mechanism for gas transport was fundamentally different than typically assumed. I proposed that hydrate formation at the gas-brine interface separates the gas and brine phases and limits hydrate formation to methane transport through the hydrate. This behavior produced temporary flow blockages that were mitigated when the hydrate skin fails due to pressure gradients across the sample. This behavior also produced different thermodynamics states on either side of the hydrate that could persist for hundreds to thousands of years. These results provide an alternative mechanism for gas transport and hydrate formation through the hydrate stability zone that does not require the gas, hydrate, and brine to be at three-phase equilibrium. This mechanism provides a first-order connection between experimentally observed micro-scale phenomena and field-scale gas transport and hydrate formation behaviors in these reservoirs.

Table of Contents

List of Tables

List of Figures

Chapter 1: Introduction

Gas hydrate, commonly referred to as hydrate, is a crystalline solid consisting of a low molecular weight gas trapped within a water cage (Kvenvolden & McMenamin, 1980). A variety of gases can be present within the hydrate lattice (e.g. carbon dioxide, ethane, propane), but methane is by far the most common guest molecule (Kvenvolden, 1988). Hydrate is a non-stoichiometric molecule, meaning that its molecular composition is not constant, and it can exist in a range of different cage structures (Sloan & Koh, 2007). Structure I, which forms most commonly in the presence of pure methane, has an approximate molecular composition of 5.75 moles of water to 1 mole of methane (Ballard et al., 2011).

Hydrate, similar to ice, is thermodynamically stable at high pressures and low temperatures and salinities where the local methane concentration exceeds the solubility (Sloan & Koh, 2007). As a result, hydrates are most commonly found in the shallow subsurface along continental margins (Boswell & Collett, 2011). Recent estimates put the total amount of carbon trapped in hydrate reservoirs at approximately 500 – 2500 gigatons, making it a significant portion of the total carbon budget (Boswell & Collett, 2011; Milkov, 2004).

There has been extensive research investigating the potential of hydrates-driven catastrophic global climate change (Archer et al., 2004; Wright et al., 2005) and tsunamogenic submarine landslides (Mienert et al., 2005; Nixon & Grozic, 2007). Since hydrate is a solid phase, studies have also investigated carbon sequestration methods

involving the formation of CO_2-hydrates in the subsurface (Boswell et al., 2017; House et al., 2006).

The potential of hydrate as a significant energy source has motivated research on the production of hydrocarbons from hydrates (e.g. Koh et al., 2016; Konno et al., 2017; Moridis, 2008). Thus far, the focus has been on sand-rich reservoirs where hydrate is frequently found disseminated with saturations of 60 – 90% (Boswell & Collett, 2011; Yamamoto et al., 2014). Of particular interest are dipping sand reservoirs that cross-cut the base of the hydrate stability zone. These reservoirs are beneath the gas hydrate stability zone (GHSZ) down-dip and within the GHSZ up-dip. Seismic and well-log data indicate that these reservoirs have free gas below and high concentrations of hydrate above the base of hydrate stability (Boswell et al., 2012a; Boswell et al., 2009; Crutchley et al., 2015; Tréhu et al., 2004). The mechanism responsible for the presence of these hydrate deposits remains a conundrum.

Several gas migration and hydrate formation mechanisms are proposed to explain these field observations: 1) the short-range migration, through diffusion, of dissolved methane into the sands (Cook & Malinverno, 2013; Malinverno & Goldberg, 2015; You & Flemings, 2017); 2) the long-range advection of dissolved methane (Nole et al., 2016; Priegnitz et al., 2013); and 3) the long-range advection of free methane gas along permeable pathways from below (Liu & Flemings, 2007; Torres et al., 2004; You & Flemings, in review).

Hydrate formation through short-range diffusion of methane is driven by local methane concentration differences between coarse-grained (sands) and fine-grained

(muds) materials (Malinverno, 2010). These sand reservoirs are typically bounded by muds that have smaller pore sizes, which increases the local methane solubility (Henry et al., 1999). This pore size contrast produces a methane concentration gradient that drives methane diffusion from the mud to the sand and resulting in hydrate formation. The degradation of organic material in the mud maintains the higher methane concentration in the mud and supports methane diffusion into the sand (Malinverno, 2010). In systems with centimeter-scale, interbedded sands and muds, this mechanism may produce high hydrate saturations throughout the sands over millions of years (Malinverno & Goldberg, 2015). In meter-scale sands, however, the muds do not provide methane fast enough to produce disseminated hydrate throughout the sands. Instead, this process forms very high hydrate saturations near the sand boundaries and nearly no hydrate in the centers of the sand (Rempel, 2011; You & Flemings, 2017).

Hydrate formation through long-range dissolved methane advection is caused by the change in methane solubility with depth. Overpressure in the sediments drives the upward advection of methane-saturated pore fluid either through the pores or along permeable pathways (Frederick & Buffett, 2011; Nole et al., 2016). Above the base of hydrate stability, the methane solubility decreases, which forces methane out of solution and drives hydrate formation. This process can produce significant saturations of hydrate throughout the sand, but requires millions of years due to the low solubility of methane in the advecting fluids (Davie & Buffett, 2003; Nole et al., 2016; Rempel & Buffett, 1997; Torres et al., 2004; Xu & Ruppel, 1999).

Long-range free gas advection into the hydrate stability zone provides ample methane to drive hydrate formation. Gas beneath the GHSZ, biogenic or thermogenic, preferentially collects in permeable sand layers (England et al., 1987; Schowalter, 1979). The mud above the sand prevents vertical gas transport (England et al., 1987; Schowalter, 1979), diverting gas updip along the sand, due to buoyancy, where it forms hydrate upon entering the GHSZ (Liu & Flemings, 2006; Torres et al., 2004; Tréhu et al., 2004). With continual gas supply, this process can rapidly produce very high hydrate saturations.

With free gas advection, hydrate formation is limited by the development of elevated local salinities (Liu & Flemings, 2007; You et al., 2015a). Hydrate formation consumes water and excludes salts (Hesse & Harrison, 1981; Torres et al., 2004; Ussler & Paull, 2001), elevating the local salinity proportionally to the hydrate saturation (Liu & Flemings, 2006). Higher salinity shifts the phase boundary to higher pressures and lower temperatures, relative to the initial condition (You et al., 2015b). At the three-phase equilibrium hydrate saturation, the hydrate stability boundary is equal to the local pressure and temperature conditions (You et al., 2015a; You et al., 2015b). At this point, no more hydrate can form and gas flows farther into the GHSZ. This process produces an upward-propagating hydrate formation front with three phases, gas, hydrate, and three-phase salinity brine, behind the front and one phase, initial brine, ahead of the front. You et al. (2015b) observed salinity-buffered hydrate formation experimentally and there have been a series of modeling investigations of this behavior at both the core-scale (You et al., 2015a) and field-scale (You & Flemings, in review). Hydrate formation during gas injection into the hydrate stability zone has never been rigorously observed in the

laboratory, however, and none of the commonly used hydrate formation methods are appropriate for investigating this behavior.

The goal of this dissertation was to gain insight into field-scale gas migration and hydrate formation behaviors in sand reservoirs. Ultimately, I wished to understand the fundamental macro-scale behaviors associated with hydrate formation during gas injection into the hydrate stability zone. I synthesized a variety of approaches by: 1) developing a new experimental methodology to rigorously investigate this process; 2) performing several experiments in a X-ray computed-tomography (CT) scanner to observe the core-scale behavior; and 3) creating a set of simple models to elucidate the major behaviors of and limitations on hydrate formation. Based on these approaches, I proposed an alternative mechanism for gas transport through the hydrate stability zone that combines these micro-scale, macro-scale, and field-scale observations.

In Chapter 2, I describe the experimental method and the CT post-processing analyses I use to investigate hydrate formation during gas injection. I present the results from one gas flooding (two-phase) and three hydrate formation (three-phase) experiments, all performed at the same experimental conditions. I derive a set of mass balance analyses to determine the amount of hydrate formed in the sample and the gas, hydrate, and brine saturations in the region where gas and hydrate are present. Finally, I use a coupled, one-dimensional diffusion model to evaluate the factors limiting hydrate formation.

The key result from Chapter 2 is that the mechanism sustaining gas flow through the hydrate stability zone is different than is commonly assumed. My results indicate that

hydrate is not limited by elevated salinities. Instead, I propose that hydrate forms at the gas-brine interface and that additional formation is limited by methane transport through the hydrate. This process produces different thermodynamics states on either side of the hydrate skin that can persist for tens to thousands of years. As a result, gas, hydrate, and brine coexist at non-equilibrium and gas continues to flow through the sample.

In Chapter 3, I present the results from an additional set of hydrate formation experiments. Most of these experiments use the same methodology as I describe in Chapter 2, but are performed at different flow rates. I also present the results from four experiments where I observe hydrate formation in the samples due to methane diffusion over week-long timescales.

The results show that a 6-fold decrease in the flow rate nearly triples the volume of hydrate formed during brine removal. Also, significant additional hydrate forms during brine shut-in at a decreasing rate. I propose that the increase in hydrate volume is due to a combination of longer experimental execution time and larger contact surface area at lower flow rates. During shut-in, I propose that hydrate continues to form as methane diffuses through the hydrate skin, but the rate decreases over time as the skin thickens and the diffusion length-scale increases.

In Chapter 4, I develop a two-dimensional model to investigate the behaviors associated with the formation of a hydrate skin around a cylindrical gas finger. I define a gas flux using the experimental data from Chapter 3, implement a simple diffusion model to determine the hydrate formed due to diffusion, and determine the gas finger progression

from the remaining available gas. I constrain key model parameters using the experimental data and compare the model output to my experimental results.

This comparison indicates that much of the behavior during my experiments can be explained by the presence of hydrate-encased gas fingers in the sample. In particular, more hydrate forms at the lower flow rate and the rate of hydrate formation increases as the model progresses. Although I use a simplistic geometry in this model, relative to natural gas-brine interfaces in porous media, the results indicate that hydrate formation is methane diffusion-limited. Thus, I propose an alternative model of hydrate formation kinetics that could be directly integrated into field-scale gas transport and hydrate formation simulations.

One of the key contributions of my dissertation is the development of an experimental methodology that directly investigates hydrate formation during gas injection. Although this process likely contributes to hydrate formation in the field, investigating it experimentally has been avoided due to inherent experimental complexities. The few experiments that have peripherally observed this behavior (Brewer et al., 1998; Yousif & Sloan, 1991) did not provide any fundamental understanding due to the experimental setup and lack of data resolution. I carefully developed this methodology through a deliberate and iterative process such that the experiments I perform yield novel insight into this behavior.

The second key contribution is the development of a conceptual and quantitative models that describe the fundamental behaviors observed in my experiments. My experiments produce results in direct contradiction to the assumptions and output of models

of hydrate formation during gas injection into the hydrate stability zone. Thus, I propose a new conceptual model that incorporates a commonly observed micro-scale behavior, hydrate formation at the gas-brine interface, to elegantly explain my observed macro-scale behaviors. I then develop a coupled one-dimensional diffusion model of hydrate formation and elevated salt dissipation to evaluate limitations on hydrate formation. This shows conclusively that, at my experimental timescales, hydrate formation at the gas-brine interface is ultimately limited by methane diffusion through the hydrate skin, not locally elevated salinities.

The third key contribution is the development of a geometric model that evaluates the fundamental behaviors associated with hydrate formation at the gas-brine interface of a cylindrical gas finger. I incorporate experimentally-observed gas fluxes into this model to improve comparability to my experiments and perform a sensitivity analysis of the results to the model parameters. This model reproduces many of the fundamental experimental behaviors and indicates that hydrate formation is mass transport-limited. This indicates a fundamentally different model of hydrate formation kinetics than is traditionally used.

FUTURE RESEARCH

The methodology I developed, experiments I performed, and models I derived together provide novel insight into an important hydrate formation mechanism. Results from these investigations elucidate many potential areas of further research and improvements that could build upon my contributions. The following paragraphs highlight

some important questions than remain open and additional studies that would be interesting to pursue.

The most important and directly applicable extension of my experimental results would be the incorporation of additional experiments performed at a range of stability conditions. All my experiments were performed at pressure, temperature, and salinity conditions deep within the hydrate stability zone. In the Gulf of Mexico, where many of these dipping sand layers exist, my experimental conditions would be comparable to those less than 200 meters below the seafloor and far above the base of hydrate stability. Free gas in these systems, however, enters the hydrate stability zone from the base and passes through a wide range of thermodynamic conditions as it flows updip. As the gas flows higher within the reservoir, the driving force for hydrate formation and three-phase equilibrium hydrate saturation both increase, which could fundamentally alter the hydrate formation behaviors. Thus, performing experiments closer to the phase boundary (e.g. near to the base of hydrate stability) would provide important information on how this behavior may vary at different points within the hydrate stability zone.

Another important study would be to use my experimental methodology on natural, potentially reconstituted, samples instead of industrial sands. Although I added a very small fraction of clay to my samples in an attempt to reduce the hydrate induction time, it is nearly impossible to recreate natural sediment compositions using industrial sediments. Heterogeneities in sample mineralogy and composition could affect the hydrate nucleation time, the gas flow behavior, and the hydrate distribution within the sample. Thus, performing hydrate formation experiments on carefully depressurized samples that

originally contained hydrates could provide an important connection between my laboratory experiments and hydrate formation in the field.

An additional interesting study would be to run these experiments with the reverse gas flow direction. I performed all my experiments with gas flowing into the top of the sample to remove the gravitational effects on flow. Obviously, this design does not directly replicate field conditions where gas flows upward due to buoyancy. My experimental flow rates, however, suggest that gas flow is capillary-controlled, as opposed to gravitationally-controlled. Thus, upward and downward gas flow may act similarly within my experimental setup. However, a relatively simple and interesting set of experiments could repeat the experiments performed in Chapter 2 with the flow direction reversed to confirm whether or not this parameter alters the behavior.

The studies I suggest above could be performed without significant alterations to my experimental methodology or additional equipment and could provide important additional insight into this process at the laboratory-scale. However, like most laboratory-scale experiments, the scalability of my results to either the micro-scale or field-scale could be improved by altering the scale at which the experiments and observations are performed. Specifically, performing similar experiments with both longer and wider and shorter and narrower samples would provide observations one step closer to these alternate scales. A larger sample would provide observations of gas flow and hydrate formation behavior and the spatial distribution of these phases for a longer period of time. A smaller sample could be made compatible with micro-CT and/or Raman spectroscopy to observe micro-scale gas flow and hydrate formation behaviors and the interactions at the phase boundaries.

Although these studies would require additional equipment and new methodology, they would provide an essential next step in moving from my conceptual and quantitative models to actual observations of these behaviors.

Finally, it is interesting to note that methane at my experimental conditions is a supercritical fluid, although this distinction is rarely made within the hydrates research community. Supercritical fluids have unique thermodynamic properties, including: surface tension and wettability and volumetric changes under pressure and temperature variations (Zappoli et al., 2014). These characteristics may affect the formation of a distinct interface between the methane and the brine and how these fluids expand after hydrate skin failure. Thus, additional research and consideration for the behavior of supercritical methane in my experiments may be useful. An initial investigation could be to perform experiments with a similar driving force, but at thermodynamic conditions where methane is not supercritical (e.g. 4.6 MPa, -3.4ºC, and 7 wt% NaCl). These experiment may indicate different hydrate formation behaviors with either supercritical and gaseous methane, which would have implications for field-scale hydrate formation depending upon the in-situ thermodynamic conditions.

REFERENCES

Archer, D., Martin, P., Buffett, B., Brovkin, V., Rahmstorf, S., and Ganopolski, A. (2004). The importance of ocean temperature to global biogeochemistry. *Earth and Planetary Science Letters, 222*(2), 333-348. doi: http://dx.doi.org/10.1016/j.epsl.2004.03.011

Ballard, A., Shoup, G., and Sloan, D. (2011). Chapter Seven - Industrial Operating Procedures for Hydrate Control *Natural Gas Hydrates in Flow Assurance* (pp. 145-162). Boston: Gulf Professional Publishing.

Boswell, R., and Collett, T. (2011). Current prospective on gas hydrate resources. *Energy & Environmental Science, 4*, 10.

Boswell, R., Schoderbek, D., Collett, T. S., Ohtsuki, S., White, M., and Anderson, B. J. (2017). The Iġnik Sikumi Field Experiment, Alaska North Slope: Design, Operations, and Implications for CO2–CH4 Exchange in Gas Hydrate Reservoirs. *Energy & Fuels, 31*(1), 140-153. doi: 10.1021/acs.energyfuels.6b01909

Brewer, P. G., Orr Jr, F. M., Friederich, G., Kvenvolden, K. A., and Orange, D. L. (1998). Gas hydrate formation in the deep sea: In situ experiments with controlled release of methane, natural gas, and carbon dioxide. *Energy and Fuels, 12*(1), 183-188.

Cook, A. E., and Malinverno, A. (2013). Short migration of methane into a gas hydrate-bearing sand layer at Walker Ridge, Gulf of Mexico. *Geochemistry, Geophysics, Geosystems, 14*(2), 283-291. doi: 10.1002/ggge.20040

Davie, M. K., and Buffett, B. A. (2003). A steady state model for marine hydrate formation: Constraints on methane supply from pore water sulfate profiles. *Journal of Geophysical Research: Solid Earth, 108*(B10), doi: 10.1029/2002jb002300

England, W. A., Mackenzie, A. S., Mann, D. M., and Quigley, T. M. (1987). The movement and entrapment of petroleum fluids in the subsurface. *Journal of the Geological Society, 144*(2), 327-347. doi: 10.1144/gsjgs.144.2.0327

Frederick, J. M., and Buffett, B. A. (2011). Topography- and fracture-driven fluid focusing in layered ocean sediments. *Geophysical Research Letters, 38*(L08614), doi: 10.1029/2010GL046027

Henry, P., Thomas, M., and Clennell, M. B. (1999). Formation of natural gas hydrate in marine sediments 2. Thermodynamic calculations of stability conditions in porous sediments. *Journal of Geophysical Research, 104*(B10), 18.

Hesse, R., and Harrison, W. E. (1981). Gas hydrates (clathrates) causing pore-water freshening and oxygen isotope fractionation in deep-water sedimentary sections of terrigenous continental margins. *Earth and Planetary Science Letters, 55*(3), 453-462. doi: http://dx.doi.org/10.1016/0012-821X(81)90172-2

House, K. Z., Schrag, D. P., Harvey, C. F., and Lackner, K. S. (2006). Permanent carbon dioxide storage in deep-sea sediments. *Proceedings of the National Academy of Sciences, 103*(33), 12291-12295. doi: 10.1073/pnas.0605318103

Koh, D.-Y., Kang, H., Lee, J.-W., Park, Y., Kim, S.-J., Lee, J., Lee, J. Y., and Lee, H. (2016). Energy-efficient natural gas hydrate production using gas exchange. *Applied Energy, 162*(Supplement C), 114-130. doi: https://doi.org/10.1016/j.apenergy.2015.10.082

Konno, Y., Fujii, T., Sato, A., Akamine, K., Naiki, M., Masuda, Y., Yamamoto, K., and Nagao, J. (2017). Key Findings of the World's First Offshore Methane Hydrate Production Test off the Coast of Japan: Toward Future Commercial Production. *Energy & Fuels, 31*(3), 2607-2616. doi: 10.1021/acs.energyfuels.6b03143

Kvenvolden, K. A. (1988). Methane Hydrate: A Major Reservoir of Carbon in the Shallow Geosphere? *Chemical Geology, 71*, 11.

Kvenvolden, K. A., and McMenamin, M. A. (1980). Hydrates of natural gas; a review of their geologic occurrence. *Report Rep. 825*.

Liu, X., and Flemings, P. B. (2006). Passing gas through the hydrate stability zone at southern Hydrate Ridge, offshore Oregon. *Earth and Planetary Science Letters*(241), 16.

Liu, X., and Flemings, P. B. (2007). Dynamic multiphase flow model of hydrate formation in marine sediments. *Journal of Geophysical Research: Solid Earth, 112*(B3), B03101. doi: 10.1029/2005jb004227

Malinverno, A. (2010). Marine gas hydrates in thin sand layers that soak up microbial methane. *Earth and Planetary Science Letters, 292*(3–4), 399-408. doi: http://dx.doi.org/10.1016/j.epsl.2010.02.008

Malinverno, A., and Goldberg, D. S. (2015). Testing short-range migration of microbial methane as a hydrate formation mechanism: Results from Andaman Sea and Kumano Basin drill sites and global implications. *Earth and Planetary Science Letters, 422*, 105-114. doi: http://dx.doi.org/10.1016/j.epsl.2015.04.019

Mienert, J., Vanneste, M., Bünz, S., Andreassen, K., Haflidason, H., and Sejrup, H. P. (2005). Ocean warming and gas hydrate stability on the mid-Norwegian margin at

the Storegga Slide. *Marine and Petroleum Geology, 22*(1–2), 233-244. doi: http://dx.doi.org/10.1016/j.marpetgeo.2004.10.018

Milkov, A. V. (2004). Global estimates of hydrate-bound gas in marine sediments: how much is really out there? *Earth-Science Reviews, 66*(3–4), 183-197. doi: http://dx.doi.org/10.1016/j.earscirev.2003.11.002

Moridis, G. J. (2008). Toward Production From Gas Hydrates: Current Status, Assessment of Resources, and Simulation-Based Evaluation of Technology and Potential.

Nixon, M. F., and Grozic, J. L. H. (2007). Submarine slope failure due to gas hydrate dissociation: a preliminary quantification. *Canadian Geotechnical Journal, 44*(3), 10. doi: 10.1139/T06-121

Nole, M., Daigle, H., Cook, A. E., and Malinverno, A. (2016). Short-range, overpressure-driven methane migration in coarse-grained gas hydrate reservoirs. *Geophysical Research Letters, 43*(18), 9500-9508. doi: 10.1002/2016gl070096

Priegnitz, M., Thaler, J., Spangenberg, E., Rücker, C., and Schicks, J. M. (2013). A cylindrical electrical resistivity tomography array for three-dimensional monitoring of hydrate formation and dissociation. *Review of Scientific Instruments, 84*(10), 104502. doi: doi:http://dx.doi.org/10.1063/1.4825372

Rempel, A. W. (2011). A model for the diffusive growth of hydrate saturation anomalies in layered sediments. *Journal of Geophysical Research: Solid Earth, 116*(B10), n/a-n/a. doi: 10.1029/2011jb008484

Rempel, A. W., and Buffett, B. A. (1997). Formation and accumulation of gas hydrate in porous media. *Journal of Geophysical Research: Solid Earth, 102*(B5), 10151-10164. doi: 10.1029/97jb00392

Schowalter, T. T. (1979). Mechanics of Secondary Hydrocarbon Migration and Entrapment. *AAPG Bulletin, 63*(5), 37.

Sloan, E. D., and Koh, C. A. (2007). *Clathrate Hydrates of Natural Gases* (3nd ed.). Boca Raton, FL: CRC Press.

Torres, M. E., Wallmann, K., Tréhu, A. M., Bohrmann, G., Borowski, W. S., and Tomaru, H. (2004). Gas hydrate growth, methane transport, and chloride enrichment at the southern summit of Hydrate Ridge, Cascadia margin off Oregon. *Earth and Planetary Science Letters, 226*(1–2), 225-241. doi: http://dx.doi.org/10.1016/j.epsl.2004.07.029

Tréhu, A. M., Flemings, P. B., Bangs, N. L., Chevallier, J., Gràcia, E., Johnson, J. E., Liu, C. S., Liu, X., Riedel, M., and Torres, M. E. (2004). Feeding methane vents

and gas hydrate deposits at south Hydrate Ridge. *Geophysical Research Letters, 31*(23), L23310. doi: 10.1029/2004gl021286

Ussler, W., and Paull, C. K. (2001). Ion Exclusion Associated with Marine Gas Hydrate Deposits *Natural Gas Hydrates: Occurrence, Distribution, and Detection* (pp. 41-51): American Geophysical Union.

Wright, J. F., Dallimore, S. R., Nixon, F. M., and Duchesne, C. (2005). In situ stability of gas hydrate in reservoir sediments of the JAPEX/JNOC/GSC et al. Mallike 5L-38 gas hydrate production research well. In S. R. Dallimore, and Collett, T. S. (Ed.), *Scientific Results from the Mallik 2002 Gas Hydrate Production Research Well Program, Mackenzie Delta, Northwest Territories, Canada* (Vol. Bulletin 585, pp. 14): Geological Survey of Canada.

Xu, W., and Ruppel, C. (1999). Predicting the occurrence, distribution, and evolution of methane gas hydrate in porous marine sediments. *Journal of Geophysical Research: Solid Earth, 104*(B3), 5081-5095. doi: 10.1029/1998jb900092

Yamamoto, K., Terao, Y., Fujii, T., Ikawa, T., Seki, M., Matsuzawa, M., and Kanno, T. (2014). *Operational Overview of the First Offshore Production Test of Methane Hydrates in the Eastern Nankai Trough.* Presented at the Offshore Technology Conference, Houston, TX.

You, K., and Flemings, P. B. (2017). Methane hydrate formation in thick sand reservoirs: 1. Short-range methane diffusion. *Marine and Petroleum Geology*. doi: https://doi.org/10.1016/j.marpetgeo.2017.10.011

You, K., and Flemings, P. B. (in review). Methane Hydrate Formation in Thick Sand Reservoirs: 2. Long-Range Gas Transport. *Journal of Geophysical Research: Solid Earth*.

You, K., DiCarlo, D., and Flemings, P. B. (2015a). Quantifying hydrate solidification front advancing using method of characteristics. *Journal of Geophysical Research: Solid Earth, 120*(10), 6681-6697. doi: 10.1002/2015jb011985

You, K., Kneafsey, T. J., Flemings, P. B., Polito, P., and Bryant, S. L. (2015b). Salinity-buffered methane hydrate formation and dissociation in gas-rich systems. *Journal of Geophysical Research: Solid Earth, 120*(2), 643-661. doi: 10.1002/2014jb011190

Yousif, M. H., and Sloan, E. D. (1991). Experimental Investigation of Hydrate Formation and Dissociation in Consolidated Porous Media. doi: 10.2118/20172-pa

Zappoli, B., Beysens, D., and Garrabos, Y. (2014). *Heat Transfers and Related Effects in Supercritical Fluids* (Vol. 108): Spring Netherlands.

Chapter 2: Experimental Investigation of Gas Flow and Hydrate Formation Within the Hydrate Stability Zone[1]

ABSTRACT

I formed methane hydrate by injecting methane gas into a brine-saturated, coarse-grained sample under hydrate-stable thermodynamic conditions. Hydrate formed to a saturation of 11%, which is much lower than that predicted assuming three-phase (gas-hydrate-brine) thermodynamic equilibrium (67%). During hydrate formation, there were temporary flow blockages. I interpreted that a hydrate skin forms a physical barrier at the gas-brine interface. The skin failed periodically when the pressure differential exceeded the skin strength. Once the skin was present, further hydrate formation was limited by the rate that methane could diffuse through the solid skin. This process produced distinct thermodynamic states on either side of the skin that allowed gas to flow through the sample. This chapter illuminates how gas can be transported through the hydrate stability zone and thus provides a mechanism for the formation of concentrated hydrate deposits in sand reservoirs. It also illustrates that models that assume local equilibrium at the core-scale and larger may not capture the fundamental behaviors of these gas flow and hydrate formation processes.

---

[1]The full content of this chapter was published in *Journal of Geophysical Research*. The citation of that publication is:

Meyer, D. W., Flemings, P. B., DiCarlo, D. A., You, K., Phillips, S. C., and Kneafsey, T. (2018). Experimental investigation of gas flow and hydrate formation within the hydrate stability zone. *Journal of Geophysical Research: Solid Earth*. doi: 10.1029/2018JB015748

I designed and performed the experiments presented in that study and prepared the manuscript for publication. My co-authors are listed in order of contribution and provided support for conceptual development of the project, experimental design and execution, and manuscript preparation.

2.1 INTRODUCTION

Gas hydrate is a crystalline compound composed of a low molecular weight gas, most commonly methane, encased in a water lattice (Kvenvolden & McMenamin, 1980). It is stable at low temperature, low salinity, and high pressure where the methane concentration is above the solubility limit (Sloan & Koh, 2007). As a result, hydrate primarily forms in marine sediments along continental margins and beneath permafrost (Boswell & Collett, 2011).

Approximately, 10% of natural hydrate occurs in coarse-grained material (Boswell & Collett, 2011), which have favorable production characteristics (Boswell & Collett, 2011; Moridis, 2008; Yamamoto et al., 2014). Some of these reservoirs consist of thick, dipping, sand layers, bounded by low permeability material, that contain gas hydrate above and free gas below the hydrate stability zone (Boswell et al., 2012a; Boswell et al., 2009; Crutchley et al., 2015; Tréhu et al., 2004). Hydrate exists in these sand layers far above the base of hydrate stability at saturations ranging between 60 – 90% (Collett et al., 2012). The processes responsible for the formation of these thick, high concentration, hydrate deposits far above the base of hydrate stability remains a conundrum.

Three mechanisms are proposed for the formation of high hydrate concentrations in sand reservoirs: 1) short-range diffusion of dissolved methane into a sand layer from surrounding fine-grained material; 2) long-range advection of dissolved methane upward into the gas hydrate stability zone (GHSZ) and associated short-range methane diffusion; 3) long-range, buoyancy-driven advection of free methane gas into the GHSZ from below.

The first two mechanisms have been modeled (Cook & Malinverno, 2013; Nole et al., 2016; You & Flemings, 2017), with some field (Davie & Buffett, 2003; Malinverno & Goldberg, 2015; You & Flemings, 2017) and experimental (Priegnitz et al., 2013; Spangenberg et al., 2005) verification. In thick sands, short-range diffusion generates high hydrate concentrations at the boundaries of the sand, but low concentrations in the center (Rempel, 2011; You & Flemings, 2017). Long-range advection and diffusion of dissolved methane can result in significant saturations of hydrate, but requires very long timescales due to the low methane solubility in water and small solubility gradient between the advecting and surrounding fluids (Davie & Buffett, 2003; Nole et al., 2016; Rempel & Buffett, 1997; Torres et al., 2004; Xu & Ruppel, 1999).

The advection of free methane gas into the GHSZ has also been modeled (Liu & Flemings, 2007; Torres et al., 2004; You et al., 2015b) and studied in the field (Haeckel et al., 2004; Liu & Flemings, 2006; Tréhu et al., 2004). In this mechanism, free methane gas below the GHSZ migrates upward, driven by buoyancy, and preferentially accumulates in high permeability, coarse-grained layers (England et al., 1987; Schowalter, 1979). The high capillary entry pressure of the fine-grained material above the sand restricts vertical gas transport (England et al., 1987; Schowalter, 1979). Instead, gas migrates up-dip into the GHSZ, forming hydrate (Liu & Flemings, 2006; Torres et al., 2004; Tréhu et al., 2004) and elevating the local pore fluid salinity (Hesse & Harrison, 1981; Torres et al., 2004; Ussler & Paull, 2001). With continual gas supply, hydrate forms until the local salinity is elevated to the three-phase concentration (Liu & Flemings, 2007; You et al., 2015a), which occurs at the three-phase (gas, liquid, and hydrate) equilibrium hydrate saturation (S_{heq}). At three-

phase equilibrium, hydrate formation is limited and gas migrates farther into the GHSZ (Liu & Flemings, 2007; Torres et al., 2004; You et al., 2015a). This process produces an upward-propagating hydrate formation front with hydrate, gas, and water present at three-phase equilibrium conditions behind the front and brine at initial salinity present ahead of the front.

I performed experiments to elucidate the process of hydrate formation through gas injection. I injected methane gas into brine-saturated, coarse-grained samples under hydrate-stable conditions. Approximately 40% of the methane injected was converted into hydrate, resulting in a bulk hydrate saturation within the affected volume of 11%, far below that predicted by bulk thermodynamic equilibrium (67%). I propose that a hydrate skin forms at the gas-brine interface that separates the gas and brine phases. The skin limits hydrate formation and forms local and distinct thermodynamic states on either side of the hydrate skin, but does not significantly impede gas flow. This process provides a mechanism for gas transport through the hydrate stability zone. It also illustrates that models that assume local thermodynamic equilibrium at the core-scale and larger may not capture the fundamental physics of gas transport and hydrate formation in the hydrate stability zone.

2.2 METHODS

2.2.1 Experimental Setup

I performed each experiment in a vertical pressure vessel consisting of steel endcaps and an X-ray transparent, aluminum cylinder surrounded by a cooling jacket

(Figure 2.1), similar to other hydrate formation cells (Kneafsey et al., 2007; Seol & Kneafsey, 2009; You et al., 2015b). I packed the sediment samples in a Viton® sleeve (17.8 cm length; 5.1 cm internal diameter; 0.25 cm wall thickness) that was sealed on each end with steel endcaps. The endcaps were fitted with stainless steel filters, to prevent sediment migration out of the sample.

I recorded five-minute moving averages of the pressure and temperature data and recorded the pump volume data every five minutes. I used three Teledyne ISCO syringe pumps (flow accuracy ± 0.9 nL/hr; pump resolution = 31.7nL) to separately control the downstream brine flow rate (outlet), upstream methane pressure (inlet), and confining pressure (Figure 2.1). I used three UNIK 5000 pressure transducers to monitor the confining (P_{conf}), methane (P_{in}), and brine (P_{out}) pressures (Figure 2.1). I recorded the confining fluid temperature using two thermistors located in the confining cell, near the top and bottom of the sample (Figure 2.1) and tracked the ambient temperature using a thermocouple near the inlet pump. I used these data to confirm that the confining and ambient temperatures were kept constant (±0.2°C) and to calculate temperature corrections for the gas pump volume. I did not directly measure the temperature inside the sample. However, the thermal diffusivity of saturated sands (α) is approximately 10^{-6} m^2 s^{-1} (Liu & Flemings, 2007), which indicates a generic timescale for conduction ($\tau = r_{smpl}^2/\alpha$) across the sample radius (r_{smpl}) of approximately 0.18 hours. Since my experiments were run over the course of 85 hours, there was ample time for heat to dissipate by conduction. Thus, the confining thermistors provided a reasonable estimation of the internal sample temperature.

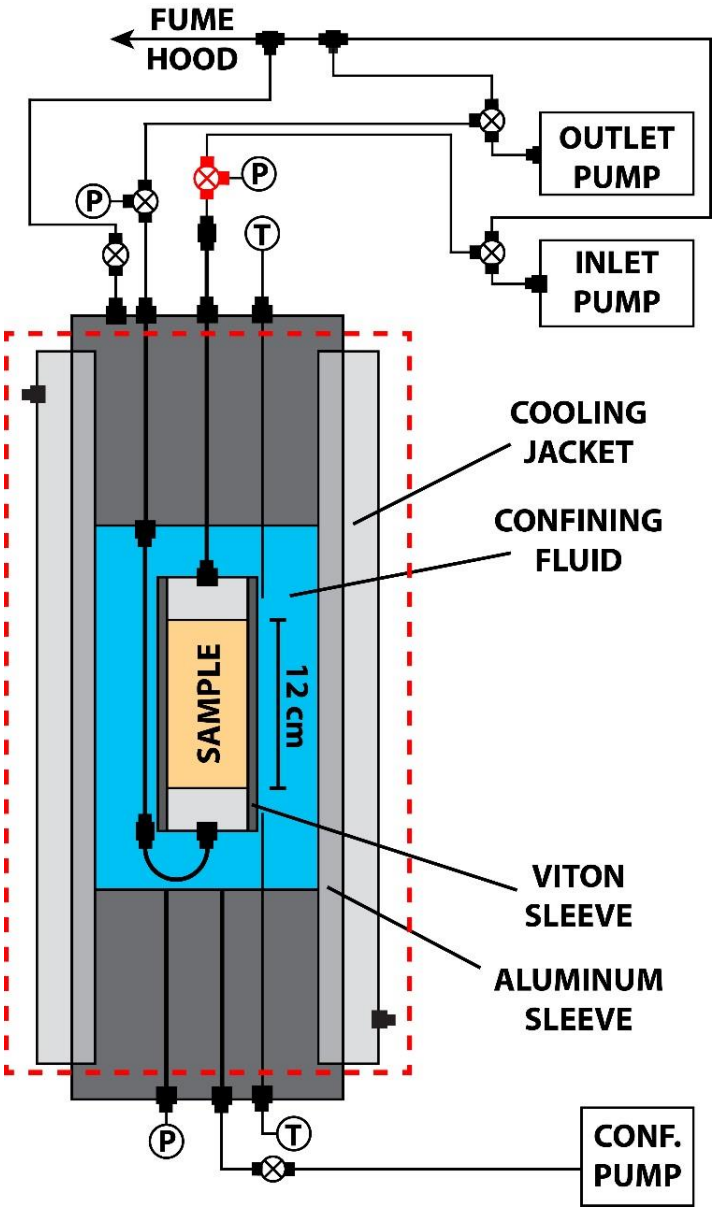

Figure 2.1: Diagram of the experimental apparatus.

The sample (approx. 12 cm length and 5 cm diameter) was suspended within the confining cell. Two thermistors (T) recorded the confining temperature, three syringe pumps controlled the fluid flow, and three pressure transducers (P) tracked the pressure of the pore and confining fluids. The inlet valve that separated the gas and brine prior to the experiment, is colored red. Red dashed line indicates the portion of the system that was in the hydrate stability zone.

Test Name	**Porosity, ϕ_{grav}**	**Salinity, C_i (wt% NaCl)**	**Pressure, P_{pore} (MPa)**	**Conf. Pressure, P_{conf} (MPa)**	**Temp, T_{conf} (°C)**	**CT[a]**
Gas-1	0.39	7	12.24	12.93	14.7	Y
Hydrate-1	0.41				1.01	Y
Hydrate-2	0.38				1.05	N
Hydrate-3	0.39				1.02	N

Table 2.1: Summary of Gas and Hydrate experimental parameters.

[a]Indicates experiments performed in the CT scanner.

2.2.2 Sample Preparation

Each sample consisted primarily of medium (362 μm median grain size; 263 μm 10th percentile; 502 μm 90th percentile), uniform (1.48 uniformity coefficient; Lambe, 1969), silica sand from Sigma-Aldrich® (Product No. 274739). I added 0.5 wt% smectite-rich clay from the Gulf of Mexico in the Eugene Island protraction area (Casey et al., 2013) to accelerate hydrate nucleation (Riestenberg et al., 2003). I stirred the dry sediment mixture with a whisk to assure a reasonably homogeneous clay distribution within the sample and packed the sample using slow, dry pluviation (Germaine & Germaine, 2009). I calculated the gravimetric porosity of the sample (ϕ_{grav}) from the mass of sediment, the total sample volume (V_{tot}), and the solid grain density ($\rho_s = 2.65\ g/mL$). I secured the sample inside the pressure vessel, filled the vessel with confining fluid, and transferred it to the vertical hanger frame.

While in the vertical position, I used two vacuum pumps to create a small pressure gradient within the sample that induced upward brine flow and pulled five pore volumes of brine through the sample. I collected the brine downstream and confirmed that no clay was entrained in the effluent brine. I then raised the pore (P_{pore}) and confining pressures to experimental conditions (Table 2.1), using the outlet and confining pumps, and measured the Skempton coefficient ($\beta = \Delta P_{pore}/\Delta P_{conf}$). The β-value was always greater than 0.85 after pressurization, suggesting that a negligible amount of gas remained in the sample.

I performed constant flow permeability tests (Olsen, 1966) at flow rates ranging from 5 – 50 mL/min on two brine-saturated samples at my experimental conditions. I determined that these samples had an intrinsic permeability of 4.9 ± 0.4 Darcy, which is a

reasonable value for clean sand packs with approximately 40% porosity (Davis & DeWiest, 1967; Onur, 2014; West, 2010).

2.2.3 Experimental Procedure

With the pore pressure (P_{pore}) at the experimental condition (Table 2.1), I pressurized the inlet pump to match P_{pore}, but kept the brine and methane separated at the inlet valve (Figure 2.1: red valve), outside the hydrate stability zone (Figure 2.1: red dashed box). I then cooled the sample to the experimental temperature (Table 2.1) and, prior to starting the experiment, identified and reduced any fluid leaks to less than 2% of the drainage rate. I then opened the inlet valve, bringing gas in contact with the brine, and rapidly (1 mL/min) removed enough brine to bring gas in direct contact with the sample. The gas and brine in the tubing were at room temperature during this process, which makes it very unlikely that hydrate formed within the tubing upstream of the sample. I then removed brine from the base of the sample at a constant rate (0.18 mL/hour) and maintained a constant gas pressure. In ended the experiments when the CT-derived low bulk density front (gas or hydrate) reached the sample outlet in order to maintain confidence in the masses of methane and brine in the sample. Detailed descriptions of my experimental equipment and procedures are included in Appendix A.

2.2.4 Experimental Parameters

I performed one gas flood (two-phase) experiment and three hydrate formation (three-phase) experiments (Table 2.1). I saturated the samples with a 7 wt% NaCl brine to reduce the predicted three-phase equilibrium hydrate saturation (S_{heq}) from 84% to 67%.

I maintained a constant effective stress ($P_{eff} = P_{conf} - P_{pore}$) of 0.7 MPa to limit sand migration and flow along the sample-sleeve boundary.

The maximum temperature at which hydrate is stable at the experimental pressure and salinity conditions is 11.5 ºC (Liu & Flemings, 2007). The gas flood experiment, Gas-1, was kept 3.2ºC greater than the hydrate stability temperature (Table 2.1). The hydrate formation experiments, Hydrate-1, Hydrate-2, and Hydrate-3, were kept 10.5ºC below the stability temperature (Table 2.1), to encourage rapid hydrate nucleation (Rees et al., 2011; Seol & Kneafsey, 2009; You et al., 2015b).

2.2.5 X-ray Computed-Tomography (CT) Scan Methods

I performed the gas flood (Gas-1) and one hydrate formation experiment (Hydrate-1) within a medical CT scanner. I collected scans, prior to the experiment, of the sample filled with only methane (dry) and only brine (wet) and then collected scans at least every 24 hours throughout the experiment. Each scan consisted of prismatic voxels (3 mm x 0.23 mm x 0.23 mm) approximately one grain wide and six grains long.

I determined the sample porosity (ϕ_{CT}) of each voxel using the CT attenuations measured in the wet (CT^{wet}) and dry (CT^{dry}) samples (Appendix B.4):

$$\phi_{CT} = \frac{CT^{wet} - CT^{dry}}{CT^{l-g}}. \quad (2.1)$$

CT^{l-g} is equal to the difference in CT attenuations of pure brine and methane. I calculated this value by assuming that the CT-derived porosity, averaged over the entire sample, equaled the gravimetric porosity (Appendix B.4). I used the CT porosity from each voxel (ϕ_{CT}), the grain density (ρ_s), and the fluid ($\rho_l = 1.063\ g/mL$) density (Hassanzadeh et al.,

2008; Pitzer, 1991) to calculate the bulk density of every voxel when only brine (ρ_b^{wet}) or methane (ρ_b^{dry}) were present in the sample. I linearly interpolated between these endpoint values to determine the bulk density of each voxel in each scan taken during the experiment (ρ_b^{exp}):

$$\rho_b^{exp} = \left[\rho_b^{dry} + \left(\left(\rho_b^{wet} - \rho_b^{dry}\right) \cdot \left(\frac{\left(CT^{exp} - CT^{dry}\right)}{\left(CT^{wet} - CT^{dry}\right)}\right)\right)\right]. \quad (2.2)$$

I calculated the methane gas phase saturation (S_g) in each voxel in Gas-1 using linear interpolation between the experimental bulk density and the bulk density endpoints of each voxel:

$$S_g = \frac{\left(\rho_b^{exp} - \rho_b^{wet}\right)}{\left(\rho_b^{dry} - \rho_b^{wet}\right)}. \quad (2.3)$$

I also used the CT scans to determine the affected voxels, defined by where the change in sample bulk density ($\Delta\rho_b = \rho_b^{exp} - \rho_b^{wet}$) exceeded the CT scanner measurement error (±0.024 g/cm^3; Appendix B.3.2). With a porosity of 40%, 0.024 g/mL equates to replacing the brine in a voxel with either 6% gas or 38% hydrate. I determined the pore volume of the affected voxels by multiplying the voxel volume (1.8×10^{-4} mL) by the initial porosity of each affected voxel (ϕ_{CT}). I then calculated the total affected volume (V_{aff}) as the sum of the individual pore volumes of each affected voxel. The affected volume may be underestimated by between 0.5 – 2.6 mL due to the fluid dispersion grooves in the sample endcap and an approximately 1mm buffer between the endcap and the first CT slice. This error decreases throughout the experiment, however, relative to the

total estimated affected volume. Appendix B contains a detailed description of my complete CT post-processing and analysis procedures.

2.3 RESULTS

2.3.1 Sample Porosity

The CT-derived porosity (Equation 2.1) in Gas-1 (Figure 2.2a: red line) and Hydrate-1 (Figure 2.2a: green line) decreased downward from 43.5% to 38% and 39%, respectively. Sediment compaction during packing resulted in low porosity regions near the sample outlets and sample handling created narrow, high porosity fingers extending down the edges of the samples (Figure 2.2b and c).

2.3.2 Pressure Differentials

In Gas-1, no significant pressure differentials ($dP = P_{in} - P_{out}$) across the sample were observed (Figure 2.3a: red line). In the hydrate formation experiments, however, temporary pressure differentials continuously formed and dissipated (Figure 2.3a: green line). Since the gas pressure was held constant, these differential pressures were the result of decreasing brine pressure. Individual pressure differentials increased at approximately 0.18 MPa/hr before exceeding some critical value and decreasing rapidly (Figure 2.3b: green line). Typically, the samples maintained a differential pressure of approximately 0.1 MPa throughout the experiments, but reached maximum values in Hydrate-1, Hydrate-2, and Hydrate-3 of 0.48, 0.25, and 0.69 MPa, respectively. Differential pressure development was correlated with a significant reduction in the gas flow rate and, when the differential

pressure dissipated, was followed by rapid gas flow into the sample (Figure 2.3b: black line).

2.3.3 Fluid Volumes

In Gas-1, the volume of methane injected (V_m; Figure 2.4: red line) was always approximately equal to the volume of brine removed (V_l; Figure 2.4: dashed black line). In the hydrate experiments (Figure 2.4: green, pink, and blue lines) the methane injected always exceeded the brine removed within the first 1.5 hours of the experiment and, after 85 hours, an average of 22.6 ± 1 mL of methane had been injected into the samples. Fluctuations in the volume data were driven by minor ambient temperature variations.

2.3.4 CT-Derived Bulk Density

In Gas-1, the bulk density decrease exceeded the CT error (Figure 2.5a: red dashed line) within the upper 2 cm, after 48 hours (Figure 2.5a: black dashed line), and the upper 3 cm, after 83 hours (Figure 2.5a: black dotted line). The gas saturation (Equation 2.3) near the inlet increased from 61% to 66%, between 48 and 83 hours, and always decreased downward. Gas flow was primarily concentrated along a narrow finger at the edge of the sample (Figure 2.5b – d) coincident with a zone of high initial porosity (Figure 2.2b).

At the beginning of Hydrate-1, the bulk density decrease exceeded the CT error (Figure 2.6a: red dashed line) within the top 0.5 cm of the sample (Figure 2.6a: solid black line) due to gas injection during experiment initialization. This decrease was concentrated in the upper corners of the sample (Figure 2.6b) where the initial porosity was high (Figure 2.2c). After 48 hours, the bulk density decreased in the region from 0 – 3.6 cm (Figure

2.6a: dashed black line) throughout the center of the sample (Figure 2.6c). Below 3.6 cm, there was flow both down the sample edge and across the sample (Figure 2.6c). After 85 hours, the bulk density decreased within the region from 3.5 – 7 cm (Figure 2.6a: dotted black line), relative to 48 hours elapsed, primarily in the center of the sample and along the opposite edge from the original preferential flow (Figure 2.6d).

2.3.5 Affected Volumes

In Gas-1, the affected volume (V_{aff}; Section 2.5), increased to 25.4 mL by the end of the experiment (Figure 2.7: red dots) at approximately 0.3 mL/hour (Figure 2.7: dashed red line). In contrast, in Hydrate-1, the affected volume increased to 60.1 mL by the end of the experiment (Figure 2.7: green dots) at approximately 0.7 mL/hour (Figure 2.7: dashed green line).

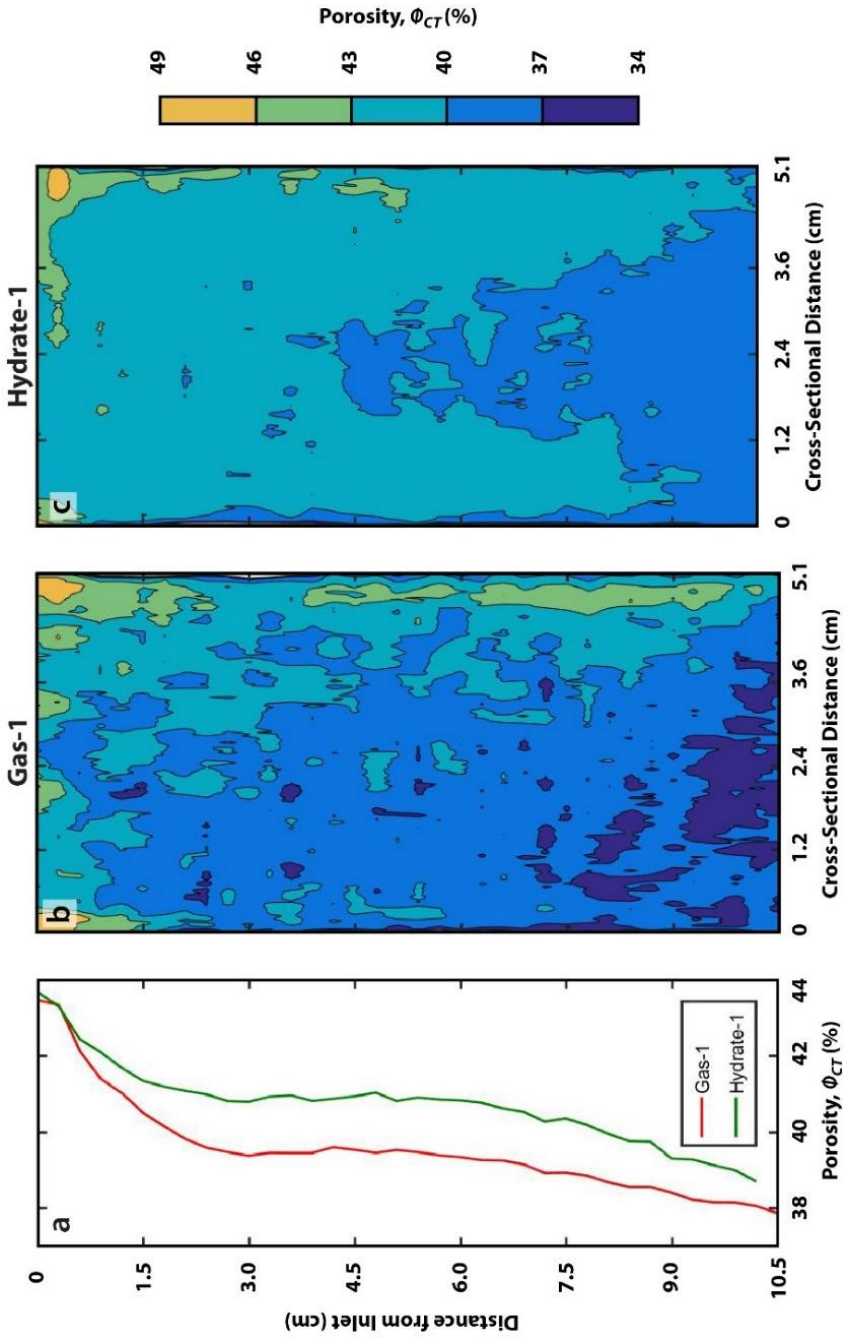

Figure 2.2: Initial porosity of samples used in the Gas-1 and Hydrate-1.

Values are calculated from the dry and wet scans (Equation 2.1). (a) CT porosity, averaged across each slice, with distance from the inlet in Gas-1 (red line) and Hydrate-1 (green line). (b) and (c) Porosity along the center plane of the sample in Gas-1 and Hydrate-1.

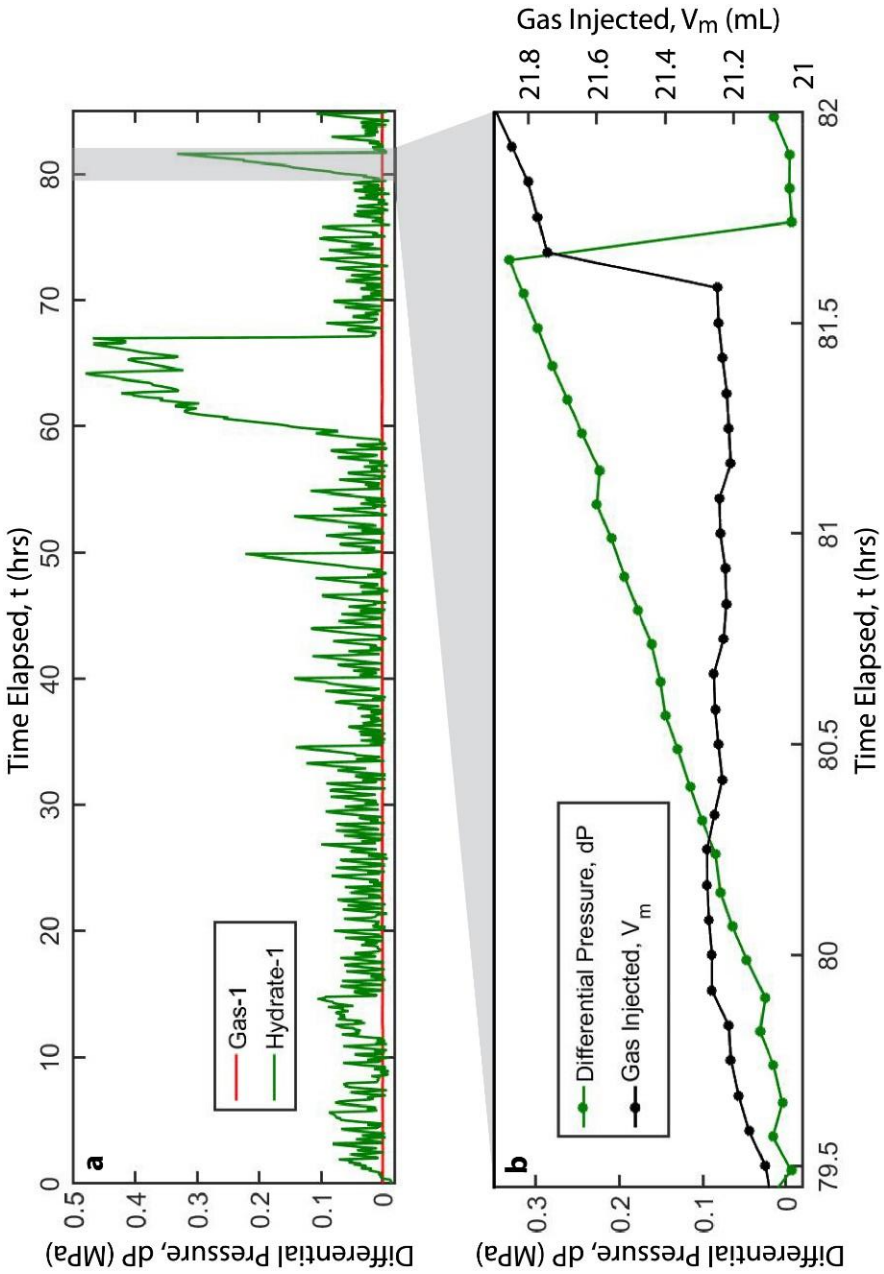

Figure 2.3: Differential pressure development in Hydrate-1.

Similar behavior was observed in all hydrate formation experiments. (a) Differential pressure (dP) results from both Gas-1 (red line) and Hydrate-1 (green line). Temporary pressure differentials, not observed in Gas-1, developed throughout Hydrate-1. (b) Development of a single pressure differential in Hydrate-1 compared to the volume of methane injected during the same period.

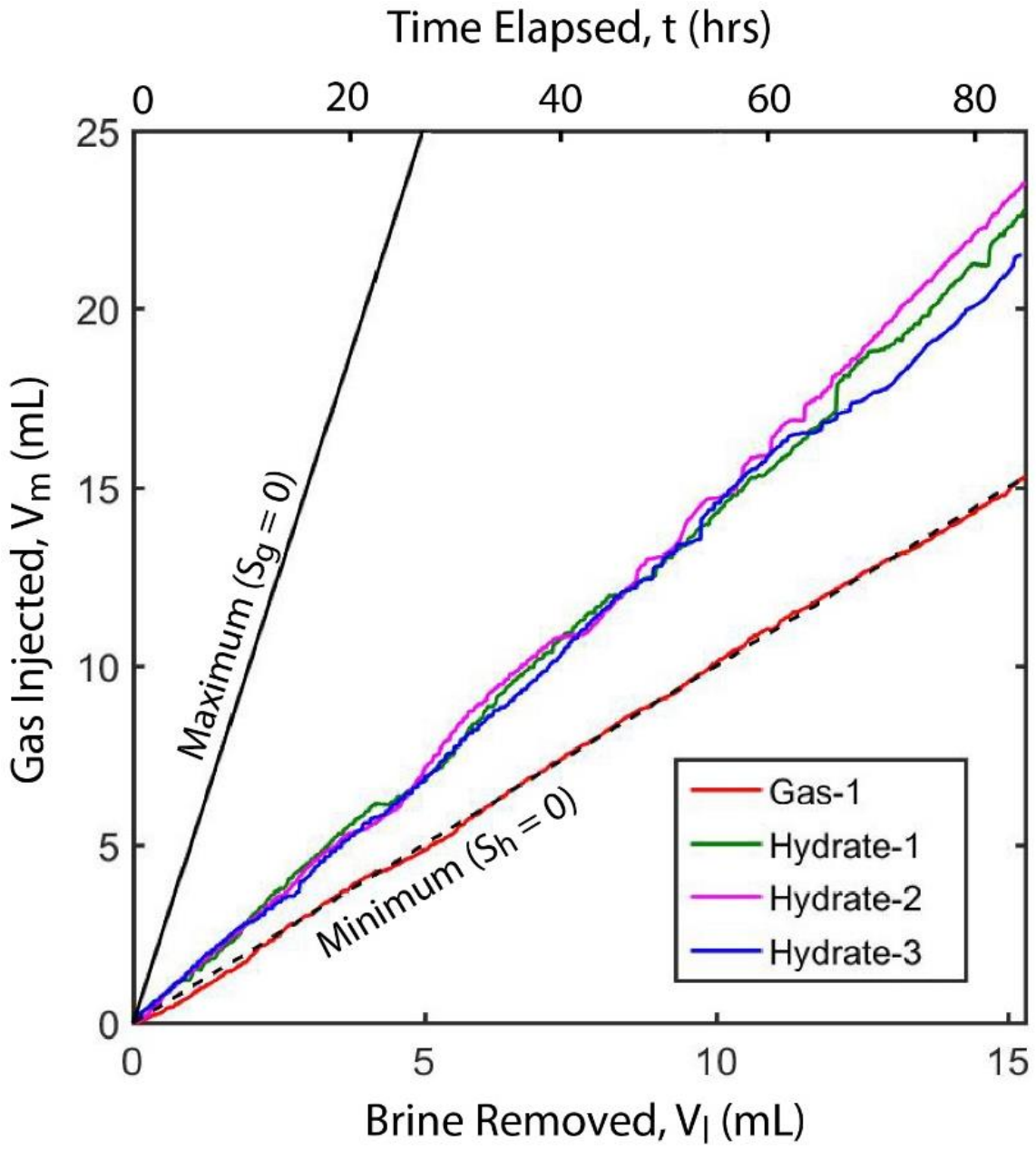

Figure 2.4: Volumes of the methane injected during the experiments.

Comparison of data from the gas flood (red line) and hydrate formation experiments (green, pink, and blue lines) to the experimental minimum (dashed black line) and maximum (solid black line) endmembers (Appendix C.2).

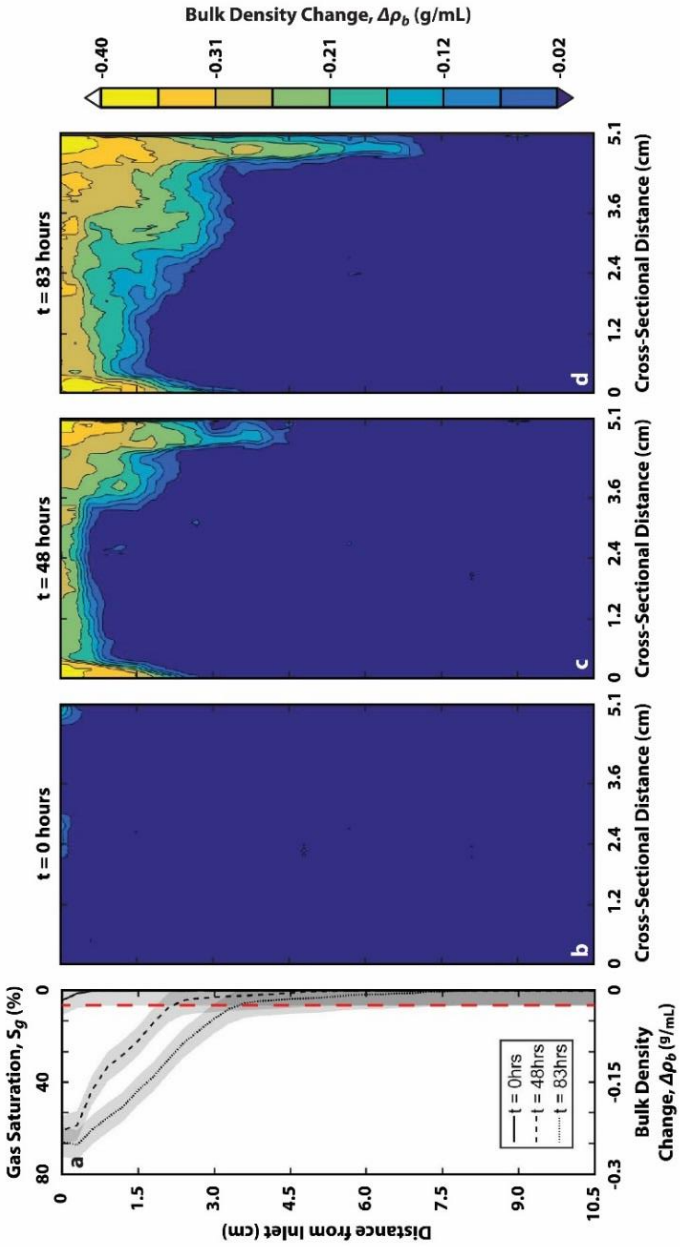

Figure 2.5: Evolution of the bulk density change during Gas-1.

(a) Change in bulk density ($\Delta\rho_b$), averaged across each slice, as a function of distance from the inlet (Equation 2.2). Gas saturation is calculated using Equation 2.3, assuming a porosity of 40%. Dashed red line indicates the CT measurement error (Section 2.2.5) and shaded regions indicate one standard deviation in the CT data. (b) – (d) Two-dimensional change in bulk density along the center plane of the sample after 0, 48, and 83 hours elapsed.

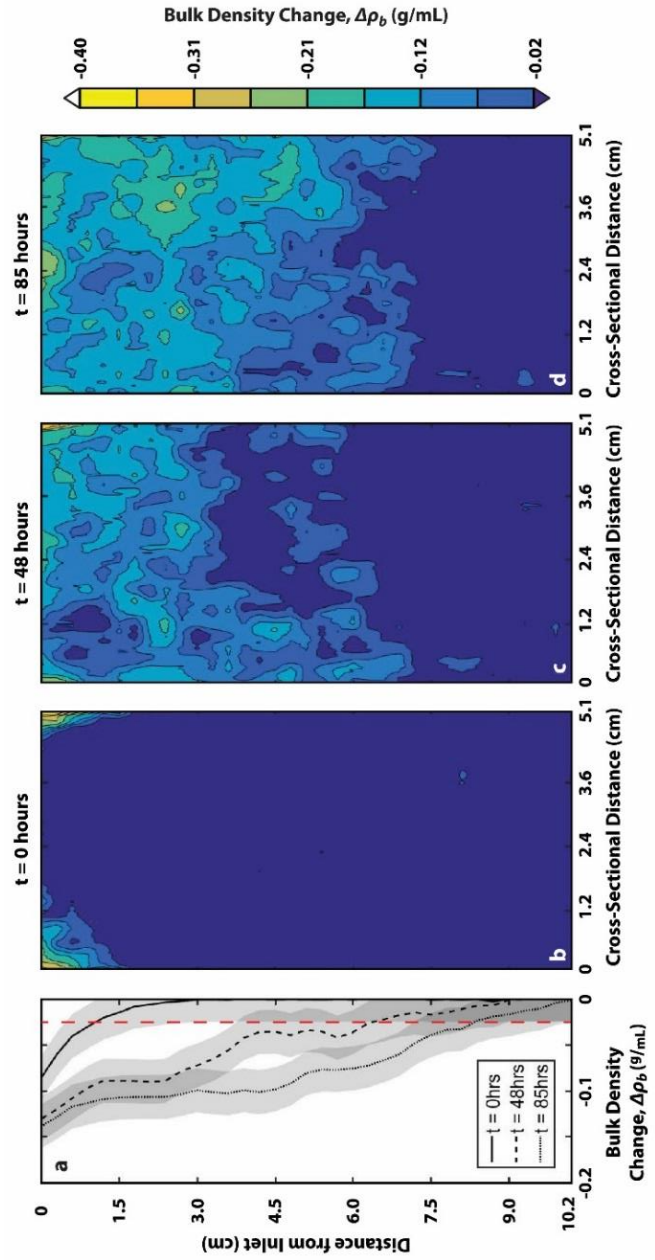

Figure 2.6: Evolution of the bulk density change during Hydrate-1.

(a) Change in bulk density ($\Delta\rho_b$), averaged across each slice, as a function of distance from the inlet (Equation 2.2). Dashed red line indicates the CT measurement error (Section 2.2.5) and shaded regions indicates one standard deviation in the CT data. (b) – (d) Two-dimensional change in bulk density along the center plane of the sample after 0, 48, and 85 hours elapsed.

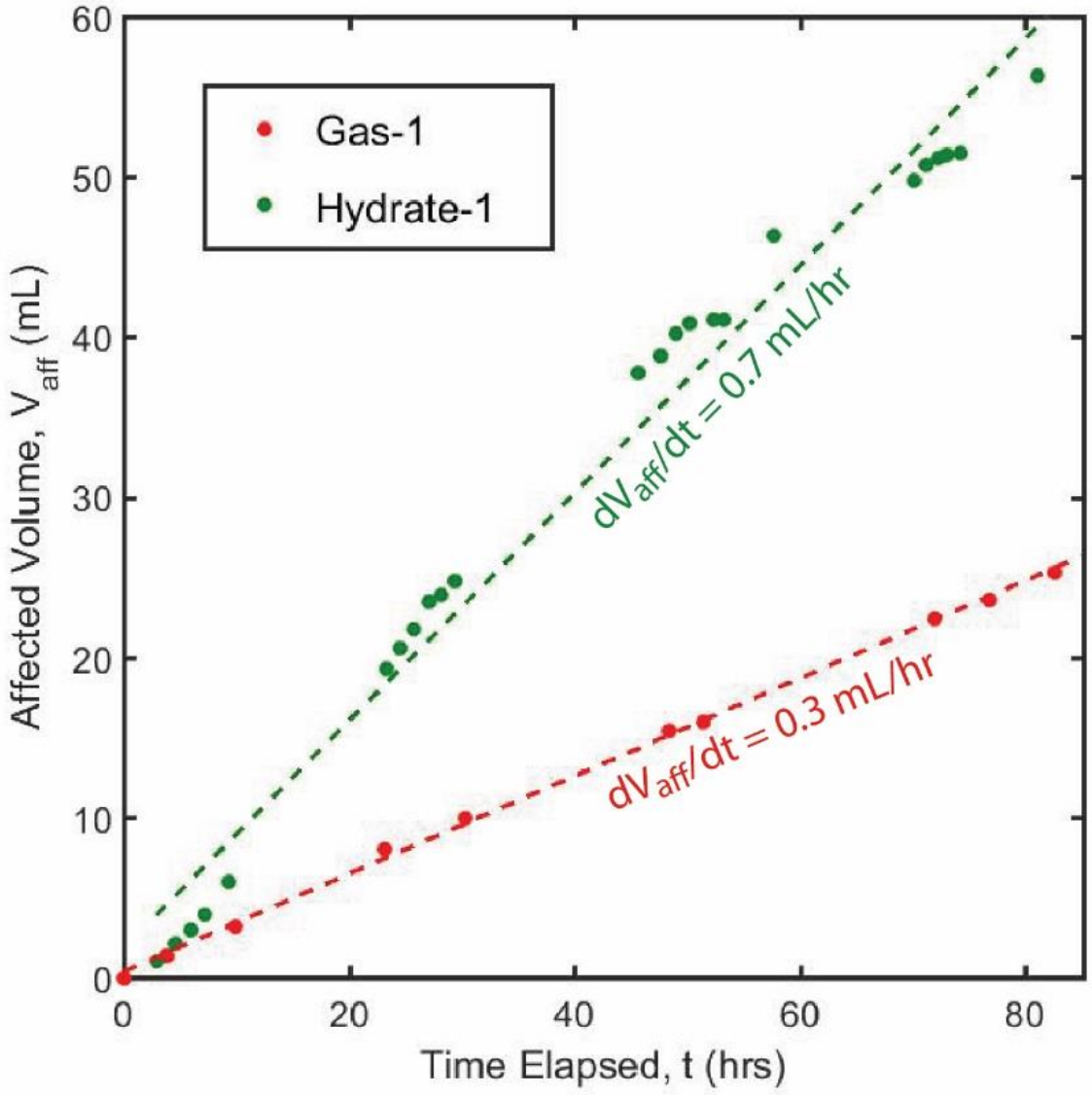

Figure 2.7: Affected volume during Gas-1 and Hydrate-1.

Dots indicate experimental data. Dashed lines indicated the best fit linear trends for each experiment.

2.4 Mass Balance Analysis

I use mass balance (Appendix C.2) to determine the relationship between the volumes of gas injected and brine removed and the amount of hydrate and gas present in the sample (Figure 2.8). I assume that: 1) the brine density is constant (maximum density increase due to elevated salinities is 13% of the initial density); 2) the mass of methane dissolved in the brine is negligible; and 3) the pore volume is constant (confirmed by monitoring the confining pump volume and axial CT slice radii).

I convert the volumes of methane injected (V_m) and brine removed (V_l) during each experiment (Figure 2.4) into an equivalent methane (m_m) and water (m_w) mass. m_m must be equal to the mass of methane gas (m_m^g) plus the mass of methane in the hydrate (m_m^h) in the sample ($m_m = m_m^g + m_m^h$). m_w must be equal to the original mass of water in the sample (m_{wi}) minus the masses of water in liquid (m_w^l) and hydrate (m_w^h) in the sample ($m_w = m_{wi} - m_w^l - m_w^h$). I calculate m_m^g and m_m^h from mass balance (Appendix C.2) and convert these values into equivalent volumes of the free gas (V^g) and hydrate (V^h) using the phase densities and stoichiometry (Table D.1).

From this mass balance, I define the following ratios (Appendix C.2): 1) the mass conversion ratio ($X_{conv} = m_m^h/m_m$) is the ratio of the mass of methane converted to hydrate to the total mass of methane injected; 2) the volumetric injection ratio ($X_{inj} = V_m/V_l$) is the ratio of the volume of methane injected to the volume of brine removed (Figure 2.8: solid line); 3) the volumetric gas phase ratio ($X^g = V^g/V_l$) is the ratio of the volume of methane gas in the sample and the volume of brine removed (Figure 2.8: dot-

dashed line); and 4) the volumetric hydrate phase ratio ($X^h = V^h/V_l$) is the ratio of the volume of hydrate in the sample and the volume of brine removed (Figure 2.8: dashed line).

With no gas conversion ($X_{conv} = 0$), the volume of methane injected equals the volume of brine removed ($X_{inj} = 1$) and all the methane is in the gaseous phase ($X^g = 1$; $X^h = 0$). With total gas conversion into hydrate ($X_{conv} = 1$), the volume of methane injected is 5.34 times the volume of brine removed ($X_{inj} = 5.34$), there is no gaseous phase ($X^g = 0$), and there is 4.93 times more hydrate present than brine removed ($X^h = 4.93$). These cases represent the minimum (Figure 2.4: dashed black line) and maximum (Figure 2.4: solid black line) hydrate formation scenarios for my experiments. An injection ratio between these endmembers indicates partial gas conversion into hydrate and the presence of both methane gas and hydrate in the sample at a particular volumetric ratio.

In Gas-1, X_{inj} was always approximately one (Figure 2.9: red line), indicating that no hydrate formed in the sample ($X_{conv} = 0$) and that gas directly replaced brine ($X^g = 1$; $X^h = 0$), as expected. In the hydrate experiments, X_{inj} and X_{conv} slowly increased (Figure 2.9: green, pink, and blue lines), to final values, averaged across all experiments, of 1.48 ± 0.06 and 0.40 ± 0.03, respectively (Figures 2.8 and 2.9: red cross), indicating that both gas and hydrate were present in the sample throughout the experiments. At this conversion ratio, the volumetric gas ($X^g = 0.90$) and hydrate ($X^h = 0.55$) phase ratios at the end of the experiments (Figure 2.8) indicate that the combined volume of gas and hydrate in the sample was 1.45 times greater than the volume of brine removed.

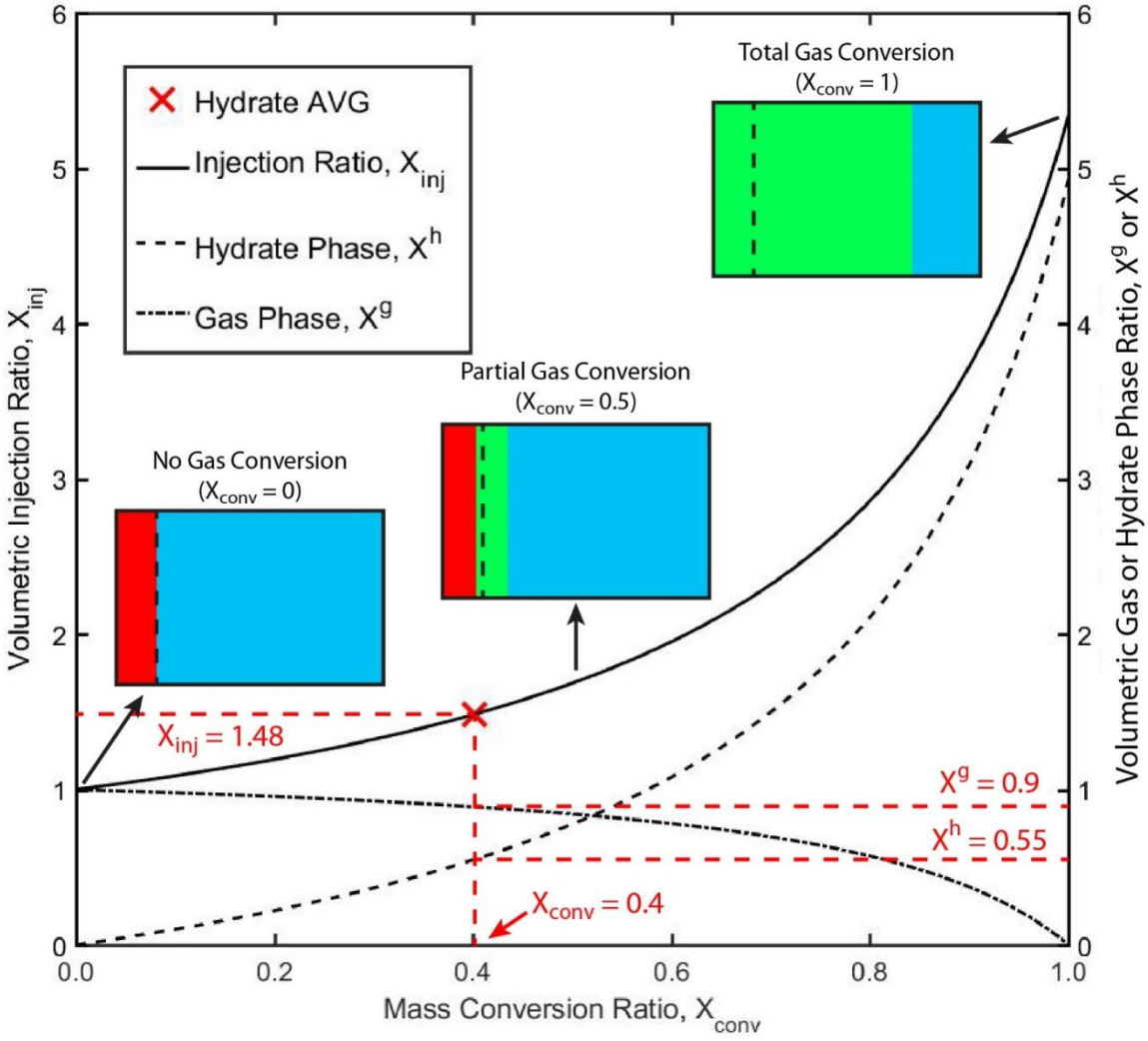

Figure 2.8: Relationship between conversion, injection, and phase ratios.

Volumetric injection ratio (X_{inj}; solid line) and volumetric hydrate (X^h; dashed line) and gas (X^g; dot-dashed line) phase ratios as a function of the mass conversion ratio (X_{conv}). Red dashed lines show the average X_{conv}, X_{inj}, X^g, and X^hat the final state of the hydrate experiments (red cross). Inset images show normalized gas (red), hydrate (green), and liquid (blue) phase volumes in a unit cell with X_{conv} equal to 0, 0.5, and 1. Black dashed line in each inset image indicates the original volume of brine removed from the unit cell.

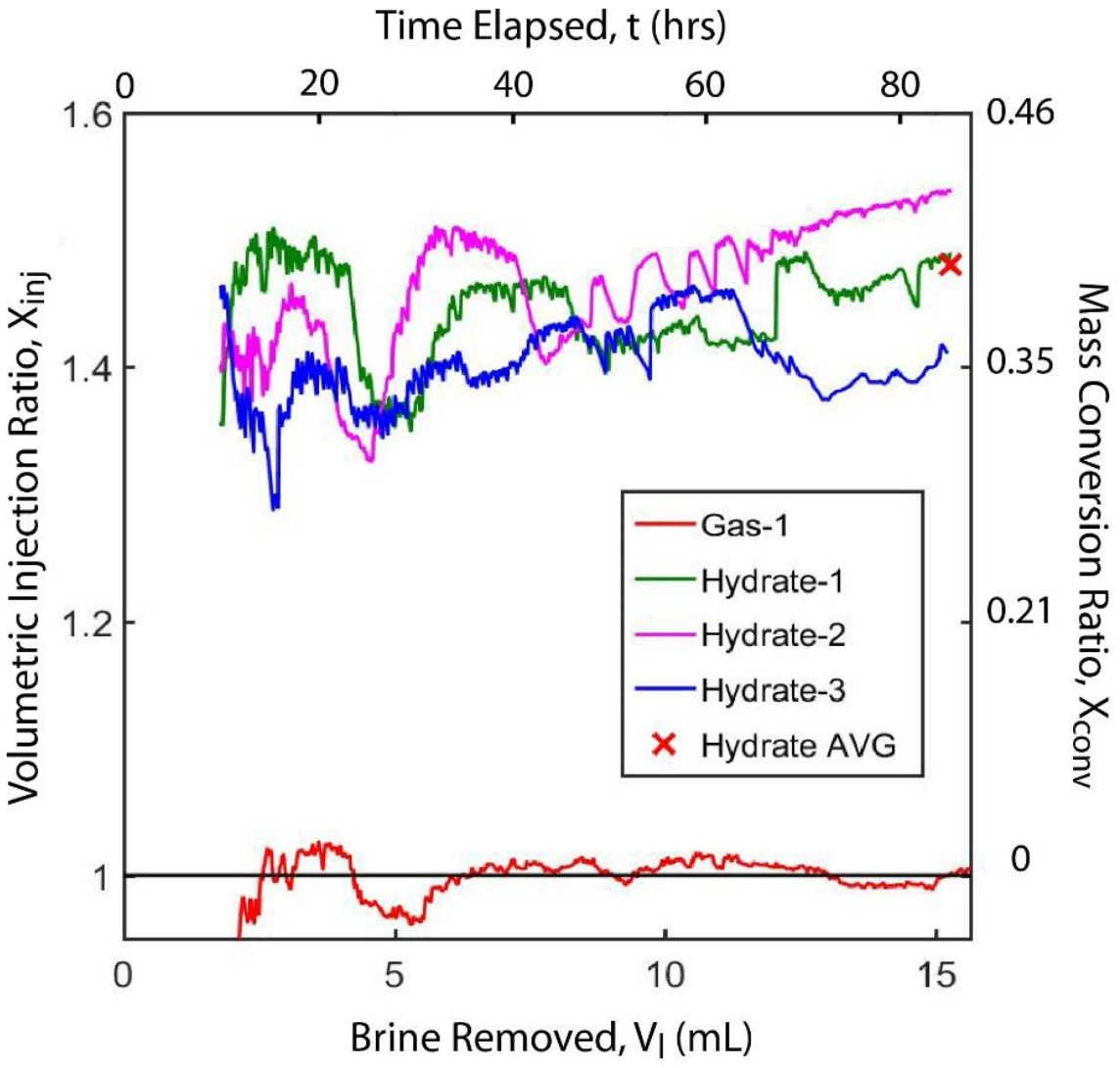

Figure 2.9: Mass balance results from the experiments.

Volumetric injection (X_{inj}) and mass conversion (X_{conv}) ratios during the gas flood (red line) and hydrate formation (green, pink, and blue lines) experiments (Appendix C.2). Red cross indicates the average X_{conv} and X_{inj} and the end of the hydrate experiments. Decrease in X_{conv} in Hydrate-3 after 62 hours was caused by a persistent gas blockage.

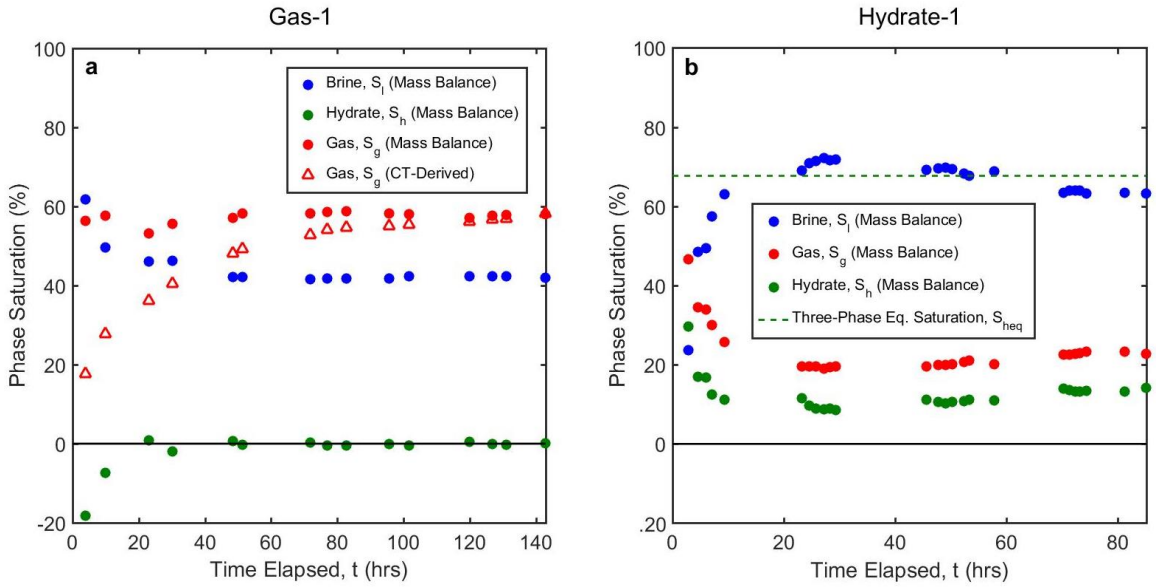

Figure 2.10: Bulk phase saturations during Gas-1 and Hydrate-1.

(a) Mass balance-derived bulk gas (red dots), brine (blue dots), and hydrate (green dots) phase saturations compared to the CT-derived bulk gas phase saturation (red triangles) within the affected volume during Gas-1. (b) Mass balance-derived bulk brine (blue dots), hydrate (green dots), and gas (red dots) phase saturations within the affected volume during Hydrate-1. Dashed green line represents the bulk hydrate saturation required to elevate the bulk salinity to the three-phase equilibrium concentration.

I calculate the bulk phase saturations of the methane gas (S_g), liquid brine (S_l), and solid hydrate (S_h) within the affected volume (V_{aff}) in my experiments using mass balance (Appendix C.1):

$$S_g = \frac{\frac{\rho_h}{M_h}\left(\frac{\rho_g M_w N V_m}{(1-C_i)} + \rho_l M_m V_l\right) - \rho_g \rho_l V_m}{V_{aff}\left(\frac{\rho_h}{M_h}\left(\frac{\rho_g M_w N}{(1-C_i)} + \rho_l M_m\right) - \rho_g \rho_l\right)}, \quad (2.4)$$

$$S_l = 1 - S_g + \frac{\rho_g M_h}{M_m \rho_h}\left(S_g - \frac{V_m}{V_{aff}}\right), \text{ and} \quad (2.5)$$

$$S_h = 1 - S_g - S_l. \quad (2.6)$$

This calculation is susceptible to changes in the gas volume due to ambient temperature fluctuations and to the underestimation of V_{aff} (Section 2.5). These errors are greatest near the beginning of the experiments when V_{aff} is smaller.

In Gas-1, the mass balance-derived bulk gas (Figure 2.10a: red dots), brine (Figure 2.10a: blue dots), and hydrate (Figure 2.10a: green dots) phase saturations within the affected volume reached steady-state values of 58%, 42%, and 0% respectively. The CT-derived bulk gas saturation (Figure 2.10a: red triangles) within the affected volume also increased to 58% during the experiment. The eventual agreement between the mass balance and CT-derived gas saturations indicates that the affected volume, at least in a gas-brine system, is an accurate measure of the volume containing gas. I assume this relationship extends to the gas-brine-hydrate system as well.

In Hydrate-1, between 23 – 85 hours, the average mass balance-derived bulk gas (Figure 2.10b: red dots), brine (Figure 2.10b: blue dots), and hydrate (Figure 2.10b: green dots) saturations within the affected volume were 21%, 68%, and 11%, respectively.

Compared to Gas-1, this indicated that hydrate formation in the sample resulted in a decrease in the amount of free gas present and an increase in the amount of brine remaining in the affected volume.

Liu and Flemings (2006) indicated that salt exclusion during hydrate formation raises the bulk salinity ($C = C_i/[1 - S_h]$) as a function of the hydrate saturation (S_h) and the initial salinity (C_i). The average S_h in the affected volume in Hydrate-1 is 11%, which would elevate the brine salinity to 8.1 wt% NaCl in that region. This indicates that both the bulk salinity and the hydrate saturation during Hydrate-1 were far below the three-phase equilibrium values (C_{eq} = 21wt% NaCl; S_{heq} = 68%).

2.5 DISCUSSION

My results illuminate how hydrate forms during gas injection into porous media at the core-scale. I interpret that, during injection, a hydrate skin forms at the gas-brine interface and separates the gas from the brine. As a result, the gas, hydrate, and brine are not at thermodynamic equilibrium. The formation of a hydrate skin has been demonstrated experimentally at the pore-scale (Davies et al., 2010; Jin et al., 2012; Katsuki et al., 2007; Taylor et al., 2007). My contribution is to demonstrate how this micro-scale phenomenon controls gas flow and hydrate formation at the macro-scale.

I show that hydrate formation occurs rapidly and consistently at my experimental conditions (Figure 2.4), temporary flow blockages develop (Figure 2.3), and hydrate and gas are distributed throughout the sample (Figures 2.6). Approximately 40% of the methane injected during the hydrate experiments is converted into hydrate (Figure 2.9),

which results in an average hydrate saturation within the affected volume of 11% (Figure 2.10b). This saturation is much less than the hydrate saturation predicted assuming three-phase equilibrium, which is 67% (Figure 2.10b: green dashed line). The brine saturation within the affected volume (Figure 2.10) in the hydrate experiments (68%) is much greater than in the gas flood experiment (42%). I present a conceptual hydrate formation model (Figure 2.11) and a one-dimensional diffusion model (Figure 2.12) that captures these macro-scale observations.

2.5.1 Macro-Scale Hydrate Formation Model

In the hydrate formation experiments, hydrate nucleates rapidly at the gas-brine interface, forming a continuous hydrate skin that blocks the pore throats along the flow path and, periodically, blocking flow entirely (Figure 11a). After blockage, continued brine removal increases the pressure differential across the hydrate skin until it fails at the weakest point. Gas then flows into the sample until the gas and brine reach mechanical equilibrium. Subsequently, hydrate nucleates and a new hydrate skin forms over time with the rate limited by nucleation kinetics and/or the rate that the hydrate solidifies into an impermeable skin (Natarajan, et al., 1994; Taylor et al., 2007; Skovborg, et al., 1993). Through this process, gas is distributed and hydrate forms throughout the sample (Figure 11b). There was a higher brine saturation (Figure 10) within a larger affected volume (Figure 7) in Hydrate-1, compared to Gas-1. I interpret that the hydrate skin blocks gas access to a larger fraction of the pores and forces gas farther into the sample than would occur without hydrate.

2.5.2 Pore-Scale Hydrate Skin Growth

The hydrate skin separates the brine and gas and limits hydrate formation to the rate that methane can diffuse through the solid hydrate (Taylor et al., 2007). I describe this process with a one-dimensional model where methane is transported by diffusion through a liquid phase within the microporous hydrate (Kuhs et al., 2000; Kuhs et al., 2004). Between the methane gas and the hydrate, there is a thin, metastable, liquid layer (Figure 2.12a), similar to the premelted water observed in ice-air systems (Dash et al., 2006; Rempel et al., 2004), into which methane gas dissolves. The methane concentration at the gas-hydrate interface equals the methane gas solubility in water (C_m^g), because there is an abundance of methane gas and no water to form hydrate. The methane concentration at the brine-hydrate interface equals the hydrate solubility in water (C_m^h), because the local concentration must be in equilibrium with hydrate.

In this model, the hydrate skin thickness (x) increases with the square root of time (Appendix D.1):

$$x = \sqrt{\frac{2D_m M_h (C_m^g - C_m^h)}{\rho_h}}\sqrt{t}. \quad (2.7)$$

The methane concentration gradient ($dC_m = [C_m^g - C_m^h/x]$; Figure 2.12b), the diffusion coefficient of methane through hydrate (D_m), and time (t) control the hydrate skin thickness (Equation 2.7). D_m can range from 10^{-14} m^2 s^{-1} (Davies et al., 2010) to 10^{-16} m^2 s^{-1} (Genov et al., 2004; Kuhs et al., 2006). For a value of D_m equal to 10^{-15} m^2 s^{-1}, the hydrate skin thickness (Figure 2.12c) is 0.04 μm after one minute, 0.28 μm after one hour, and 2.6 μm at my experimental timescale (85 hours). Over this period,

the growth rate decreases 70-fold due the increasing length scale through which methane must diffuse (Figure 2.12c).

I independently estimate the average hydrate skin thickness (x_{avg}) from the hydrate saturation (S_h), the gravimetric porosity (ϕ_{grav}), and the gas-brine interfacial area per porous medium volume (A_i):

$$x_{avg} = \frac{\phi_{grav} S_h}{A_i}. \quad (2.8)$$

Brusseau et al. (2006; 2007) experimentally determined the relationship between the water saturation (S_l) and the interfacial area in sand packs during drainage. This area increases linearly with the water saturation with a slope dependent upon the grain size. For the sand used in this study A_i, in units of cm^{-1}, is calculated by:

$$A_i = 147[1 - S_l]. \quad (2.9)$$

This relationship is robust for both imbibition and drainage, which have fundamentally different pore-filling processes. Therefore, I can assume that this relationship is also applicable to the intermittent gas flow in my experiments. The brine saturation at the end of Hydrate-1, prior to hydrate formation ($S_l = 1 - S_g$), is 77%, which indicates an A_i equal to 34 cm^{-1} (Equation 2.9). From Equation 2.8, I calculate that x_{avg} equals 13.3 μm at the end of Hydrate-1. This value is greater than predicted by my diffusion model (2.8 μm) at my experimental timescale, but is similar to experimental observations (Taylor et al., 2007) of hydrate skins between 10 – 60 μm thick.

I interpret that, initially, hydrate formation occurs more rapidly than described by diffusion, but decreases dramatically once the hydrate skin fully solidifies as has been

observed (Davies et al., 2010; Taylor et al., 2007). It is also possible that the methane concentration gradient through the hydrate may be controlled by the hydrate cage occupancy in the presence of excess gas and excess water. This condition would increase the difference in methane concentration by a factor of 7.2 (Huo et al., 2003), which would increase the hydrate growth rate by a factor of 2.7; this increase results in a skin thickness of 7.6 μm after 85 hours, using the same parameters as above. While these results suggest that the early formation process is more complicated than can be described by simple diffusion, the net results is that a very thin hydrate skin forms quickly and that methane transport is very limited once this hydrate forms. As a results, the skin is thicker near the inlet, where it is older, and thinner at the outlet, where it is younger.

2.5.3 Salinity at Brine-Hydrate Interface

As hydrate forms at the brine-hydrate interface, salt is excluded and the local salinity increases. The salt concentration gradient drives salt diffusion away from the hydrate and competes with the hydrate-driven salt flux to control the local salinity. I derived a salt flux that decreases with time and is equal to the mass of salt excluded by hydrate formation (Appendix D.2). I then solve for the salt concentration with distance from the hydrate over time with this salt source using Laplace transformation (Appendix D.3). I assume a D_m equal to 10^{-15} m^2 s^{-1} and a characteristic length (L_c) of 100 μm (approximately one-third of a grain diameter). Immediately after initial hydrate formation (Figure 2.12d: blue line), the salinity increases at the brine-hydrate boundary, producing a concentration gradient near the hydrate skin that causes NaCl to diffuse away from the hydrate. As the hydrate skin grows, the hydrate formation rate and, subsequently, the salt

source decline. As a result, the salt gradient dissipates rapidly and the salinity rises across the characteristic length at an approximately uniform concentration (Figure 2.12d: red, green, and pink lines). By the end of my experiments (85 hours), the bulk salinity reaches 7.2 wt% NaCl, which is far below C_{eq} (21 wt% NaCl).

Increasing hydrate formation rate, through a larger D_m or dC_m or longer characteristic length, does not change the fundamental behaviors of the model: the salt loss due to diffusion quickly exceeds the salt source due to hydrate formation. As a result, I envision that the brine adjacent to the hydrate is well-mixed with approximately uniform, but gradually increasing, salinity. This model shows that hydrate formation is primarily limited by methane diffusion across the hydrate skin.

2.5.4 Field-Scale Implications

The rapid diffusion of salt away from the hydrate skin produces different thermodynamic states on either side of the skin. On the gas-side, hydrate, premelt water (Figure 2.12a), and methane gas are present in three-phase equilibrium. On the brine-side, hydrate and brine at a salinity well below the three-phase concentration are present in two-phase equilibrium. Since methane transport through the skin is very slow, these states can coexist for tens to thousands of years. This transport limitation provides a mechanism for gas to coexist with water and hydrate at the pore-scale within systems that are generally assumed to be at two-phase (liquid-hydrate) equilibrium conditions.

The formation of the hydrate skin, however, does not significantly impede gas flow through the sample. In my experiments, flow was maintained with the development of a pressure differential of approximately 0.1 MPa. In the field, the collection of a continuous,

10-meter gas column, which is not an uncommon occurrence in active hydrocarbon regions (Boswell et al., 2012b; Frye et al., 2012), would provide this pressure gradient. Thus, this mechanism could explain vertical gas migration far above the base of hydrate stability without requiring bulk thermodynamic equilibrium. This behavior is similar to a non-equilibrium flow model recently presented by Fu et al. (2018) and to hydrate formation on the walls of a fracture separating gas and water within the hydrate stability zone (Ginsburg & Soloviev, 1997; Riedel et al., 2006).

This behavior could generate the high hydrate saturations observed in the field. The hydrate saturation that I observed at laboratory timescales is low (11%), compared to field observations (60 – 90%). However, methane will continue to diffuse through the skin and form additional hydrate at the brine-hydrate interface. Over thousands of years this could significantly increase the bulk hydrate saturation. Additionally, I suspect this saturation is strongly dependent on the flow rate and expect lower flow rates, such as those observed in the field (Liu & Flemings, 2007; Torres et al., 2002), to produce higher hydrate saturations.

Finally, these results suggest that models that assume the gas, hydrate, and brine are at thermodynamic equilibrium at the core-scale and larger (Darnell & Flemings, 2015; Liu & Flemings, 2007; Reagan & Moridis, 2008, 2009; Torres et al., 2004) may not capture the physics of gas transport and hydrate formation within the hydrate stability zone. A fundamental challenge is to incorporate the core-scale behaviors I observed into field-scale models that describe hydrate formation in geologic systems.

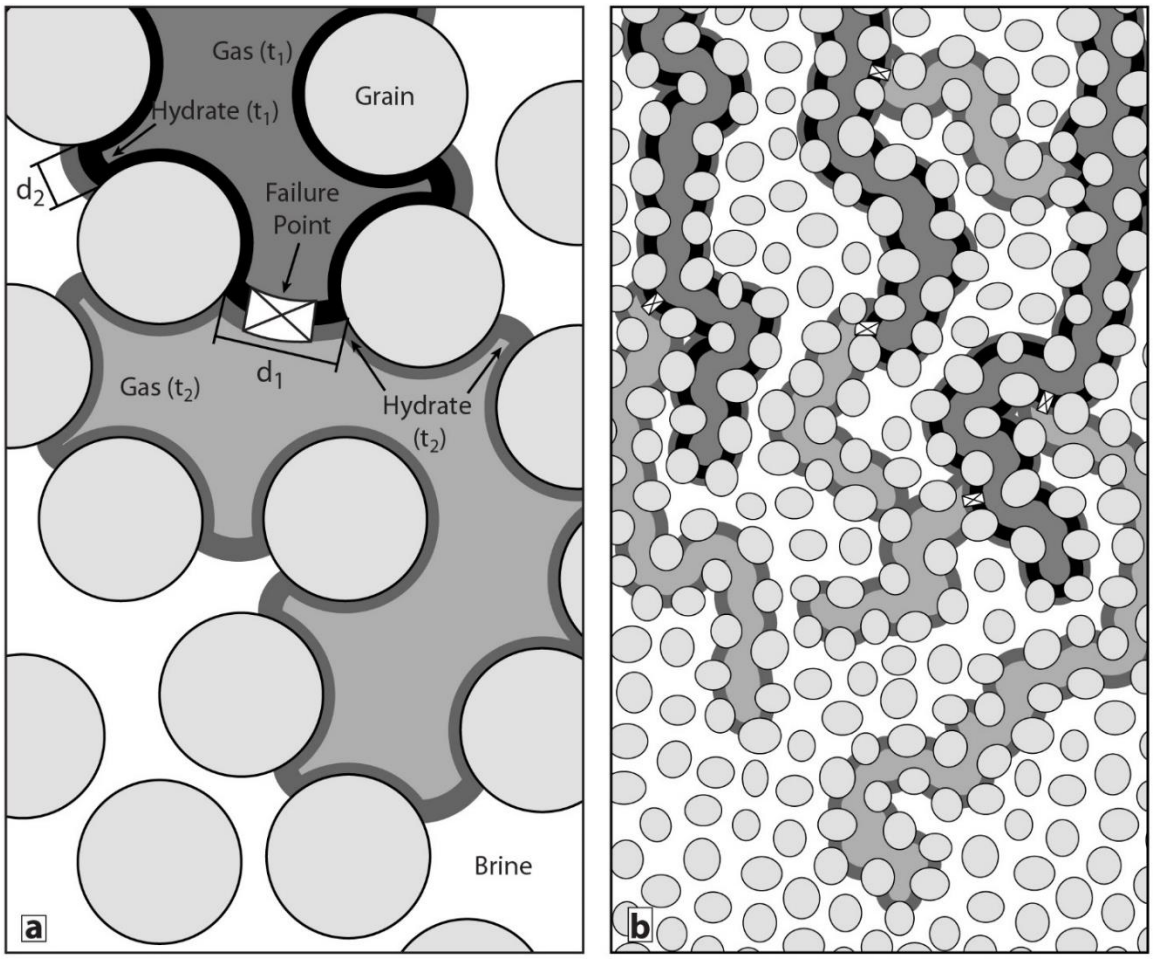

Figure 2.11: Conceptual model of experiments at the pore- and core-scales.

(a) At the pore-scale, between times t_0 and t_1, gas flows through the pores until it reaches mechanical equilibrium with the brine. A solid hydrate skin then forms at the gas-brine interface and blocks flow. Between t_1 and t_2, methane diffuses through the skin, forming additional hydrate as a differential pressure develops across the skin. At t_2, the hydrate skin fails and gas progresses farther into the sample, forming a new hydrate skin. (b) At the core-scale, multiple interconnected gas flow paths, encased in hydrate skins, progress through the sample over time.

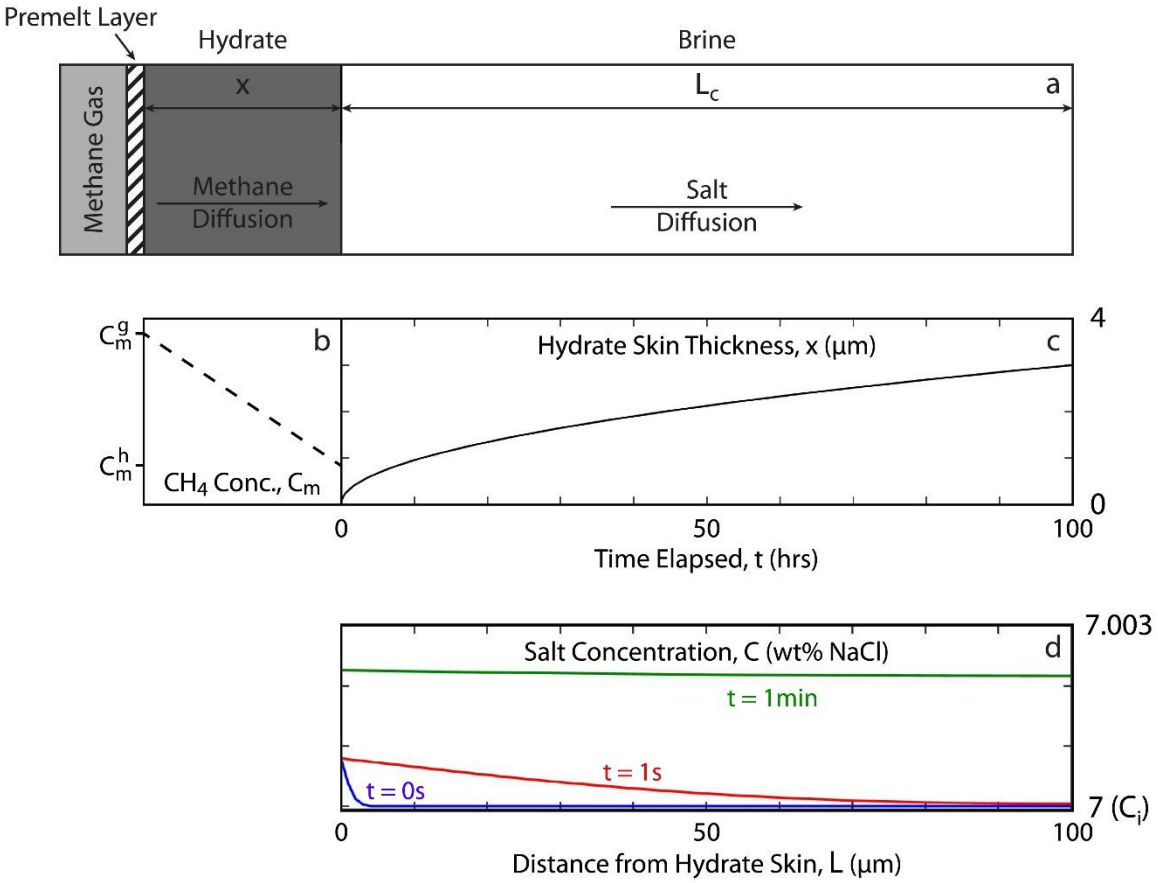

Figure 2.12: Model of hydrate formation and salinity evolution.

(a) Cartoon of the model domain. Gas and brine are separated by a hydrate skin. Gas and hydrate are separated by a thin, liquid layer (premelt). The brine phase has a characteristic length (L_c). The hydrate skin increases in thickness (x) as methane diffuses across the hydrate. (b) Methane concentration profile across the hydrate (dashed line). (c) Hydrate skin thickness over time (solid line) calculated using Equation 2.7. (d) Salt concentration in the brine after 0 seconds (blue line), 1 second (red line), and 1 minute (green line) elapsed ($D_m = 10^{-15}$ m^{2}s^{-1}; $L_c = 100$ μm).

2.6 CONCLUSIONS

I injected free methane gas into a brine-saturated sand pack under hydrate-stable conditions to form methane hydrate and observed temporary flow blockages throughout the experiments. On average, hydrate and free gas occupied 11% and 21% of the pore space, respectively. This hydrate saturation is much lower than predicted when assuming gas, hydrate, and brine are at three-phase equilibrium in the sample (67%). I interpret that as free gas enters the sample, hydrate nucleates rapidly at the gas-brine interface and forms a continuous barrier that separates the gas and brine phases. Occasionally, the hydrate skin fails due to the development of a significant pressure differential across the skin. This behavior leads to low saturations of gas and hydrate distributed throughout the sample.

A long-standing question is how free gas migrates through the hydrate stability zone in geologic systems. I suggest that gas flow is assisted by the mechanical separation of gas and brine phases by a hydrate skin. Where gas is present, there is three-phase equilibrium (gas, premelt, and hydrate), and, where brine is present, there is two-phase equilibrium (brine and hydrate). Methane slowly diffuses through the hydrate from the gas to the brine and forms additional hydrate at the brine-hydrate interface. Over geologic time, this transport process could result in high hydrate saturations distributed throughout the reservoir, as is observed in the field.

NOMENCLATURE

Symbol	Name	Dimension	Unit
A_i	interfacial area per porous media volume	(L^{-1})	(cm^{-1})
C	salinity	(M M^{-1})	(wt. %)
C_{eq}	three-phase equilibrium salinity	(M M^{-1})	(wt. %)
C_i	initial salinity	(M M^{-1})	(wt. %)
C_m	methane concentration	(M L^{-3})	(mol m^{-3})
C_m^g	solubility of methane in water	(M L^{-3})	(mol m^{-3})
C_m^h	solubility of hydrate in water	(M L^{-3})	(mol m^{-3})
CT^{avg}	average CT attenuation of wet and dry sample	(-)	(Houndsfield)
CT^{dry}	CT attenuation value of dry sample	(-)	(Houndsfield)
CT^{err}	CT attenuation error	(-)	(Houndsfield)
CT^{exp}	experimental CT attenuation value	(-)	(Houndsfield)
CT^{l-g}	brine-methane CT attenuation contrast	(-)	(Houndsfield)
CT^{wet}	CT attenuation value of wet sample	(-)	(Houndsfield)
D_c	diffusion coefficient of salt in water	(L^2 T^{-1})	(m^2 s^{-1})
D_m	diffusion coefficient of methane in hydrate	(L^2 T^{-1})	(m^2 s^{-1})
dC_m	methane concentration gradient	(M L^{-3} L^{-1})	(mol m^{-3} m^{-1})
dP	differential pressure	(M L^{-1} T^{-2})	(MPa)
dt	time-step	(T)	(s)
dx	change in hydrate skin thickness	(L)	(m)
L	distance from the brine-hydrate interface	(L)	(m)
L_c	characteristic length	(L)	(m)
L_{filt}	median filter diameter	(L)	(pixels)
m_m	total mass of methane injected	(M)	(kg)
m_m^g	mass of methane in the gaseous phase	(M)	(kg)
m_m^h	mass of methane in the hydrate phase	(M)	(kg)
m_w	total mass of brine removed	(M)	(kg)
m_{wi}	initial mass of brine	(M)	(kg)
m_w^h	mass of water in the hydrate phase	(M)	(kg)
m_w^l	mass of brine in the liquid phase	(M)	(kg)
M_h	hydrate molecular mass	(M M^{-1})	(kg mol^{-1})
M_m	methane molecular mass	(M M^{-1})	(kg mol^{-1})
M_{salt}	sodium chloride molecular mass	(M M^{-1})	(kg mol^{-1})
M_w	water molecular mass	(M M^{-1})	(kg mol^{-1})
N	hydration number for SI methane hydrate	(-)	(-)

P_{conf}	confining pressure	(M L^{-1} T^{-2})	(MPa)
P_{eff}	effective pressure	(M L^{-1} T^{-2})	(MPa)
P_{in}	inlet pressure	(M L^{-1} T^{-2})	(MPa)
P_{out}	outlet pressure	(M L^{-1} T^{-2})	(MPa)
P_{pore}	pore pressure	(M L^{-1} T^{-2})	(MPa)
q_h	hydrate formation rate	(M T^{-1})	(mol s^{-1})
q_{salt}	salt flux	(M T^{-1})	(mol s^{-1})
r_{smpl}	sample radius	(L)	(m)
S_g	methane gas phase saturation	(-)	(-)
S_h	solid hydrate phase saturation	(-)	(-)
S_{heq}	three-phase equilibrium hydrate saturation	(-)	(-)
S_l	liquid brine phase saturation	(-)	(-)
t	time elapsed	(T)	(s)
T_{conf}	confining temperature	(K)	(ºC)
V^g	volume of gaseous phase	(L^3)	(cm^3)
V^h	volume of hydrate phase	(L^3)	(cm^3)
V_{aff}	affected volume	(L^3)	(cm^3)
V_l	volume of liquid brine removed	(L^3)	(cm^3)
V_m	volume of methane gas injected	(L^3)	(cm^3)
V_{tot}	total sample volume	(L^3)	(cm^3)
x	hydrate skin thickness	(L)	(m)
x_{avg}	average hydrate skin thickness	(L)	(m)
X^g	volumetric gas phase ratio	(-)	(-)
X^h	volumetric hydrate phase ratio	(-)	(-)
X_{conv}	mass conversion ratio	(-)	(-)
X_{inj}	volumetric injection ratio	(-)	(-)
α	thermal diffusivity coefficient	(L^2 T^{-1})	(m^2 s^{-1})
β	Skempton compressibility coefficient	(-)	(-)
$\Delta\rho_b$	bulk density change	(M L^{-3})	(g cm^{-3})
ϕ	sample porosity	(-)	(-)
ϕ_{CT}	CT-derived sample porosity	(-)	(-)
ϕ_{grav}	gravimetrically-derived sample porosity	(-)	(-)
ρ_b^{avg}	average bulk density of wet and dry sample	(M L^{-3})	(kg m^{-3})
ρ_b^{dry}	bulk density of unsaturated sample	(M L^{-3})	(kg m^{-3})
ρ_b^{err}	equivalent bulk density error	(M L^{-3})	(g cm^{-3})

ρ_b^{exp}	experimental sample bulk density	(M L^{-3})	(kg m^{-3})
ρ_b^{wet}	bulk density of saturated sample	(M L^{-3})	(kg m^{-3})
ρ_g	gas phase density	(M L^{-3})	(kg m^{-3})
ρ_h	solid hydrate density	(M L^{-3})	(kg m^{-3})
ρ_l	liquid phase density	(M L^{-3})	(kg m^{-3})
ρ_s	solid grain density	(M L^{-3})	(kg m^{-3})
τ	generic heat conduction timescale	(T)	(s)

ACKNOWLEDGEMENTS

This work was supported by the U.S. Department of Energy under Contract No. DE-FE0010406, DE-FE0028967, and DE-FE0023919. Timothy Kneafsey was supported by the U.S. Department of Energy, Office of Fossil Energy, Office of Natural Gas and Petroleum Technology, through the National Energy Technology Laboratory, under Award Number DE-AC02-05CH11231. All of the X-ray CT images and acquired data used in the figures are archived in the Digital Rocks Portal (www.digitalrocksportal.org) with the project name "Methane hydrate formation during gas injection into saturated sand." All other experimental and analytical data referenced in this article are accessible through the presented figures, tables, and references. These data can also be requested by e-mail from the corresponding author (meyerdw3@utexas.edu). I thank Peter Polito, Joshua O'Connell, and Skyler Dong for their assistance and advice in assembling the experimental apparatus and executing these experiments.

REFERENCES

Beer, F. P., and Johnston, R. (1992). *Mechanics of Materials* (2nd ed.). New York City: McGraw-Hill Higher Education.

Boswell, R., and Collett, T. (2011). Current prospective on gas hydrate resources. *Energy & Environmental Science, 4*, 10.

Boswell, R., Collett, T. S., Frye, M., Shedd, W., McConnell, D. R., and Shelander, D. (2012a). Subsurface gas hydrate in the northern Gulf of Mexico. *Marine and Petroleum Geology, 34*, 27. doi: 10.1016/j.marpetgeo.2011.10.003

Boswell, R., Frye, M., Shelander, D., Shedd, W., McConnell, D. R., and Cook, A. (2012b). Architecture of gas-hydrate-bearing sands from Walker Ridge 313, Green Canyon 955, and Alaminos Canyon 21: Northern deepwater Gulf of Mexico. *Marine and Petroleum Geology, 34*(1), 134-149. doi: http://dx.doi.org/10.1016/j.marpetgeo.2011.08.010

Boswell, R., Shelander, D., Lee, M., Latham, T., Collett, T., Guerin, G., Moridis, G., Reagan, M., and Goldberg, D. (2009). Occurrence of gas hydrate in Oligocene Frio sand: Alaminos Canyon Block 818: Northern Gulf of Mexico. *Marine and Petroleum Geology, 26*(8), 1499-1512. doi: 10.1016/j.marpetgeo.2009.03.005

Brusseau, M. L., Peng, S., Schnaar, G., and Costanza-Robinson, M. S. (2006). Relationships among air-water interfacial area, capillary pressure, and water saturation for a sandy porous medium. *Water Resources Research, 42*(3), n/a-n/a. doi: 10.1029/2005wr004058

Brusseau, M. L., Peng, S., Schnaar, G., and Murao, A. (2007). Measuring Air−Water Interfacial Areas with X-ray Microtomography and Interfacial Partitioning Tracer Tests. *Environmental Science & Technology, 41*(6), 1956-1961. doi: 10.1021/es061474m

Casey, B., Germaine, J. T., Flemings, P. B., Reece, J. S., Gao, B., and Betts, W. (2013). Liquid limit as a predictor of mudrock permeability. *Marine and Petroleum Geology, 44*, 256-263. doi: http://dx.doi.org/10.1016/j.marpetgeo.2013.04.008

Collett, T. S., Lee, M. W., Zyrinova, M. V., Mrozewski, S. A., Guerin, G., Cook, A. E., and Goldberg, D. S. (2012). Gulf of Mexico Gas Hydrate Joint Industry Project Leg II logging-while-drilling data acquisition and analysis. *Marine and Petroleum Geology, 34*, 21.

Cook, A. E., and Malinverno, A. (2013). Short migration of methane into a gas hydrate-bearing sand layer at Walker Ridge, Gulf of Mexico. *Geochemistry, Geophysics, Geosystems, 14*(2), 283-291. doi: 10.1002/ggge.20040

Crutchley, G. J., Fraser, D. R. A., Pecher, I. A., Gorman, A. R., Maslen, G., and Henrys, S. A. (2015). Gas migration into gas hydrate-bearing sediments on the southern Hikurangi margin of New Zealand. *Journal of Geophysical Research: Solid Earth, 120*(2), 725-743. doi: 10.1002/2014jb011503

Darnell, K. N., and Flemings, P. B. (2015). Transient seafloor venting on continental slopes from warming-induced methane hydrate dissociation. *Geophysical Research Letters, 42*(24), 10,765-710,772. doi: 10.1002/2015gl067012

Dash, J. G., Rempel, A. W., and Wettlaufer, J. S. (2006). The physics of premelted ice and its geophysical consequences. *Reviews of Modern Physics, 78*(3), 695-741.

Davidson, D. W., Handa, Y. P., Ratcliffe, C. I., Ripmeester, J. A., Tse, J. S., Dahn, J. R., Lee, F., and Calvert, L. D. (1986). Crystallographic Studies of Clathrate Hydrates. Part I. *Molecular Crystals and Liquid Crystals, 141*(1-2), 141-149. doi: 10.1080/00268948608080205

Davie, M. K., and Buffett, B. A. (2001). A numerical model for the formation of gas hydrate below the seafloor. *Journal of Geophysical Research: Solid Earth, 106*(B1), 497-514. doi: 10.1029/2000jb900363

Davie, M. K., and Buffett, B. A. (2003). A steady state model for marine hydrate formation: Constraints on methane supply from pore water sulfate profiles. *Journal of Geophysical Research: Solid Earth, 108*(B10), n/a-n/a. doi: 10.1029/2002jb002300

Davies, S. R., Sloan, E. D., Sum, A. K., and Koh, C. A. (2010). In Situ Studies of the Mass Transfer Mechanism across a Methane Hydrate Film Using High-Resolution Confocal Raman Spectroscopy. *The Journal of Physical Chemistry C, 114*(2), 1173-1180. doi: 10.1021/jp909416y

Davis, S. N., and DeWiest, R. J. M. (1967). *Hydrogeology*. New York, NY: John Wiley and Sons.

England, W. A., Mackenzie, A. S., Mann, D. M., and Quigley, T. M. (1987). The movement and entrapment of petroleum fluids in the subsurface. *Journal of the Geological Society, 144*(2), 327-347. doi: 10.1144/gsjgs.144.2.0327

Frye, M., Shedd, W., and Boswell, R. (2012). Gas hydrate resource potential in the Terrebonne Basin, Northern Gulf of Mexico. *Marine and Petroleum Geology, 34*(1), 150-168. doi: https://doi.org/10.1016/j.marpetgeo.2011.08.001

Fu, X., Cueto-Felgueroso, L., and Juanes, R. (2018). Nonequilibrium Thermodynamics of Hydrate Growth on a Gas-Liquid Interface. *Physical Review Letters, 120*(14), 144501. doi: 10.1103/PhysRevLett.120.144501

Genov, G., Kuhs, W. F., Staykova, D. K., Goreshnik, E., and Salamatin, A. N. (2004). Experimental studies on the formation of porous gas hydrates. *American Mineralogist, 89*(8-9), 1228-1239. doi: 10.2138/am-2004-8-910

Germaine, J. T., and Germaine, A. V. (2009). *Geotechnical Laboratory Measurements for Engineers*. Hoboken, NJ: John Wiley & Sons, Inc.

Ginsburg, G. D., and Soloviev, V. A. (1997). Methane migration within the submarine gas-hydrate stability zone under deep-water conditions. *Marine Geology, 137*(1–2), 49-57. doi: http://dx.doi.org/10.1016/S0025-3227(96)00078-3

Haeckel, M., Suess, E., Wallmann, K., and Rickert, D. (2004). Rising methane gas bubbles form massive hydrate layers at the seafloor. *Geochimica et Cosmochimica Acta, 68*(21), 4335-4345. doi: http://dx.doi.org/10.1016/j.gca.2004.01.018

Hassanzadeh, H., Pooladi-Darvish, M., Elsharkawy, A. M., Keith, D. W., and Leonenko, Y. (2008). Predicting PVT data for CO2–brine mixtures for black-oil simulation of CO2 geological storage. *International Journal of Greenhouse Gas Control, 2*(1), 65-77. doi: https://doi.org/10.1016/S1750-5836(07)00010-2

Hesse, R., and Harrison, W. E. (1981). Gas hydrates (clathrates) causing pore-water freshening and oxygen isotope fractionation in deep-water sedimentary sections of terrigenous continental margins. *Earth and Planetary Science Letters, 55*(3), 453-462. doi: http://dx.doi.org/10.1016/0012-821X(81)90172-2

Hoog, F. R. d., Knight, J. H., and Stokes, A. N. (1982). An Improved Method for Numerical Inversion of Laplace Transforms. *SIAM Journal on Scientific and Statistical Computing, 3*(3), 357-366. doi: 10.1137/0903022

Huo, Z., Hester, K., Sloan, E. D., and Miller, K. T. (2003). Methane hydrate nonstoichiometry and phase diagram. *AIChE Journal, 49*(5), 1300-1306. doi: 10.1002/aic.690490521

Jin, Y., Konno, Y., and Nagao, J. (2012). Growth of Methane Clathrate Hydrates in Porous Media. *Energy & Fuels, 26*(4), 2242-2247. doi: 10.1021/ef3001357

Katsuki, D., Ohmura, R., Ebinuma, T., and Narita, H. (2007). Methane hydrate crystal growth in a porous medium filled with methane-saturated liquid water. *Philosophical Magazine, 87*(7), 1057-1069. doi: 10.1080/14786430601021652

Kneafsey, T. J., Tomutsa, L., Moridis, G. J., Seol, Y., Freifeld, B. M., Taylor, C. E., and Gupta, A. (2007). Methane hydrate formation and dissociation in a partially saturated core-scale sand sample. *Journal of Petroleum Science and Engineering, 56*(1–3), 108-126. doi: http://dx.doi.org/10.1016/j.petrol.2006.02.002

Kuhs, W. F., Staykova, D. K., and Salamatin, A. N. (2006). Formation of Methane Hydrate from Polydisperse Ice Powders. *The Journal of Physical Chemistry B, 110*(26), 13283-13295. doi: 10.1021/jp061060f

Kuhs, W. F., Klapproth, A., Gotthardt, F., Techmer, K., and Heinrichs, T. (2000). The formation of meso- and macroporous gas hydrates. *Geophysical Research Letters, 27*(18), 2929-2932. doi: doi:10.1029/2000GL006112

Kuhs, W. F., Genov, G., Goreshnik, E., Zeller, A., Techmer, K. S., and Bohrmann, G. (2004). The Impact of Porous Microstructures of Gas Hydrates On Their Macroscopic Properties.

Kvenvolden, K. A., and McMenamin, M. A. (1980). Hydrates of natural gas; a review of their geologic occurrence. *Report Rep. 825*.

Lambe, T. W. (1969). *Soil Mechanics*. New York: John Wiley & Sons, Inc.

Liu, X., and Flemings, P. B. (2006). Passing gas through the hydrate stability zone at southern Hydrate Ridge, offshore Oregon. *Earth and Planetary Science Letters*(241), 16.

Liu, X., and Flemings, P. B. (2007). Dynamic multiphase flow model of hydrate formation in marine sediments. *Journal of Geophysical Research: Solid Earth, 112*(B3), B03101. doi: 10.1029/2005jb004227

Malinverno, A., and Goldberg, D. S. (2015). Testing short-range migration of microbial methane as a hydrate formation mechanism: Results from Andaman Sea and Kumano Basin drill sites and global implications. *Earth and Planetary Science Letters, 422*, 105-114. doi: http://dx.doi.org/10.1016/j.epsl.2015.04.019

Moridis, G. J. (2008). Toward Production From Gas Hydrates: Current Status, Assessment of Resources, and Simulation-Based Evaluation of Technology and Potential.

Natarajan, V., Bishnoi, P. R., and Kalogerakis, N. (1994). Induction phenomena in gas hydrate nucleation. *Chemical Engineering Science, 49*(13), 2075-2087. doi: http://dx.doi.org/10.1016/0009-2509(94)E0026-M

Nole, M., Daigle, H., Cook, A. E., and Malinverno, A. (2016). Short-range, overpressure-driven methane migration in coarse-grained gas hydrate reservoirs. *Geophysical Research Letters, 43*(18), 9500-9508. doi: 10.1002/2016gl070096

Olsen, H. W. (1966). Darcy's Law in Saturated Kaolinite. *Water Resources Research, 2*(2), 9.

Onur, E. M. (2014). *Predicting the Permeability of Sandy Soils from Grain Size Distribution.* Master of Science, Kent State University, Ohio.

Pini, R., Krevor, S. C. M., and Benson, S. M. (2012). Capillary pressure and heterogeneity for the CO2/water system in sandstone rocks at reservoir conditions. *Advances in Water Resources, 38*, 48-59. doi: http://dx.doi.org/10.1016/j.advwatres.2011.12.007

Pitzer, K. S. (1991). Ion interaction approach: Theory and data correlation. In K. S. Pitzer (Ed.), *Activity Coefficients in Electrolyte Solutions* (2nd ed., pp. 75-153). Boca Raton, FL: CRC Press.

Priegnitz, M., Thaler, J., Spangenberg, E., Rücker, C., and Schicks, J. M. (2013). A cylindrical electrical resistivity tomography array for three-dimensional monitoring of hydrate formation and dissociation. *Review of Scientific Instruments, 84*(10), 104502. doi: doi:http://dx.doi.org/10.1063/1.4825372

Reagan, M. T., and Moridis, G. J. (2008). Dynamic response of oceanic hydrate deposits to ocean temperature change. *Journal of Geophysical Research: Oceans, 113*(C12). doi: doi:10.1029/2008JC004938

Reagan, M. T., and Moridis, G. J. (2009). Large-scale simulation of methane hydrate dissociation along the West Spitsbergen Margin. *Geophysical Research Letters, 36*(23). doi: doi:10.1029/2009GL041332

Rees, E. V. L., Kneafsey, T., and Seol, Y. (2011). Methane Hydrate Distribution from Prolonged and Repeated Formation in Natural and Compacted Sand Samples: X-Ray CT Observations. *Journal of Geological Research, 2011*. doi: 10.1155/2011/791815

Rempel, A. W. (2011). A model for the diffusive growth of hydrate saturation anomalies in layered sediments. *Journal of Geophysical Research: Solid Earth, 116*(B10), n/a-n/a. doi: 10.1029/2011jb008484

Rempel, A. W., and Buffett, B. A. (1997). Formation and accumulation of gas hydrate in porous media. *Journal of Geophysical Research: Solid Earth, 102*(B5), 10151-10164. doi: 10.1029/97jb00392

Rempel, A. W., Wettlaufer, J. S., and Worster, M. G. (2004). Premelting dynamics in a continuum model of frost heave. *Journal of Fluid Mechanics, 498,* 227-244. doi: Doi: 10.1017/s0022112003006761

Riedel, M., Novosel, I., Spence, G. D., Hyndman, R. D., Chapman, R. N., Solem, R. C., and Lewis, T. (2006). Geophysical and geochemical signatures associated with gas hydrate–related venting in the northern Cascadia margin. *GSA Bulletin, 118*(1-2), 23-38. doi: 10.1130/b25720.1

Riestenberg, D., West, O., Lee, S., McCallum, S., and Phelps, T. J. (2003). Sediment surface effects on methane hydrate formation and dissociation. *Marine Geology, 198*(1–2), 181-190. doi: http://dx.doi.org/10.1016/S0025-3227(03)00100-2

Schowalter, T. T. (1979). Mechanics of Secondary Hydrocarbon Migration and Entrapment. *AAPG Bulletin, 63*(5), 37.

Seol, Y., and Kneafsey, T. J. (2009). X-ray computed-tomography observations of water flow through anisotropic methane hydrate-bearing sand. *Journal of Petroleum Science and Engineering, 66*(3–4), 121-132. doi: http://dx.doi.org/10.1016/j.petrol.2009.01.008

Skempton, A. W. (1954). The Pore-Pressure Coefficients A and B. *Géotechnique, 4*(4), 143-147. doi: 10.1680/geot.1954.4.4.143

Skovborg, P., Ng, H. J., Rasmussen, P., and Mohn, U. (1993). Measurement of induction times for the formation of methane and ethane gas hydrates. *Chemical Engineering Science, 48*(3), 445-453. doi: http://dx.doi.org/10.1016/0009-2509(93)80299-6

Sloan, E. D., and Fleyfel, F. (1991). A molecular mechanism for gas hydrate nucleation from ice. *AIChE Journal, 37*(9), 1281-1292. doi: 10.1002/aic.690370902

Sloan, E. D., and Koh, C. A. (2007). *Clathrate Hydrates of Natural Gases* (3nd ed.). Boca Raton, FL: CRC Press.

Spangenberg, E., Kulenkampff, J., Naumann, R., and Erzinger, J. (2005). Pore space hydrate formation in a glass bead sample from methane dissolved in water. *Geophysical Research Letters, 32*(24), n/a-n/a. doi: 10.1029/2005gl024107

Taylor, C. J., Miller, K. T., Koh, C. A., and Sloan, E. D. (2007). Macroscopic investigation of hydrate film growth at the hydrocarbon/water interface. *Chemical*

Engineering Science, 62(23), 6524-6533. doi: http://dx.doi.org/10.1016/j.ces.2007.07.038

Torres, M. E., Wallmann, K., Tréhu, A. M., Bohrmann, G., Borowski, W. S., and Tomaru, H. (2004). Gas hydrate growth, methane transport, and chloride enrichment at the southern summit of Hydrate Ridge, Cascadia margin off Oregon. *Earth and Planetary Science Letters, 226*(1–2), 225-241. doi: http://dx.doi.org/10.1016/j.epsl.2004.07.029

Torres, M. E., McManus, J., Hammond, D. E., de Angelis, M. A., Heeschen, K. U., Colbert, S. L., Tryon, M. D., Brown, K. M., and Suess, E. (2002). Fluid and chemical fluxes in and out of sediments hosting methane hydrate deposits on Hydrate Ridge, OR, I: Hydrological provinces. *Earth and Planetary Science Letters, 201*(3), 525-540. doi: https://doi.org/10.1016/S0012-821X(02)00733-1

Tréhu, A. M., Flemings, P. B., Bangs, N. L., Chevallier, J., Gràcia, E., Johnson, J. E., Liu, C. S., Liu, X., Riedel, M., and Torres, M. E. (2004). Feeding methane vents and gas hydrate deposits at south Hydrate Ridge. *Geophysical Research Letters, 31*(23), L23310. doi: 10.1029/2004gl021286

Uchida, T., Takagi, A., Kawabata, J., Mae, S., and Hondoh, T. (1995). Raman spectroscopic analyses of the growth process of CO2 hydrates. *Energy Conversion and Management, 36*(6), 547-550. doi: https://doi.org/10.1016/0196-8904(95)00064-K

Ussler, W., and Paull, C. K. (2001). Ion Exclusion Associated with Marine Gas Hydrate Deposits *Natural Gas Hydrates: Occurrence, Distribution, and Detection* (pp. 41-51): American Geophysical Union.

West, T. R. (2010). *Geology Applied to Engineering*. Long Grove, IL: Waveland Press.

Xu, W., and Ruppel, C. (1999). Predicting the occurrence, distribution, and evolution of methane gas hydrate in porous marine sediments. *Journal of Geophysical Research: Solid Earth, 104*(B3), 5081-5095. doi: 10.1029/1998jb900092

Yamamoto, K., Terao, Y., Fujii, T., Ikawa, T., Seki, M., Matsuzawa, M., and Kanno, T. (2014). *Operational Overview of the First Offshore Production Test of Methane Hydrates in the Eastern Nankai Trough.* Presented at the Offshore Technology Conference, Houston, TX.

You, K., and Flemings, P. B. (2017). Methane hydrate formation in thick sand reservoirs: 1. Short-range methane diffusion. *Marine and Petroleum Geology*. doi: https://doi.org/10.1016/j.marpetgeo.2017.10.011

You, K., DiCarlo, D., and Flemings, P. B. (2015a). Quantifying hydrate solidification front advancing using method of characteristics. *Journal of Geophysical Research: Solid Earth, 120*(10), 6681-6697. doi: 10.1002/2015jb011985

You, K., Kneafsey, T. J., Flemings, P. B., Polito, P., and Bryant, S. L. (2015b). Salinity-buffered methane hydrate formation and dissociation in gas-rich systems. *Journal of Geophysical Research: Solid Earth, 120*(2), 643-661. doi: 10.1002/2014jb011190

Chapter 3: Effect of Flow Rate on Gas Flow and Hydrate Formation Within the Hydrate Stability Zone[2]

ABSTRACT

I formed methane hydrate in brine-saturated, coarse-grained samples, under hydrate-stable conditions, at various applied flow rates. Decreasing the flow rate resulted in higher hydrate saturation, lower brine saturation, a smaller affected volume, and larger average pressure differentials across the sample. I interpret that longer execution times at lower flow rates allow for additional methane transport that increases the hydrate skin thickness. Thicker skins sustain larger pressure differentials that, upon failure, distribute gas closer to the failure point. In several experiments, I stopped brine flow and supplied methane gas to the sample for an additional 800 hours. During this period, hydrate continued to form, pressure differentials developed, and the bulk density changed within the affected volume. I interpret that there is gas present in the sample that is disconnected from the gas source. Hydrate forms around the disconnected gas due to methane transport through the skin that surrounds it, causing the internal gas pressure to decline and leading to inward collapse and net volume decrease. This lowers the brine pressure and creates a differential pressure across the sample that induces gas flow. Gas conversion into hydrate

[2]The full content of this chapter was submitted to *Journal of Geophysical Research* in 2018. The citation for that publication is:

Meyer, D. W., Flemings, P. B., and DiCarlo, D. A. (in review). Effect of flow rate on gas flow and hydrate formation within the hydrate stability zone. *Journal of Geophysical Research: Solid Earth*.

I performed the experiments presented in that study and prepared the manuscript for publication. My co-authors are listed in order of contribution and provided support for the conceptual development of the project and manuscript preparation.

and gas flow into the sample result in density increase and decrease, respectively. This study indicates that lower gas flow rates through the hydrate stability zone can produce very high saturations of hydrate, but requires a larger differential pressure to sustain flow.

3.1 INTRODUCTION

Methane hydrate, henceforth referred to as hydrate, is a crystalline solid comprised of methane gas trapped within a water cage (Kvenvolden & McMenamin, 1980). Hydrate is stable at high pressure and low temperature and salinity conditions and forms when the local methane concentration exceeds the solubility of methane in water (Sloan & Koh, 2007). Hydrates occur in marine environments and beneath permafrost regions (Boswell & Collett, 2011; Kvenvolden, 1993; Shipley et al., 1979) and are estimated to contain between 500 – 2500 gigatons of carbon globally (Boswell & Collett, 2011; Milkov, 2004).

Hydrates contained within sand reservoirs have been of particular interest as a potential energy resource due to their favorable production characteristics (e.g. Koh et al., 2016; Konno et al., 2017; Moridis, 2008). Some reservoirs consist of meter-scale sand layers, bounded by muds, that cross-cut the base of the hydrate stability zone. High concentrations of hydrate (60 - 90%) far above and free gas below the base of the hydrate stability zone have been observed in these reservoirs (Boswell et al., 2012a; Boswell et al., 2009; Crutchley et al., 2015; Tréhu et al., 2004). The processes responsible for the formation of these thick, high concentration, hydrate deposits remains a conundrum.

There are several potential mechanisms to explain hydrate formation in these reservoirs (Malinverno & Goldberg, 2015; Nole et al., 2016; Rempel, 2011; Xu & Ruppel, 1999). One primary proposed mechanism, however, is the transport of free methane gas over hundreds of kilometers into the GHSZ from below (Crutchley et al., 2015; Liu & Flemings, 2006; Liu & Flemings, 2007; Torres et al., 2004). Methane gas below the GHSZ is driven upward by buoyancy, preferentially accumulating in high permeability, coarse-

grained layers (England et al., 1987; Schowalter, 1979). The fine-grained material above the sand restricts vertical gas transport, due to its high capillary entry pressure (England et al., 1987; Schowalter, 1979), forcing gas to migrate up-dip into the GHSZ, forming hydrate (Liu & Flemings, 2006; Torres et al., 2004; Tréhu et al., 2004). Modeling investigations (Liu & Flemings, 2007; You et al., 2015) previously suggested that hydrate formation is limited by elevated salinities that create bulk three-phase (gas-hydrate-brine) equilibrium conditions that then allow for upward gas flow.

In Chapter 2, I developed an experimental method to investigate the fundamental behaviors of hydrate formation during gas injection into the hydrate stability zone and presented the results from several experiments. Based on these experiments, I proposed that a continuous hydrate skin nucleates rapidly at the gas-brine interface upon gas injection, forming a barrier that separates the gas and brine phases. This provides an alternative mechanism for gas transport through the hydrate stability zone where hydrate formation is limited by methane transport through the hydrate skin, rather than elevated salinities. Since those experiments were performed at the same flow rate, however, it is not clear whether the behavior is sustainable at lower flow rates.

In this chapter, I performed five additional hydrate formation experiments at Mid (0.06 mL/hr) and Low (0.03 mL/hr) applied brine flow rates. I also performed brine shut-in experiments after the brine removal period, by stopping brine flow, but continuing to supply gas to the sample for approximately 800 hours. During brine removal, I find that decreasing the flow rate: 1) generates higher hydrate saturation, 2) produces larger temporary pressure differentials between the upstream and downstream transducers, and

3) decreases the brine saturation within the affected volume. During brine shut-in, I find that: 1) the hydrate continues to form, but at a rate decreasing with time, 2) the bulk density within the affected volume decreases near the gas inlet and increases below this, and 3) there are periods of no gas flow associated with the development of pressure differentials. I interpret that decreasing the flow rate allows more time for hydrate skin development, resulting in higher hydrate saturations, and that, after halting brine removal, methane transport across the skin continues to drive hydrate formation. This finding suggests that, over thousands of years, hydrate formation during gas injection could form very high hydrate saturations, in coexistence with free gas, far above the base of hydrate stability in natural systems.

3.2 METHODS

I performed three 'Mid' flow experiments at a brine removal rate of 0.06 mL/hr, and two 'Low' flow experiments at a brine removal rate of 0.03 mL/hr (Table 3.1). I compared these experiments to three I performed at a 'High' flow rate of 0.18 mL/hr (Table 3.1) that were presented in Chapter 2. In addition, for each flow rate, I performed one brine shut-in experiment for approximately 800 hours (Table 3.1). I also performed one short shut-in experiment (~150 hours) after Low-1 (Table 1) in an X-ray computed-tomography (CT) scanner to observe the core-scale behavior during this period. All experiments were performed in a vertical pressure vessel consisting of steel endcaps and an X-ray transparent, aluminum cylinder surrounded by a cooling jacket (Figure 3.1). The samples were kept

approximately 10.5ºC below the stability temperature (Table 3.1), to encourage rapid hydrate nucleation (Rees et al., 2011; Seol & Kneafsey, 2009; You et al., 2015).

I performed the experiments using the methodology described in Chapter 2, with the one exception that the samples were always kept vertical after packing. This modification to the packing procedure helped maintain a more homogeneous sample porosity. I packed the samples using slow, dry pluviation (Germaine & Germaine, 2009) and consisted of clean, silica sand (362 μm median grain size) mixed with 0.5 wt% smectite-rich clay (Casey et al., 2013) to accelerate hydrate nucleation (Riestenberg et al., 2003). I then saturated each sample with 7 wt% sodium chloride (NaCl) brine by pulling five pore volumes of fluid through the sample while under vacuum; using brine reduced the maximum potential hydrate saturation to 67%, relative to fresh water. I then pressurized and cooled the whole system to experimental conditions (Table 1). In the brine removal period, I withdrew brine from the base of the sample as a constant rate with methane gas connected to the top of the sample at a constant pressure. In the brine shut-in period, I stopped brine removal, but continued to supply gas throughout this period. A detailed description of my experimental equipment and procedure is included in Appendix A.

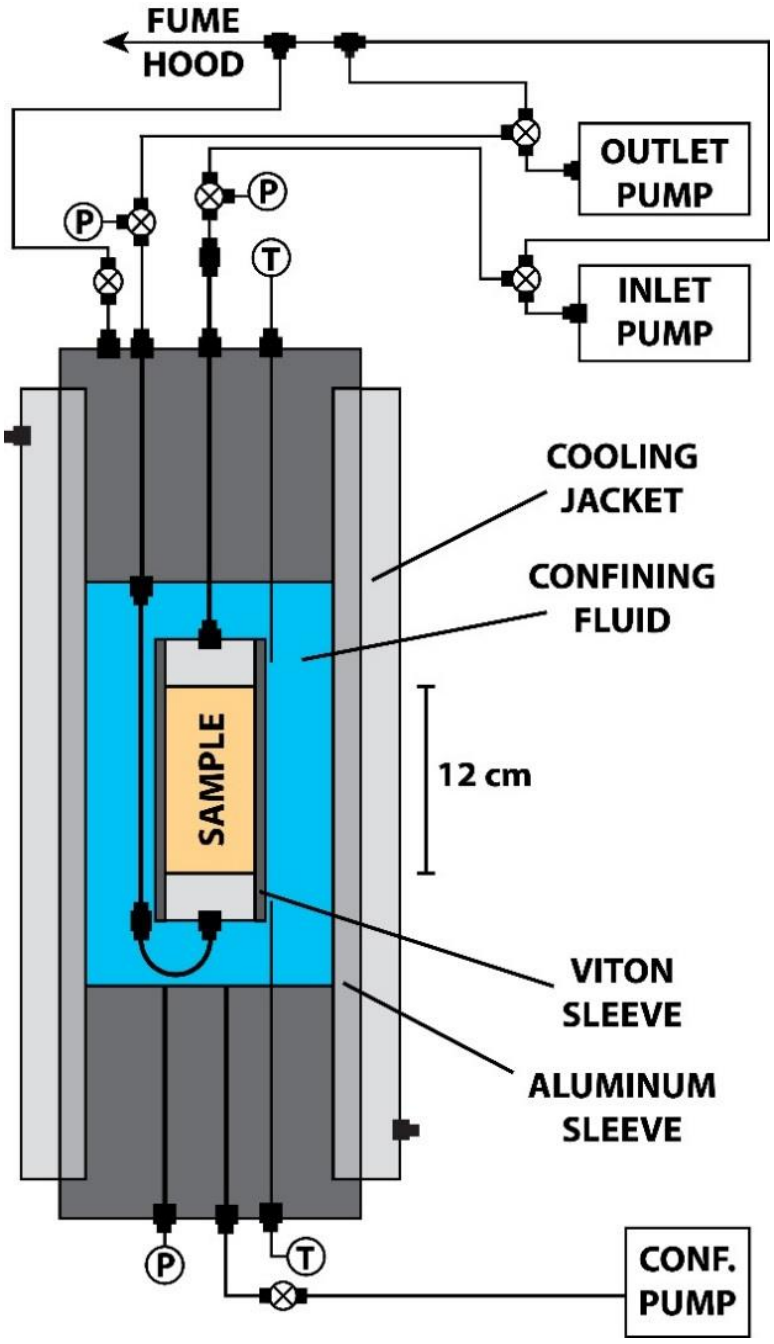

Figure 3.1: Diagram of the experimental apparatus.

The sample (approx. 12 cm length and 5 cm diameter) was suspended within the confining cell. Two thermistors (T) recorded the confining temperature, three syringe pumps controlled the fluid flow, and three pressure transducers (P) tracked the pressure of the pore and confining fluids.

Test	Porosity, ϕ	Salinity, C (wt% NaCl)	Pressure, P (MPa)	Temp, T (ºC)	Stable Temp[b] (ºC)	Brine Flow Rate (mL/hr)	CT	Shut-In
High-1[a]	0.41	7	12.24	1.01	11.5	0.18	Y	N
High-2[a]	0.38			1.05			N	N
High-3[a]	0.39			1.02			N	Y
Mid-1	0.40			0.64		0.06	N	N
Mid-2	0.40			1.38			N	N
Mid-3	0.40			0.98			N	Y
Low-1	0.38			1.03		0.03	Y	Y[c]
Low-2	0.39			0.98			N	Y

Table 3.1: Summary of High, Mid, and Low flow experimental parameters.

[a]Experiments presented previously in Chapter 2.
[b]Maximum temperature at which hydrate is stable at experiment pressure and salinity conditions.
[c]The shut-in for this experiment was only run for 150 hours. I only present the CT data in this dissertation.

I performed two experiments, High-1 and Low-1, within a medical X-ray computed-tomography (CT) scanner (Table 3.1). I collected scans, prior to each experiment, of the samples filled with only methane (dry) and only brine (wet) and then collected scans at least every 24 hours during the experiments. From the wet and dry CT scans, I determined the porosity (ϕ_{CT}) and bulk density endpoints of each voxel (Appendix B.4). From the CT scans taken during each experiment, I determined the bulk density (ρ_b) and the total affected volume (V_{aff}). The affected volume is defined by the region of the sample where the bulk density decrease, relative to the initial condition, exceeds the CT measurement error (± 0.024 g/mL). Full derivation and definition of these CT-derived results can be found in Chapter 2.

3.3 RESULTS

3.3.1 Sample Porosity

The CT-derived porosity, averaged over each slice, decreased downward from 44% to 39% in High-1, and was constant at 40% in Low-1 (Figure 3.2a). Sample handling created narrow, high porosity fingers extending down the edges of the sample in High-1 (Figure 3.2b). A modification to the packing method eliminated these high porosity artifacts in Low-1 (Figure 3.2c).

3.3.2 Pressure Differentials

I observed temporary pressure differentials ($dP = P_{in} - P_{out}$) between the inlet (P_{in}) and outlet (P_{out}) transducers (Figure 3.1) during both the removal and shut-in periods

of each experiment (Figure 3.3). The pressure differentials were generally greater for the Low experiments (Figure 3.3c) than for the High experiments (Figure 3.3a). The average critical pressure differential (dP_{crit}), defined as the maximum value prior to a rapid reduction in dP, during brine removal in the High (Figure 3.3a), Mid (Figure 3.3b), and Low (Figure 3.3c) experiments, was 0.06, 0.10, and 0.16 MPa, respectively. During shut-in, large pressure differentials developed in all experiments (Figure 3.3d). However, in contrast to the brine removal period, there was no correlation between the average magnitude of dP_{crit} and the original brine removal rate.

3.3.3 Fluid Volumes

The volume of methane injected (V_m) during brine removal, relative to the volume of brine removed (V_l), was greatest in the Low experiments (Figure 3.4a: green dots) and least in the High experiments (Figure 3.4a: blue dots). During shut-in, methane continued to flow into the sample, but the flow rate decreased with time in all experiments (Figure 3.4b). The gas flow rate immediately after shut-in was highest for High-3 (Figure 3.4b: blue line), which had the highest brine flow rate (0.18 mL/hr) during the removal period, and lowest for Low-2 (Figure 3.4b: green line), which had the lowest brine flow rate (0.03 mL/hr) during the removal period. At later times (> 200 hours elapsed), the gas flow rates decreased in all experiments (Figure 3.4b). There were also extended periods of no methane flow into the sample followed by short periods of rapid gas flow (Figure 3.4b inset: green line). These cycles were associated with the development of differential pressures (Figure 3.4b inset: black line) that were qualitatively similar to those observed during brine removal (Figure 3.3a, b, and c). During dP development, no methane flowed into the

sample and, during dP reduction, methane flowed into the sample at rates 10 times faster than the applied brine removal rate (Figure 3.4b inset).

3.3.4 CT-Derived Bulk Density

At the beginning of brine removal in High-1, bulk density decrease exceeded the CT measurement error (Appendix B.3.2) within the top 0.5 cm of the sample (Figure 3.5a: solid black line) due to gas injection during experiment initialization. This density decrease was concentrated at the sample edges (Figure 3.5b) where the initial porosity was high (Figure 3.2b). After 4.7 mL of brine had been removed, $\Delta\rho_b$ exceeded the CT measurement error within 1.5 cm of the inlet (Figure 3.5a: dashed black line). Below this region, the density decreased along the sample edges (Figure 3.5c). After 9.4 mL of brine removed, $\Delta\rho_b$ exceeded the CT measurement error within 4 cm of the inlet (Figure 3.5a: dotted black line). Below this region, the density decreased at the sample edge and across the sample (Figure 3.5d).

At the beginning of brine removal in Low-1 (Figure 3.6a: solid black line), the only discernible change in bulk density from the initial was concentrated at the gas inlet (Figure 3.6b). After 5 mL of brine was removed, $\Delta\rho_b$ exceeded the CT measurement error within 1 cm of the inlet (Figure 3.6a: dashed black line). Below this region, the density decreased along the edges of the sample (Figure 3.6c). After 9.4 mL of brine was removed (Figure 3.6a: dotted black line), $\Delta\rho_b$ exceeded the CT measurement error within 3 cm of the inlet. Below this region, the density decreased primarily down one half of the sample (Figure 3.6d).

After a 167-hour shut-in of Low-1, the bulk density within the affected volume decreased within the region from 0 – 1.5 cm by as much as 0.25 g/mL (Figure 3.7a: red line) and increased within the region from 1.5 – 6.3 cm by as much as 0.45 g/mL (Figure 3.7a: green line). Throughout the affected volume, behind the red line in Figure 3.7b, the average bulk density increased by 0.016 g/mL. A two-dimensional slice through the sample (Figure 3.7b) shows that density increased within 1.5 to 4 cm of front of the affected volume (Figure 3.7b: red line) and decreased near the inlet.

3.3.5 Affected Volumes

During brine removal, the affected volume (V_{aff}; Section 2) increased linearly with the volume of brine removed (Figure 3.8a); the slope of High-1 was greater than that of the Low-1. During the shut-in of Low-1, V_{aff} decreased modestly (Figure 3.8b) because the bulk density in certain voxels increased (Figure 3.7b), which reduced $\Delta\rho_b$, relative to the brine-saturated conditions, to below the CT measurement error. As a result, those voxels were no longer considered "affected" in the determination of the affected volume. However, since I know these voxels contain gas and/or hydrate, it is reasonable to subsequently include them in V_{aff} and to assume that the affected volume remains constant during brine shut-in and is equal to the value at the end of brine removal.

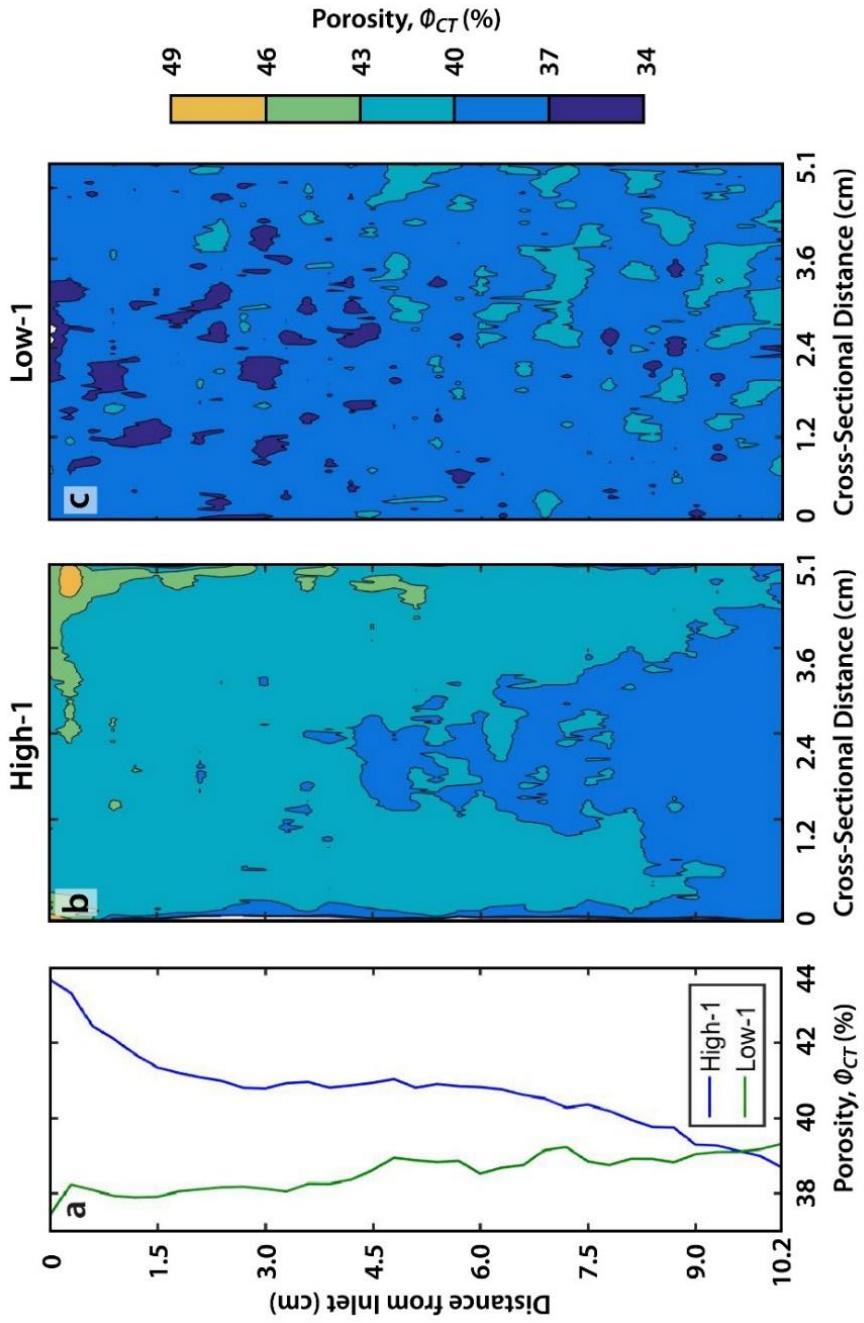

Figure 3.2: Initial porosity of the samples used in High-1 and Low-1.

Values were derived from the wet and dry scans (Equation 2.1). (a) CT porosity, averaged across each slice, with distance from the inlet in High-1 (blue line) and Low-1 (green line). (b) and (c) Cross-sectional porosity along the center of the samples in High-1 and Low-1.

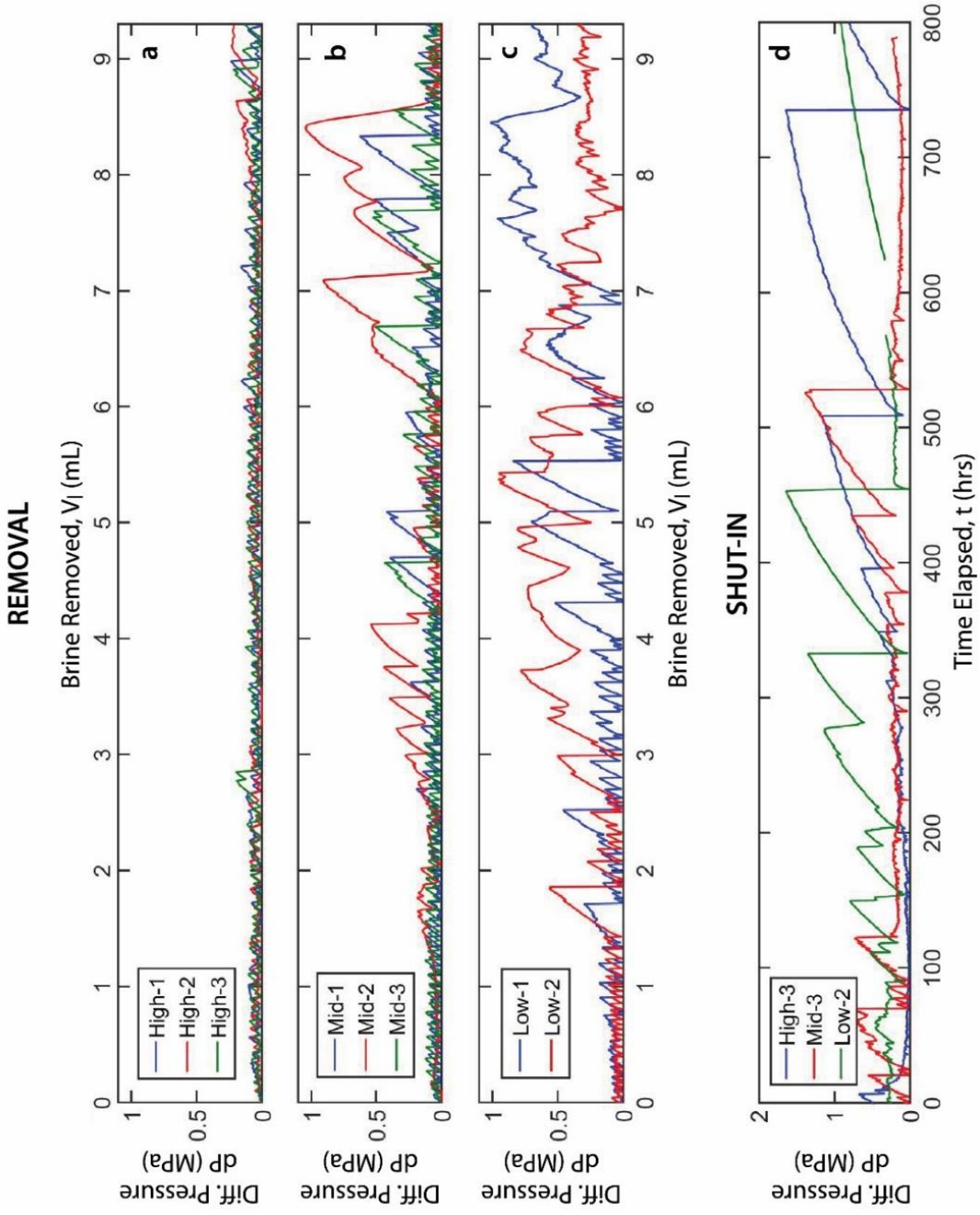

Figure 3.3: Differential pressure during brine removal and shut-in.

(a) dP in High-1 (blue line), High-2 (red line), and High-3 (green line). (b) dP in Mid-1 (blue line), Mid-2 (red line), and Mid-3 (green line). (c) dP in Low-1 (blue line) and Low-2 (red line). (d) dP in High-3 (blue line), Mid-3 (red line), and Low-2 (green line) during shut-in.

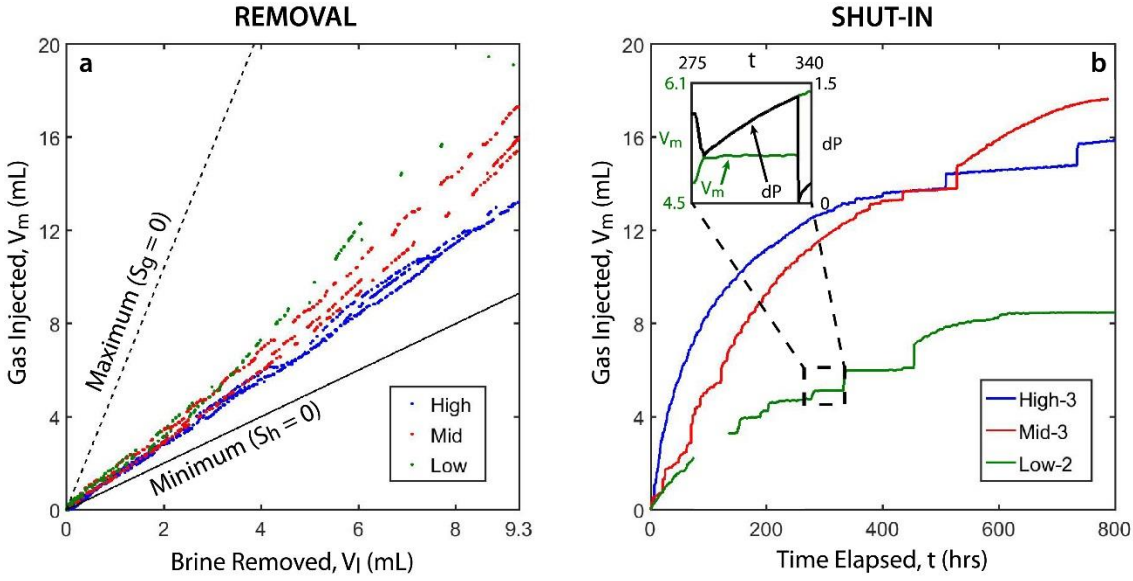

Figure 3.4: Volumes of the gas injected during brine removal and shut-in.

(a) V_m during brine removal in High (blue dots), Mid (red dots), and Low (green dots) experiments compared to the minimum (solid black line) and maximum (dashed black line) endmembers (Section 4). For clarity, these results have been filtered to remove data where the pressure differential was greater than 0.02 MPa. (b) V_m during the brine shut-in of High-3 (blue line), Mid-3 (red line), and Low-2 (green line). Inset show V_m from 275 to 340 hours elapsed during the brine shut-in of Low-2 (green line) compared to the differential pressure over the same time period.

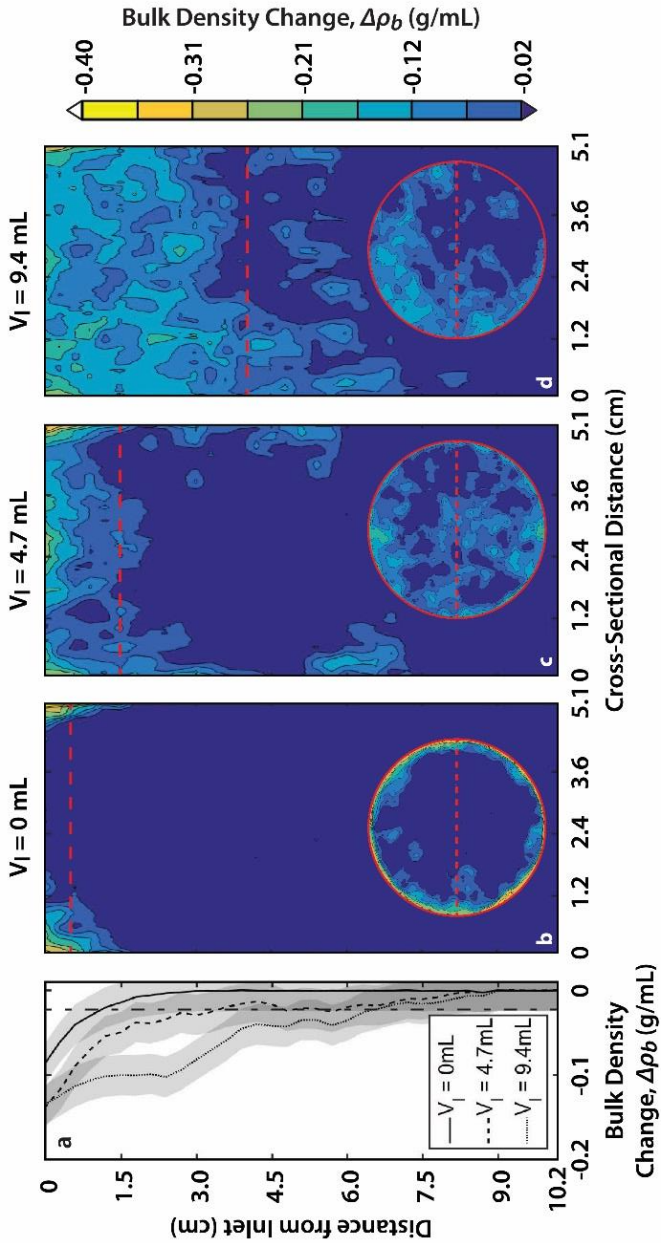

Figure 3.5: Evolution of the bulk density change during High-1.

(a) Change in bulk density ($\Delta\rho_b$), averaged across each slice, as a function of distance from the inlet (Equation 2.2). Dot-dashed black line indicates the CT measurement error and shaded regions indicate one standard deviation in the CT data. (b) – (d) Two-dimensional $\Delta\rho_b$ along the center of the sample after 0, 4.7, and 9.4 mL of brine removed at location marked by dotted red line in circular inset. Inset images show axial slices of the sample from each scan at the location marked by the dashed red line.

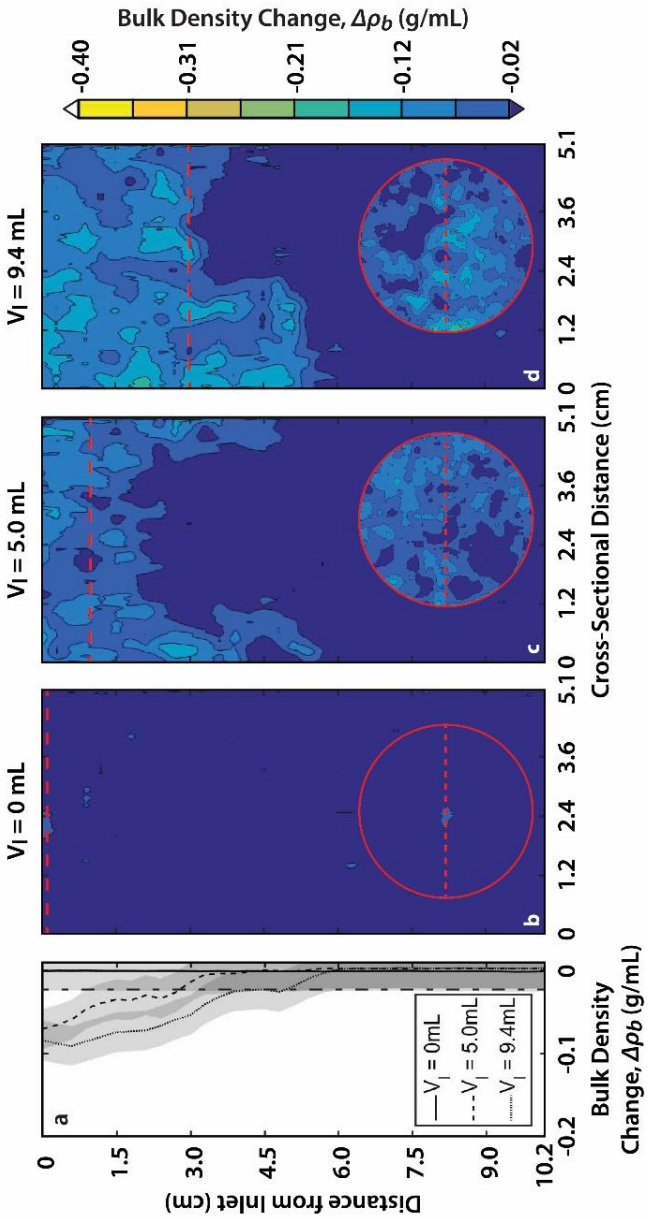

Figure 3.6: Evolution of the bulk density change during Low-1.

(a) Change in bulk density ($\Delta\rho_b$), averaged across each slice, as a function of distance from the inlet (Equation 2.2). Dot-dashed black line indicates the CT measurement error and shaded regions indicate one standard deviation in the CT data. (b) – (d) Two-dimensional $\Delta\rho_b$ along the center of the sample after 0, 5.0, and 9.4 mL of brine removed at location marked by dotted red line in circular inset. Inset images show axial slices of the sample from each scan at the location marked by the dashed red line.

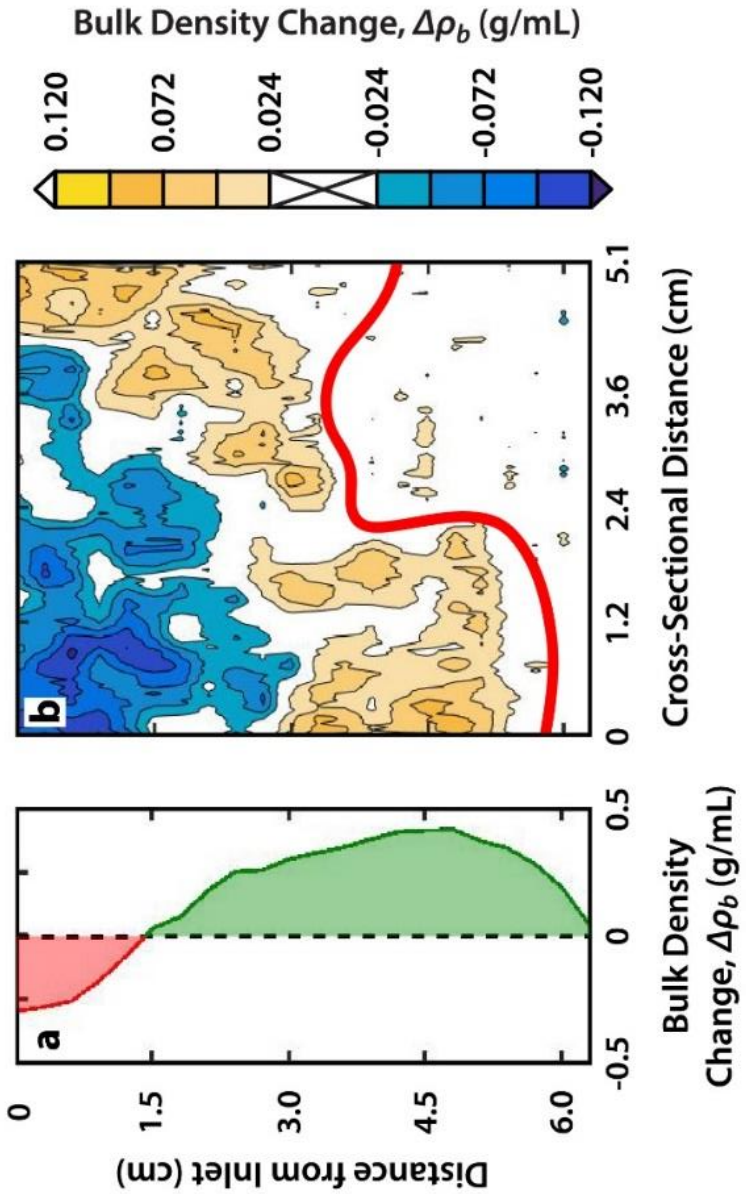

Figure 3.7: Evolution of the bulk density change during shut-in of Low-1.

Change in bulk density ($\Delta\rho_b$) is relative to the end of the brine removal period of Low-1 (Figure 3.6d). No major density changes occurred beyond 6.3 cm from the sample inlet. (a) $\Delta\rho_b$, averaged across each slice, as a function of distance from the inlet. Red zone indicates an average decrease in density and green zone indicates an average increase in density. (b) Two-dimensional $\Delta\rho_b$ along the center of the sample. Red line indicates the lower boundary of the affected volume after brine removal (Figure 3.6d).

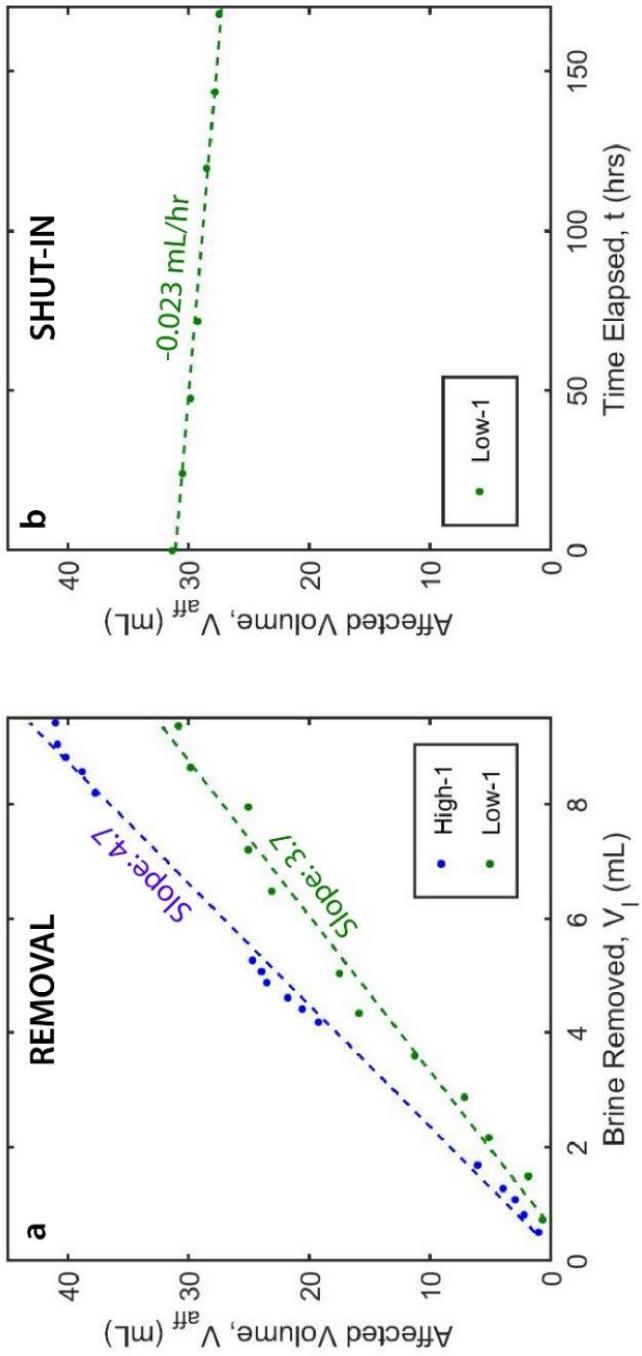

Figure 3.8: Affected volume during brine removal and shut-in.

Dashed lines indicate best fit linear trends for each experiment. (a) V_{aff} during brine removal in High-1 (blue dots) and Low-1 (green dots). (b) V_{aff} during the shut-in of Low-1 (green dots).

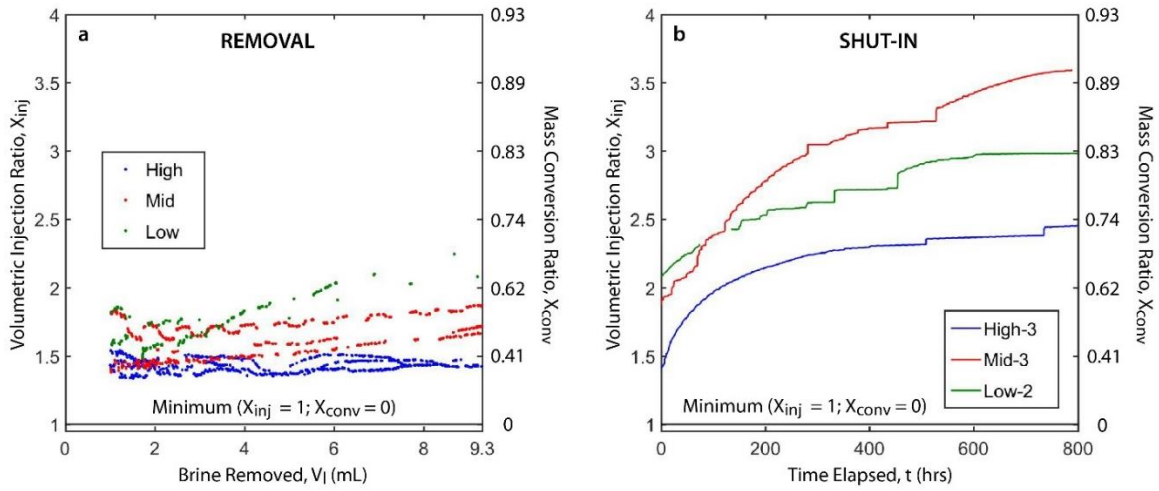

Figure 3.9: Mass balance results during brine removal and shut-in.

Volumetric injection (X_{inj}) and mass conversion (X_{conv}) ratios during the High, Mid, and Low experiments. (a) X_{inj} and X_{conv} in the High (blue dots), Mid (red dots), and Low (green dots) experiments. For clarity, these results have been filtered to remove data where the pressure differential was greater than 0.02 MPa. (b) X_{inj} and X_{conv} in High-3 (blue line), Mid-3 (red line), and Low-2 (green line).

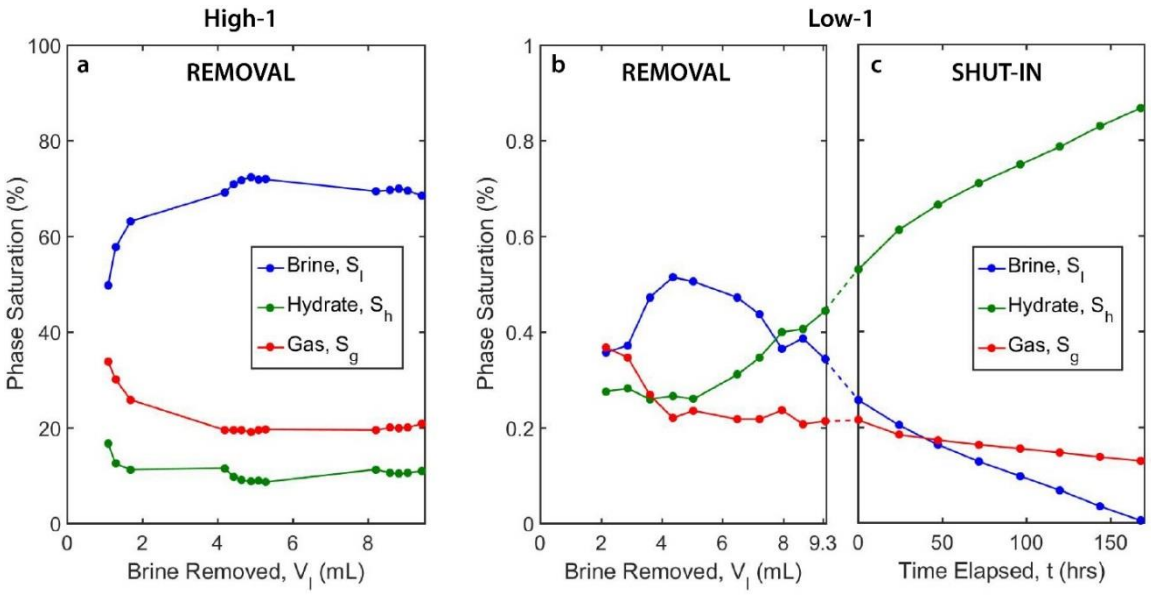

Figure 3.10: Phase saturations during High-1 and Low-1.

Mass balance-derived, bulk brine (blue dots), hydrate (green dots), and gas (red dots) phase saturations within the CT-derived affected volume during brine removal in (a) High-1 and (b) Low-1 and (c) brine shut-in in Low-1. The derivation of the mass balance solution for phase saturations during brine removal is presented in (Meyer et al., 2018); the phase saturations during brine shut-in are calculated using the same method, but assume a constant affected volume.

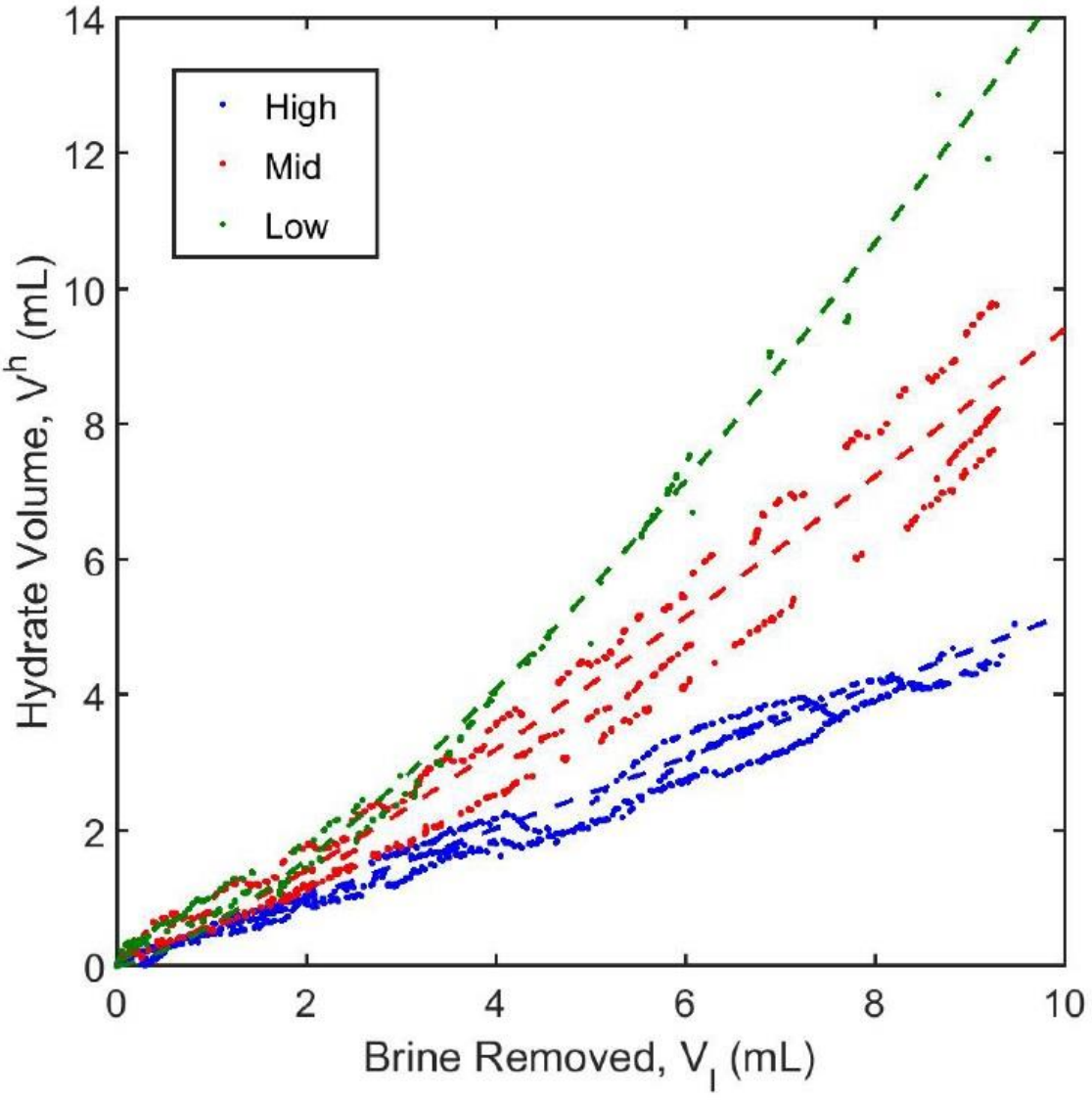

Figure 3.11: Volume of hydrate formed during brine drainage.

Volume of hydrate formed (V^h) in the High (blue dots), Mid (red dots), and Low (green dots) experiments. Blue, red, and green dashed lines indicate best fit power regressions for the High ($V^h = 0.49{V_l}^{1.02}$), Mid ($V^h = 0.62{V_l}^{1.18}$), and Low ($V^h = 0.6{V_l}^{1.39}$) experiments, respectively.

3.4 MASS BALANCE ANALYSIS

The volumetric injection ratio (X_{inj}) is the ratio of the volume of methane injected to the volume of brine removed and the mass conversion ratio (X_{conv}) is the ratio of the mass of methane converted to hydrate to the total mass of methane injected (Section 2.4). With no gas conversion ($X_{conv} = 0$), the volume of methane injected equals the volume of brine removed ($X_{inj} = 1$). With total gas conversion ($X_{conv} = 1$), the volume of methane injected is 5.34 times the volume of brine removed ($X_{inj} = 5.34$) at my experimental conditions. These cases represent the minimum (Figure 3.4: solid black line) and maximum (Figure 3.4: dashed black line) hydrate formation scenarios for my experiments.

In all experiments, X_{inj} was greater than the minimum endmember (Figure 3.9: black line) and increased over time (Figure 3.9), indicating the partial and increasing conversion of the injected methane into hydrate. During brine removal, X_{conv} was greatest in the Low experiments (Figure 3.9a: green dots), which were performed at the lowest flow rate, and lowest in the High experiments (Figure 3.9a: blue dots), which were performed at the highest flow rate. During the shut-ins of High-3 (Figure 3.9b: blue line), Mid-3 (Figure 3.9b: red line), and Low-2 (Figure 3.9b: green line), X_{conv} continued to increase, but at rates that decreased with time.

I calculate the saturations of methane gas (S_g), liquid brine (S_l), and solid hydrate (S_h) within the affected volume (V_{aff}) during brine removal using water and methane mass balance (Section 2.4). In High-1, the average bulk gas (Figure 3.10a: red dots), brine (Figure 3.10a: blue dots), and hydrate (Figure 3.10a: green dots) saturations within the

affected volume were 22%, 67%, and 11%, respectively. By contrast, in Low-1, the average bulk gas (Figure 3.10b: red dots), brine (Figure 3.10b: blue dots), and hydrate (Figure 3.10b: green dots) saturations within the affected volume were 25%, 42%, and 32%, respectively.

During brine shut-in, I calculate the phase saturations using the same mass-balance solution for brine removal (Section 2.4). However, I assume that the affected volume is constant, because I did not observe an increase in V_{aff} in Low-1 during shut-in (Figure 3.8b). In Low-1, the hydrate saturation increased from 53% to 87% (Figure 3.10c: green dots) and the gas (Figure 3.10c: red dots) and brine (Figure 3.10c: blue dots) saturations decreased from 21% to 13% and from 26% to 0.4%, respectively. The continuous increase in hydrate saturation and complete consumption of brine suggests that brine is likely being drawn into the affected volume to supply water for additional hydrate formation. It is also possible, however, that V_{aff} is increasing, but is offset by reductions V_{aff} due to the density increases. In this case, this calculation would underestimate the brine saturation and overestimate the gas and hydrate saturations.

I calculate the volume of hydrate in the sample (V^h; Figure 3.11) during removal from the hydrate saturation and the affected volume. For the experiments not performed in the CT scanner, I assume the affected volume is equal to the total pore volume in the sample and use the mass balanced-derived hydrate saturation where hydrate is distributed evenly throughout the sample. At the end of the High experiments (Figure 3.11: blue dots), an average of 4.8 mL of hydrate formed in the sample. By contrast, in the Mid (Figure 3.11: red dots) and Low (Figure 3.11: green dots) experiments, an average of 8.6 and 13.2 mL

of hydrate formed by the end of the experiments. The best fit power regressions for the data from each experiment (Figure 3.11: dashed lines) indicate that hydrate forms at approximately 2.4 times the rate, per volume of brine removed, in the Low experiments than the High experiments.

3.5 DISCUSSION

A 6-fold decrease in the brine flow rate increases the average hydrate saturation within the affected volume from 11% to 32% and decreases the average brine saturation from 68% to 47% (Figure 3.10). Decreasing the brine flow rate has little effect on the gas saturation (Figure 3.10). Lower flow rates also produce greater average pressure differentials across the sample (Figure 3.3) and reduce the affected volume by 21% (Figure 3.8).

During shut-in, methane flows into the sample at a decreasing rate with time (Figure 3.4a). The gas flow rate immediately after shut-in was greater for High-3 (Figure 3.4b: blue line) than Low-2 (Figure 3.4b: green line), but, at later times (> 200 hours elapsed), the gas flow rate is very low in all experiments. Throughout the shut-in, hydrate saturations increase and brine saturations decrease significantly, while the gas saturation decreases slightly (Figure 3.10c). The bulk density within the affected volume increases overall, but decreases near the inlet and increases near the front of the affected volume (Figure 3.7). Pressure differentials develop during shut-in (Figure 3.3d) and are associated with little to no gas flow into the sample (Figure 3.4b inset).

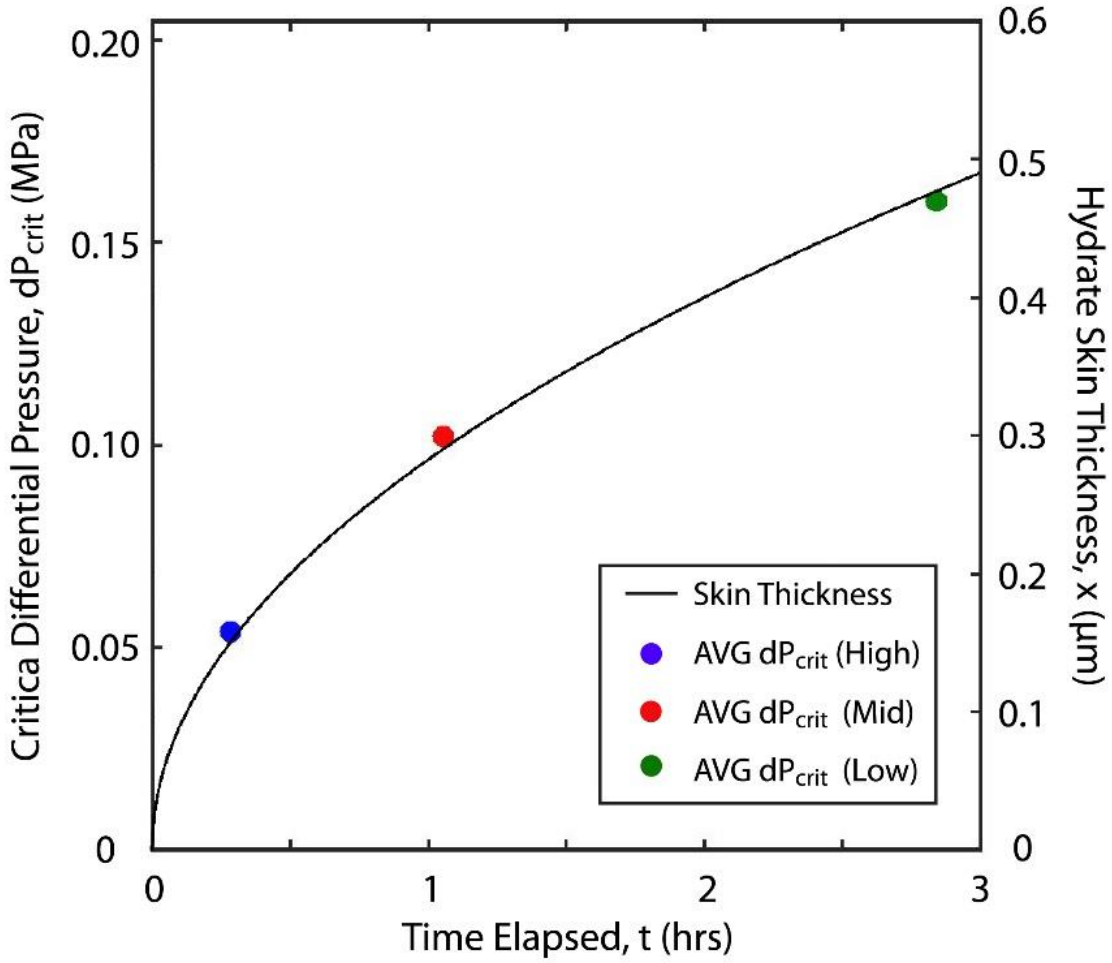

Figure 3.12: Average critical differential pressures during brine removal.

Average critical differential pressures (dP_{crit}) as a function of the average time requires to reach that differential pressure for the High (blue dot), Mid (red dot), and Low (green dot) experiments. Black line shows the hydrate thickness as a function of time as modeled by Meyer et al. (2018). This model assumes a methane diffusion coefficient through hydrate (D_m) of 10^{-15} m^2 s^{-1} (Davies et al., 2010; Genov et al., 2004; Kuhs et al., 2006), a methane concentration at the gas-hydrate interface (C_m^g) of 146 mol m^{-3}, and a methane concentration at the brine-hydrate interface (C_m^h) of 61 mol m^{-3}.

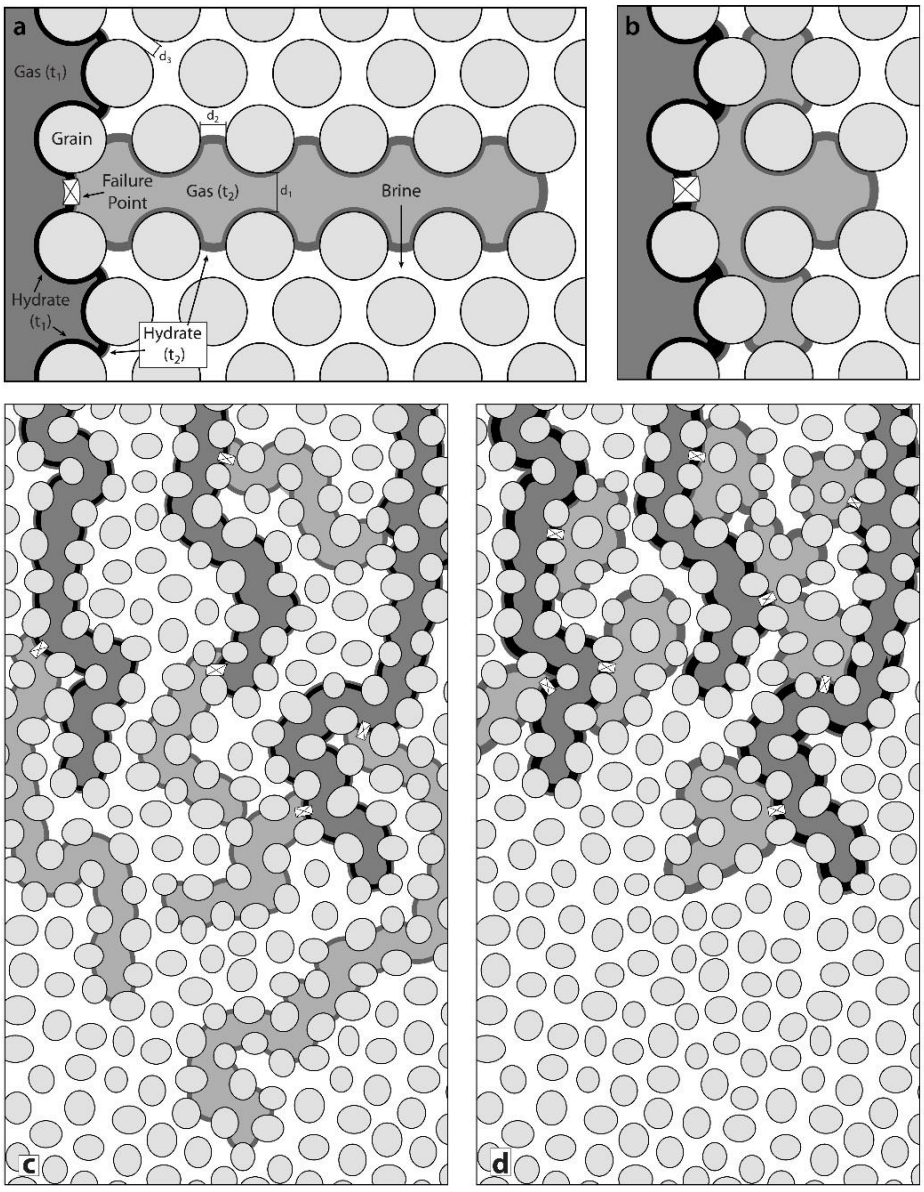

Figure 3.13: Conceptual model of High and Low experiments.

Model of gas progression and hydrate skin growth at different flow rates. t_1 and t_2 represent two time-steps. (a) High experiments have thin hydrate skins that sustain small pressure differentials. Upon failure, gas only flows through the largest pore throat sizes ($d_1 > d_2 > d_3$). (b) Low experiments have thick hydrate skins that sustain large pressure differentials. Upon failure, gas flows through many pore throat sizes. (c) In High experiments, gas is concentrated in narrow fingers. (d) In Low experiments, gas is distributed near the failure point.

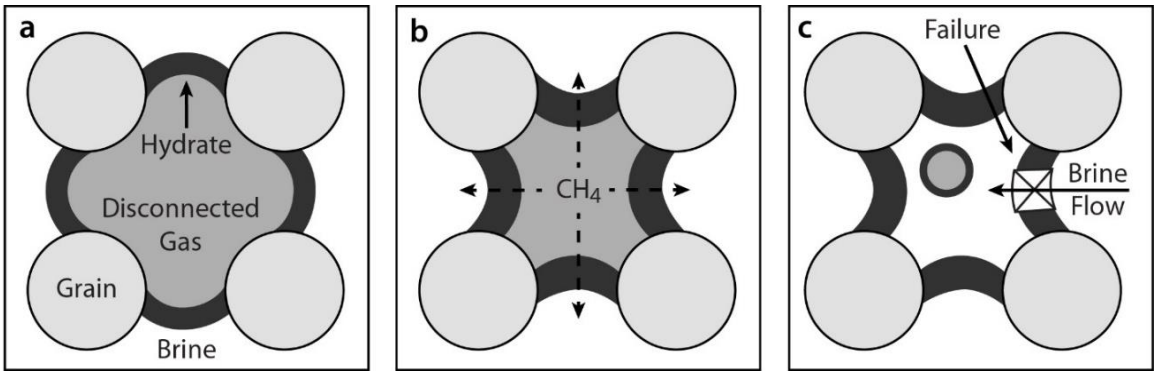

Figure 3.14: Conceptual model of gas conversion into hydrate during shut-in.

(a) Disconnected gas phase separated from brine by a hydrate skin. (b) Methane diffusion across the gas-hydrate-brine interface reduces the internal gas pressure and the hydrate skin collapses inwards. (c) Eventual failure of hydrate skin allows brine flow, which compresses the remaining gas and forms a new hydrate skin. This cycle continues until all the gas is converted into hydrate.

3.5.1 Flow blockages due to hydrate formation

The development of pressure differentials (Figure 3.3a, b, and c) is coincident with no gas flow (Figure 3.4b inset), indicating flow blockages. The increase in differential pressure (dP) is driven by the removal of brine from the sample. Thus, the rate of increase of dP is proportional to the brine removal rate such that, once a blockage is formed, dP rises faster for the High experiments than for the Low experiments. The re-establishment of flow is recorded by an abrupt decrease in dP at dP_{crit} and rapid gas flow into the sample (Figure 3.4b inset). dP_{crit} generally increases with time during the experiments and, on average, is greater and takes longer to develop in the Low experiments than the High experiments (Figure 3.12: dots).

I infer that the flow blockage is caused by the formation of a hydrate skin at the gas-brine interface, as described in Chapter 2, and that dP_{crit} records the differential pressure necessary to break the hydrate skin. dP_{crit} is a function of the skin strength, which is related to its thickness. I describe the hydrate skin thickness with a one-dimensional diffusion model in Chapter 2. It is striking that both the skin thickness and the magnitude of dP_{crit} can be modeled as a function of the square root of time (Figure 3.12: black line); this finding suggests that these processes are inter-related. I interpret that the pressure differentials rise with time during the experiments due to the extra time for the skin thickness to increase. Furthermore, I interpret that dP_{crit} is greater in the Low experiments because the lower brine flow rates extend the time for the hydrate skin to thicken during the flow blockages.

3.5.2 Hydrate formation as a function of the brine removal rate

The fraction of methane converted to hydrate is much greater in the Low experiments than the High experiments (Figure 3.9a). As a result, as much as 2.7 times more hydrate is formed in the Low experiments than the High experiments for a given volume of brine removed (Figure 3.11). Furthermore, the CT results show that the affected volume, the region where I interpret that gas and hydrate are present, is 21% smaller in the Low experiments than the High experiments for a given volume of brine removed (Figure 3.8a). As a result, the hydrate saturations are 300% higher and the brine saturations are 30% lower within the affected volume in the Low experiments, compared to the High experiments (Figure 3.10).

I interpret that these behaviors are controlled by how gas enters unaffected regions of the sample. The hydrate skin allows for the development of large pressure differentials such that gas flow primarily takes place during periods of rapidly changing pressure gradients upon skin failure. The range of pore throat sizes the gas can access depends on the magnitude of the pressure differential. Small differentials limit flow to large pore throats, resulting in narrow flow paths (e.g. capillary fingering) that distribute gas further from the failure point (Figure 3.13a). In contrast, large differentials exceed a wider range of entry pressures such that flow occurs through multiple, interconnecting flow paths that distribute gas close to the failure point (Figure 3.13b). At the core-scale, this results in gas flow along a few fingers that invade further into the sample (Figure 3.13c) in the High experiments (small average dP) and gas flow along many fingers that are distributed close to the failure point (Figure 3.13d) in the Low experiments (large average dP).

Ultimately, I interpret that the greater conversion of methane to hydrate in the Low experiments (and thus higher hydrate saturations for a given volume of brine removed), compared to the High experiments, is due to two factors. Lower flow rates extend the time for methane transport across the hydrate skin, which allows more hydrate to form at the gas-brine interface. Also, through the mechanism described above, lower flow rates result in a larger gas-brine contact surface area where hydrate can be formed.

3.5.3 Hydrate formation during shut-in

During shut-in, the gas flow rate, and hence the hydrate formation rate, is greatest in the experiments that had the highest brine flow rate during the removal period and decreases over time in all experiments (Figure 3.4). I interpret that the High experiments have a thinner average hydrate skin at the end of brine removal, compared to the Low experiments, which allows for more rapid methane diffusion through the skin. As the skin thickness increases, however, the concentration gradient decreases, reducing the diffusion rate and driving the gradual decrease in gas flow rate observed in all experiments.

The pressure differentials formed during shut-in are generally larger in magnitude than those formed during brine removal and do not appear to scale with the brine flow rate during the removal period (Figure 3.3d). I interpret that these pressure differentials result from the presence of disconnected, hydrate-encased free gas that is gradually converting to hydrate (Figure 3.14), similar to the collapse of a hydrate-encased gas bubble (Davies et al., 2010; Tohidi et al., 2001). Initially, the disconnected gas is at the same pressure as the brine and these phases are separated by a hydrate skin (Figure 3.14a). As methane diffuses across the skin and forms hydrate at the gas-brine interface, the internal gas pressure

declines, causing the brine to press on the hydrate skin (Figure 3.14b). Eventually, the pressure differential between the disconnected gas and brine exceeds the critical pressure and causes the hydrate skin to fail (Figure 3.14c).

The volume of gas injected after skin failure (e.g. Figure 4b: inset) indicates that the total volume change during pressure differential development are typically less than 1 mL spread throughout the affected volume (~30 mL). This volume change could be achieved through the combination of gas conversion to hydrate and compression upon skin failure as this process results in a 47% decrease in net volume. This volume decrease draws brine towards the collapsing hydrate and causes the brine phase pressure to decrease, producing a pressure differential between the interconnected gas and brine. Eventually, the pressure differential causes the skin to fail along the interconnected gas and gas flows into the sample. I envision that, at the core-scale, the region where density increases during shut-in (Figure 3.7b near inlet) is where disconnected gas is converting to hydrate, while the region where density is decreasing during shut-in (Figure 3.7b near red line) is where gas is flowing into the pore space.

3.5.4 Field-scale implications

My experiments indicate that decreasing the flow rate can significantly increase the final hydrate saturation, but also require larger pressure differentials to maintain gas flow. In my experiments, the pressure differentials during removal are created by removing brine from the sample, but in the field this requires the collection of a continuous gas column beneath the hydrate. The critical gas column height ($h = dP/g \cdot \Delta\rho_{l-g}$) is equal to the critical ifferential pressure (dP_{crit}) divided by the brine-gas density contrast ($\Delta\rho_{l-g} = \rho_l -$

ρ_g) and gravitational acceleration (g). This relationship indicates that the High, Mid, and Low experiments would require, on average, a gas column of 6, 10, and 16 meters high, respectively; this is not uncommon in active hydrocarbon systems (Boswell et al., 2012b; Frye et al., 2012). The average gas flow rates in the field, however, are likely slower than can be achieved experimentally (Liu & Flemings, 2007; Torres et al., 2002), which suggests that larger pressure differentials may be required. Thus, it is possible that hydrate would form to such high saturations that upward gas flow ceases entirely. Where gas is able to flow, however, there is certain to be significant additional hydrate formation driven by methane diffusion through the skin. This work strongly indicates that, under the right conditions, this process could produce very high saturations of hydrate distributed throughout a coarse-grained reservoir over tens to thousands of years.

3.6 CONCLUSIONS

I form methane hydrate in brine-saturated sand packs under hydrate-stable conditions by removing brine at a constant rate and allowing methane gas to flow into the sample at a constant pressure. I then halt the brine flow and maintain the upstream methane pressure for approximately 800 hours. Decreasing the brine flow rate increases the average hydrate saturation at the end of brine removal from 11% – 32% and hydrate continues to form over the course of the shut-in periods. These findings are consistent with my previous conceptual model where hydrate forms a solid skin at the gas-liquid interface that separates the gas and brine phases. I interpret that lower flow rates provide extra time for methane transport, which results in higher hydrate saturations and thicker hydrate skins. Since the

mechanism for methane transport is the same during the brine removal and shut-in periods, hydrate continues to form at a decreasing rate. At my comparatively short experimental timescales, this process distributes high saturations of hydrate throughout a large portion of the sample. This result strongly suggests that over thousands of years this mechanism could explain the presence of very high hydrate saturations present far above the base of gas hydrate stability.

NOMENCLATURE

Symbol	Name	Dimension	Unit
C	salinity	(M M^{-1})	(wt. %)
C_m^g	solubility of methane in water	(M L^{-3})	(mol m^{-3})
C_m^h	solubility of hydrate in water	(M L^{-3})	(mol m^{-3})
D_m	diffusion coefficient of methane in hydrate	(L T^{-2})	(m s^{-2})
d	pore throat size	(L)	(m)
dP	differential pressure	(M L^{-1} T^{-2})	(MPa)
dP_{crit}	critical differential pressure	(M L^{-1} T^{-2})	(MPa)
g	gravitational acceleration	(M T^{-2})	(m s^{-2})
h	critical gas column height	(L)	(m)
P	experimental pressure	(M L^{-1} T^{-2})	(MPa)
P_{in}	inlet pressure	(M L^{-1} T^{-2})	(MPa)
P_{out}	outlet pressure	(M L^{-1} T^{-2})	(MPa)
S_g	methane gas phase saturation	(-)	(-)
S_h	solid hydrate phase saturation	(-)	(-)
S_l	liquid brine phase saturation	(-)	(-)
T	experimental temperature	(K)	(ºC)
t	time elapsed	(T)	(s)
V^h	volume of hydrate	(L^3)	(cm^3)
V_{aff}	affected volume	(L^3)	(cm^3)
V_l	volume of brine removed	(L^3)	(cm^3)
V_m	volume of methane injected	(L^3)	(cm^3)
X_{conv}	mass conversion ratio	(-)	(-)
X_{inj}	volumetric injection ratio	(-)	(-)
$\Delta\rho_b$	bulk density change	(M L^{-3})	(g cm^{-3})
$\Delta\rho_{l-g}$	brine-gas density contrast	(M L^{-3})	(g cm^{-3})
ϕ_{grav}	gravimetrically-derived sample porosity	(-)	(-)
ϕ_{CT}	CT-derived sample porosity	(-)	(-)
ρ_b	sample bulk density	(M L^{-3})	(g cm^{-3})
ρ_g	gas phase density	(M L^{-3})	(g cm^{-3})
ρ_l	liquid phase density	(M L^{-3})	(g cm^{-3})

ACKNOWLEDGMENTS

This work was supported by the U.S. Department of Energy under Contract No. DE-FE0010406, DE-FE0028967, and DE-FE0023919. Supporting data for this work is available upon request from the corresponding author. All of the x-ray CT images and acquired data used in the figures are archived in the Digital Rocks Portal (www.digitalrocksportal.org) with the project name "Methane hydrate formation during gas injection into saturated sand." All other experimental and analytical data referenced in this article are accessible through the presented figures, tables, and references. These data can also be requested by e-mail from the corresponding author (meyerdw3@utexas.edu). I thank Peter Polito and Joshua O'Connell for their assistance and advice in assembling the experimental apparatus and executing these experiments.

REFERENCES

Boswell, R., and Collett, T. (2011). Current prospective on gas hydrate resources. *Energy & Environmental Science, 4*, 10.

Boswell, R., Collett, T. S., Frye, M., Shedd, W., McConnell, D. R., and Shelander, D. (2012a). Subsurface gas hydrate in the northern Gulf of Mexico. *Marine and Petroleum Geology, 34*, 27. doi: 10.1016/j.marpetgeo.2011.10.003

Boswell, R., Frye, M., Shelander, D., Shedd, W., McConnell, D. R., and Cook, A. (2012b). Architecture of gas-hydrate-bearing sands from Walker Ridge 313, Green Canyon 955, and Alaminos Canyon 21: Northern deepwater Gulf of Mexico. *Marine and Petroleum Geology, 34*(1), 134-149. doi: http://dx.doi.org/10.1016/j.marpetgeo.2011.08.010

Boswell, R., Shelander, D., Lee, M., Latham, T., Collett, T., Guerin, G., Moridis, G., Reagan, M., and Goldberg, D. (2009). Occurrence of gas hydrate in Oligocene Frio sand: Alaminos Canyon Block 818: Northern Gulf of Mexico. *Marine and Petroleum Geology, 26*(8), 1499-1512. doi: 10.1016/j.marpetgeo.2009.03.005

Casey, B., Germaine, J. T., Flemings, P. B., Reece, J. S., Gao, B., and Betts, W. (2013). Liquid limit as a predictor of mudrock permeability. *Marine and Petroleum Geology, 44*, 256-263. doi: http://dx.doi.org/10.1016/j.marpetgeo.2013.04.008

Collett, T. S., Lee, M. W., Zyrinova, M. V., Mrozewski, S. A., Guerin, G., Cook, A. E., and Goldberg, D. S. (2012). Gulf of Mexico Gas Hydrate Joint Industry Project Leg II logging-while-drilling data acquisition and analysis. *Marine and Petroleum Geology, 34*, 21.

Crutchley, G. J., Fraser, D. R. A., Pecher, I. A., Gorman, A. R., Maslen, G., and Henrys, S. A. (2015). Gas migration into gas hydrate-bearing sediments on the southern Hikurangi margin of New Zealand. *Journal of Geophysical Research: Solid Earth, 120*(2), 725-743. doi: 10.1002/2014jb011503

Davies, S. R., Sloan, E. D., Sum, A. K., and Koh, C. A. (2010). In Situ Studies of the Mass Transfer Mechanism across a Methane Hydrate Film Using High-Resolution Confocal Raman Spectroscopy. *The Journal of Physical Chemistry C, 114*(2), 1173-1180. doi: 10.1021/jp909416y

England, W. A., Mackenzie, A. S., Mann, D. M., and Quigley, T. M. (1987). The movement and entrapment of petroleum fluids in the subsurface. *Journal of the Geological Society, 144*(2), 327-347. doi: 10.1144/gsjgs.144.2.0327

Frye, M., Shedd, W., and Boswell, R. (2012). Gas hydrate resource potential in the Terrebonne Basin, Northern Gulf of Mexico. *Marine and Petroleum Geology, 34*(1), 150-168. doi: https://doi.org/10.1016/j.marpetgeo.2011.08.001

Genov, G., Kuhs, W. F., Staykova, D. K., Goreshnik, E., and Salamatin, A. N. (2004). Experimental studies on the formation of porous gas hydrates. *American Mineralogist, 89*(8-9), 1228-1239. doi: 10.2138/am-2004-8-910

Germaine, J. T., and Germaine, A. V. (2009). *Geotechnical Laboratory Measurements for Engineers*. Hoboken, NJ: John Wiley & Sons, Inc.

Koh, D.-Y., Kang, H., Lee, J.-W., Park, Y., Kim, S.-J., Lee, J., Lee, J. Y., and Lee, H. (2016). Energy-efficient natural gas hydrate production using gas exchange. *Applied Energy, 162*(Supplement C), 114-130. doi: https://doi.org/10.1016/j.apenergy.2015.10.082

Konno, Y., Fujii, T., Sato, A., Akamine, K., Naiki, M., Masuda, Y., Yamamoto, K., and Nagao, J. (2017). Key Findings of the World's First Offshore Methane Hydrate Production Test off the Coast of Japan: Toward Future Commercial Production. *Energy & Fuels, 31*(3), 2607-2616. doi: 10.1021/acs.energyfuels.6b03143

Kuhs, W. F., Staykova, D. K., and Salamatin, A. N. (2006). Formation of Methane Hydrate from Polydisperse Ice Powders. *The Journal of Physical Chemistry B, 110*(26), 13283-13295. doi: 10.1021/jp061060f

Kvenvolden, K. A. (1993). Gas hydrates—geological perspective and global change. *Reviews of Geophysics, 31*(2), 173-187. doi: 10.1029/93rg00268

Kvenvolden, K. A., and McMenamin, M. A. (1980). Hydrates of natural gas; a review of their geologic occurrence. *Report Rep. 825*.

Liu, X., and Flemings, P. B. (2006). Passing gas through the hydrate stability zone at southern Hydrate Ridge, offshore Oregon. *Earth and Planetary Science Letters*(241), 16.

Liu, X., and Flemings, P. B. (2007). Dynamic multiphase flow model of hydrate formation in marine sediments. *Journal of Geophysical Research: Solid Earth, 112*(B3), B03101. doi: 10.1029/2005jb004227

Malinverno, A., and Goldberg, D. S. (2015). Testing short-range migration of microbial methane as a hydrate formation mechanism: Results from Andaman Sea and Kumano Basin drill sites and global implications. *Earth and Planetary Science Letters, 422*, 105-114. doi: http://dx.doi.org/10.1016/j.epsl.2015.04.019

Meyer, D. W., Flemings, P. B., DiCarlo, D. A., You, K., Phillips, S. C., and Kneafsey, T. (2018). Experimental investigation of gas flow and hydrate formation within the hydrate stability zone. *Journal of Geophysical Research: Solid Earth*. doi: 10.1029/2018JB015748

Milkov, A. V. (2004). Global estimates of hydrate-bound gas in marine sediments: how much is really out there? *Earth-Science Reviews, 66*(3–4), 183-197. doi: http://dx.doi.org/10.1016/j.earscirev.2003.11.002

Moridis, G. J. (2008). Toward Production From Gas Hydrates: Current Status, Assessment of Resources, and Simulation-Based Evaluation of Technology and Potential.

Nole, M., Daigle, H., Cook, A. E., and Malinverno, A. (2016). Short-range, overpressure-driven methane migration in coarse-grained gas hydrate reservoirs. *Geophysical Research Letters, 43*(18), 9500-9508. doi: 10.1002/2016gl070096

Rees, E. V. L., Kneafsey, T., and Seol, Y. (2011). Methane Hydrate Distribution from Prolonged and Repeated Formation in Natural and Compacted Sand Samples: X-Ray CT Observations. *Journal of Geological Research, 2011*. doi: 10.1155/2011/791815

Rempel, A. W. (2011). A model for the diffusive growth of hydrate saturation anomalies in layered sediments. *Journal of Geophysical Research: Solid Earth, 116*(B10), n/a-n/a. doi: 10.1029/2011jb008484

Riestenberg, D., West, O., Lee, S., McCallum, S., and Phelps, T. J. (2003). Sediment surface effects on methane hydrate formation and dissociation. *Marine Geology, 198*(1–2), 181-190. doi: http://dx.doi.org/10.1016/S0025-3227(03)00100-2

Schowalter, T. T. (1979). Mechanics of Secondary Hydrocarbon Migration and Entrapment. *AAPG Bulletin, 63*(5), 37.

Seol, Y., and Kneafsey, T. J. (2009). X-ray computed-tomography observations of water flow through anisotropic methane hydrate-bearing sand. *Journal of Petroleum Science and Engineering, 66*(3–4), 121-132. doi: http://dx.doi.org/10.1016/j.petrol.2009.01.008

Shipley, T. H., Houston, M. H., Buffler, R. T., Shaub, J., McMillen, K. J., Ladd, J. W., and Worzel, J. L. (1979). Seismic Evidence for Widespread Possible Gas Hydrate Horizons on Continental Slopes and Rises. *The American Association of Petroleum Geologists Bulletin, 63*(12), 10.

Sloan, E. D., and Koh, C. A. (2007). *Clathrate Hydrates of Natural Gases* (3nd ed.). Boca Raton, FL: CRC Press.

Tohidi, B., Anderson, R., Clennell, M. B., Burgass, R. W., and Biderkab, A. B. (2001). Visual observation of gas-hydrate formation and dissociation in synthetic porous media by means of glass micromodels. *Geology, 29*(9), 4.

Torres, M. E., Wallmann, K., Tréhu, A. M., Bohrmann, G., Borowski, W. S., and Tomaru, H. (2004). Gas hydrate growth, methane transport, and chloride enrichment at the southern summit of Hydrate Ridge, Cascadia margin off Oregon. *Earth and Planetary Science Letters, 226*(1–2), 225-241. doi: http://dx.doi.org/10.1016/j.epsl.2004.07.029

Torres, M. E., McManus, J., Hammond, D. E., de Angelis, M. A., Heeschen, K. U., Colbert, S. L., Tryon, M. D., Brown, K. M., and Suess, E. (2002). Fluid and chemical fluxes in and out of sediments hosting methane hydrate deposits on Hydrate Ridge, OR, I: Hydrological provinces. *Earth and Planetary Science Letters, 201*(3), 525-540. doi: https://doi.org/10.1016/S0012-821X(02)00733-1

Tréhu, A. M., Flemings, P. B., Bangs, N. L., Chevallier, J., Gràcia, E., Johnson, J. E., Liu, C. S., Liu, X., Riedel, M., and Torres, M. E. (2004). Feeding methane vents and gas hydrate deposits at south Hydrate Ridge. *Geophysical Research Letters, 31*(23), L23310. doi: 10.1029/2004gl021286

You, K., Kneafsey, T. J., Flemings, P. B., Polito, P., and Bryant, S. L. (2015). Salinity-buffered methane hydrate formation and dissociation in gas-rich systems. *Journal of Geophysical Research: Solid Earth, 120*(2), 643-661. doi: 10.1002/2014jb011190

Xu, W., and Ruppel, C. (1999). Predicting the occurrence, distribution, and evolution of methane gas hydrate in porous marine sediments. *Journal of Geophysical Research: Solid Earth, 104*(B3), 5081-5095. doi: 10.1029/1998jb900092

Chapter 4: Gas Flow Within the Hydrate Stability Zone Through Hydrate-Encased Gas Finger

ABSTRACT

I injected methane into a brine-saturated sand pack that was at temperatures and pressures within the hydrate stability zone. Hydrate formed rapidly to saturations of 10 – 30% in coexistence with free gas that continuously advanced into the sample. At lower injected rates, a greater fraction of the injected gas formed hydrate. I interpret that during injection, a hydrate skin forms at the gas-brine interface and separates the gas and brine. As a result, gas, hydrate, and brine co-exist at non-equilibrium for month-long timescales. I present a model where hydrate forms around a cylindrical gas finger that advances under a constant gas flux. As the finger extends by advection, methane simultaneously diffuses through the hydrate skin, forming hydrate at the hydrate-brine interface and thickening the skin. I provide experimental and quantitative modeling support for an alternative, mechanistic model of gas transport and hydrate formation within the hydrate stability zone.

4.1 INTRODUCTION

Hydrate is a crystalline solid consisting of a low molecular weight gas, most commonly methane, trapped in a water cage (Kvenvolden and McMenamin, 1980). Hydrates are stable at low temperature and salinity and high pressure where the local methane concentration exceeds the methane solubility in water (Sloan and Koh, 2007). Hydrates are commonly found in the shallow subsurface along continental margins and in permafrost regions (Boswell and Collett, 2011). Studies have estimated that 500 – 2500 gigatons of carbon are trapped in hydrates (Boswell and Collett, 2011; Milkov, 2004), making it a significant portion of the global carbon budget and motivating research into hydrates as both a global climate change hazard (Archer et al., 2004; Wright et al., 2005) and potential energy resource (Koh et al., 2016; Konno et al., 2017; Moridis, 2008).

Along continental margins, hydrates are stable between the seafloor and the base of the gas hydrate stability zone (GHSZ), where the in-situ temperature exceeds the stability conditions. A typical assumption is that any methane present within the GHSZ, in excess of the local methane solubility in water, will solidify into hydrate. However, there is ample evidence of gas migration over hundreds of meters through the hydrate stability zone in the field (Chun et al., 2011; Lüdmann & Wong, 2003; Riedel et al., 2006). The primary mechanisms proposed to explain this behavior are: 1) kinetic limitations on hydrate nucleation (Haeckel et al., 2004; Sun & Mohanty, 2006; Tréhu et al., 2004); 2) self-limited hydrate formation through the development of locally elevated salinities (Liu and Flemings, 2007; You et al., 2015; You and Flemings, in review); and 3) concentrated

gas flow through fracture networks supported by hydrate formation along the fracture walls (Ginsburg and Soloviev, 1997; Riedel et al., 2006).

To investigate the mechanism controlling gas flow through the GHSZ, I injected methane at various flow rates into a brine-saturated sand pack that was within the hydrate stability zone (e.g. high pressure and low temperature). My experimental results indicated that gas progressed through the sample encased in a hydrate skin that limited hydrate formation by methane transport through the hydrate. I reproduced the experimental behaviors using a simple numerical model of hydrate formation at the gas-brine interface of an advecting, cylindrical gas finger. I couple the model to my experimental results to constrain the model parameters. The gas finger advance rate, fraction of the gas injected that is converted into hydrate, volume of hydrate formed, and bulk hydrate saturations from the model are strikingly similar to those observed in the experiments. In this study, I present experimental and modeling evidence of an alternative gas transport and hydrate formation process. This mechanism eliminates the common assumption that the system is well-mixed and instantaneously achieve thermodynamic equilibrium, but may still produce high saturations of hydrate while sustaining vertical gas flow.

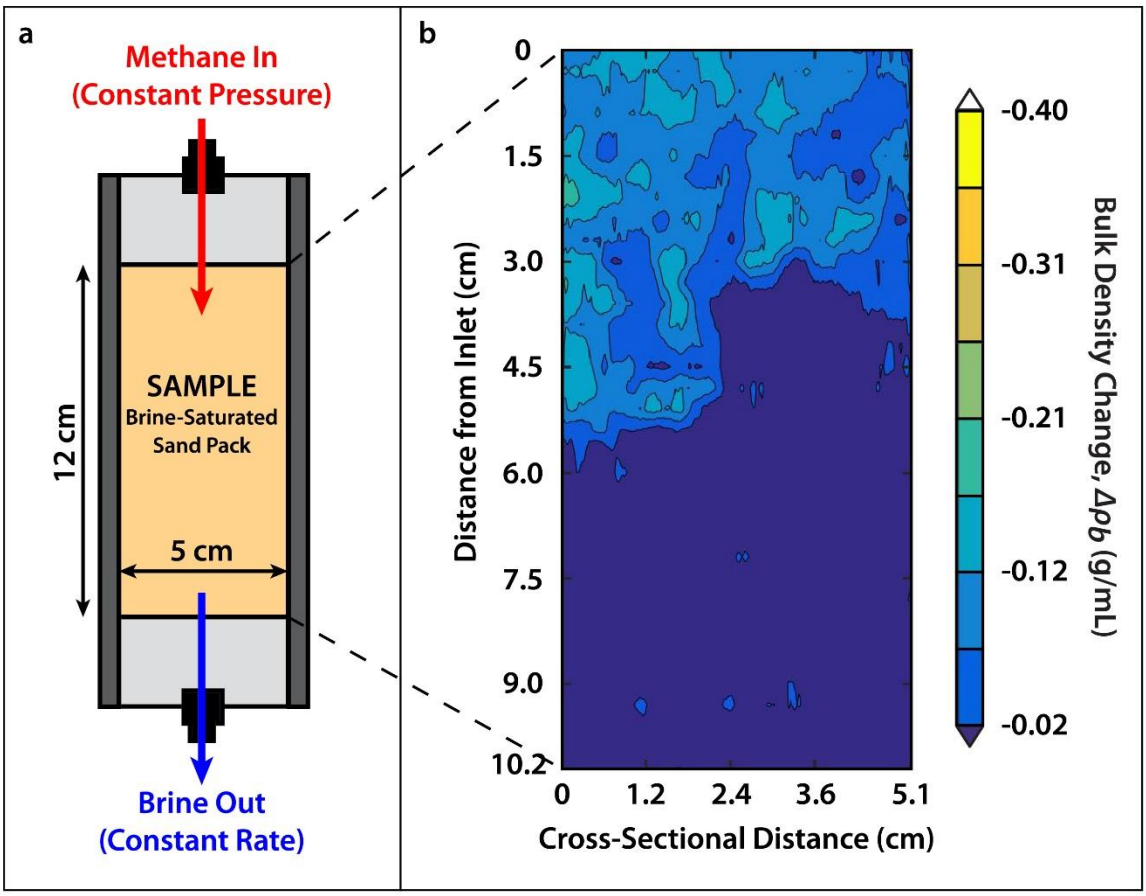

Figure 4.1: Experimental procedure and characteristic CT scan results.

(a) Sample geometry and boundary conditions. (b) CT-derived change in bulk density ($\Delta\rho_b$), relative to initial density, along center plan of the sample in one experiment.

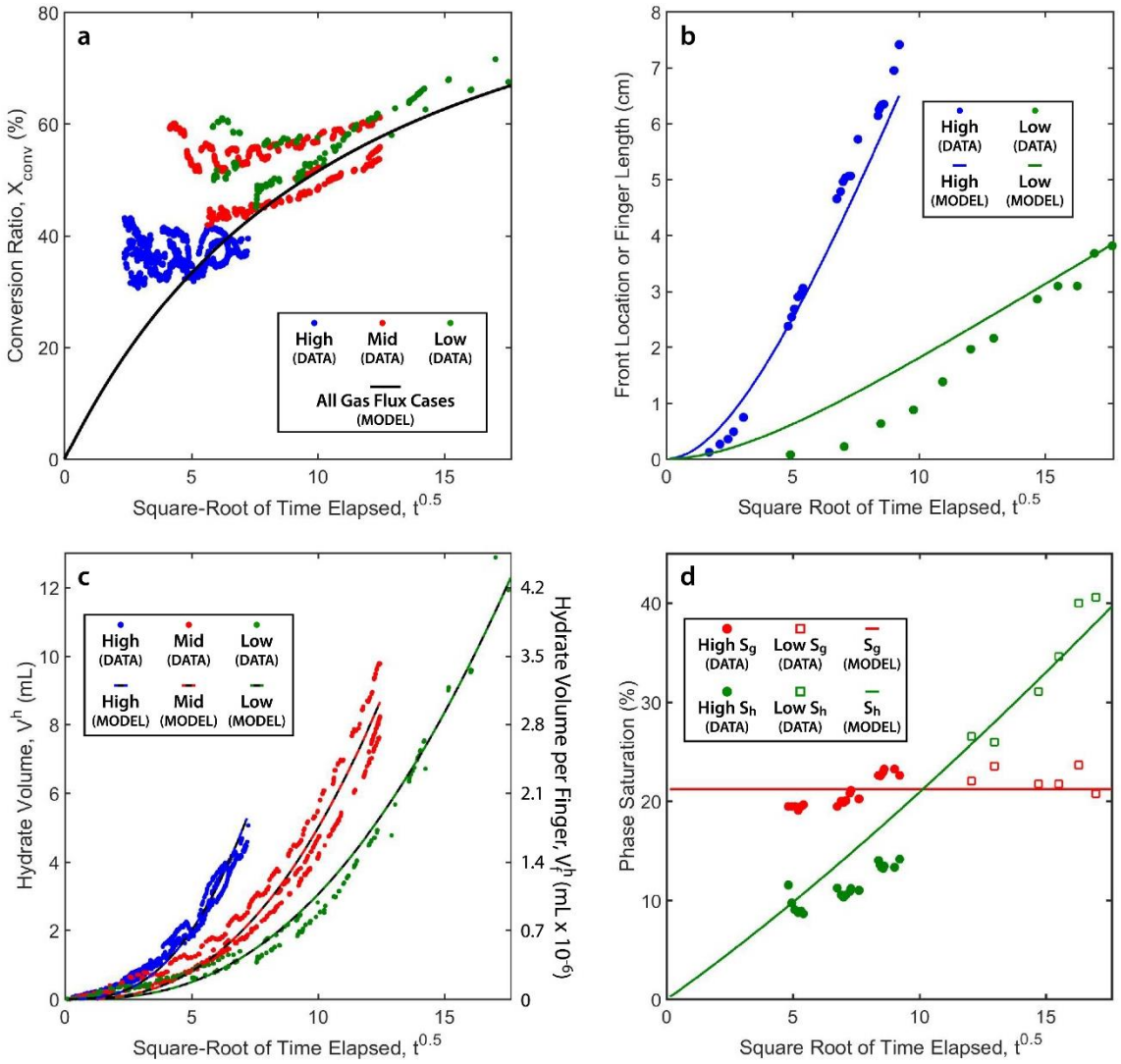

Figure 4.2: Comparison of experimental and modeled results.

Experimental results from the High, Mid, and Low experiments are indicated by markers. Modeled results, using the parameters in Table 1, from the High, Mid, and Low cases are indicated by lines. All values are presented as a function of the square root of time elapsed (t). (a) Conversion ratio (X_{conv}). (b) Average location of the low density front (from CT scans) in the experiments compared to the modeled finger length. (c) Volume of hydrate (V^h) formed. (d) Bulk hydrate (S_h) and gas (S_g) saturations within the affected volume.

4.2 Hydrate Formation Behavior During Gas Injection

I inject gas into an unconsolidated, brine-saturated, sand sample by withdrawing brine at a constant rate from the downstream end while supplying gas at a constant pressure to the upstream end (Figure 4.1a). I observe core-scale density changes in the samples over time using a X-ray computed-tomography (CT) scanner. I calculate the volume of hydrate formed (V^h) and the conversion ratio (X_{conv}), defined as the ratio of the masses of methane converted to hydrate to the total methane injected, from the methane mass entering the sample and brine mass removed. I performed experiments at High (0.18 mL/hr), Mid (0.06 mL/hr), and Low (0.03 mL/hr) brine removal rates and removed a constant volume of brine. Thus, the duration of the Low experiments were six times longer than the High experiments. The experimental methodology is described in detail in Meyer et al. (2018).

While removing brine, a low density front developed at the upstream end and gradually advanced downstream (Figure 4.1b). I calculated the average front location from the affected volume, defined as the pore volume where the bulk density decrease exceeded the measurement error (± 0.024 g/mL), and the cross-sectional area of the pore space. The front location advanced at a faster rate in the High (Figure 4.2a: blue dots), compared to the Low (Figure 4.2a: green dots), experiment. I interpret that hydrate, gas, and brine are present behind the front and that additional hydrate is forming within this region. As a result, X_{conv} increased throughout the High (Figure 4.2b: blue dots), Mid (Figure 4.2b: red dots), and Low (Figure 4.2b: green dots) experiments to average final values of 38%, 57%, and 72%, respectively. V^h also increased over time in the High (Figure 4.2c: blue dots), Mid (Figure 4.2c: red dots), and Low (Figure 4.2c: green dots) experiments through both

gas advection farther into the sample and methane diffusion through the skin. I calculate the bulk hydrate (S_h) and gas (S_g) phase saturations within the affected volume (Figure 4.2d). The average gas saturation in the High (Figure 4.2d: red dots) and Low (Figure 4.2d: red squares) experiments is 21%. The hydrate saturation increased with time from 8% to 14% in the High experiment (Figure 4.2d: green dots) and from 26% to 44% in the Low experiment (Figure 4.2d: green squares).

4.3 Hydrate Formation Model

I interpret that gas progresses through the sample encased in a hydrate skin such that the conversion ratio at any point is described by the ratio of the cross-sectional areas of the hydrate skin to the gaseous phase. The geometry of these phases within the pore space is likely complicated. To provide a first-order understanding of this behavior, however, I present a simple model that assumes a cylindrical geometry (Figure 4.3). Gas enters a cylindrical gas finger (Figure 4.3a) with a constant radius (r_g) at a constant mass flux (q_m). Hydrate immediately forms a thin skin at the gas-brine interface and additional hydrate forms at the hydrate-brine interface as methane diffuses through the hydrate, as has been observed experimentally (Davies et al., 2010; Taylor et al., 2007). As gas is injected, the gas finger advances and, concurrently, the hydrate skin thickens laterally by diffusion (Figure 4.3a).

I illustrate the characteristic model behavior with the High (Figure 4.3b) and Low (Figure 4.3c) gas flux cases using the parameters in Table 1. In each case, the same total mass of methane enters the domain, but the duration of the Low case is longer than the

High case. In the High case, the gas finger extends farther into the domain and has a thinner skin (Figure 4.3b). In contrast, in the Low case, the finger is shorter, but has a significantly thicker skin (Figure 4.3c). For any q_m, the increase in X_{conv} is primarily a function of the time elapsed (t), but is also proportional to the diffusion coefficient of methane through hydrate (D_m; Figure 4.3d) and the gas finger radius (Figure 4.3e). Larger D_m and smaller r_g both results in greater increase in X_{conv} due to the increased methane transport rate and reduced mass of free gas in the domain, respectively. In all cases, however, X_{conv} increases with time at a decreasing rate as methane diffuses and the hydrate skin thickens.

4.4 Comparison to Experimental Data

I constrain the model parameters (Table 4.1) using my experimental data. I determine the local mass flux of methane into the gas finger (q_m) from the product of the total mass flux into the sample, averaged over the experiments, and the fraction of the sample cross-section where gas is present (Appendix E). The gas finger radius (r_g) is determined by fitting the modeled increase in X_{conv} over time to the average values at the end of the experiments (Figure 4.3e: black dots). I use a diffusion coefficient of methane in hydrate (D_m) equal to 10^{-15} m^{-2} s as a moderate value within the potential range of 10^{-14} m^2 s^{-1} to 10^{-16} m^2 s^{-1} (Davies et al., 2010; Genov et al., 2004; Kuhs et al., 2006). At this D_m, I find that r_g equal to 4.45 μm best reproduces the experimental results (Figure 4.3e: red line).

Symbol	Name	Value	Unit
q_m (High)	High Gas Flux	3.7×10^{-15}	kg s^{-1}
q_m (Mid)	Mid Gas Flux	1.5×10^{-15}	kg s^{-1}
q_m (Low)	Low Gas Flux	0.9×10^{-15}	kg s^{-1}
D_m	Diffusion Coefficient of Methane in Hydrate	1×10^{-15}	m^2 s^{-1}
S_g	Gas Saturation	21.25	%
r_g	Gas Finger Radius	4.5×10^{-6}	m
r_c	Characteristic Radius	15.3×10^{-6}	M
ϕ	Porosity	0.4	-

Table 4.1: Model parameters used in the High, Mid, and Low cases.

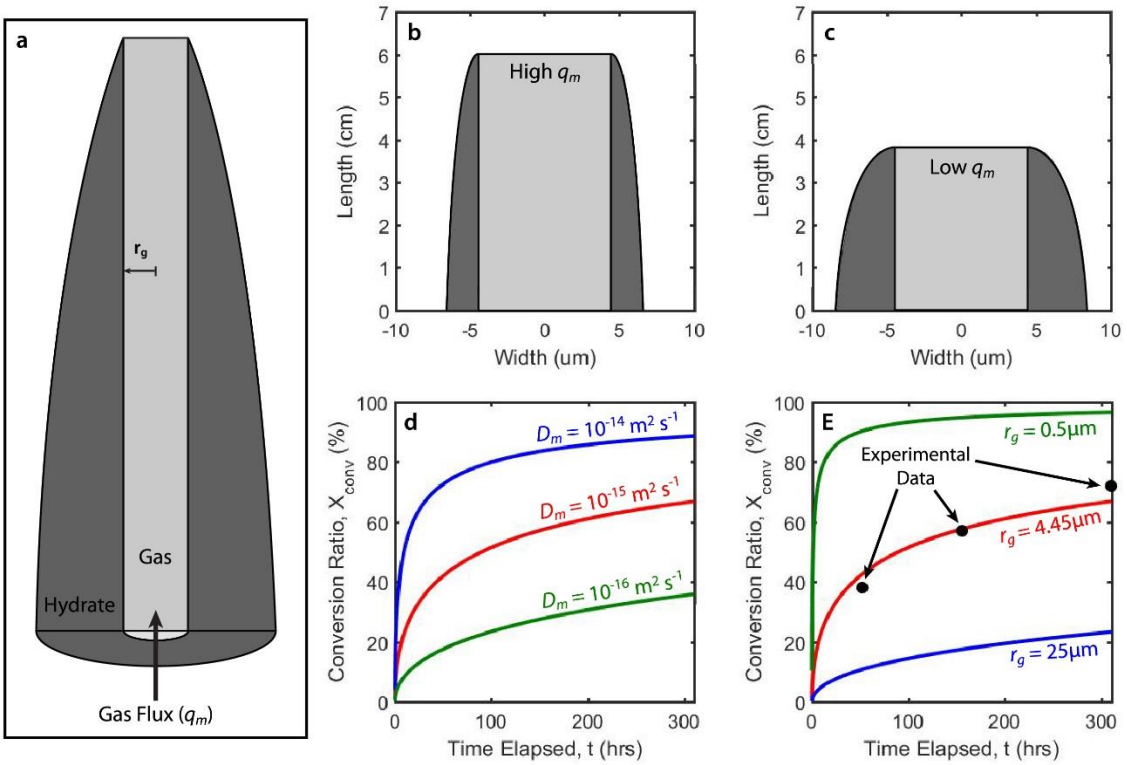

Figure 4.3: Description of model behavior.

All model parameters are listed in Table 4.1. (a) Physical picture of advancing gas finger driven by a constant local gas flux (q_m). Finger is radially-symmetric with a constant radius (r_g). Additional hydrate forms through time such that the skin thickness varies with distance from the inlet. (b) Physical dimensions of gas finger over time in High q_m case (Table 4.1). (c) Physical dimensions of gas finger over time in Low q_m case (Table 4.1). (d) Change in X_{conv} over time with high (blue line), mid (red line), and low (green line) D_m. (e) Change in conversion ratio (X_{conv}) over time at thick (blue line), moderate (red line), and thin (green line) r_g. Black dots indicate average observed final value for X_{conv} in the experiments.

Since the final X_{conv} in the model are constrained by the experimental data, the model produces X_{conv} values (Figure 4.2a: black line) similar to those in the experiments (Figure 4.2a: dots). It is striking, however, that the model underestimate the conversion ratio at early times in all cases, but that the agreement improves with time. Micro-scale experiments have shown that initial hydrate formation occurs very rapidly, but that the formation rate quickly decreases as the hydrate skin solidifies and formation becomes transport limited (Davies et al., 2010; Taylor et al., 2007). Thus, my model may not fully capture the formation dynamics on the timescale of seconds to hours, but appears to reproduce the dominant behaviors over timescales exceeding several days.

The model also produces very similar results to the experiments for values unconstrained by the input parameters. The average finger velocity in the High (Figure 4.2b: blue line) and Low (Figure 4.2b: green line) gas flux cases, indicated by the finger length with time, closely matches the average front velocity observed using the CT scans in the experiments (Figure 4.2b: dots). As the fingers extends, the volume of hydrate formed around each finger (V_f^h) increases in the model (Figure 4.2c: dashed lines) at a similar rate as observed in the experiments (Figure 4.2c: dots). The saturations of gas (S_g) and hydrate (S_h) within the characteristic volume around the finger are calculated from the characteristic radius (r_c; Appendix E) and the volumes of gas and hydrate present. The modeled S_g is constrained by the experimental results (Figure 4.2d: red markers) and is constant with time (Figure 4.2d: red line). In contrast, the modeled S_h increases over time (Figure 4.2d: green line), as hydrate continues to form along the entire length of the finger,

and produces similar magnitudes to those observed in the experiments (Figure 4.2d: green markers).

4.5 Model Sensitivity to Diffusion Coefficient

I performed a sensitivity analysis of the model calibration and results to the assigned diffusion coefficient of methane through hydrate (D_m). The model results presented in Figure 4.2 can be reproduced at any D_m through systematic alterations in the other model parameters (Table 4.2). I found that, for a particular change in D_m (ΔD_m), the prescribed local gas flux in all cases changes linearly with ΔD_m. In contrast, the gas finger and characteristic radii both change according to the square-root of ΔD_m. This analysis shows that: 1) I can systematically determine the appropriate model input parameters for any change in D_m and 2) that my model behaviors are consistent, even with dramatic changes in the geometry.

4.6 Field-Scale Hydrate Growth

In my model, the hydrate growth rate is limited by the diffusion of methane through the hydrate skin such that the skin thickness (x) increases according to the square-root of time (Meyer et al., 2018). Thus, I can calculate the diffusion-limited reaction rate (r_{diff}^{m}) as a function of the hydrate saturation (Appendix F):

$$r_{diff}^{m} = \frac{A_{gw}^{2} D_m (C_m^g - C_m^h)}{\phi S_h}. \quad (4.1)$$

I calculate the gas-brine contact surface area per porous media volume in my model ($A_{gw} = 2r_g/r_c^2$) from the finger density and circumference. r_{diff}^m decreases as the hydrate saturation increases due to thicker hydrate skins (Figure 4.4: blue line). Once all the water is converted into hydrate ($S_h = 1 - S_g$), only hydrate and gas remain and no more hydrate forms ($r_{diff}^m = 0$). My cylindrical gas finger geometry is a simplistic estimate of A_{gw}, but provides a first-order understanding of the reaction rate under methane transport limitation. Modeling and experimental (Brusseau et al., 2006; Brusseau et al., 2007) investigations have developed alternative models for A_{gw} that may provide more appropriate contact geometries. My generalized solution for the reaction rate could be combined with these more complex geometries to simulate the kinetics of hydrate formation within field-scale numerical models.

The traditional model of hydrate formation and dissociation kinetics (Clarke and Bishnoi, 2001; Englezos et al., 1987; Kim et al., 1987; Moridis et al., 2008; Sloan & Koh, 2007; Sun and Mohanty, 2006; Yousif et al., 1991) describes the reaction rate (r_{trad}^m) by:

$$r_{trad}^m = kA_{gw}(f - f_{eq}). \quad (4.2)$$

The kinetic constant (k) is usually described by Arrhenius temperature dependence. The gas-brine contact surface area (A_{gw}) is a function of the total pore surface area and the gas, water, and hydrate phase saturations (Sun and Mohanty, 2006). The local (f) and equilibrium (f_{eq}) fugacity of methane and the experimental conditions are equal to the experimental and equilibrium pressures, respectively. r_{trad}^m increases rapidly at lower S_h

(< 20%) until reaching a maximum value and then slowly decreasing until there is only gas and hydrate remaining (Figure 4.4: red line).

The kinetic model I propose is fundamentally different than traditional kinetic models (e.g. Equation 4.2). In my model, the reaction rate is controlled by the rate of methane diffusion through the hydrate. This model is derived from my hydrate formation experiments in porous media that were designed to best replicate field conditions (Meyer et al., 2018). In contrast, traditional kinetic models describe the reaction rate by the difference in the chemical potentials between the local and equilibrium conditions. These models were derived from hydrate formation and dissociation experiments performed in semi-batch stirred reactor chambers (Englezos et al., 1987; Kim et al., 1987); these experiments may not be appropriate for direct application to field conditions. The controls on hydrate formation kinetics are still unclear, but my model suggests that a fundamentally different process may be controlling hydrate formation during gas injection than predicted by traditional kinetic models.

Parameter	**High D_m**	**Mid D_m**	**Low D_m**
D_m ($m^2\ s^{-1}$)	10^{-14}	10^{-15}	10^{-16}
High q_m ($kg\ s^{-1}$)	2.9×10^{-14}	2.9×10^{-15}	2.9×10^{-16}
Mid q_m ($kg\ s^{-1}$)	1.2×10^{-14}	1.2×10^{-15}	1.2×10^{-16}
Low q_m ($kg\ s^{-1}$)	0.7×10^{-14}	0.7×10^{-15}	0.7×10^{-16}
r_g (μm)	14.1	4.45	1.41
r_c (μm)	48.3	15.3	4.8

Table 4.2: Sensitivity of model parameters to D_m

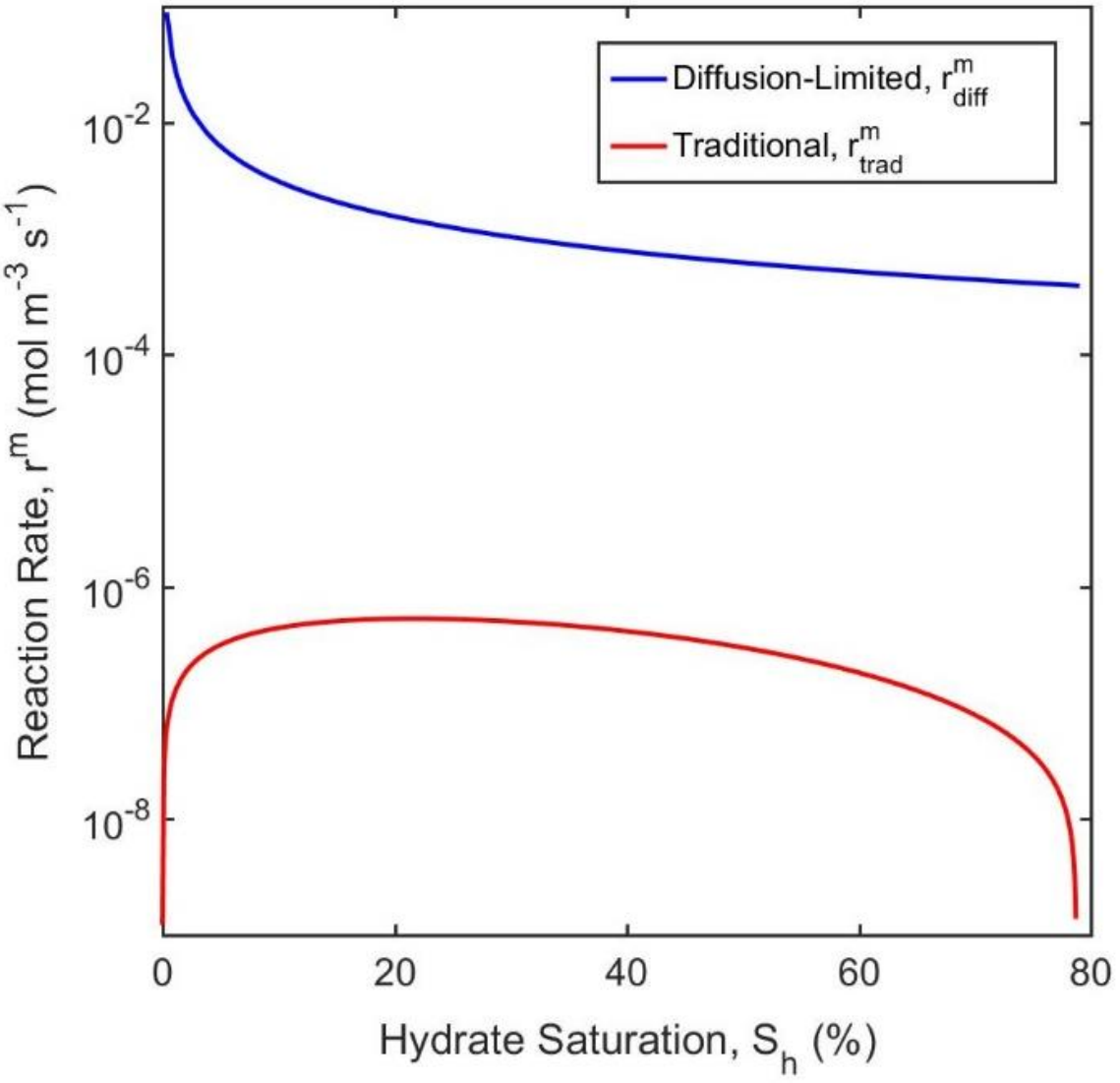

Figure 4.4: Comparison of kinetic models of hydrate formation.

Reaction rate as a function of hydrate saturation from the diffusion-limited (blue line) and traditional (red line) kinetic models. Methane diffusion model assumes cylindrical gas fingers and is calculated using Equation 1. Equilibrium kinetic model is calculated from Equation 2.

4.7 DISCUSSION

I have developed a simple, micro-scale model of hydrate-encased gas fingers advancing into a porous medium under a constant gas flux that captures my macro-scale experimental behavior: 1) faster finger advance rates at high gas fluxes; 2) greater hydrate volumes at lower gas fluxes during brine removal; and 3) increasing bulk hydrate saturation over time. My model not only captures the temporal changes in these parameters, but also independently reproduces their experimentally-observed absolute magnitudes. Additionally, systematic alterations to the model parameters produce consistent results at any prescribed diffusion coefficient.

My calibration of the model parameters at a range of methane diffusion coefficients suggests that the gas fingers are 2.8 – 28 μm in diameter and are 9.6 – 96 μm apart. The median grain size in my experiments was 360 μm, which suggests average pore throat and body diameters of 16 μm and 44 μm, respectively (Glover and Walker, 2009; Nelson, 2009), and a pore spacing of approximately 210 μm, assuming rhombic grain packing. Thus, with large D_m, gas may move through individual pore throats such that a gas finger consists of a series of interconnected pores filled with gas. In contrast, with small D_m, my model suggests that there may be multiple gas fingers per pore throat.

I envision that the system will evolve such that ultimately the hydrate skins around individual tubes will meet and form a solid hydrate phase. My model suggests that the characteristic timescale for this to occur is on the order of months. At this point, further hydrate formation will be limited, but gas will continue to be transported through the gas

finger. As such, it appears that this model captures a mechanism for long term gas transport through the hydrate stability zone.

A common existing approach to describe gas transport through the hydrate stability zone at the macro-scale typically assumes that all the system components are well-mixed and that the gas, hydrate, and brine are at stable three-phase equilibrium (Liu and Flemings, 2007; You et al., 2015; You and Flemings, in review). In contrast, my model suggests that the formation of hydrate at the gas-brine interface is a potential mechanism for gas transport through the hydrate stability zone, similar to other studies (Fu et al., 2018; Ginsburg and Soloviev, 1997; Riedel et al., 2006). In this case, the reaction rate is controlled by gas-brine contact surface area and the thickness of the hydrate skin, which is fundamentally different than the commonly used traditional models of hydrate formation.

4.8 CONCLUSIONS

I performed the first rigorous experimental investigation of hydrate formation during gas injection and interpreted that the presence of hydrate skin separating the gas and brine may sustain gas transport. I developed a simple model of hydrate-encased gas fingers advancing through porous media under a constant gas flux that captured the fundamental behaviors observed during the experiments. My calibration of the finger radius and characteristic spacing indicated that fingers may progress between pores through interconnected pore throats. I then developed a general solution for the reaction rate as a function of hydrate saturation that indicates a fundamentally different relationship than typically assumed by equilibrium kinetic models. This hydrate growth model can be

directly integrated into field-scale gas transport and hydrate formation models. I have provided experimental and modeling evidence of an alternative hydrate formation process that is controlled by fundamentally different physics than typically assumed. My results have implications for the in-situ stability during formation as well as for energy production and carbon release from these systems during global temperature changes.

NOMENCLATURE

Symbol	Name	Dimension	Unit
A_c	characteristic area	(L^2)	(m^2)
A_{gw}	gas-brine contact surface area	(L^2 L^{-3})	(m^2 m^{-3})
C_m^g	solubility of methane in water	(M L^{-3})	(mol m^{-3})
C_m^h	solubility of hydrate in water	(M L^{-3})	(mol m^{-3})
dt	time interval	(T)	(s)
D_m	diffusion coefficient of methane in hydrate	(L^2 T^{-1})	(m^2 s^{-1})
k	gridblock index	(-)	(-)
$L_{f,n}$	finger length at time-step n	(L)	(m)
$L_{k,n}$	hydrate skin thickness at time-step n	(L)	(m)
m_m	total mass of methane injected	(M)	(kg)
m_m^g	mass of methane in the gaseous phase	(M)	(kg)
m_m^h	mass of methane in the hydrate phase	(M)	(kg)
M_h	hydrate molecular mass	(M L^{-3})	(kg mol^{-1})
n	time-step	(-)	(-)
n_f	number of gas fingers	(-)	(-)
q_m	local gas flux	(M T^{-1})	(kg s^{-1})
$Q_{k,n}$	methane flux due to diffusion	(M T^{-1})	(mol s^{-1})
r_c	characteristic radius	(L)	(m)
r_g	gas finger radius	(L)	(m)
r_h	initial hydrate skin radius	(L)	(m)
$r_{k,n}$	total hydrate skin thickness radius	(L)	(m)
r_{smpl}	sample radius	(L)	(m)
r_{diff}^m	diffusion-limited reaction rate	(M L^{-3} T^{-1})	(mol m^{-3} s^{-1})
r_{trad}^m	traditional reaction rate	(M L^{-3} T^{-1})	(mol m^{-3} s^{-1})
$S_{g,n}$	gas saturation at time-step n	(-)	(-)
$S_{h,n}$	hydrate saturation at time-step n	(-)	(-)
t	time elapsed	(T)	(s)
v_k	gas finger velocity	(M T^{-1})	(m s^{-1})
$V_{c,n}$	characteristic volume at time-step n	(L^3)	(m^3)
$V_{f,n}^g$	volume of gas phase at time-step n	(L^3)	(cm^3)
$V_{f,n}^h$	volume of hydrate phase at time-step n	(L^3)	(cm^3)
V_l	volume of liquid brine removed	(L^3)	(cm^3)
x	hydrate skin thickness	(L)	(m)
X_{conv}	mass conversion ratio	(-)	(-)
X_m^h	mass fraction of methane in hydrate	(M M^{-1})	(kg kg^{-1})
ρ_g	gas phase density	(M L^{-3})	(kg m^{-3})
ρ_h	hydrate phase density	(M L^{-3})	(kg m^{-3})
ϕ	porosity	(-)	(-)

ACKNOWLEDGEMENTS

This work was supported by the U.S. Department of Energy under Contract No. DE-FE0010406, DE-FE0028967, and DE-FE0023919. I would like thank Dr. David DiCarlo at the Hildebrand Petroleum and Geosystems Engineering Department at UT Austin for his insight into the applicability of the model to general porous media.

REFERENCES

Archer, D., Martin, P., Buffett, B., Brovkin, V., Rahmstorf, S., and Ganopolski, A. (2004). The importance of ocean temperature to global biogeochemistry. *Earth and Planetary Science Letters, 222*(2), 333-348. doi: http://dx.doi.org/10.1016/j.epsl.2004.03.011

Boswell, R., and Collett, T. (2011). Current prospective on gas hydrate resources. *Energy & Environmental Science, 4*, 10.

Brusseau, M. L., Peng, S., Schnaar, G., and Costanza-Robinson, M. S. (2006). Relationships among air-water interfacial area, capillary pressure, and water saturation for a sandy porous medium. *Water Resources Research, 42*(3), n/a-n/a. doi: 10.1029/2005wr004058

Brusseau, M. L., Peng, S., Schnaar, G., and Murao, A. (2007). Measuring Air−Water Interfacial Areas with X-ray Microtomography and Interfacial Partitioning Tracer Tests. *Environmental Science & Technology, 41*(6), 1956-1961. doi: 10.1021/es061474m

Chun, J.-H., Ryu, B.-J., Son, B.-K., Kim, J.-H., Lee, J. Y., Bahk, J.-J., Kim, H.-J., Woo, K. S., and Nehza, O. (2011). Sediment mounds and other sedimentary features related to hydrate occurrences in a columnar seismic blanking zone of the Ulleung Basin, East Sea, Korea. *Marine and Petroleum Geology, 28*(10), 1787-1800. doi: https://doi.org/10.1016/j.marpetgeo.2011.06.006

Clarke, M., and Bishnoi, P. R. (2001). Determination of the activation energy and intrinsic rate constant of methane gas hydrate decomposition. *The Canadian Journal of Chemical Engineering, 79*(1), 143-147. doi: doi:10.1002/cjce.5450790122

Davies, S. R., Sloan, E. D., Sum, A. K., and Koh, C. A. (2010). In Situ Studies of the Mass Transfer Mechanism across a Methane Hydrate Film Using High-Resolution Confocal Raman Spectroscopy. *The Journal of Physical Chemistry C, 114*(2), 1173-1180. doi: 10.1021/jp909416y

Englezos, P., Kalogerakis, N., Dholabhai, P. D., and Bishnoi, P. R. (1987). Kinetics of formation of methane and ethane gas hydrates. *Chemical Engineering Science, 42*(11), 2647-2658. doi: http://dx.doi.org/10.1016/0009-2509(87)87015-X

Fu, X., Cueto-Felgueroso, L., and Juanes, R. (2018). Nonequilibrium Thermodynamics of Hydrate Growth on a Gas-Liquid Interface. *Physical Review Letters, 120*(14), 144501. doi: 10.1103/PhysRevLett.120.144501

Genov, G., Kuhs, W. F., Staykova, D. K., Goreshnik, E., and Salamatin, A. N. (2004). Experimental studies on the formation of porous gas hydrates. *American Mineralogist, 89*(8-9), 1228-1239. doi: 10.2138/am-2004-8-910

Ginsburg, G. D., and Soloviev, V. A. (1997). Methane migration within the submarine gas-hydrate stability zone under deep-water conditions. *Marine Geology, 137*(1–2), 49-57. doi: http://dx.doi.org/10.1016/S0025-3227(96)00078-3

Glover, P. W., and Walker, E. (2009). Grain-size to effective pore-size transformation derived from electrokinetic theory. *GEOPHYSICS, 74*(1), E17-E29. doi: 10.1190/1.3033217

Haeckel, M., Suess, E., Wallmann, K., and Rickert, D. (2004). Rising methane gas bubbles form massive hydrate layers at the seafloor. *Geochimica et Cosmochimica Acta, 68*(21), 4335-4345. doi: http://dx.doi.org/10.1016/j.gca.2004.01.018

Kim, H. C., Bishnoi, P. R., Heidemann, R., and Rizvi, S. S. H. (1987). *Kinetics of Methane Hydrate Decomposition* (Vol. 42).

Koh, D.-Y., Kang, H., Lee, J.-W., Park, Y., Kim, S.-J., Lee, J., Lee, J. Y., and Lee, H. (2016). Energy-efficient natural gas hydrate production using gas exchange. *Applied Energy, 162*(Supplement C), 114-130. doi: https://doi.org/10.1016/j.apenergy.2015.10.082

Konno, Y., Fujii, T., Sato, A., Akamine, K., Naiki, M., Masuda, Y., Yamamoto, K., and Nagao, J. (2017). Key Findings of the World's First Offshore Methane Hydrate Production Test off the Coast of Japan: Toward Future Commercial Production. *Energy & Fuels, 31*(3), 2607-2616. doi: 10.1021/acs.energyfuels.6b03143

Kuhs, W. F., Staykova, D. K., and Salamatin, A. N. (2006). Formation of Methane Hydrate from Polydisperse Ice Powders. *The Journal of Physical Chemistry B, 110*(26), 13283-13295. doi: 10.1021/jp061060f

Kvenvolden, K. A., and McMenamin, M. A. (1980). Hydrates of natural gas; a review of their geologic occurrence. *Report Rep. 825*.

Liu, X., and Flemings, P. B. (2007). Dynamic multiphase flow model of hydrate formation in marine sediments. *Journal of Geophysical Research: Solid Earth, 112*(B3), B03101. doi: 10.1029/2005jb004227

Lüdmann, T., and Wong, H. K. (2003). Characteristics of gas hydrate occurrences associated with mud diapirism and gas escape structures in the northwestern Sea of Okhotsk. *Marine Geology, 201*(4), 269-286. doi: https://doi.org/10.1016/S0025-3227(03)00224-X

Meyer, D. W., Flemings, P. B., DiCarlo, D. A., You, K., Phillips, S. C., and Kneafsey, T. (2018). Experimental investigation of gas flow and hydrate formation within the hydrate stability zone. *Journal of Geophysical Research: Solid Earth*. doi: 10.1029/2018JB015748

Milkov, A. V. (2004). Global estimates of hydrate-bound gas in marine sediments: how much is really out there? *Earth-Science Reviews, 66*(3–4), 183-197. doi: http://dx.doi.org/10.1016/j.earscirev.2003.11.002

Moridis, G., Kowalsky, M. B., and Pruess, K. (2008). *TOUGH+HYDRATE v1.2 User's Manual: A Code for the Simulation of System Behavior in Hydrate-Bearing Geologic Media*: Lawrence Berkeley National Laboratory.

Moridis, G. J. (2008). Toward Production From Gas Hydrates: Current Status, Assessment of Resources, and Simulation-Based Evaluation of Technology and Potential.

Nelson, P. H. (2009). Pore-throat sizes in sandstones, tight sandstones, and shales. *AAPG Bulletin, 93*(3), 12.

Riedel, M., Novosel, I., Spence, G. D., Hyndman, R. D., Chapman, R. N., Solem, R. C., and Lewis, T. (2006). Geophysical and geochemical signatures associated with gas hydrate–related venting in the northern Cascadia margin. *GSA Bulletin, 118*(1-2), 23-38. doi: 10.1130/b25720.1

Sloan, E. D., and Koh, C. A. (2007). *Clathrate Hydrates of Natural Gases* (3nd ed.). Boca Raton, FL: CRC Press.

Sun, X., and Mohanty, K. K. (2006). Kinetic simulation of methane hydrate formation and dissociation in porous media. *Chemical Engineering Science, 61*(11), 3476-3495. doi: https://doi.org/10.1016/j.ces.2005.12.017

Taylor, C. J., Miller, K. T., Koh, C. A., and Sloan, E. D. (2007). Macroscopic investigation of hydrate film growth at the hydrocarbon/water interface. *Chemical Engineering Science, 62*(23), 6524-6533. doi: http://dx.doi.org/10.1016/j.ces.2007.07.038

Tréhu, A. M., Flemings, P. B., Bangs, N. L., Chevallier, J., Gràcia, E., Johnson, J. E., Liu, C. S., Liu, X., Riedel, M., and Torres, M. E. (2004). Feeding methane vents and gas hydrate deposits at south Hydrate Ridge. *Geophysical Research Letters, 31*(23), L23310. doi: 10.1029/2004gl021286

Wright, J. F., Dallimore, S. R., Nixon, F. M., and Duchesne, C. (2005). In situ stability of gas hydrate in reservoir sediments of the JAPEX/JNOC/GSC et al. Mallike 5L-38 gas hydrate production research well. In S. R. Dallimore, and Collett, T. S. (Ed.), *Scientific Results from the Mallik 2002 Gas Hydrate Production Research Well*

Program, Mackenzie Delta, Northwest Territories, Canada (Vol. Bulletin 585, pp. 14): Geological Survey of Canada.

You, K., and Flemings, P. B. (in review). Methane Hydrate Formation in Thick Sand Reservoirs: 2. Long-Range Gas Transport. *Journal of Geophysical Research: Solid Earth*.

You, K., DiCarlo, D., and Flemings, P. B. (2015). Quantifying hydrate solidification front advancing using method of characteristics. *Journal of Geophysical Research: Solid Earth, 120*(10), 6681-6697. doi: 10.1002/2015jb011985

Yousif, M. H., Abass, H. H., Selim, M. S., and Sloan, E. D. (1991). Experimental and Theoretical Investigation of Methane-Gas-Hydrate Dissociation in Porous Media. doi: 10.2118/18320-pa

Appendices

APPENDIX A: DETAILED METHODOLOGY OF HYDRATE FORMATION EXPERIMENTS

A.1 Equipment

1. Hydrate vessel components (Figure A.1):
    a. Aluminum sleeve
    b. Top vessel endcap (Figure A.2)
    c. Bottom vessel endcap (Figure A.3)
    d. Vessel endcap (#240) O-rings (x4)'
    e. Thermistors (x2)
    f. Pressure transducers and O-rings
    g. Internal fluid tubing
    h. Viton® Sample sleeve
    i. Sample endcaps (x2)
    j. Sample endcap internal (#116) O-rings (x2)
    k. Sample endcap external (Flat: #326; Taper: #327) O-rings (x2)
2. Cooling jacket components (Figure A.4):
    a. PVC cooling jacket with inlet and outlet ports
    b. Vessel insulation jacket
    c. Top and bottom vessel insulation
    d. Insulated coolant tubes and valves
    e. Plastic spacers (x2)
    f. Aluminum washers (x2)
    g. Internal (#247) O-rings (x4)
    h. External (#256) O-rings (x4)
    i. Retainer rings (x2)
3. Environmental chamber (Figures A.5 and A.6):
    a. Chiller (Figure A.7)
    b. Data acquisition system (Figure A.8)
    c. Temperature control system (Figure A.8)
    d. Pump controller (Figures A.10 and A.11)
    e. Computer and monitor
    f. Heat lamps
    g. Internal LED lights
    h. Power supply
4. Teledyne ISCO syringe pumps (Figure A.10):
    a. Inlet, outlet, and confining pumps
    b. Inlet/outlet port with HiP 3-way valves
    c. Teledyne ISCO pump controller (detail in Figure A.11)
5. X-ray computed-tomography (CT) scanner (Figure A.12):
    a. Vertical positioning system

b. CT scanner console (Figure A.13)

6. Other Equipment (not pictured):
    a. Vessel insulation
    b. Fluid tubing
    c. Top ring collar
    d. Bottom ring collar
    e. Aluminum hanger plate and ring
    f. Sample packing equipment (Figure A.14)
        i. Pluviation device
        ii. Deflection cone
        iii. Large cookie sheet
        iv. Pluviation blocks
        v. Digital calipers
        vi. Paintbrush
        vii. PVC tube (6” ID x18” length)
    g. Sample saturation equipment (Figure A.15):
        i. Vacuum pumps w/ release valves and tubing (x2)
        ii. 250 mL empty vacuum flasks (x2)
        iii. 250 mL vacuum flasks with desiccant (x2)
        iv. 1 L vacuum flask
        v. Rubber stoppers with hole (x5)
        vi. Short 1/4" thin-walled steel tubing (x4)
        vii. Long 1/4" thin-walled steel tubing with 1/8” converter (x1)
        viii. 1000 mL of pore fluid
    h. Experimental preparation equipment:
        i. Vertically-oriented pipe clamp
        ii. Set of small, fine files
        iii. Vacuum grease
        iv. Spanner wrenches (x2)
        v. Electronic scale
        vi. Pressurized methane gas
        vii. Methane gas regulator
        viii. Pressurized nitrogen gas
        ix. Nitrogen gas regulator
        x. Compressed air
        xi. Gravitational filling device
        xii. Ring stand
        xiii. Ring stand ring clamp
        xiv. Confining oil (~3 L)

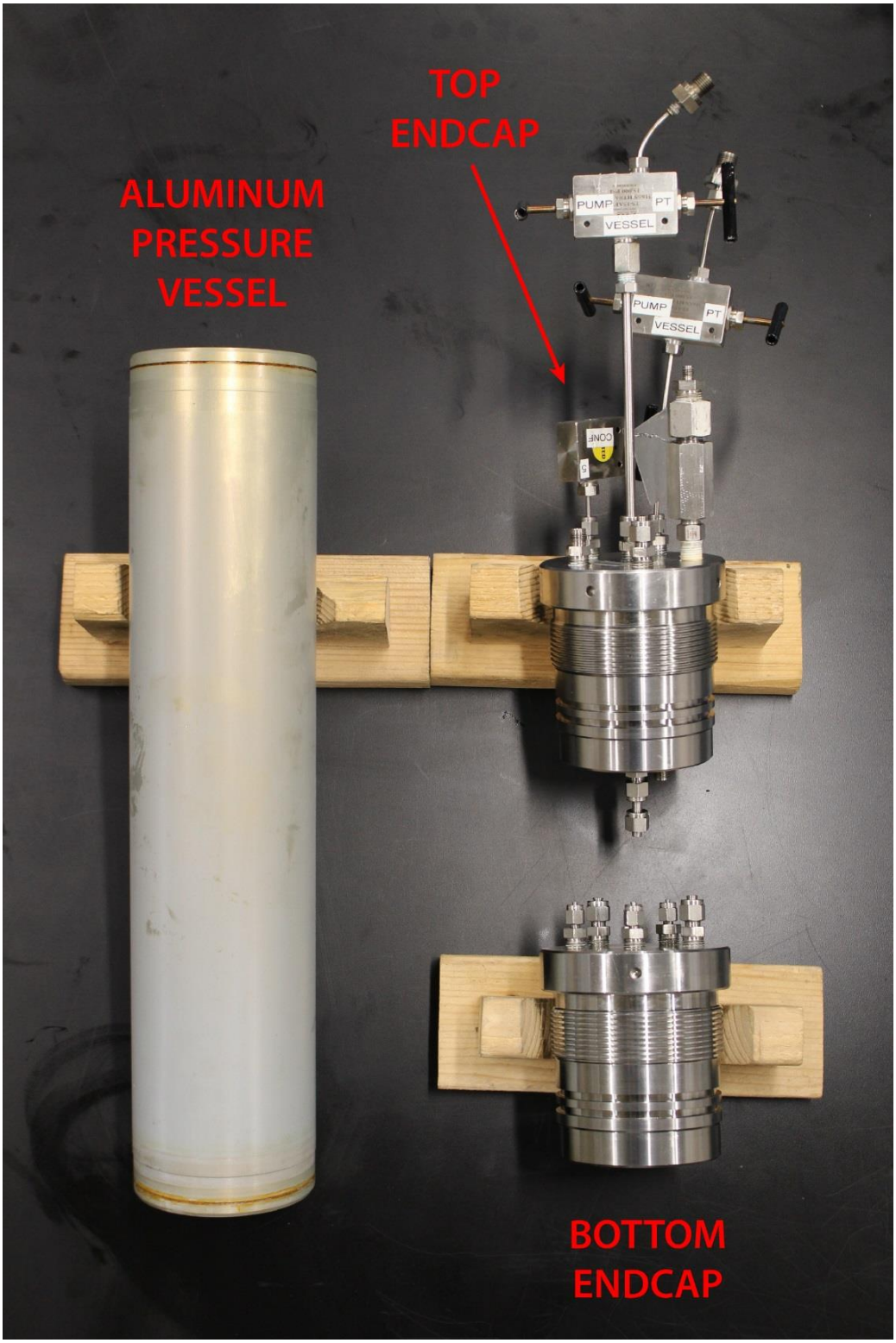

Figure A.1: Picture of hydrate formation vessel components.

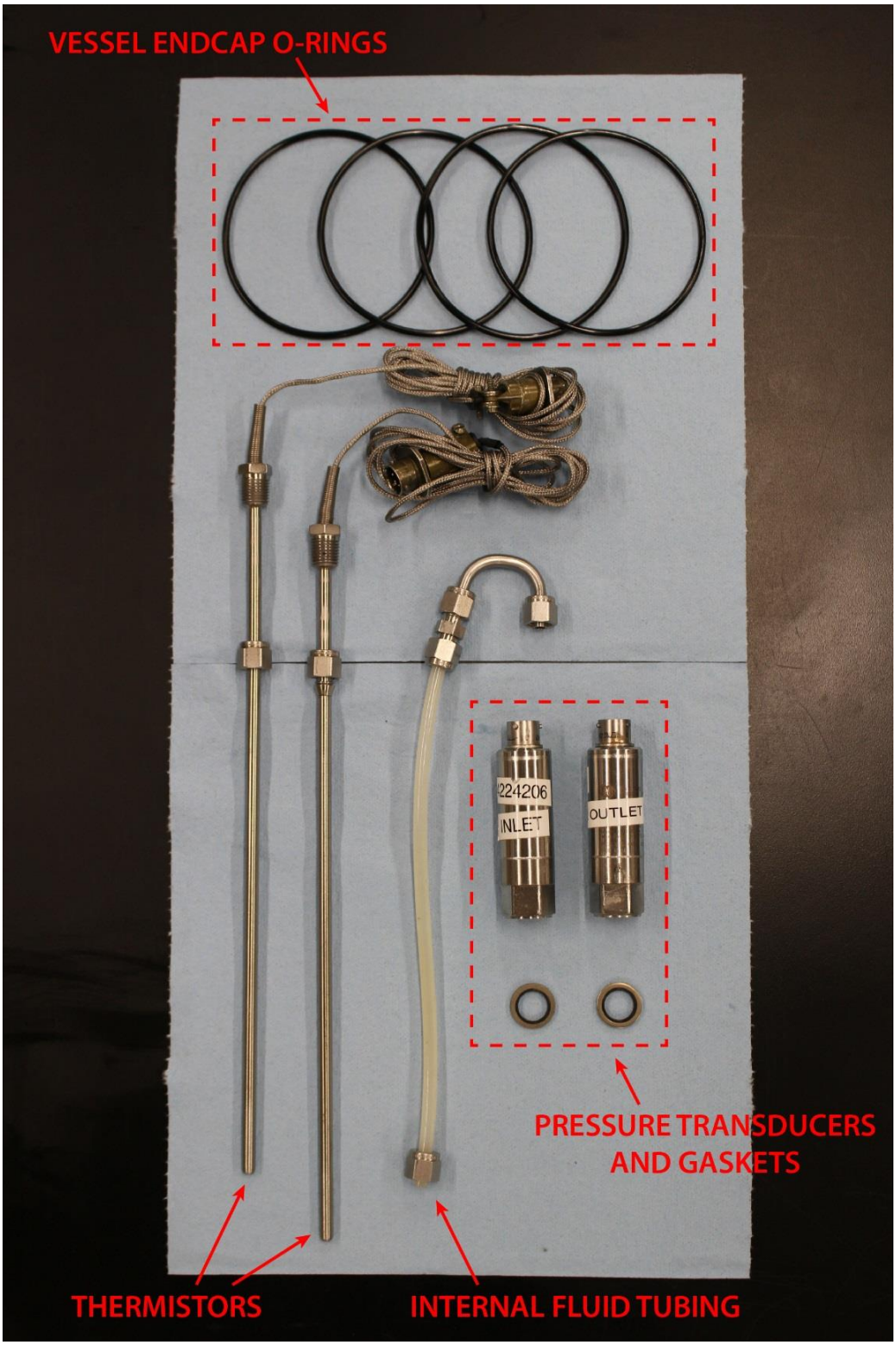

Figure A.1: Continued.

Figure A.1: Continued.

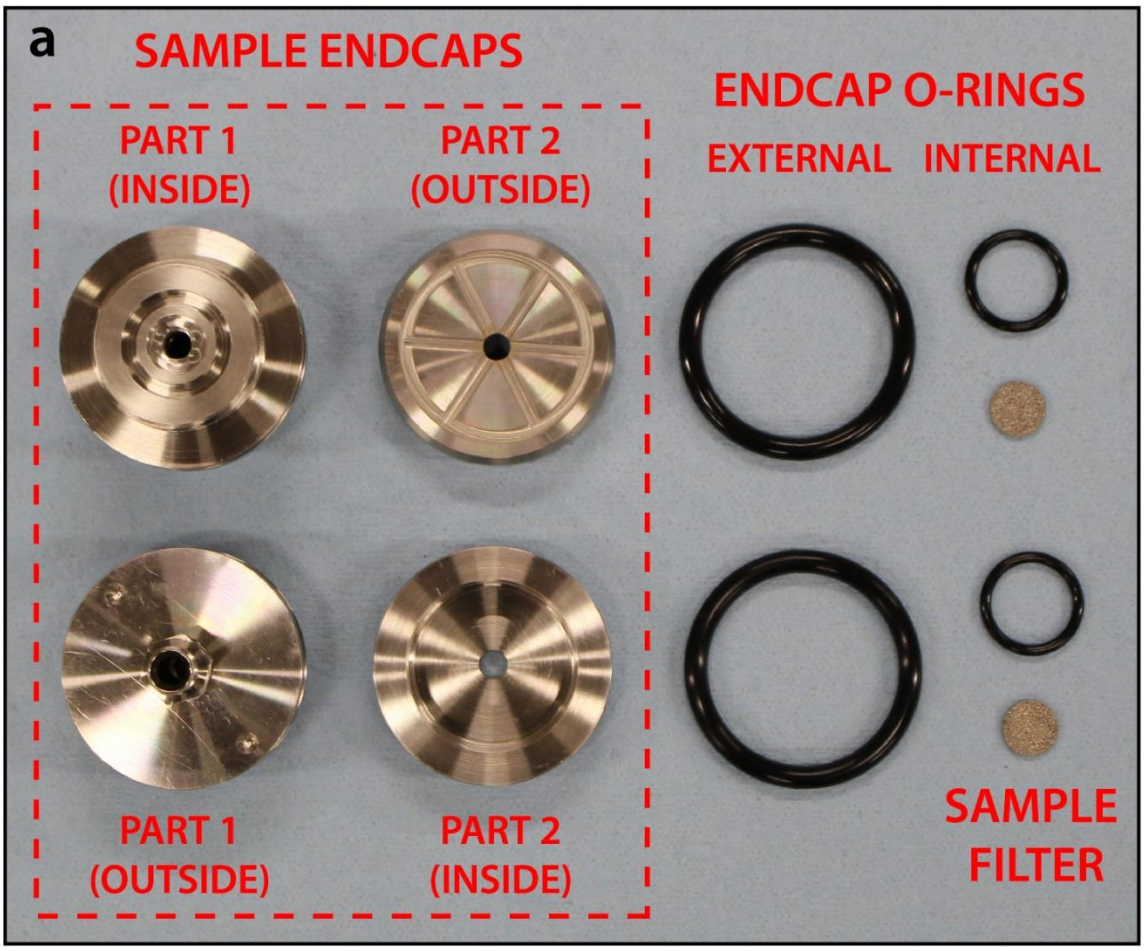

Figure A.1: Continued.

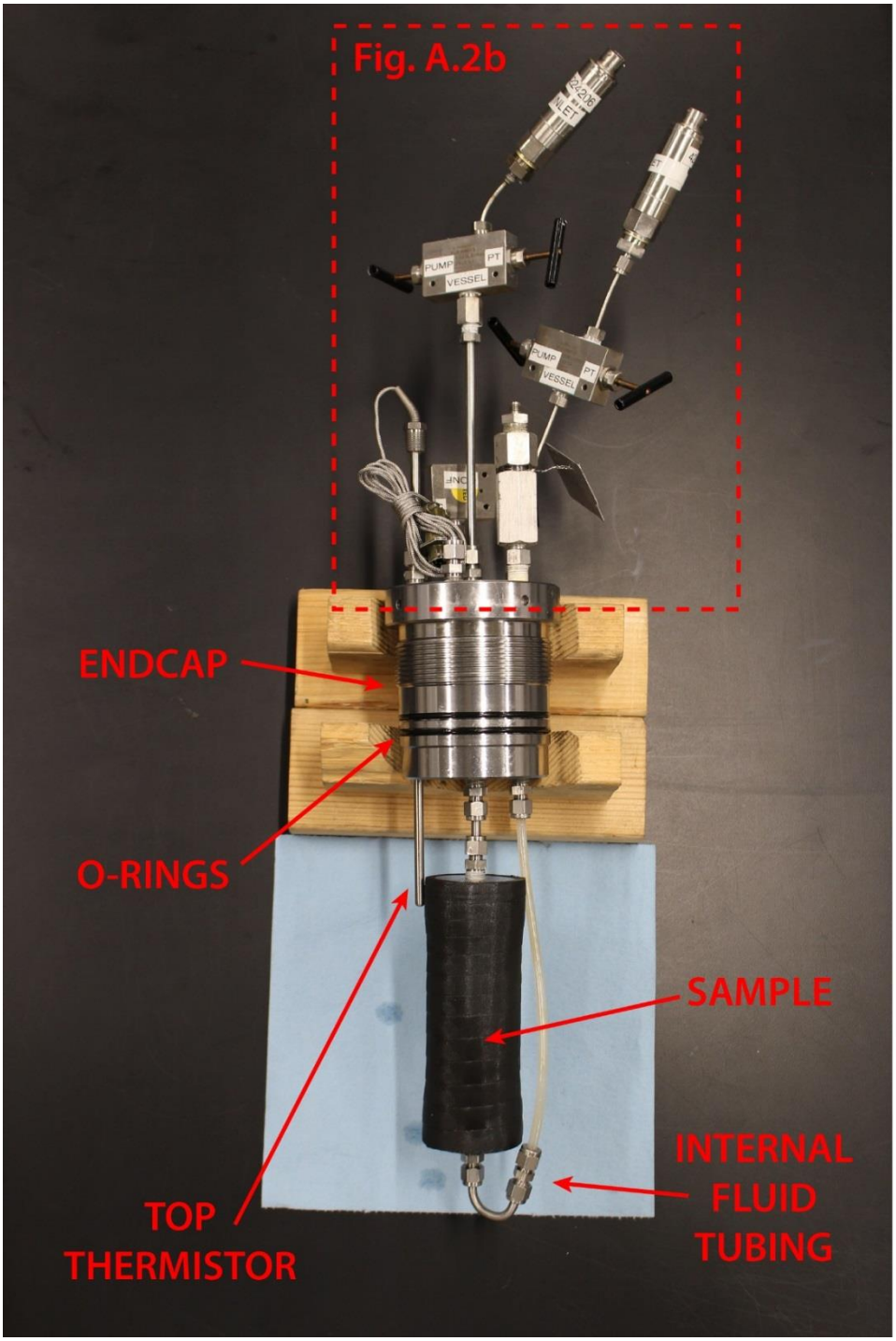

Figure A.2: Picture of top vessel endcap.

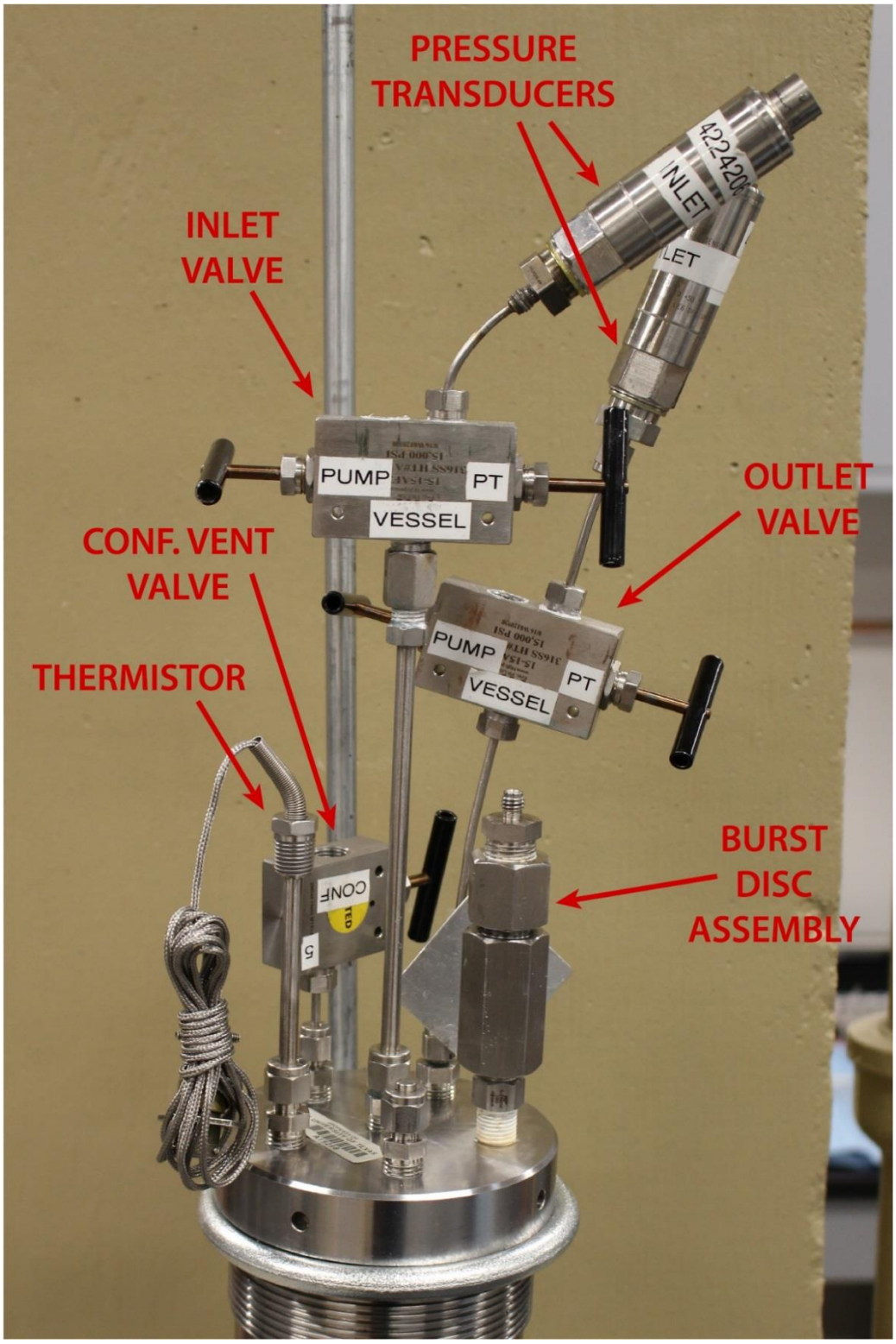

Figure A.2: Continued.

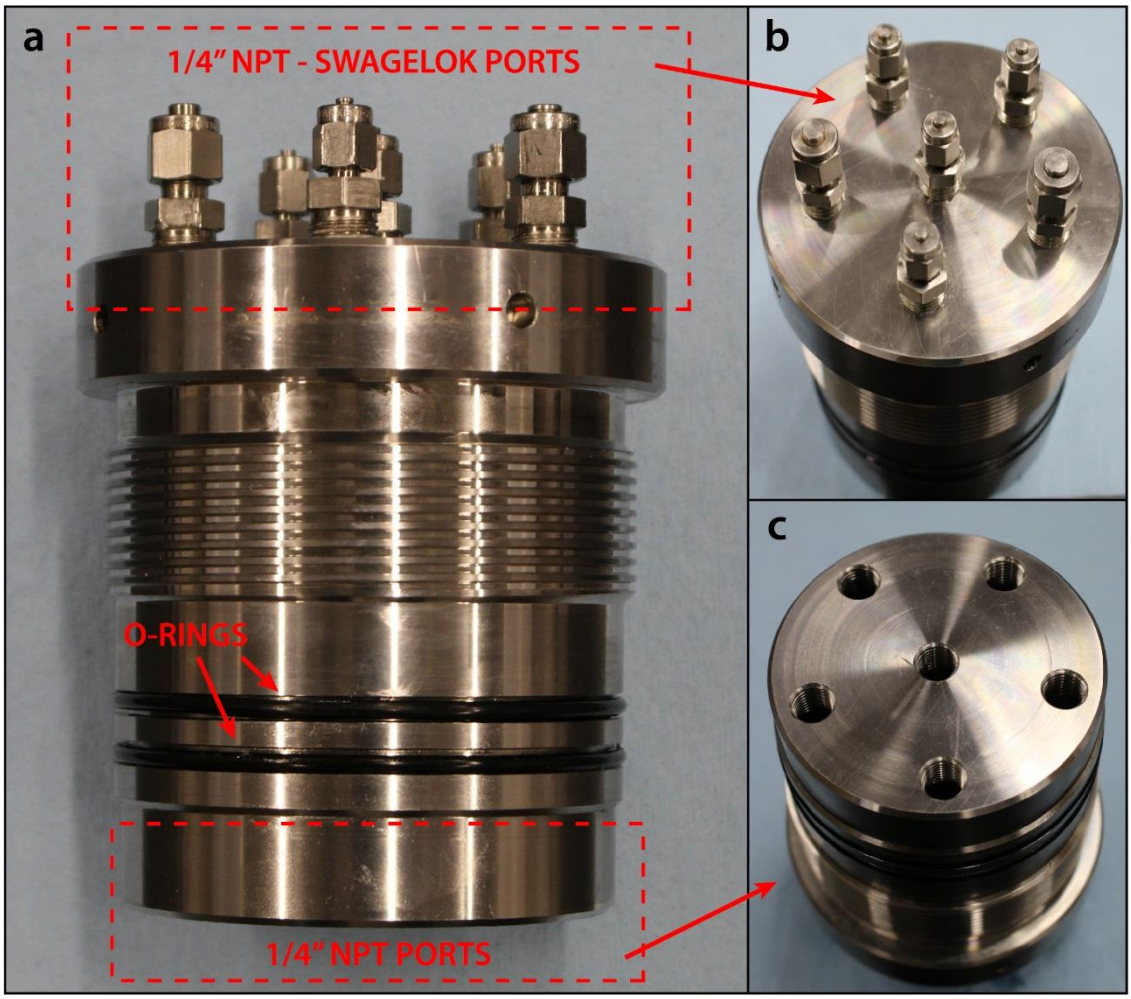

Figure A.3: Picture of bottom vessel endcap.

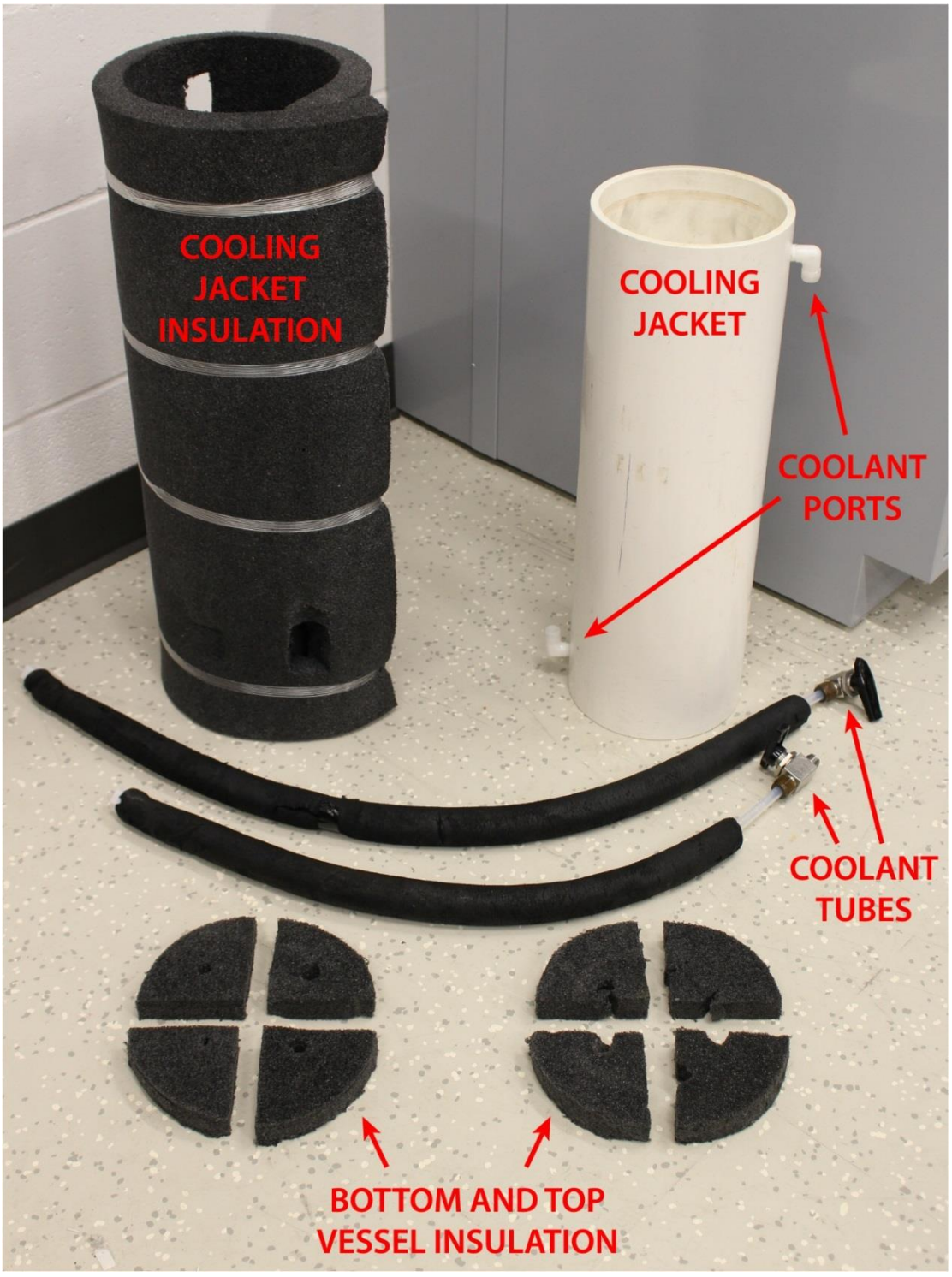

Figure A.4: Picture of cooling jacket components.

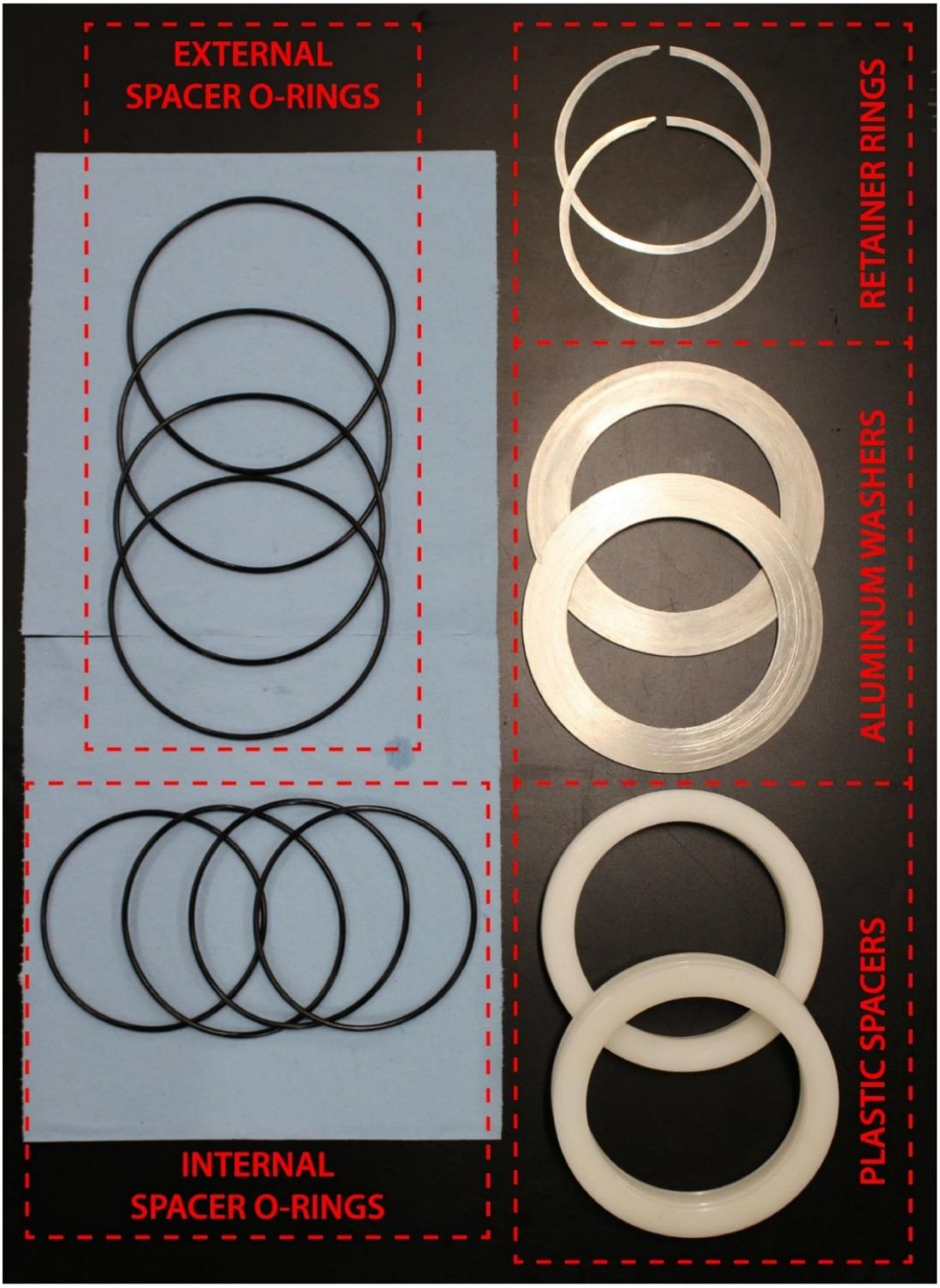

Figure A.4: Continued.

Figure A.5: Pictures of the exterior of environmental chamber.

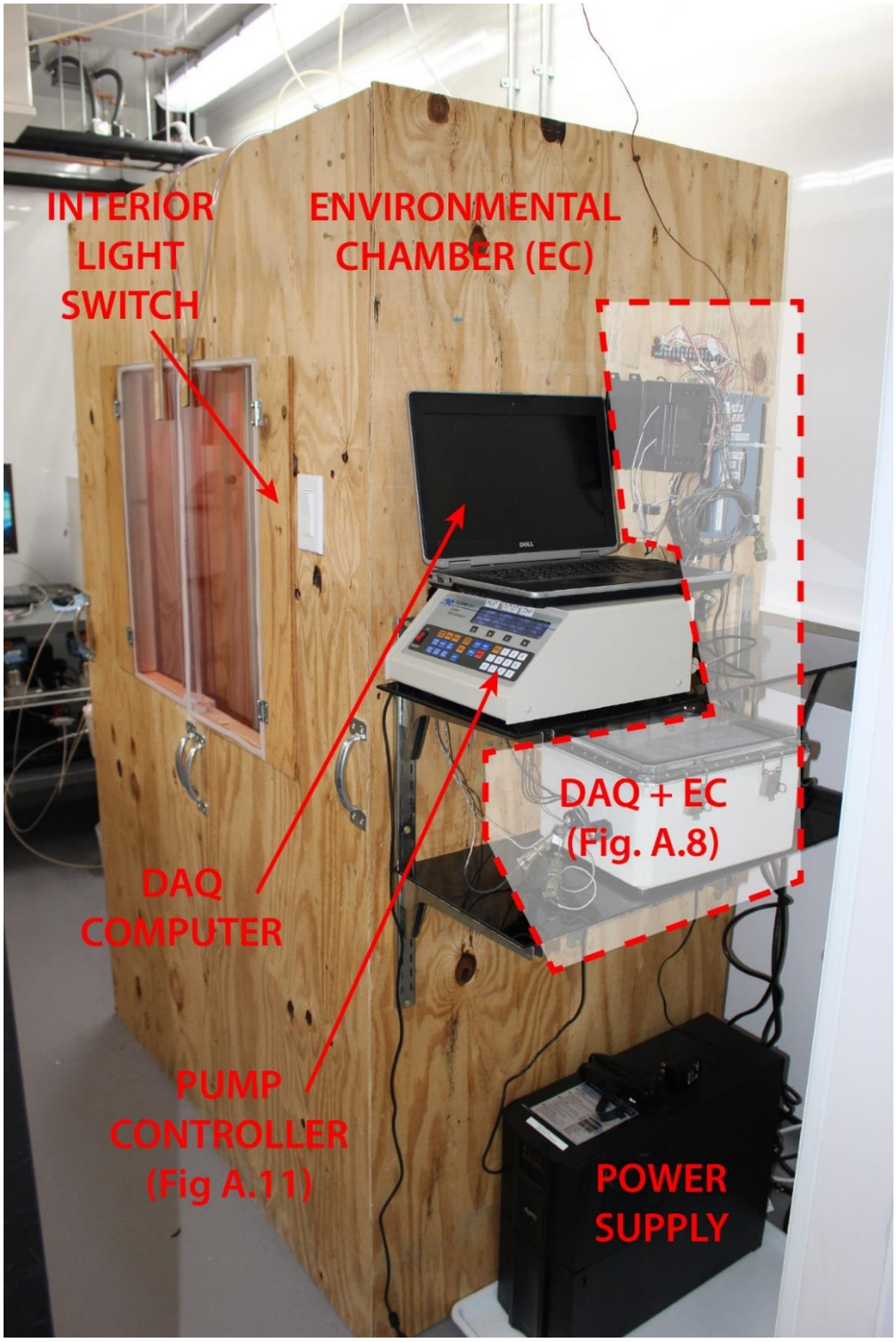

Figure A.5: Continued.

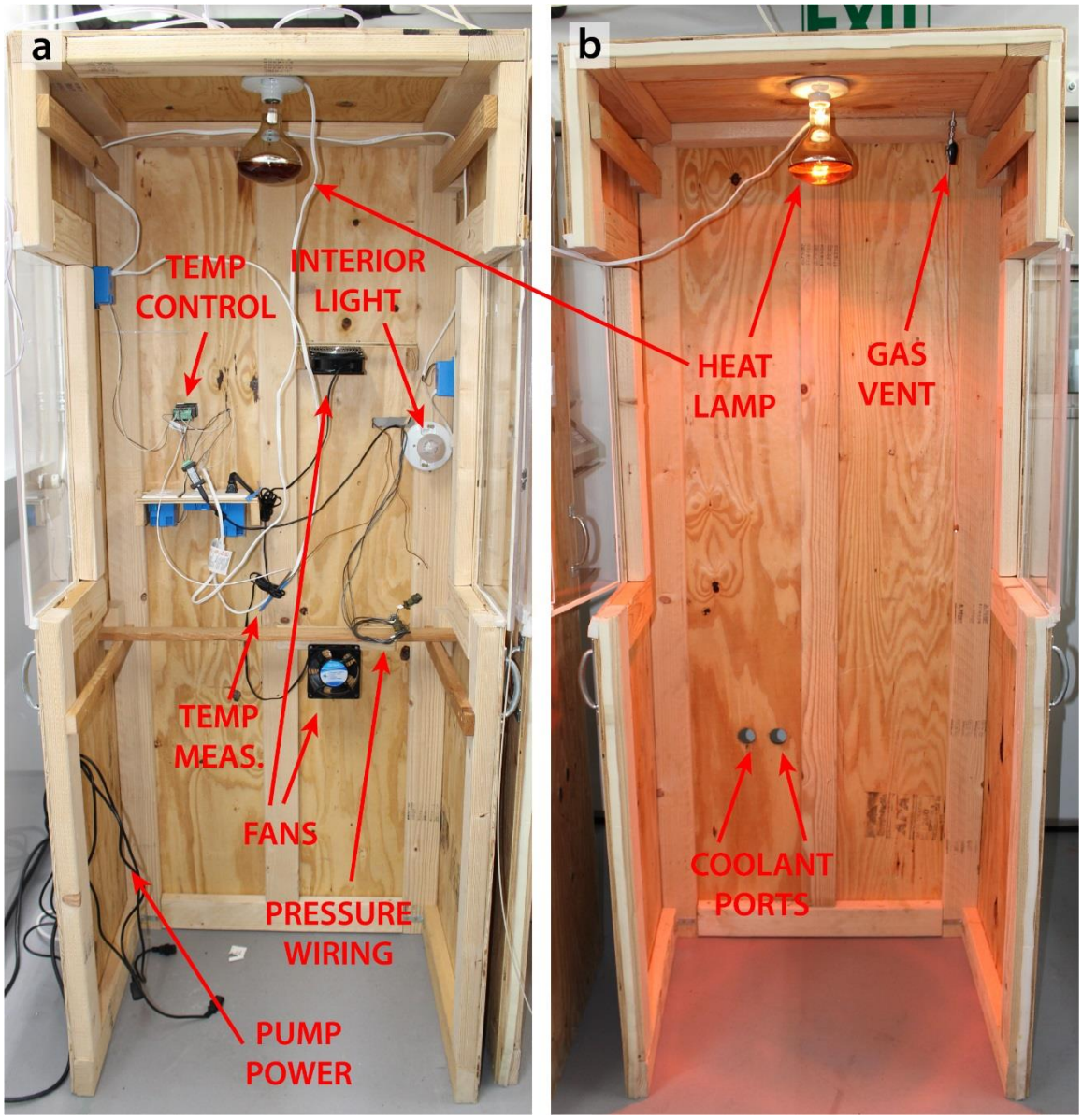

Figure A.6: Pictures of the interior of environmental chamber.

Figure A.7: Picture of chiller.

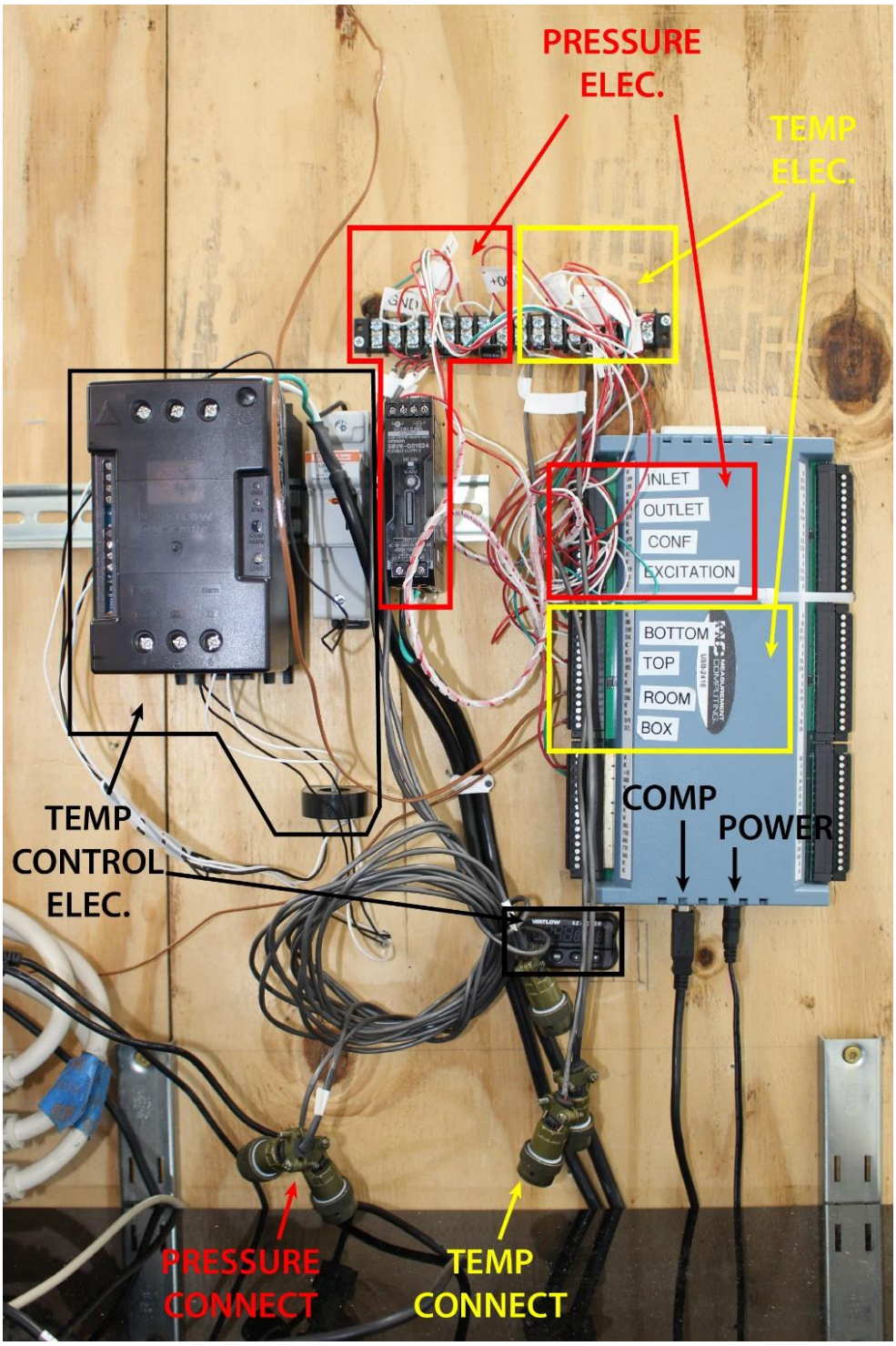

Figure A.8: Picture of the temperature control and DAQ electronics.

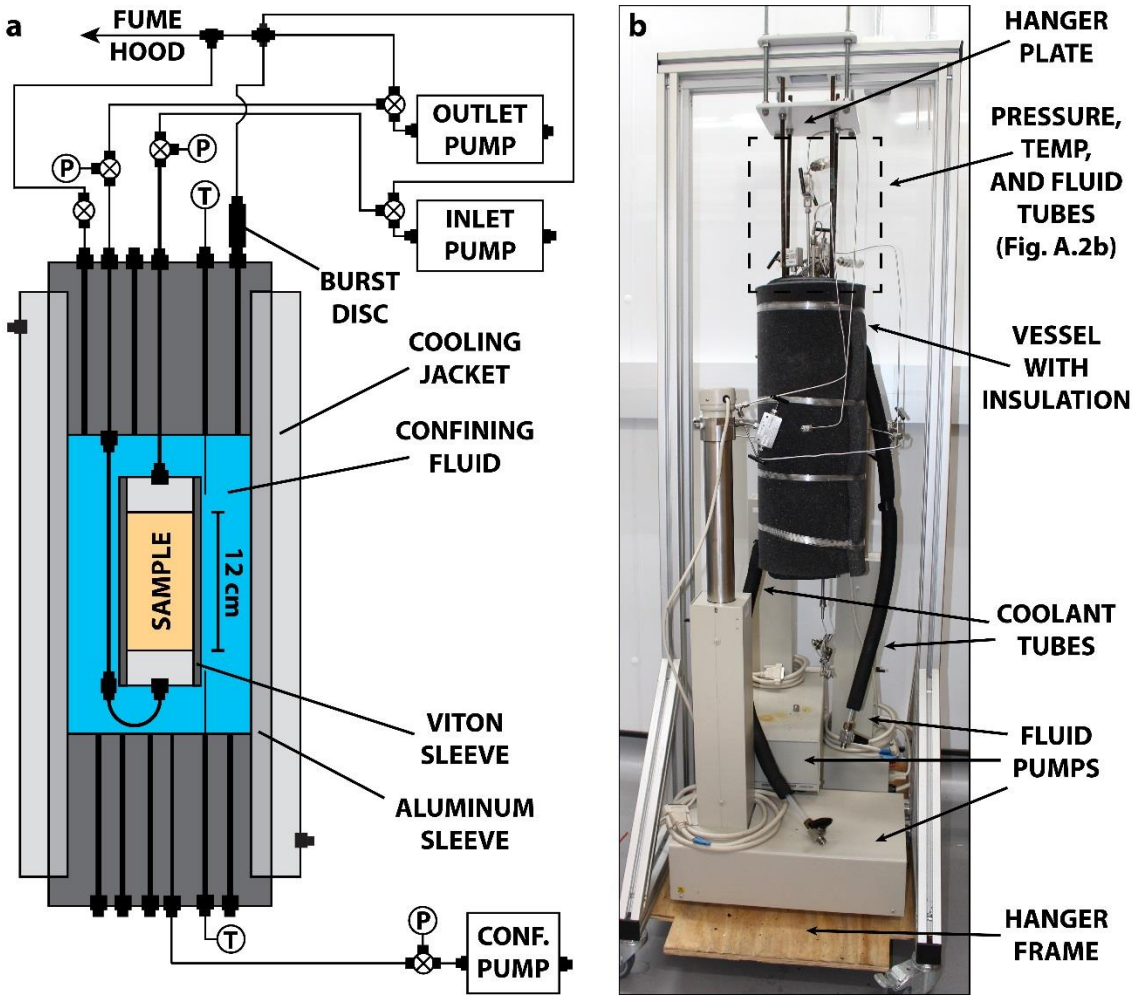

Figure A.9: Picture and schematic of the experimental setup.

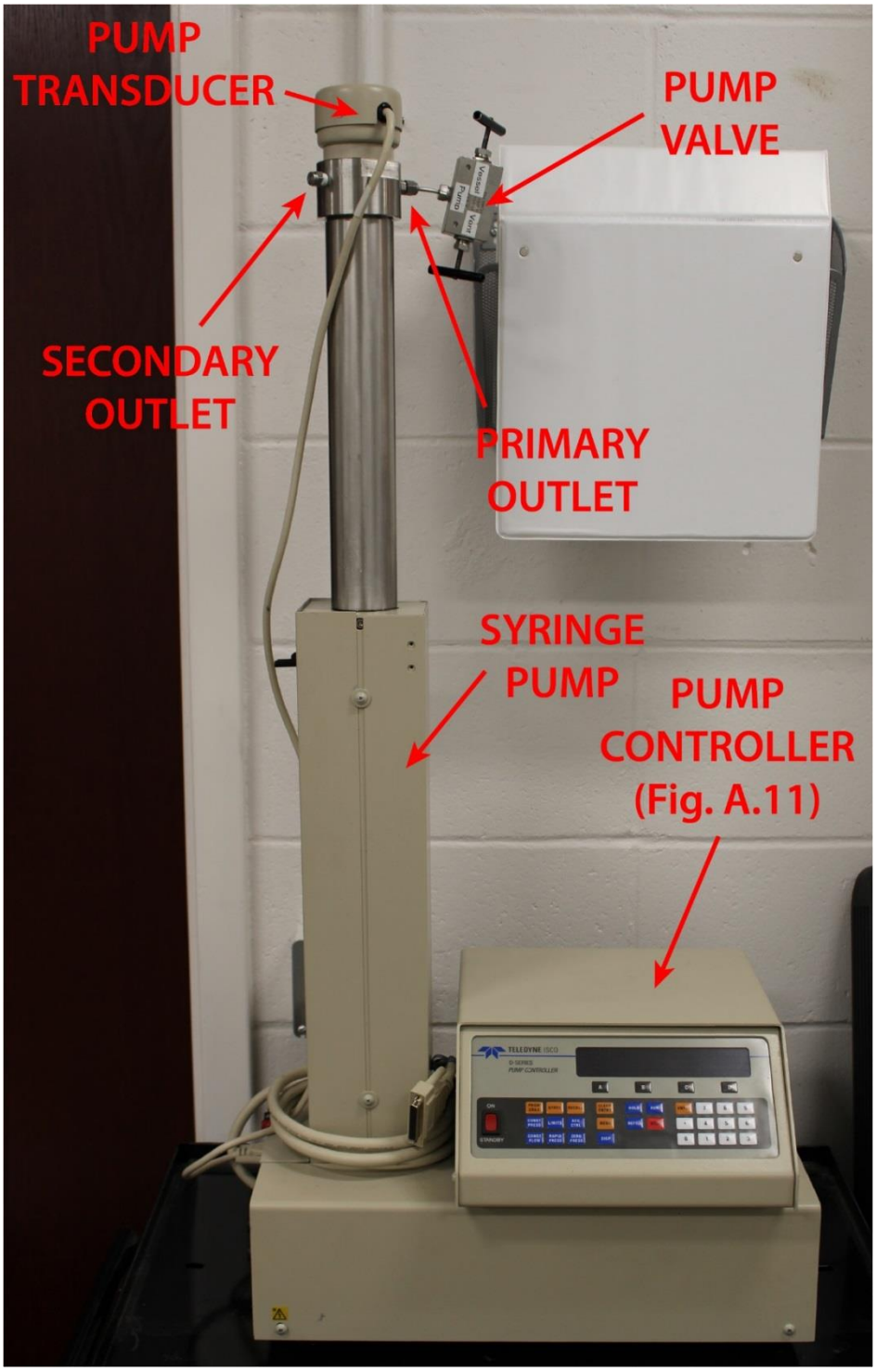

Figure A.10: Picture of a Teledyne ISCO syringe pump and controller.

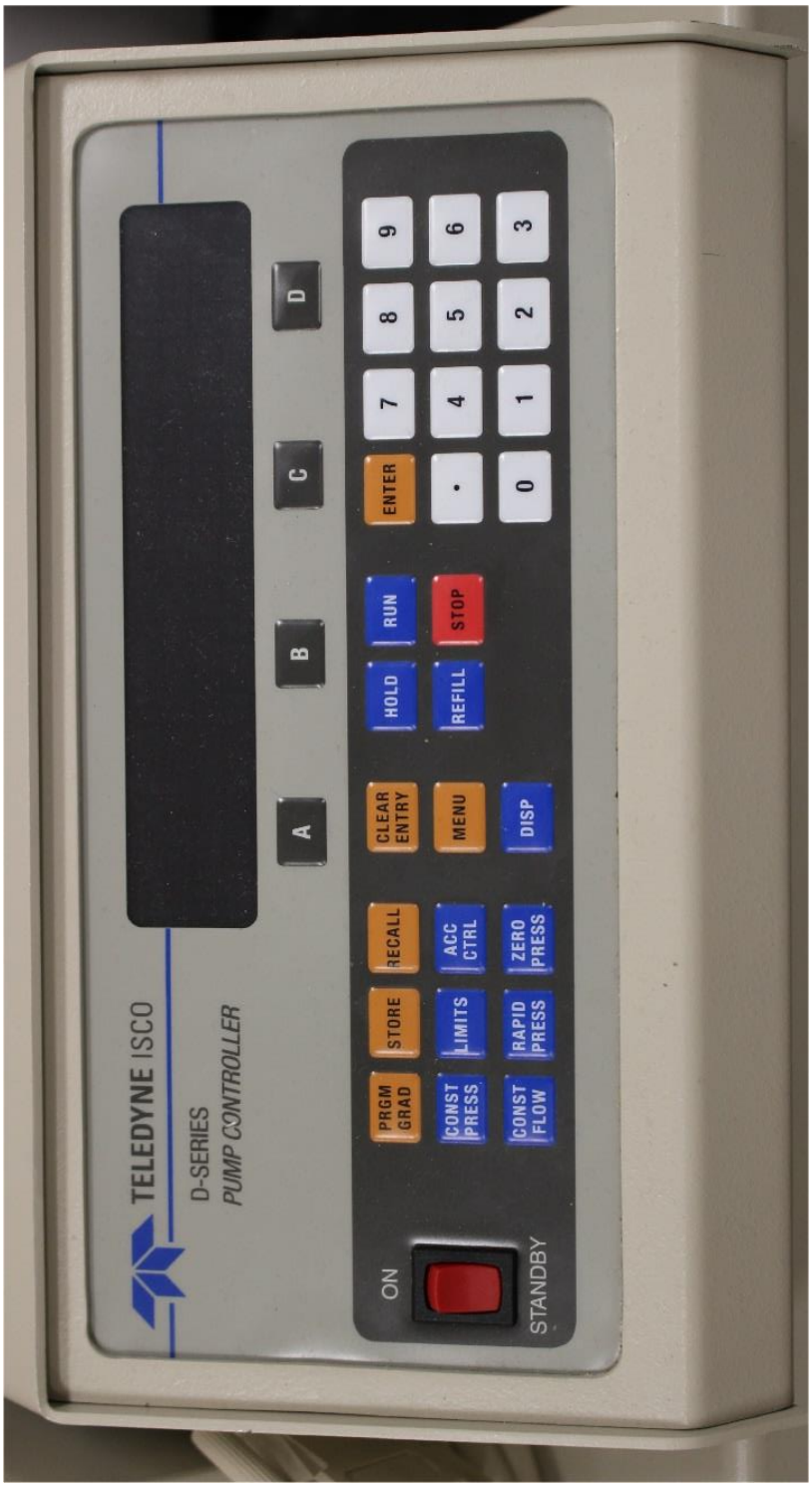

Figure A.11: Picture of a Teledyne control panel.

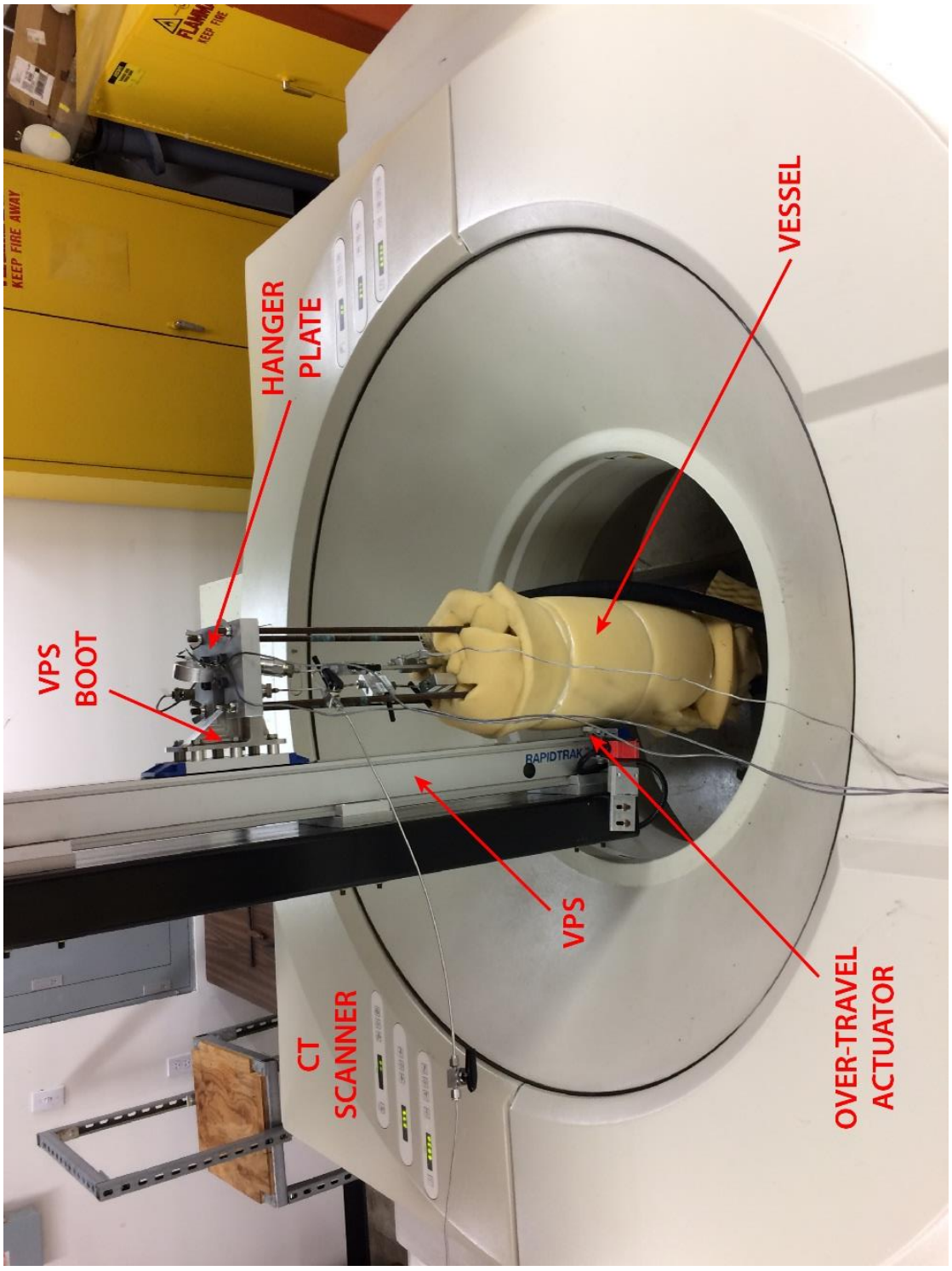

Figure A.12: Picture of the computed tomography (CT) scanner.

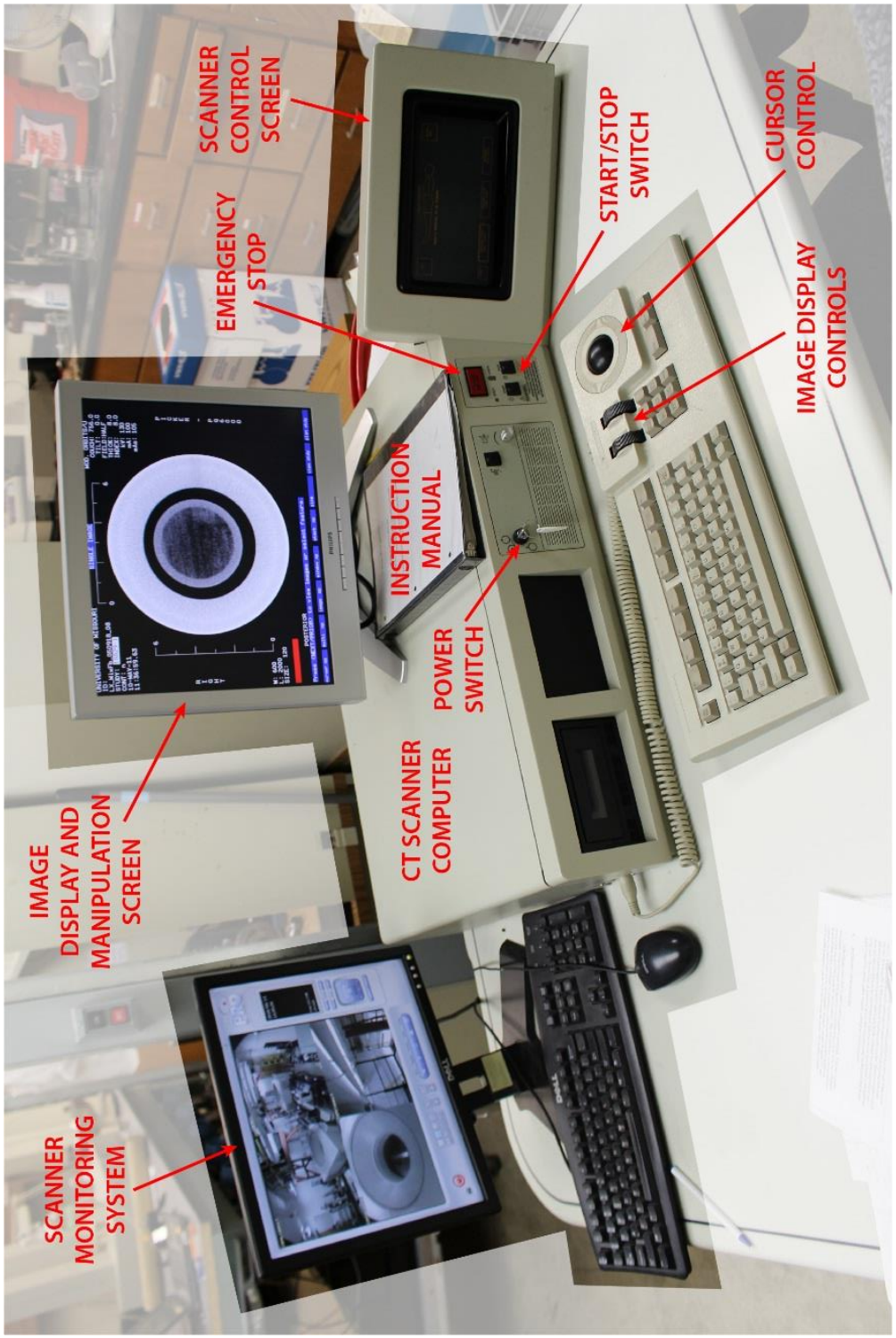

Figure A.13: Picture of the CT scanner control panel.

A.2 Data Storage Structure

1. HVTXXXX\
    a. Formation\
        i. CT Scans\
            - Processed\
                This folder holds the folders and data output by the CT scan processing code. This includes scan information, .MAT files of the raw attenuations, the initial PILE files, and the .TIFF files of each slice.
            - Raw Data\
                This folder contains the raw data for each scan output by the scanner in its original format and file structure. The primary useful data in this folder are the PILE files for each scan.
        ii. Figures\
            - Any figures created in Matlab or Illustrator associated with this experiment are stored here. The excel figures remain in the reports and data files.
        iii. Matlab Files\
            - This folder contains the MatLab files produced from the raw pump and DAQ data for manipulation and plotting in MatLab. They typically include the following files:
            - HVTXXXX.mat – A combination of DAQ and Pump data that has been interpolated according to the timestamp. This allows for plotting of volumes and temperatures at the same scale.
            - HVTXXXX_DAQ.mat – A collection of the most important data recorded by the DAQ, usually the timestamps and all the pressures and temperatures from the equipment that is functioning properly
            - HVTXXXX_Pump.mat – A collection of the most important data recorded off the pumps. Typically includes the timestamps, change in brine and methane volumes, MOC-predicted methane consumption, mass balance phase saturations, and MOC-predicted three-phase hydrate saturation.
        iv. Raw Data\
            - This folder contains the raw data recorded from the DAQ the pumps during the experiment.
            - Occasionally, this folder may contain OLD datasheets that have since been updated using the new templates, or other

Excel documents containing some additional post-processing that was not included in the overall analysis.

v. Reports\
   - This folder contains any and all pertinent information and communication concerning the experiment and its preliminary analysis.
   - HVTXXXX_Email_Updates.pdf – At the end of the experiment, I concatenated all the email conversations concerning the experiment into one PDF file, by order of date, to maintain a permanent record.
   - Update_Template.docx – A suggested template for the presentation of the pertinent information to report throughout the experiment. A separate report was sent out around every 24 hours containing this information and a preliminary analysis of the experiment. These reports are saved in this folder as a separate files.

vi. HVTXXXX_Analysis.xlsx – This template contains the mass balance equations and is used to post-process the pump data throughout the experiment. It requires the input of some essential sample parameters as well. Some of the figures for each report will come from here.

vii. HVTXXXX_Data_Workup.xlsx – This template is used to save and plot the raw volume, pressure, and temperature data throughout the experiment and make it more accessible that then RAW formats. Some of the figures for each report will come from here.

viii. HVTXXXX_Worksheet.pdf – The worksheet contains some important information concerning the equipment used to run the experiment and some essential experimental parameters.

b. LeakTest\
   i. Raw Data\
      - This folder contain the raw data recorded from the DAQ and the pumps during the leak tests.
   ii. HVTXXXX_LeakTest_Workup.xlsx - This template is used to save and plot the raw volume, pressure, and temperature data throughout the leak test and make it more accessible that then RAW formats. All the leak test analysis can be done in this document.

c. PermTest\
   i. Raw Data\
      - This folder contains the raw data recorded off the pumps during the perm test.
   ii. HVTXXXX_PermTest_Workup.xlsx - This template is used to post-process the raw data from the permeability test and determine the average intrinsic sample permeability.

A.3 Sample Preparation

A.3.1 Sample Sleeve Preparation

1. Take a new Viton® sample sleeve (Figure A.1c) and assure that it is 7" in length.
2. If the length is wrong or there is no new Viton® sleeve is available, then cut one to the correct length using the band saw:
    a. Put on protective hand and eyewear.
    b. Plug in the shop vacuum and attach it to the vent port on the back of the band saw.
    c. Mark 7" on the sleeve using the silver permanent marker about every inch around the sleeve.
    d. Make sure the band saw is unplugged.
    e. Sit the sleeve next to the blade and adjust the blade guard so that it sits just above the height of the sleeve (~2.5").
    f. Start the vacuum.
    g. Plug the band saw in and start it.
    h. Square up the sleeve with the blade and very slowly push the sleeve into the blade. Your fingers should be holding the sleeve at either end of the sleeve along the front edge.
    i. Check to make sure the cut is in the correct spot and then slowly push the sleeve into the blade.
    j. Continuously check to make sure that you are following the cut path.
    k. Once the cut is complete, turn off the band saw and unplug it.
    l. Clean up the area around the cut using the vacuum. Do not forget to open up the band saw and clean out the inside.
    m. Unplug and put away the vacuum.
3. Clean out the inside of the sample sleeve with water and dry it thoroughly.
4. Label the sample sleeve with the experiment number (HVTXXXX)

A.3.2 Sample Endcap Preparation

1. Thoroughly clean any old grease and sand off both pieces of each sample endcap and both the internal and external O-rings for each endcap (Figure A.1d).
2. Clean the sample filters (Figure A.1d) with isopropyl alcohol and blow air through them or place them in the oven to dry them out.
3. Inspect all O-rings for any damage and replace if necessary.
4. Place a dried sample filter into the central groove in the exterior piece of each endcap.
5. Apply a small amount of vacuum grease to each internal O-ring (Figure A.1d) and place them into the internal O-ring groove.
6. Wipe away any grease on the internal endcap surface.

7. Screw the interior piece of each endcap onto the exterior piece as tight as your hands can manage. There will be a small gap between the exterior and interior pieces.
8. Apply vacuum grease to the external O-rings (Figure A.1d) and install them into the external grooves.
9. Wipe away any grease on the external endcap surface.
10. Set both endcaps aside in a place where they will stay clean.

A.3.3 Sample Material Preparation

1. Put on a filter mask and goggles.
2. Clean out a metal mixing bowl and tare the electronic scale to its weight.
3. Weigh out 995 grams of Sigma Aldrich sand in the bowl.
4. Clean off a plastic weighing tray and tare the electronic scale to its weight.
5. Weigh out 5 grams of clay from Eugene Island Site 330 in the weighing tray.
6. Combine the two components together in the metal bowl and use a whisk to gently mix them together and break apart any flocculated clay particles.
7. Transfer the sand-clay mixture into a plastic bucket and record the total initial mass.

A.3.4 Sample Packing

1. Figure A.14 illustrates the setup of the sample packing equipment.
2. Clean off the metal cookie sheet and place it in a clear space.
3. Clean off a sample stand and set it in the middle of the cookie sheet.
4. Place a sample endcap, with the fitting set into the cutout, on the sample stand.
5. Slide the Viton® sleeve onto the sample endcap and assure that it is flush with the external edge of the endcap.
6. Slide the aluminum pluviation cone into the top of the sample sleeve until the base of the cone is flush with the top edge of the sleeve.
7. Place the PVC jacket over and around the pluviation setup (sample stand, bottom sample endcap, sample sleeve, and pluviation cone).
8. Set the digital calipers to 3.2 inches and lock them in place. This is the desired distance between the top of the pluviation cone and the top of the sediment. That distance will allow the top sample endcap to be flush with the top of the sleeve while making good contact with the sediment.
9. Clean out the pluviation device and, while holding it over the sample, fill it with the sand-clay mixture from the bucket. Sediment should begin flowing out the bottom of the pluviation device in a circular pattern.
10. Slowly move the pluviation device around the edge of the sample cross section while lightly tapping the base to maintain consistent sediment flow. Sand deflected by the pluviation cone will collect on the sample base and cookie sheet.
11. Occasionally check the distance between the top of the pluvation cone and the top of the sediment:

a. Raise the pluvation device up and slide the sediment bucket underneath it. Put both to the side.
b. Take the calipers and check the distance at various points around the pluvation cone to see how much more sediment is needed and to assure the sediment is level.
c. If more sand is needed, bring the bucket and pluvation device above the sample and remove the bucket to restart sediment flow.

12. Once the sediment is 3.2 inches from the top of the pluvation cone, put the pluvation device in the bucket and put it to the side.
13. Remove the PVC jacket, hold it over the cookie sheet, and clean any sand off the inside edge of the base.
14. Holding the sample by the bottom, twist and remove the pluvation cone.
15. Brush off the base of the sample to remove and sand.
16. Transfer the sample to the other sample stand off the cookie sheet.
17. Pick up and clean off the other sample stand over the cookie sheet using the paintbrush.
18. Insert the other sample endcap into the top of the sample sleeve using the sample stand. Make sure the sleeve goes in straight and level and try to not distort the sample sleeve. Once the sample hits the sediment, avoid additional disturbance.
19. Measure the final length of the sleeve to determine the final sample length.
20. Pour the sand-clay mixture remaining in the pluvation device and on the cookie sheet back into the bucket. Clean off both items using the paintbrush.
21. Weigh the final total mass of the bucket and sand.
22. Measure the final length of the sleeve and any offset between the sleeve and the top endcap.
23. After packing, keep the sample vertical. Rotating it horizontally will produce high porosity zones along the sample edges.

A.3.5 Gravimetric Porosity Calculation

1. Calculate the mass of sand in the sample from the total initial and final mass of the bucket and sand.
2. Calculate the volume of sand (V_{sand}) in the sample from the mass of sand in the sample and the solid grain density (2.65 g/mL).
3. Calculate the sample length by subtracting the thickness of both sample endcaps (6.1cm).
4. Calculate the total sample volume (V_{TOT}) from the radius (2.54cm) and final sample length.
5. Calculate the gravimetric porosity (ϕ_{grav}) using Equation A.1:

$$\phi_{grav} = 1 - \frac{V_{sand}}{V_{TOT}} \quad \text{(A.1)}$$

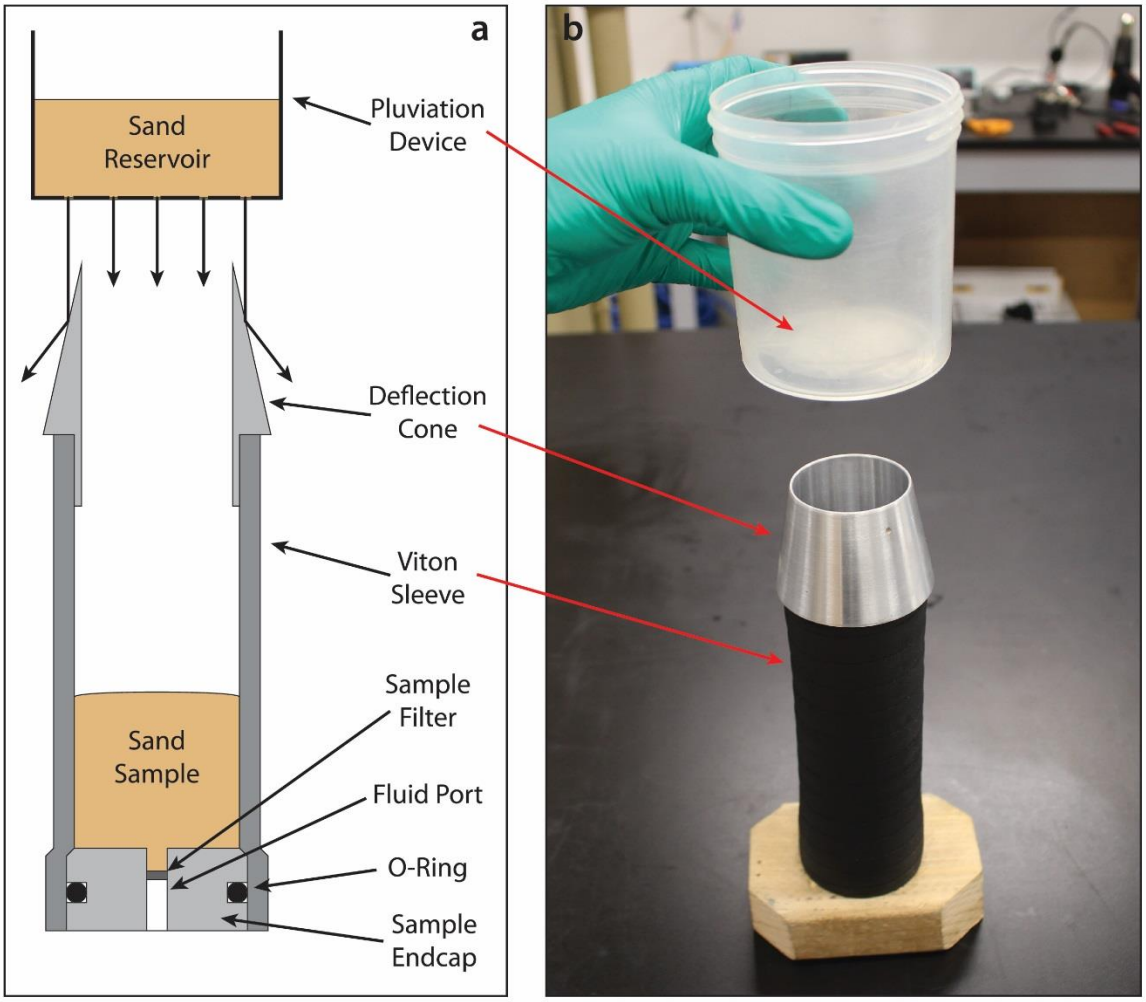

Figure A.14: Slow pluviation sample packing setup.

Sample material is slowly "rained" into the sample sleeve through holes in the bottom of the sand reservoir. The deflection cone assures that only sand grains that dropped straight from the reservoir fall into the sample.

A.4 Hydrates Vessel Preparation and Assembly

A.4.1 Cooling Jacket and Bottom Vessel Endcap Installation

1. Clean both PVC cooling jacket spacers (Figure A.4b) paying particular attention to the O-ring grooves along the internal and external edges.
2. Clean four internal and external cooling jacket O-rings (Figure A.4b).
3. Apply vacuum grease to each O-ring and put them in the appropriate O-ring groove in each PVC spacers. The internal O-rings are slightly small than the internal diameter of the spacer to assure that they stretch around the pressure vessel when they are in place.
4. Clean off the exterior of the aluminum sleeve (Figure A.1a).
5. Slide a PVC spacer over one end of the aluminum sleeve at an angle ensuring that the internal O-rings remain solidly in the groove. As you slide the rest of the spacer onto the aluminum sleeve, work your fingers around the internal diameter to keep the O-ring in the groove. With the internal O-ring in place, slide the spacer down the sleeve until it stops.
6. Slide the aluminum spacer (Figure A.4b) around the aluminum sleeve until it rests on the PVC spacer.
7. Slice the retainer ring (Figure A.4b) down around the aluminum ring until it snaps into place in the retainer groove.
8. Rest the aluminum sleeve on the end that you just attached the PVC spacer, aluminum spacer, and retainer ring to so that the open end is pointing up.
9. Slide the cooling jacket (Figure A.4a) over the aluminum sleeve and onto the PVC spacer until it stops against the aluminum spacer.
10. Repeat Step A.4.1.5 to slide the other PVC spacer onto the aluminum sleeve.
11. Slide the PVC spacer into the annulus between the cooling jacket and aluminum sleeve until it stops.
12. Attach the aluminum spacer and retainer ring using the same method as Steps A.4.1.6 and A.4.1.7.
13. Secure the vessel in the pipe clamp, using paper towels or a rubber sheet to protect the cooling jacket from the clamp teeth.
14. Prepare the bottom vessel endcap:
    a. Attach the ring clamp to the ring stand.
    b. Place the bottom vessel endcap (Figure A.3) into the ring clamp with the external fittings facing up. The endcap rest on the ring clamp by the wider, exterior portion of the endcap.
    c. Clean the internal surfaces, threads, and O-ring grooves on the endcap.
    d. Use a flashlight to check for sediment or metal fragments in the threads. Use compressed air to remove any debris.
    e. Check the threads for burrs or divots with your finger/fingernails. Use the set of small, fine files to gently remove the defect.
    f. Clean two vessel endcap O-rings (Figure A.1b), apply vacuum grease to them both, and slide both into the appropriate O-ring grooves (Figure A.3).

15. Remove the bottom thermistor (Figure A.1b) from the bottom vessel endcap (Figure A.3) and seal the thermistor port with a Swagelok nut.
16. Remove the bottom vessel endcap from the ring clamp and thread it gently into the aluminum sleeve. If the endcap resists you, remove and try threading it again. Screw the endcap in by hand as much as possible.
17. With about 1 inch of endcap left to screw in, the O-rings will start coming in contact with the vessel wall and rotational resistance will increase significantly. At this point, use the spanner wrenches to screw the endcap the rest of the way into the vessel.
18. Slide the ring collar around the aluminum sleeve until it rests on the retainer ring and tighten the bolts on either side to secure it in place. With this in place, the bottom endcap cannot be removed.

A.4.2 Top Vessel Endcap and Sample Installation

1. Remove the vessel from the pipe clamp and re-secure it to the clamp with the open end facing upward.
2. Prepare the top vessel endcap (Figure A.2) using the same cleaning methods as described in Section A.4.1.14a-f.
3. Attach the sample to the central fitting along the internal face of the top vessel endcap such that the sample is hanging vertically from the top vessel endcap.
4. Connect the internal fluid tubing (Figure A.1b) to the fitting in the bottom sample endcap. You may have the twist the tubing around the sample to get it short enough to attach to the sample.
5. Finger tighten both fittings as much as possible and then cinch up the fittings with combination wrenches. Hold the fitting in the endcap with one wrench and tighten the nut using another wrench.
6. Check that all the other internal fittings are tight, but do not overtighten them.
7. Remove the top vessel endcap and sample from the ring clamp and slide it into the open side of the aluminum vessel.
8. Screw the top endcap into the vessel using the sample procedure as described in Section A.4.1.16-17.

A.4.3 Hanging the Hydrates Vessel

1. Mount the two halves of the top ring collar hanger onto the vessel so they are flush with the retainer rings and the all-thread holes are facing out. Tighten down the bolts to secure them in place.
2. Thread another lock nut approximately 2” onto the other end of each all-thread and place a lock washer on top of it.
3. If this experiment is being performed in the CT scanner, continue to Section A.8.1 for directions on mounting the vessel in the CT scanner.
4. Open the environmental chamber (Figures A.5 and A.6) and pull the hanger frame (Figure A.9) out of the box.

5. Hang the vessel from the hanger plate (Figure A.9) requires TWO people:
    a. PERSON 1: pick up the vessel, maintaining a vertical orientation, and aligns the all-threads with the holes in the hanger plate.
    b. PERSON 2: assist in getting the all-threads through the hanger plate, place a washer on each all-thread, and attach wingnuts onto each all-thread.
    c. Once all the wingnuts are attached, one person can adjust the nuts until the vessel is vertical.
    d. Tighten down the locknuts against the hanger plate to secure the vessel in place.
6. Push the hanger frame back into the box.

A.4.4 Filling the Vessel with Confining Oil

1. Remove the nut from the thermistor port in the bottom vessel endcap (Figure A.3) and install the bottom thermistor (Figure A.1b).
2. Remove the nut from a 1/4" Swagelok fitting on the top vessel endcap.
3. Open the confining vent valve (Figure 2b).
4. Assure that all external fittings are tight.
5. Mount the gravitational filling device onto the ring clamp and slide the nylon tubing over the open 1/4" fitting in the top vessel endcap.
6. Secure the ring clamp to a shelf on the exterior of the environmental chamber (Figure A.5b) and slide the gravitation filling device to at higher elevation than the vessel.
7. Fill the vessel with confining oil:
    a. Pour confining oil into the bucket of the gravitational filling device. The head gradient will push oil into the vessel, which will displace the air.
    b. Oil will flow at approximately 125 mL/min, which will fill the vessel in approximately 15 minutes. The bucket will have to be refilled every 5 – 6 minutes.
    c. The internal volume of HV1 is approximately 1600 mL.
    d. The internal volume of HV2 is approximately 2200 mL.
    e. When confining oil starts flowing out of the confining fluid vent, close the valve to stop the flow.
    f. Remove the top thermistor (Figures A.1b and A.2b) and reinstall it when oil starts to flow out of the fitting (I believe that, at this point, the thermistor in HV1 cannot be removed, but pull it out as far as possible).
    g. Place the bucket of the filling device at a lower elevation than the vessel and disconnect the tubing from the fitting on the top vessel endcap. Allow the bucket to drain into the confining oil reservoir.
    h. Reattach the cap to the open fitting in the top vessel endcap and tighten it.

A.4.5 Data Acquisition Setup

1. Connect the pressure transducer and thermistor cables on the DAQ (Figure A.8) to their corresponding instruments (Ch. 0 = Inlet; Ch. 1 = Outlet; Ch. 2 = Confining).
2. Open the data acquisition LabView VI on the computer and run the program at a 1 second collection interval.
3. Double check that each instrument is attach to the appropriate DAQ channel and that the transducer serial numbers correspond to the ones being used.
4. Make the current settings for the transducers the default:
    a. Stop the DAQ program
    b. Right-click on the drop-down object for each transducer and highlight "Data Operations"
    c. Select "Make Current Value Default"
    d. Save the VI
5. Restart the DAQ program and run it at a 1 second collection interval to keep track of the internal conditions during saturations and pressurization.

A.4.6 Confining Pressure Setup

1. Set the maximum flow rate on the confining pump to 5 mL/min:
    a. Navigate on the pump console (Figure A.11) to the limits menu.
    b. Select Option 5.
    c. Select the confining pump.
    d. Enter a flow rate of 5 mL/min.
    e. Press "Enter".
    f. Press "Enter" again.
    g. Press "Previous" twice to get back to the main menu.
2. Fill the confining pump with at least 150mL of confining oil:
    a. Zero the pressure on the confining pump.
    b. Place the end of the confining fluid tubing attached to the confining pump into the confining oil reservoir.
    c. Set the confining pump to refill. You will see the pressure on the pump decrease to negative values.
    d. At approximately 150 mL, stop the confining pump.
    e. Keep the tubing in the oil until the pump pressure returns to 0 psi.
    f. Run the confining pump at 5 mL/min.
    g. Stop the confining pump when oil comes out of the tubing to remove any air in the pump and/or tubing.
3. Place a bucket under the 1/8" fitting in the bottom endcap and remove the cap.
4. Attach the confining fluid tubing to this fitting and tighten it.

5. Set the confining pump to run at constant pressure at 10 psi and check all the fittings for leaks.

A.4.7 Gas Leak Test Procedure

1. Refer to Figure A.9 for valves and tubing connections relevant to this process.
2. Increase the set pressure on the confining pump to 200 psi (0.14 MPa).
3. Pressurize the sample to 1775 psi (12.24 MPa) and fill the inlet and outlet pumps with 50mL of nitrogen:
    a. Close the outlet pump valve to the "Vent."
    b. Close the inlet pump valve to the "Vent."
    c. Close the outlet valve to the "Pump."
    d. Close the inlet valve to the "Pump."
    e. Open the outlet pump valve to the "Vessel."
    f. Open the inlet pump valve to the "Vessel."
    g. Open the outlet valve to the "Pressure Transducer (PT)."
    h. Open the inlet valve to the "PT".
    i. Empty the inlet and outlet pumps entirely (use a bucket to collect any fluid that comes out).
    j. Zero the pressure on the inlet and outlet pumps.
    k. Attach the "Vessel" tubing on the outlet pump valve to the "Pump" fitting on the outlet valve and tighten the fitting.
    l. Attach the "Vessel" tubing on in the inlet pump valve to the "Pump" fitting on the inlet valve and tighten the fitting.
    m. Open the outlet pump valve to the "Vent."
    n. Attach a regulator to the pressurized nitrogen (N_2) canister.
    o. Attach the vent tubing on the outlet pump valve to the regulator.
    p. Assure that the regulator is completely closed by turning the knob in the "decrease" direction until it stops.
    q. Open the main valve on the canister entirely.
    r. Increase the pressure on the pump and tubing by increasing the regulator pressure until the pressure is approximately 100psi. Confirm the pressure by looking at the pump controller.
    s. Refill the outlet pump to approximately 50mL to fill it with gas.
    t. Slowly open the outlet valve to the "Pump" to pressurize the sample to 100psi.
    u. Stepwise increase the confining and pore pressures to 1875 psi (12.93 MPa) and 1775 psi (12.24 MPa), respectively. Assure that the pore pressure never exceeds the confining pressure. Confirm the pressures on the pump console and the DAQ during pressurization.
    v. Slowly open the inlet valve to the "Pump" to pressurize the inlet pump to 1775psi.
    w. Refill the inlet pump to approximately 50mL to fill it with gas.

x. Close the outlet pump valve to the N_2 canister.
y. Set the outlet pump to constant pressure at 1775 psi (12.24 MPa).
z. Close the N_2 main valve.
aa. Vent off the pressure remaining on the regulator and vent tubing by loosening the vent tubing connected to the regulator.
bb. Close the regulator entirely by turning the knob in the "decrease" direction until it stops.
cc. Disconnect the regulator, and return the N_2 canister to its storage zone.

4. Once the system is equilibrated, stop all the pumps, restart the pump console, and set it to the home screen where you can monitor all three pumps.
5. Open the ISCO pump application in LabVIEW and change the data file name to "HVTXXXX_Pump_GasLeakTest" and confirm that the recording interval is set to 1 second.
6. Start the pump operator and watch the pump console to confirm that nothing happens. If any of the pumps begin moving, switch off the pump console and try again.
7. On the pump operator, switch the confining pump from constant pressure mode and, again, confirm that the pump does not start refilling.
8. Confirm the set pressure for the confining pump on the operator is at 1875 psi and start the pump. Confirm on the console that the pump is running in the correct mode.
9. Set the outlet pump to constant pressure mode and confirm that its set pressure is at 1775 psi. Start the outlet pump and confirm on the console that it is running in the proper mode.
10. Stop the DAQ program.
11. Restart the DAQ program and record the data to a file name with the structure, 'HVTXXXX_DAQ_GasLeakTest'.
12. Start the data logging on the pump operator.
13. Change the recording intervals on both the DAQ program and pump operator to 300 seconds. Check both data files to confirm they are recording properly.
14. At this point, the outlet and confining pumps monitor the following systems:
    a. Outlet pump (Figure A.15: red fittings):
        i. Internal seals for the inlet and outlet pumps.
        ii. Primary filling port on the inlet and outlet pump cylinders.
        iii. Secondary filling port on the inlet and outlet pump cylinders.
        iv. The inlet and outlet pump valves, HiP fittings, and valve stems.
        v. The inlet and outlet valves, HiP fittings, and valve stems.
        vi. Outlet pressure transducer and adapter.
        vii. Inlet pressure transducer and adapter.
        viii. Swagelok and NPT fittings in the top vessel endcap connected to the inlet and outlet valves.
        ix. Swagelok fittings and 3 NPT fittings inside the pressure vessel as well as the sample endcap O-ring seals. These fittings are only under 100 psi effective stress and are unlikely to leak.

b. Confining pump (Figure A.15: green fittings):
    i. Internal seals for the confining pump.
    ii. Primary filling port on the confining pump cylinder.
    iii. Secondary filling port on the confining pump cylinder.
    iv. The confining pump valve and associated HiP fittings and valve stems.
    v. Confining pressure transducer and adapter.
    vi. Swagelok and NPT fittings in the top and bottom vessel endcap.
    vii. NPT fitting and adapter for the burst disc assembly.

15. Monitor the pump controller to confirm there are no major leaks. If there is, isolate the following sections of the system to try and find the leak source:
    a. Close the inlet valve to the "Pump."
    b. Close the inlet valve to the "PT."
    c. Close the outlet valve to the "PT."
    d. Close the outlet valve to the "Pump." If closing this section fixing the leaks and a – c did not, then you have a leak between the inlet and outlet valves. This likely means you need to depressurize the whole system in order to fix the leak. Steps A.4.7.23 – 28 describe this process.
    e. Close the outlet pump valve to the "Vessel."

    After closing a section, continue to monitor the pump controller to see if the flow rate on the outlet pump decreases significantly. If not, then reopen that section and move on to the next. If you find the source of the leak, keep that section closed, depressurize it, and fix it before repressurizing.
16. Once you are confident there are no major leaks, let the system sit and record data for at least 48 hours. This will give you a baseline leak rate for the entire system.
17. Plot these data in the leak test workup spreadsheet to produce the following plots:
    a. Volume record of the inlet, outlet, and confining pumps over time compared to the top confining temperature.
    b. Comparison between the temperatures in the room and environmental chamber and the top and bottom confining temperatures over time.
    c. Comparison between the confining, inlet, and outlet pressures over time.
18. Leak tests are always different and inherently unpredictable. Therefore, it is impossible to provide an exact methodology for eliminating them. However, here are some helpful tips:
    a. When analyzing data from experiments performed in the refrigerated lab, calculate leak rates at the same point in each temperature cycle, preferably the middle when the temperature is stable, to quantify leak rates with greater confidence.
    b. When analyzing data from experiments performed in the CT lab, focus on portions of the data where the confining and room temperatures are relatively stable to quantify leak rates with greater confidence.
    c. BE PATIENT! An extra day of leak test data is worth the time if it means the experiment will run successfully.

d. Continuously isolate smaller sections of the experimental setup and keep track of what is leak and what is not.
e. Any leak that can be quantified by a pump is great. However, a leak on the PTs will only be indicated by a drop in pressure.
f. Any portion of the system that will eventually be in contact with gas needs to have the leaks reduced to approximately 2% of the experimental flow rate. If an accurate leak rate can be quantified, then the experimental results should be corrected for that.
g. Any portion of the system that will eventually be in contact with brine can have larger leaks present. Brine is far more viscous and leaks typically disappear once the system is saturated.
h. If there is a leak between the inlet and outlet valves that is less than 10% of the flow rate, you can move forward with saturation. You will performed another leak test on this region later.
i. If the data are ever unclear, collect more data to highlight whatever trends are occurring in the volume or pressure data.
j. If you are not sure what to do, discuss the results with someone else in the group and come to a consensus on the next step.

19. Once the leak test is concluded, open any portions of the system that are disconnected from the outlet pump and make sure the pressure is equilibrated.
20. Stop both the inlet and outlet pumps.
21. Stop the pump and DAQ applications.
22. Restart the DAQ application without recording the data and set the measurement interval to 1 second to monitor the system pressures.
23. Restart the pump console to regain local control of the pumps and restart the confining and outlet pumps at constant pressure.
24. Copy the final raw leak test data from the lab computer and save it in the 'LeakTest/Raw Data/' subdirectory of the experimental data folder.
25. Stop the outlet pump.
26. Slowly open the outlet pump valve to the "Vent" until the pressure on the inlet and outlet pumps and transducers begin to drop. If they do not drop simultaneously, close the outlet valve and check that all portions of the system are open. Otherwise, keep the valve open and let the pore pressure decrease.
27. As the pore pressure continues to drop, stepwise reduce the confining pressure to maintain 250 – 500 psi of confining stress.
28. Once the pore pressure is at 0 psi, open the outlet valve to the "Vent" entirely and reduce the confining pressure to 10 psi.
29. Let the confining pressure equilibrate and then close the outlet valve to the "Vent."
30. If this experiment is being performed in the CT scanner, continue to Section A.8.2 to determine the location of the sample in the vessel and collect the unsaturated scan.

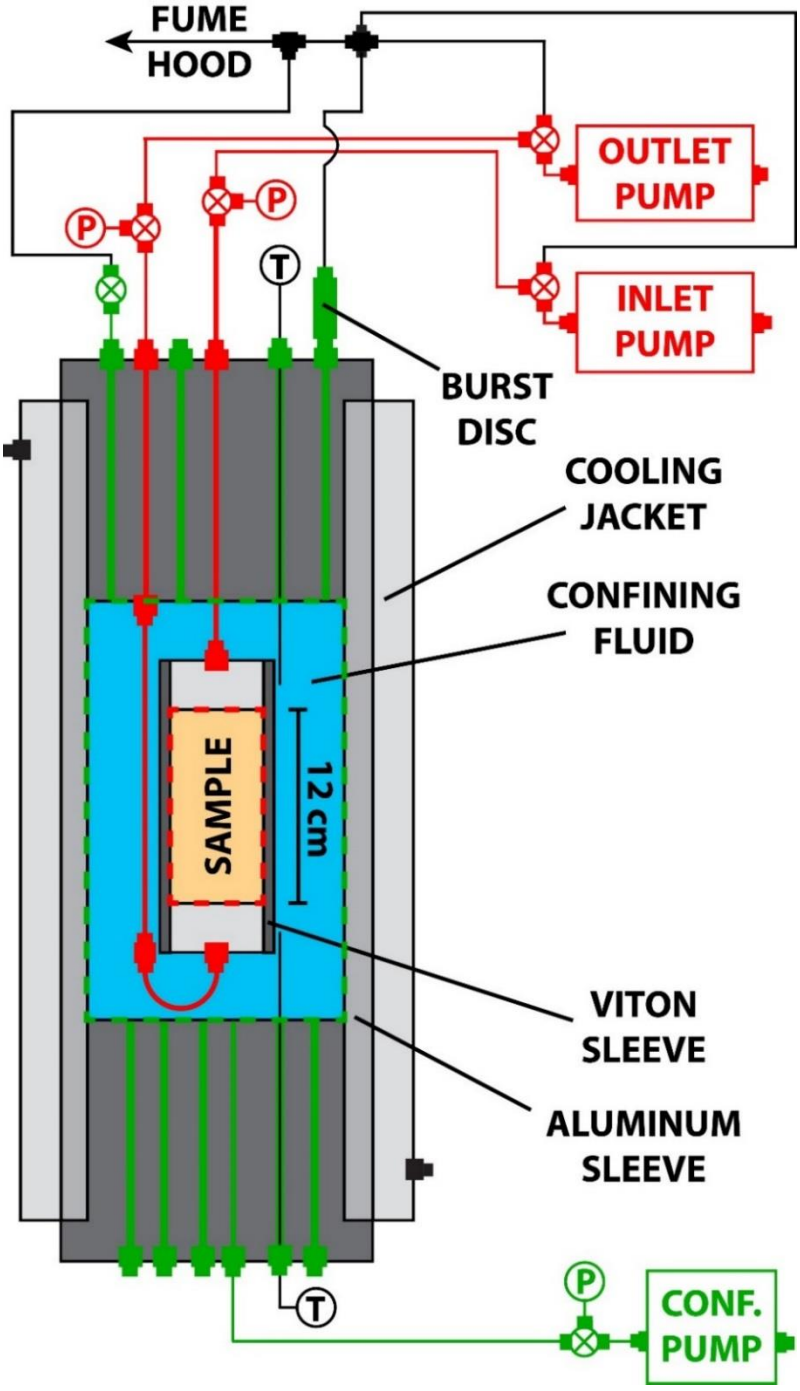

Figure A.15: Gas leak test schematic.

Red tubing and fittings are pressurized with nitrogen. Green tubing and fittings are pressurized with confining oil.

A.5 Sample Saturation and Equilibration

A.5.1 Pore Fluid Preparation

1. Triple rinse a 1-liter vacuum flask and a 500mL Teflon storage bottle with de-ionized water. Dry the flask and bottle with paper towels.
2. Place the vacuum flask in a drying over for about 10 minutes to assure it is completely dry.
3. Place the vacuum flask on an electronic scale and tare the scale.
4. Fill the vacuum flask with 930 grams of deionized water.
5. Place a plastic weighing tray on the scale and tare the scale.
6. Weigh out 70 grams of reagent-grade sodium chloride (NaCl)
7. Pour the NaCl into the vacuum flask and use a clean stirring rod to stir the mixture until all the salt dissolves.
8. Cap the vacuum flask with a rubber stopper and cover the vacuum port with Parafilm® to reduce evaporation.
9. Place the Teflon bottle on an electronic scale and tare the scale.
10. Fill the vacuum flask with 465 grams of deionized water.
11. Place a plastic weighing tray on the scale and tare the scale.
12. Weigh out 35 grams of reagent-grade sodium chloride (NaCl)
13. Pour the NaCl into the Teflon bottle and close the bottle with the cap. Invert the bottle several times until the salt dissolves

A.5.2 Vacuum Saturation Procedure

1. Disconnect the “Pump” fluid tubing on the inlet and outlet valves.
2. Arrange the vacuum pumps and flasks according to Figure A.16:
    a. Connect the upstream vacuum pump to the top port of a vacuum flask filled with desiccant (Flask 1).
    b. Connect the side port of Flask 1 to the side port of the 1-liter vacuum flask containing the pore fluid (Flask 2).
    c. Push the 1/4" metal tube with the 1/4" to 1/8” Swagelok adapter through the stopper in the top of Flask 2 until it touches the bottom of the flask.
    d. Connect the top port of Flask 2 to the “Pump” port on the outlet valve using a long piece of 1/8” nylon tubing and a 1/8” Swagelok to 1/8” HiP adapter. Tighten all the fittings to assure a good seal.
    e. Connect the downstream pump to the top port of a vacuum flask filled with desiccant (Flask 3).
    f. Connect the side port of Flask 3 to the top port of an empty vacuum flask (Flask 4).
    g. Connect the side port of Flask 4 to the top port of another empty vacuum flask (Flask 5).

h. Connect the side port of Flask 5 to the "Pump" port of the inlet valve with a long piece of vacuum tubing using a barbed fitting to 1/8" HiP adapter. Be sure there is no tension on the vacuum tubing that could break the seal.

3. Turn on the downstream vacuum pump and close the release valve.
4. Open the inlet valve to the downstream vacuum pump. The inlet and outlet pressures will drop to approximately -10 psi, indicating the system is under vacuum. If the pressure does not drop this much, then one of vacuum tubing connections is loose. Play with these connections until you maximize the pressure drop.
5. Let the pump run for 2 minutes.
6. Turn on the upstream vacuum pump and close the release the valve. The pore fluid will cavitate while under vacuum.
7. Open the outlet valve to the upstream vacuum pump. Fluid may begin to flow into the sample if the upstream vacuum integrity is not good. However, you wanted this to happen anyways, therefore, unless the flow rate is really slow, you can skip to Step 9 in this section.
8. Slowly open the release valve on the upstream vacuum pump until water begins to flow through the nylon tubing into the sample. This process creates a "high" pressure in the upstream pump that will "push" pore fluid into the sample. There should be a noticeable pressure differential of approximately 3 psi between the inlet and outlet pressure transducers. If the flow rate is slow, open the valve on the upstream pump a little more.
9. After around 250mL of pore fluid have been pulled out of the pore fluid flask, pore fluid will begin flowing into the empty flasks on the downstream end.
10. Let the system run until both empty flasks are full to assure that approximately 7 pore volumes of fluid have flowed through the sample.
11. Close the inlet and outlet valves to the vacuum pumps simultaneously.
12. Open the release valves on both vacuum pumps and turn them off.
13. Open the inlet valve to the pore fluid to release the vacuum on the sample while also assuring that only pore fluid enters the sample. Watch the inlet and outlet pressures to determine when the vacuum has dissipated and then close the inlet valve. This should occur quickly, but more time is not an issue.
14. Disassemble the vacuum pump system and dispose of the pore fluid in the brine waste container.
15. Rinse out the flasks and tubing that contained brine. If the desiccant got saturated, spread it into a metal container, rinse it off, and put it into the oven to dry out.

A.5.3 Pressurizing the System to Experimental Conditions

1. Fill the outlet pump with 150mL pore fluid:
    a. Close the outlet pump valve to the "Vent."
    b. Open the outlet pump valve to the "Vessel"

c. Triple rinse the outlet pump with the pore fluid in the Teflon bottle by refilling it to approximately 30 mL with the outlet tubing, stopping it, and then emptying it into the waste container three times.
d. Zero the pressure on the outlet pump.
e. Refill the outlet pump with 150mL of pore fluid and wait for any subsequent vacuum to dissipate.
f. Remove the tubing from the brine and run the pump at 10 mL/min until brine flows out of the tubing.
g. Stop the outlet pump.

2. Connect the outlet tubing to the "Pump" port on the outlet valve and open the outlet valve to the "Pump".
3. Increase the pressure on the confining pump to 100 psi (0.7 MPa).
4. Increase the pressure on the outlet pump to 10 psi (0.07 MPa).
5. Stepwise increase the pressures on outlet and confining pumps by 200 psi (1.4 MPa) to 1775 psi (12.24 MPa) and 1875 psi (12.93 MPa), respectively. Make sure the pressure on the confining pump is always greater than the pressure on the outlet pump.
6. If desired, perform a constant flow permeability test at this point in the procedure (Section A.9).
7. Fill the inlet pump with 150mL of methane at 1775 psi (12.24 MPa):
    a. Close the inlet pump valve to the "Vent."
    b. Open the inlet pump valve to the "Vessel."
    c. Empty the inlet pump.
    d. Zero the pressure on the inlet pump.
    e. Connect the inlet tubing to the inlet valve and tighten the fitting.
    f. Open the inlet pump valve to the "Vent."
    g. Attach a regulator to the pressurized methane (CH_4) canister.
    h. Attach the vent tubing on the inlet pump valve to the regulator with a valve inline to the vent. Assure the venting valve is closed and all the fittings are tight.
    i. Assure that the regulator is completely closed by turning the knob in the "decrease" direction until it stops.
    j. Open the main valve on the canister entirely.
    k. Increase the pressure on the pump and tubing by increasing the regulator pressure until the pressure is approximately 50psi. Confirm the pressure by looking at the pump controller.
    l. Refill the inlet pump to approximately 150mL to make space for gas.
    m. Increase the pressure on the regulator to 1775 psi (12.24 MPa) and confirm the pressure on the pump.
    n. Close the inlet pump valve to the CH_4 canister.
    o. Set the pump to constant pressure at 1775 psi (12.24 MPa).
    p. Close the CH_4 main valve.

q. Vent off the pressure remaining on the regulator and vent tubing by slowly opening the vent valve.
r. Close the regulator entirely by turning the knob in the "decrease" direction until it stops.
s. Disconnect the regulator, and return the CH_4 canister to its storage zone.

8. Setup up the methane venting system (Figure A.9a):
    a. Attach one 3-way and one 4-way 1/8" Swagelok fittings to each other with a short length of stainless steel tubing to create a venting manifold.
    b. Connect the burst disc outlet, confining fluid vent outlet, and brine pump vent outlet to the vent manifold using stainless steel tubing.
    c. Connect the piece of nylon tubing hanging from the vent tubing at the top of the environmental chamber (Figure A.6) to the vent manifold.
    d. Leave the tubing attached to the "Vent" port on the gas pump valve detached for the moment.
    e. Assure the valve to the fume hood is open.
9. If the experiment is being performed in the refrigerated lab:
    a. Install the vessel in the insulation jacket and top and bottom insulation caps (Figure A.4a). Maintain access to the cooling jacket inlet and outlet ports. Use reinforced tape to hold the insulation in place.
    b. Attach the 3/8" insulated coolant tubing with the valves to both the inlet and outlet ports of the cooling jacket (Figure A.4a).
    c. Close the environmental chamber, assure the seam is well sealed, and connect the heat lamp (Figure A.6) power cables.
    d. Plug in the environmental chamber.
    e. Adjust the chamber set temperature to 15ºC (Figure A.8).
    f. Let the experimental apparatus sit for approximately 12 hours to fully equilibrate to temperature and pressure.

A.5.4 Compressibility Factor Test

1. Assure that the flow rates on the outlet and confining pumps are stable.
2. Stop the outlet pump and close the outlet valve to the "Pump".
3. Increase the confining pressure (P_{conf}) by 100 psi (0.7 MPa) and record the change in the pore pressure (ΔP_{pore}).
4. Calculate the compressibility factor (β) using Equation A.2:
    a. $$\beta = \frac{\Delta P_{pore}}{\Delta P_{conf}} \quad \text{(A.2)}$$
5. Confirm that the compressibility factor is greater than 0.6, indicating that the sample is will saturated. This value will increase with time as any remaining air goes into solution, but I typically see initial β-values greater than 0.85 using this method.
6. Return the confining pump to 1875 psi.
7. Restart the outlet pump at constant pressure.

A.6 System Leak Testing Procedure

1. Once the system is equilibrated, stop all the pumps, restart the pump console, and set it to the home screen where you can monitor all three pumps.
2. Open the ISCO pump application in LabVIEW and change the data file name to "HVTXXXX_Pump_LeakTest" and confirm that the recording interval is set to 1 second.
3. Start the pump operator and watch the pump console to confirm that nothing happens. If any of the pumps begin moving, switch off the pump console and try again.
4. On the pump operator, set the confining pump to constant pressure mode and, again, confirm that the pump does not start refilling.
5. Confirm the set pressure for the confining pump on the operator is at 1875 psi and start the pump. Confirm on the console that the pump is running in the correct mode.
6. Set the inlet and outlet pumps to constant pressure mode and confirm that their set pressures are at 1775 psi. Start both pumps and confirm on the console that they are running in the proper mode.
7. Stop the DAQ program.
8. Restart the DAQ program and record the data to a file name with the structure, 'HVTXXXX_DAQ_LeakTest'.
9. Start the data logging on the pump operator.
10. Change the recording intervals on both the DAQ program and pump operator to 300 seconds. Check both data files to confirm they are recording properly.
11. At this point, the pumps are tracking leaks on the following systems:
    a. Pump A (Figure A.17: red fittings):
        i. Internal seals for the inlet pump.
        ii. Primary filling port on the inlet pump cylinder.
        iii. Secondary filling port on the inlet pump cylinder.
        iv. The inlet pump valve and associated HiP fittings and valve stems.
        v. A part of the inlet valve and associated HiP fittings and valve stems.
    b. Pump B (Figure A.17: blue fittings):
        i. Internal seals for the outlet pump.
        ii. Primary filling port on the outlet pump cylinder.
        iii. Secondary filling port on the outlet pump cylinder.
        iv. The outlet pump valve and associated HiP fittings and valve stems.
        v. The outlet valve and associated HiP fittings and valve stems.
        vi. A part of the inlet valve and associated HiP fittings and valve stems.
        vii. Outlet pressure transducer and adapter.
        viii. Inlet pressure transducer and adapter.
        ix. Swagelok and NPT fittings in the top vessel endcap connected to the inlet and outlet valves.

x. Swagelok fittings and 3 NPT fittings inside the pressure vessel as well as the sample endcap O-ring seals. These fittings are only under 100 psi effective stress and are unlikely to leak.

c. Pump C (Figure A.17: green fittings):
    i. Internal seals for the confining pump.
    ii. Primary filling port on the confining pump cylinder.
    iii. Secondary filling port on the confining pump cylinder.
    iv. The confining pump valve and associated HiP fittings and valve stems.
    v. Confining pressure transducer and adapter.
    vi. Swagelok and NPT fittings in the top and bottom vessel endcap.
    vii. NPT fitting and adapter for the burst disc assembly.

12. During this leak test, never open the "Pump" port on the inlet valve. You want to keep the gas and brine separate.
13. Monitor the pump controller to confirm there are no major leaks. If there are, isolate and fix the problem. The fittings most likely to have leaks are those pressurized with gas. Leak detector can help identify large leaks. Depressurize the system as much as necessary to safely fix the leak. Vent the methane to the vent lines if you need to depressurize the whole pump.
14. Once you are confident there are no major leaks, let the system sit and record data for at least 48 hours. This will give you a baseline leak rate for the entire system.
15. Plot these data in the leak test workup spreadsheet to produce the following plots:
    a. Volume record of the inlet, outlet, and confining pumps over time compared to the top confining temperature.
    b. Comparison between the temperatures in the room and environmental chamber and the top and bottom confining temperatures over time.
    c. Comparison between the confining, inlet, and outlet pressures over time.
16. Leak tests are always different and inherently unpredictable. Therefore, it is impossible to provide an exact methodology for eliminating them. I previously provided helpful tips on how to run leak tests (Step A.4.7.18).
17. Once this initial leak test is concluded, you can move into the final leak test:
    a. Stop the outlet pump.
    b. Open the inlet valve to the "Pump" to hydraulically connect the inlet and outlet pumps and bring gas and brine in contact. The inlet pump may run to account for the pressure differential between the pumps. Let the flow rate stabilize.
    c. Set the outlet pump to "refill" mode, remove 1 mL of brine, and then stop the outlet pump.
    d. This process fills the inlet valve with gas and tests for any leaks on the fittings previously in contact with brine.
    e. If you find a leak, there is not much you can do. Try the following in this order:
        i. Close the inlet valve to the "PT."

ii. Use leak detector to try to determine the location.
iii. VERY gently tighten the HiP fittings to the PT and the sample by a 1/8 to 1/16 turn. This is really a last resort and consult with your lab manager first.

f. Once you have reduced the leak as much as possible, run the system for as long as possible to very accurately quantify the leak rate. If it is greater than 5-10% of your flow rate, you may consider starting over.

31. Once the leak tests are concluded, stop both the inlet pump.
32. Stop the pump and DAQ applications.
33. Restart the DAQ application without recording the data and set the measurement interval to 1 second to monitor the system pressures.
34. Restart the pump console to regain local control of the pumps and restart the confining and outlet pumps at constant pressure.
35. Copy the final raw leak test data from the lab computer and save it in the 'LeakTest/Raw Data/' subdirectory of the experimental data folder.

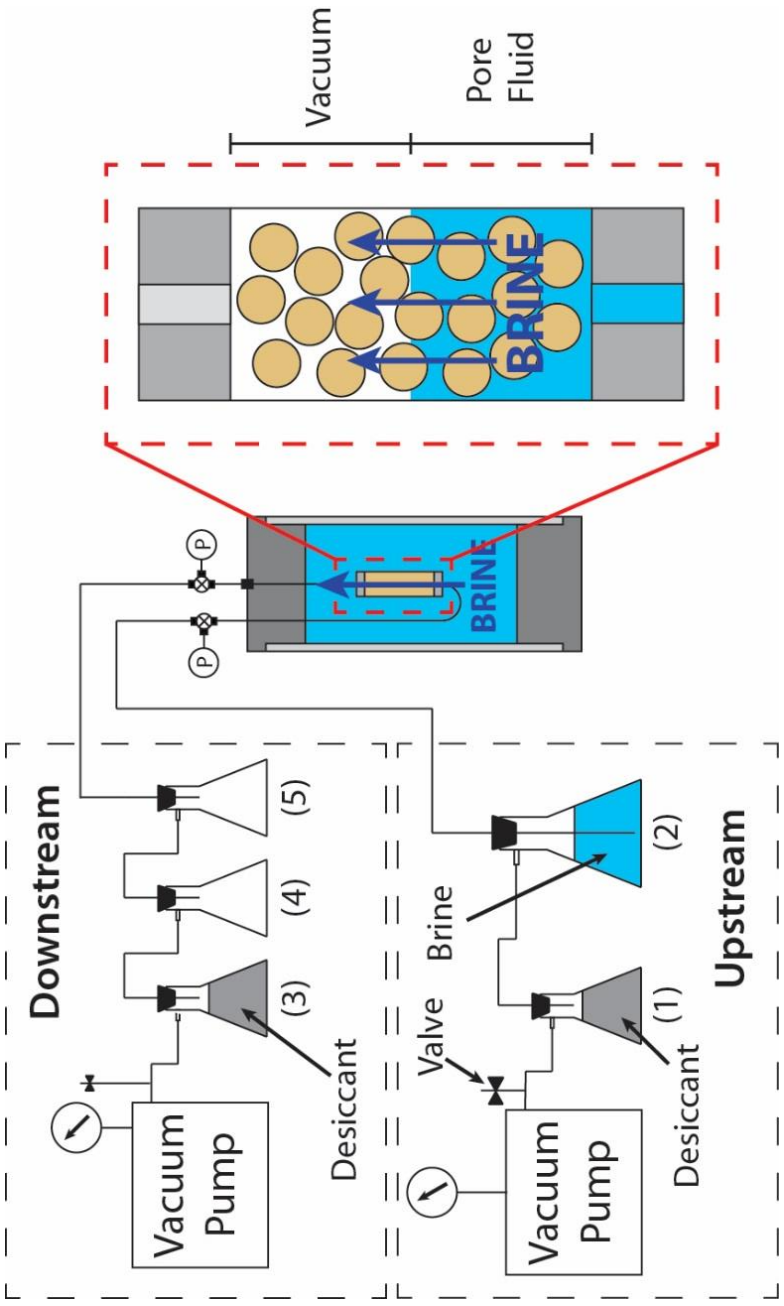

Figure A.16: Sample vacuum saturation setup.

Sample is saturated by putting the sample under a vacuum and pulling several pore volumes of brine through the outlet. Flow is initiated by reducing the vacuum on the upstream end, which creates a pressure gradient across the sample. The effluent is collected by two empty vacuum flasks located downstream.

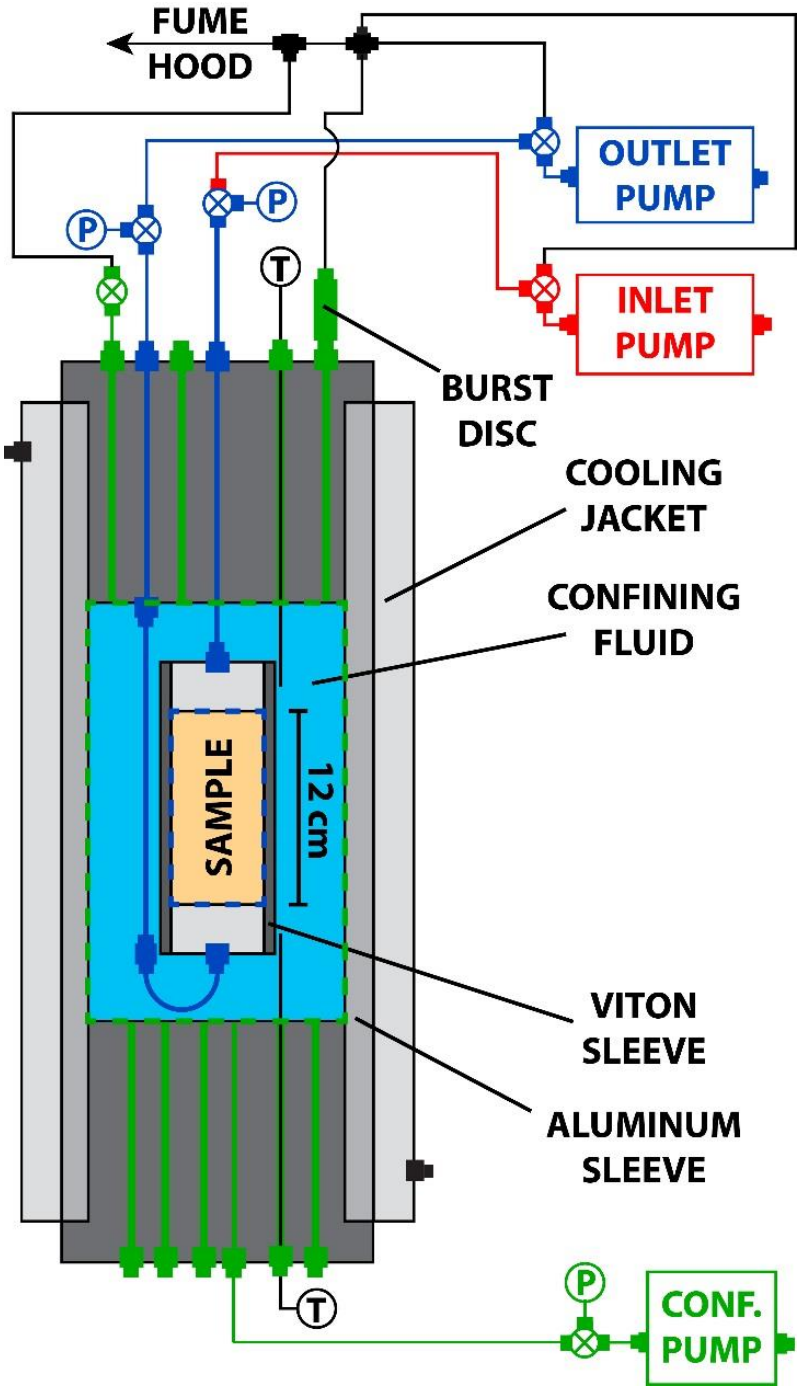

Figure A.17: System leak test schematic.

Red tubing and fittings are pressurized with methane. Blue tubing and fittings are pressurized with brine. Green tubing and fittings are pressurized with confining oil.

A.7 Experiment Execution Procedures

A.7.1 Cooling System to Experimental Conditions

1. If the experiment is being performed in the CT scanner, skip to Step 11.
2. Move the chiller (Figure A.7) next to the environmental chamber.
3. Connect the bottom coolant tubing to the outlet valve of the chiller (Figure A.7).
4. Connect the top coolant tubing to the inlet valve of the chiller (Figure A.7).
5. Feed both inlet and outlet coolant tubing through the holes near the base of the environmental chamber.
6. Connect the outlet coolant tubing to the valve of the inlet tubing (Figure A.4a) on the cooling jacket (bottom fitting) and tighten the fittings.
7. Connect the inlet coolant tubing to the valve of the outlet tubing (Figure A.4a) on the cooling jacket (top fitting) and tighten the fittings.
8. Fill the chiller to within an inch of the top of the reservoir, or between the fill lines, with the dilute ethylene glycol coolant.
9. Make sure the inlet and outlet valves are open to flow and start the chiller.
10. As the cooling jacket fills with coolant, the coolant level in the chiller with decrease. Replace the lost fluid with additional coolant.
11. Set the chiller temperature to 0.5ºC.
12. Let the system sit for at least 12 hours to come to thermal equilibrium.
13. Assure the average temperature on the top and bottom thermistors are at 1 ºC. Make adjustments to the chiller set temperature if necessary.

A.7.2 Experiment Execution

1. If the experiment is being performed in the CT scanner, collect the saturated scan at this point using the same parameters as described in Step A.8.2.14.
2. Confirm that inlet pump is set to the experimental pressure and is running in constant pressure mode
3. Use the outlet pump to remove a set amount of brine from the sample depending on the vessel being used:
    a. HV1: 6.5mL at 2mL/min
    b. HV2: 16mL at 2mL/min
    c. If the experiment is being performed in the CT scanner. You should stepwise remove brine 0.5 – 1 mL at a time, taking an axial scan of the top of the sample in between.
4. Stop the outlet pump once with correct amount of brine is removed or once you observed low densities in the CT scan. This process brings gas in contact with the sample and assures the inlet tube does not get clogged with hydrate.
5. Let the system sit for 10 minutes to allow the flow rate to stabilize.
6. Set the outlet pump refill rate to the experimental flow rate.
7. Start the outlet pump and confirm that the pump is refilling at the correct rate.

8. Stop the pump operator and change the file name to ‘HVTXXXX_Pump_Data’.
9. Restart the pump console to reset the system to local control and assure that all the pumps are stopped. Set the console to the home screen.
10. Start the pump operator and watch the pump console to confirm that nothing happens. If any of the pumps begin moving, switch off the pump console and try again.
11. On the pump operator, switch the confining pump to constant pressure mode and, again, confirm that the pump does not start refilling.
12. Set the outlet pump to refill mode and set the flow rate to the experimental rate.
13. Set the inlet pump to constant pressure mode and set the pressure to 1775 psi.
14. Start both pumps and confirm on the console that they are running in the proper modes.
15. Stop the DAQ program.
16. Restart the DAQ program and record the data to a file name with the structure, ‘HVTXXXX_DAQ_Data’.
17. Start the data logging on the pump operator.
18. Change the recording intervals on both the DAQ program and pump operator to 300 seconds. Check both data files to confirm they are recording properly.
19. Assure that both of the files are being written to and that the data is recording correctly.
20. To perform a shut-in experiment:
    a. Remove a set amount of brine from the sample.
    b. Stop the outlet pump.
    c. Shut the outlet valve to the “Pump”
    d. Continue to record data for as long as you desire the shut-in experiment to run.

A.7.3 Experiment Monitoring

1. If the experiment is being performed in the CT scanner, you must collect a CT scanner every 24 hours at the very least. The maximum frequency is approximately every 45 minutes and is limited by the cooling of the X-ray tube. Collect every scan using the same protocols as those described in Step A.8.2.14. The unsaturated, saturated, and experimental scans are post-processed using the procedures described in Appendix B
2. Every 24 hours, download the data collected from the DAQ and pump applications and import it into the two spreadsheets in the ‘Formation’ subdirectory of the experimental data folder (‘Formation/HVTXXXX_Analysis.xlsx’ and ‘Formation/HVTXXXX_DAQ_Workup.xlsx’).
3. The DAQ workup spreadsheet is the exact same template as the leak test spreadsheet and will produce the same figures as described in Step A.6.15.
4. Initialization of the analysis spreadsheet will require the following information on the experiment (marked in yellow):
    a. Sample length (L)

b. Gravimetric porosity (ϕ_{grav})
c. Experimental flow rate (dV_l/dt)
d. Methane density (ρ_g)
e. Gas volume correction factor – Difference in gas density at the ambient and experimental temperature ($V_m\ Corr.$)
f. Front velocity – Average rate of increase in the affected volume taken from CT data at the end of the experiment (v_{fr})
g. Initial salinity (C_i)
h. Predicted hydrate saturation required to produce bulk three-phase equilibrium ($MOC\ S_h$)

5. The analysis spread sheet will automatically produce the following figures:
    a. Volume of gas injected as a function of time. These data are compared to the minimum, maximum, and expected solutions. This plot is reproduced as a separate chart as well for reporting purposes.
    b. Volume of gas injected as a function of the volume of brine removed. This data is compared to the minimum, maximum, and expected solutions.
    c. Rate of gas injection as a function of the volume of brine removed at 5-hour, 10-hour, and 20-hour moving averages. This data is compared to the minimum, maximum, and expected solutions.
    d. Mass balance-derived bulk phase saturations as a function of time.
    e. Mass balance-derived bulk phase saturations that have been corrected for the pore volume behind the formation front as a function of time compared to the fraction of gas injected that was converted into hydrate (conversion ratio).
6. The analysis spreadsheet also contains blank tabs for information on any CT scans collected and the pressure excursions, including the effective pore throat diameter and hydrate skin thickness required to produce the observed pressure excursions. The information in these tabs needs to be provided separately from the data collected by the DAQ and pump applications.
7. From these data, create daily experimental progress reports that contain at least the following information:
    a. Cover sheet with important experiment information:
        i. Name
        ii. Sample porosity (include CT data if available)
        iii. Sample clay fraction
        iv. Confining temperature
        v. Pore pressure
        vi. Initial salinity
        vii. Flow rate
    b. CT bulk density images, if available.
    c. Comparison the gas injection volume and room/box temperature as a function of time.

d. Mass balance-derived bulk phase saturations as a function of time.
e. Mass balance-derived bulk phase saturations as a function of time that have been corrected for the pore volume behind the front, if available.
f. Room, box, and confining temperatures as a function of time.
g. Inlet, outlet, and confining pressures as a function of time.
h. Any additional information that may be helpful in analyzing the progression of the experiment.

8. Save the progress reports in the subdirectory 'Formation/Reports/' in the experimental data directory as 'XXX_Hour_Update.pdf'
9. Send out the progress report as a PDF to the appropriate people in a constantly growing email chain named 'HVTXXXX Updates.pdf'.

A.7.4 Experiment Termination and Vessel Deconstruction

1. At the end of the experiment, stop the pump and DAQ applications.
2. Restart the DAQ application without recording the data and set the measurement interval to 1 second to monitor the system pressures.
3. Restart the pump console (Figure A.11) to regain local control of the pumps and restart the confining pump at constant pressure.
4. Assure all valves are all open to the "Pump" and "Vessel" such that the inlet and outlet pumps are hydraulically connected.
5. Assure the fume hood is running and that all the fittings in the venting system are tightened.
6. Slowly open the inlet pump valve to the "Vent" until the pressures on the inlet and outlet transducers and the inlet and outlet pumps begin to drop. If they do not drop simultaneously, stop venting and check that all the valves are open.
7. As the pore pressure continues to drop, stepwise reduce the confining pressure to maintain 250 – 500 psi of confining stress.
8. Once the pore pressure is at 0 psi, open the inlet pump valve to the "Vent" entirely and reduce the confining pressure to 10 psi.
9. Turn off the chiller (Figure A.7), close the valves and disconnect the insulated tubing on the chiller side of the valves. Lift the tubing up to drain the fluid back into the chiller.
10. If the experiment is being performed in the refrigerated lab:
    a. Feed the tubes back through the holes in the environmental chamber and move the chiller out of the way.
    b. Turn off the environmental chamber, disconnect the heat lamps (Figure A.6), and separate the chamber halves (Figure A.5 and A.6).
11. Remove the vessel insulation (Figure A.4a).
12. Lead the coolant tubing connected to the top of the cooling jacket (Figure A.9) into the coolant container.
13. Open the valve and disconnect the tubing from the cooling jacket.
14. Lead the coolant tubing connected to the bottom of the cooling jacket (Figure A.9) into the coolant container.

15. Open the valve and let the cooling jacket drain completely.
16. Disconnect the coolant tubing.
17. If the experiment is being performed in the refrigerated lab:
    a. Close the environmental chamber, reconnect the heat lamps (Figure A.6), and turn the chamber back on.
18. Let the system sit for at least 12 hours to allow the hydrate to dissociate.
19. Produce a final report with an initial analysis and distribute it.
20. Concatenate and save the email record, including all responses into a single PDF and save it under the 'Reports' subdirectory.
21. Copy the final raw experimental data from the lab computer and save it in the 'Formation/Raw Data/' subdirectory of the experimental data folder.
22. Disconnect the vent tubing from the confining vent valve.
23. Stop the confining pump and reduce the confining pressure to atmospheric pressure:
    a. Set the confining pump to refill at 5 mL/min.
    b. Let the confining pump run for 1-2 minutes.
    c. Stop the confining pump and let the produced vacuum dissipate.
    d. If there is still pressure remove fluid for another more minute.
    e. Once the pump indicates no pressure (or a negative pressure) in the vessel, slowly open the confining vent valve and check to see if any confining fluid flows out.
    f. Close the confining vent valve (Figure A. 2b). If fluid came out, repeat from Step A.7.4d. If fluid did not come out, move forward with draining the vessel.
24. Place the oil container below the free 1/4" Swagelok fitting in the bottom vessel endcap and remove the container cap.
25. Remove the nut from the 1/4" Swagelok fitting.
26. Open the confining vent valve and assure that confining fluid is flowing into the oil container.
27. Once the vessel is completely drained, replace the cap on the opening fitting in the bottom vessel endcap and close the confining vent valve.
28. Disconnect the confining fluid tubing from the bottom vessel endcap and seal the fitting with a nut.
29. Remove the bottom thermistor (Figure A.1b) and seal the port with a Swagelok nut.
30. Shut down the DAQ and pump applications and lab computer.
31. Disconnect the pressure transducers and thermistors (Figure A.8).
32. Disconnect all remaining fittings connecting the pumps and vent system to the vessel.
33. Loosen the locknuts at the hanger plate (Figure A.9).
34. With a partner, dismount the vessel from the hanger plate by removing the wingnuts.
35. Secure the vessel in the pipe clamp.
36. Remove the hanger collar.
37. Use spanner wrenches to remove the top vessel endcap.

38. Set the top vessel endcap and sample onto the holding blocks (Figure A.1a) and clean up the loose oil.
39. Loosen the Swagelok fittings on the top and bottom sample endcaps and remove the sample.
40. Remove the top and bottom sample endcaps (Figure A.1c) from the Viton® sleeve and discard the sample material.
41. At this point, the system is ready to be cleaned and prepared for the next experiment.

A.8 CT Scanner Procedures

A.8.1 Mounting Vessel into CT Scanner

1. Orient the hanger plate, such that the inlet fitting on the cooling jacket (bottom) aligns with the cutout. The side with the cutout will be facing the electronic vertical positioning system (VPS). This orientation avoids the coolant tubing getting caught on the bottom VPS over-travel actuators (Figure A.12).
2. Slide the hanger plate onto the all-threads and secure it in place with washers and wingnuts.
3. Lower the hoist chain such that the hook is within 2-feet of the floor.
4. Remove the vessel from the pipe clamp and rest it vertically by the orange scaffolding.
5. Attach hoist hook to the ring on the hanger plate (Figure A.12).
6. Raise the hoist chain to lift the vessel until it is 2-feet off the floor.
7. Lift the vessel up to the second level of the scaffolding with the chain hoist.
8. Climb to the second level, remove the guard chains and roll the chain hoist and the vessel along the rail to the hanger boot.
9. Position the bolt head on the bottom of the hanger plate over the hole in the hanger boot and gently lower vessel into place.
10. Secure the hanger plate to the hanger boot with the 4 hex bolts provided.
11. Lift up on the chain hoist slightly and slide the plate out from underneath the VPS.
12. Remove the plywood cover from the hole in the scaffolding.
13. Assure that the CT scanner is in the vertical orientation.
14. Lower the VPS into position until the chain goes slack. Remove the chain hoist and slide it back across the rail into position in front of the chain hoist actuator.
15. Turn on the CT scanner (Figure A.13) and gantry and run the warmup sequence.
16. Make sure that the couch is set to 22mm. If not, move the couch through the console.
17. Turn on the master power to the VPS on the big grey box behind the VPS on the second level of the scaffolding. It is the big red, circular switch.
18. Turn on the VPS by pushing the white, power button on the same grey box.
19. Assure that the yellow indicators for the chain hoist and first stage actuator are lit up. If not, then check to make sure the chain hoist is in front of the actuator and that the VPS is lowered fully.

20. Press and hold the black RESET button until the VPS starts its homing sequence. You may have to hold the button for 5-10 seconds. You'll hear a click when you first press it and then, after a few seconds, the VPS system will slowly move down and back up again to upper limit actuators. Once the VPS moves below the upper limit actuators, you can release the RESET button.
21. At this point, the VPS is now linked to the CT couch and its position can be controlled through the CT console. Two important notes to consider when working with the VPS:
    a. The VPS can be moved between 22 – 1170mm without hitting the over-travel actuators.
    b. If you hit the positive or negative over-travel actuators you will have to completely reset VPS. There's instructions on how to do this in the black binder by the CT console.
22. Lower the vessel into position in the CT scanner (Figure A.12) by moving the couch to position 700mm using the CT console (Figure A.13).
23. Return to Step A.4.4.1 to continue setting up the vessel.

A.8.2 Sample Location Determination and Unsaturated Scan

1. Increase the set pressure on the confining pump to 200 psi (0.14 MPa).
2. Pressurize the sample with methane to 1775 psi (12.24 MPa):
    a. Close the outlet valve to the "Pump."
    b. Close the inlet valve to the "Pump."
    c. Open the outlet valve to the "Pressure Transducer (PT)."
    d. Open the inlet valve to the "PT".
    e. Attach a regulator to the pressurized methane (CH_4) canister.
    f. Attach the vent tubing on the outlet pump valve to the regulator with a valve inline to the vent. Assure the venting valve is closed and all the fittings are tight.
    g. Assure that the regulator is completely closed by turning the knob in the "decrease" direction until it stops.
    h. Open the main valve on the canister entirely.
    i. Increase the pressure on the pump and tubing by increasing the regulator pressure until the pressure is approximately 100psi. Confirm the pressure by looking at the pump controller.
    j. Refill the outlet pump to approximately 25mL to fill it with gas.
    k. Slowly open the outlet valve to the "Pump" to pressurize the sample to 100psi.
    l. Stepwise increase the confining and pore pressures to 1875 psi (12.93 MPa) and 1775 psi (12.24 MPa), respectively. Assure that the pore pressure never exceeds the confining pressure. Confirm the pressures on the pump console and the DAQ during pressurization.
    m. Close the outlet pump valve to the CH_4 canister.
    n. Set the outlet pump to constant pressure at 1775 psi (12.24 MPa).

o. Close the CH_4 main valve.
p. Vent off the pressure remaining on the regulator and vent tubing by opening the vent valve.
q. Close the regulator entirely by turning the knob in the "decrease" direction until it stops.
r. Disconnect the regulator, and return the CH_4 canister to its storage zone.

3. Move the chiller (Figure A.7) next to the CT scanner.
4. Connect the bottom coolant tubing to the outlet valve of the chiller (Figure A.7).
5. Connect the top coolant tubing to the inlet valve of the chiller (Figure A.7).
6. Connect the outlet coolant tubing to the valve of the inlet tubing (Figure A.2a) on the cooling jacket (bottom fitting) and tighten the fittings.
7. Connect the inlet coolant tubing to the valve of the outlet tubing (Figure A.2a) on the cooling jacket (top fitting) and tighten the fittings.
8. Fill the chiller to within an inch of the top of the reservoir, or between the fill lines, with the dilute ethylene glycol coolant.
9. Make sure the inlet and outlet valves are open to flow and start the chiller.
10. As the cooling jacket fills with coolant, the coolant level in the chiller with decrease. Replace the lost fluid with additional coolant.
11. Set the chiller temperature to 15 ºC.
12. Wrap the vessel in the insulation jacket (Figure A.4a) and add the top and bottom insulation caps (Figure A.4a). Maintain access to the cooling jacket inlet and outlet ports. Use reinforced tape to hold the insulation in place.
13. Let the system sit for at least 12 hours to come to thermal equilibrium.
14. Perform a coarse resolution scan to locate the top and bottom of the sample:
    a. Starting at a couch position of 690mm, take single slices at the following parameters until a slice lands inside the sample:
        i. KV = 130
        ii. MA = 100
        iii. INDEX = 10
        iv. THICK = 3
    b. Reset the couch position to the position of the slice just prior to the one in the sample and take single slices a with the following parameters:
        i. KV = 130
        ii. MA = 100
        iii. INDEX = 1
        iv. THICK = 3
    c. Record the slice where the sample endcap is no longer visible.
    d. Repeat Steps 12a – c for the top of the sample starting at a couch position of 790mm.
15. Create a standardized plan for scanning that will be used for every scan in the experiment:
    a. Determine the actual sample length by subtracting the top and bottom sample positions.

b. Find the nearest sample length that is a factor of 3 and split the difference between that length and the actual length to determine the actual start (START) and end (END) positions.
c. Divide the length by three and add one to determine the number of scans (N_SLICES).

16. Collect the unsaturated scan with the following parameters:
    a. START
    b. END
    c. N_SLICES
    d. KV = 130
    e. MA = 100
    f. INDEX = 3
    g. THICK = 3
    h. Start the scan with the tube heat at exactly 20%. Warm the tube to approximately 22%, set up the scan to run, and then start the scan just as the tube heat drops to 20%.
17. Confirm the sampling plan is appropriate for the system. If not, then delete the scan, alter the protocol, and collect another scan.
18. Once the scan is complete, stop both the outlet pump.
19. Slowly open the outlet pump valve to the "Vent" until the pressure on the inlet and outlet pumps and transducers begin to drop. If they do not drop simultaneously, close the outlet valve and check that all portions of the system are open. Otherwise, keep the valve open and let the pore pressure decrease.
20. As the pore pressure continues to drop, stepwise reduce the confining pressure to maintain 250 – 500 psi of confining stress.
21. Once the pore pressure is at 0 psi, open the outlet valve to the "Vent" entirely and reduce the confining pressure to 10 psi.
22. Let the confining pressure equilibrate and then close the outlet valve to the "Vent."
23. Return to Section A.4.8 to move forward with sample saturation.

A.9 Constant Flow Permeability Test

1. Fill the inlet pump with 200mL pore fluid:
    a. Close the inlet pump valve to the "Vent."
    b. Open the inlet pump valve to the "Vessel"
    c. Empty the inlet pump entirely.
    d. Triple rinse the inlet pump with the pore fluid in the Teflon bottle by refilling it to approximately 30 mL with the inlet tubing, stopping it, and then emptying it into the waste container three times.
    e. Zero the pressure in the inlet pump.
    f. Refill the inlet pump with 200mL of pore fluid and wait for the vacuum on the pump to dissipate.

    g. Remove the inlet tubing from the brine and run the pump at 10 mL/min until brine flows out of the tubing.
    h. Stop the pump.
2. Connect the inlet tubing to inlet valve.
3. Increase the pressure on the inlet pump to 1775 psi (12.24 MPa).
4. Stop the inlet pump.
5. Open the inlet valve to the "Pump" to hydraulically connect the inlet and outlet pumps. The outlet pump will likely change in volume slightly to correct for the pressure differential between the pumps.
6. Set the maximum flow rates on the inlet and outlet pumps to 60 mL/min.
7. Once the system is equilibrated, stop all the pumps, restart the pump console, and set it to the home screen where you can monitor all three pumps.
8. Open the ISCO pump application in LabVIEW and change the data file name to "HVTXXXX_Pump_PermTest" and confirm that the recording interval is set to 1 second.
9. Start the pump operator and watch the pump console to confirm that nothing happens. If any of the pumps begin moving, switch off the pump console and try again.
10. On the pump operator, set the confining pump to constant pressure mode and, again, confirm that the pump does not start moving.
11. Confirm the set pressure for the confining pump on the operator is at 1875 psi and start the pump. Confirm on the console that the pump is running in the correct mode.
12. Set the outlet pump to constant pressure mode and confirm that its set pressure is at 1775 psi. Start the outlet pump and confirm on the console that it is running in the proper mode.
13. Set the inlet pump to refill at 5 mL/min and run the pump. Confirm that the inlet pump is running at approximately the same rate to maintain constant pressure.
14. Stop the inlet pump when it is filled with approximately 400 mL of pore fluid.
15. Stop the DAQ program.
16. Restart the DAQ program and record the data to a file name with the structure, 'HVTXXXX_DAQ_PermTest' at 1-second intervals.
17. Start the data logging on the pump operator.
18. Permeability test procedure:
    a. Initially, the pump that has the most brine is declared the "full" pump and the pump that has the least brine is declared the "empty" pump. This reference switches pumps with every test.
    b. Stop the "full" pump.
    c. Set the "empty" pump to constant pressure.
    d. Record the pressure differential between the transducers for at least 1 minute.
    e. Start the "full" pump at constant flow at your desired rate. The "empty" pump will refill automatically to maintain pressure. Run the pump for as long as possible to get a good set of pressure differential and flux data.

f. Stop the pump at constant flow and let the constant pressure pump stabilize.
g. Switch the pump that is under constant pressure.
h. Resume from Step b with the pumps switching roles. Start at a low flow rate with a minimum of 5 mL/min. Stepwise increase the flow rate to a maximum of 50 mL/min. Perform replicates of flow in different directions to determine any gravitational effects.

19. Stop the DAQ and pump applications and restart the pump console to regain local control. Close both applications.
20. Refill (or empty, if applicable) the outlet pump to 150 mL of pore fluid.
21. Close the inlet valve to the "Pump."
22. Run the outlet pump in constant pressure mode at 1775 psi (12.24 MPa).
23. Run the inlet pump in constant pressure mode at 10 psi (0.07 MPa).
24. Reset the maximum flow rate on the inlet and outlet pumps to 10 mL/min.
25. Copy the raw data from the permeability test of the lab computed and save it in the subdirectory 'PermTest/Raw Data' of the experimental data folder. This data can be processed later using the worksheet in the 'PermTest' subdirectory.
26. Stop the inlet pump and disconnect the inlet tubing from the inlet valve. A small amount of brine will leak out.
27. Clean the inlet pump:
    a. Empty the inlet pump of all pore fluid.
    b. Triple rinse the inlet pump with the deionized water by refilling it to approximately 30 mL with the inlet tubing, stopping it, and then emptying it into the waste container three times.
    c. Close the inlet pump valve to the "Vessel."
    d. Open the inlet pump valve to the "Vent."
    e. Fill the inlet pump with 30mL of air.
    f. Close the inlet pump valve to the "Vent."
    g. Pressurize the air in the inlet pump by running it at constant flow.
    h. Open the inlet pump valve to the "Vessel" to blow out any water in the inlet tubing.
    i. Repeat steps c – h three times.
    j. Zero the pressure on the inlet pump.
28. Return to Step A.5.3.7 to continue pressurizing the system to experimental conditions.

APPENDIX B: X-RAY COMPUTED-TOMOGRAPHY POST-PROCESSING PROCEDURE

B.1 Introduction

I performed several of my experiments in the X-ray computed-tomography (CT) scanner in the Hildebrand Department of Petroleum and Geosystems Engineering (PGE) at the University of Texas at Austin. The CT scanner (Figure A.12) was modified to rotate 90-degrees to allow for scans in the horizontal or vertical orientation, though I performed my experiments vertically. I designed my experimental apparatus specifically to be compatible with the CT scanner and vertical positioning system (VPS) in order to collect this additional source of information about my experiments.

I developed a semi-automated CT data post-processing program customized to extract the best information from my CT scans as possible. Once the initial experimental parameters are input into the data file, this program automatically determines the porosity, bulk density, bulk density change, gas saturation for two-phase (gas and brine) experiments, and affected volume for each scan and produces the orthogonal slices presented in the experiments. Some portions of this program were modified from scripts I received from other researchers and I have acknowledged those contributions in code comments. The execution of this program is highly specific to my experiments and data structure, but significant portions of the code could be easily applied to other studies.

B.2 CT Slice Extraction and Format

I collected scans at least every 24 hours throughout the experiment using a scan energy of 130 keV. Each CT scan consisted of approximately 35 images that cross-cut the flow axis. The images were spaced 3 mm apart and contained 2.6×10^5 square pixels with

0.23 mm wide (voxel resolution: 3mm x 0.23 mm x 0.23 mm). The scanner saved each scan in onboard memory until it could be extracted by the lab computer. I extracted the data using a customized Linux script, provided by the CT lab manager, that produced a binary data file (referred to henceforth as a "PILE" file) with data from all the slice of each scan. I then used the *pile_to_tif_mat* subroutine to produce: 1) a 512-by-512 matrix of raw CT attenuation values in Houndsfield units and 2) a grayscale TIFF image of the data. I only used the TIFF images to quickly view the data output from the script and confirm there was no file corruption and that the script was parsing the data correctly. I performed all other post-processing calculations and data imaging starting from the uncorrected attenuation data.

B.3 CT Slice Masking and Filtering

B.3.1 Masking

The CT slices are approximately twice as wide at the sample diameter. Thus, each slice contains attenuation values for material far outside of the sample cross-section including, the sample sleeve, confining fluid, aluminum sleeve, and coolant (Figure B.1). I remove these data so that they are not included in the data and for visualization purposes.

I determine the radius of the sample and the center of the sample within each slice using a modified subroutine obtained from Dr. David DiCarlo at PGE. This process locates the matrix cells in each slice that are within the sample cross-section. I then make a mask matrix equal to the sample diameter and fill the cells within the "sample" with ones and leave the rest of the cells equal to zero. Finally, I iterate through each slice and multiply the mask and the cells in the raw matrix that span the sample cross-section, located using

the sample center and radius. This process produces a new matrix populated by the attenuation values within the sample cross-section and zeros in the corners.

B.3.2 Filtering

CT attenuation data always has anomalous values produced by fluctuations in the X-ray source and detector electronics. These values can frequently result in the CT images looking "grainy" or "spotty," which should not be interpreted as real data. To remove these values, many studies apply coarsening schemes or filters that help smooth the data and retain "real" heterogeneities. In my post-processing, I decided to use median filters to maintain the number of pixels in each slice, while eliminating these anomalous values.

I determined the appropriate median filter size by calculating the CT measurement error (CT^{err}) as a function of median filter size. I collected and analyzed the attenuation data from the confining oil in 40 axial scans taken at experimental conditions and at the same position and scanning parameters. I applied median filters to these data with radii ranging from 1 – 50 pixels, which replaced the value at each individual pixel with the median value of the surrounding pixels. This method did result in some rounding at the edges of the confining oil, but was generally better at maintaining edges than other averaging schemes. I then calculated the average standard deviation of the whole dataset, equivalent to CT^{err}, for each median filter size (Figure B.2).

I convert CT^{err} to an equivalent bulk density error (ρ_b^{err}; Figure B-1) using the midpoint attenuation of the sample between the saturated and unsaturated scans (CT^{avg};

1061 Houndfield units) and the midpoint bulk density of the wet and dry samples (ρ_b^{avg}; 1.84 g/cm^3):

$$\rho_b^{err} = \rho_b^{avg}\left(\frac{CT^{err}}{CT^{avg}}\right). \quad \text{(B.1)}$$

The CT measurement error (Figure B-1: black dots) decreases proportionally to the median filter size (L_{filt}) according to the following power law (Figure B-1: black dashed line):

$$CT^{err} = \pm\left(\left(24.78 \cdot {L_{filt}}^{-0.55}\right) + 6.9\right). \quad \text{(B.2)}$$

From this analysis, I decided to use a 10-pixel median filter for my post-processing as a balance between: 1) standard-deviation reduction, 2) mean preservation, 3) data retention, and 4) conservation of actual heterogeneity, similar to previous studies (Pini et al., 2012; Seol & Kneafsey, 2009). With this filter, the CT^{err} ± 13.4 Houndsfield units and the density threshold is ± 0.024 g/cm^3 (Figure B.2: red cross).

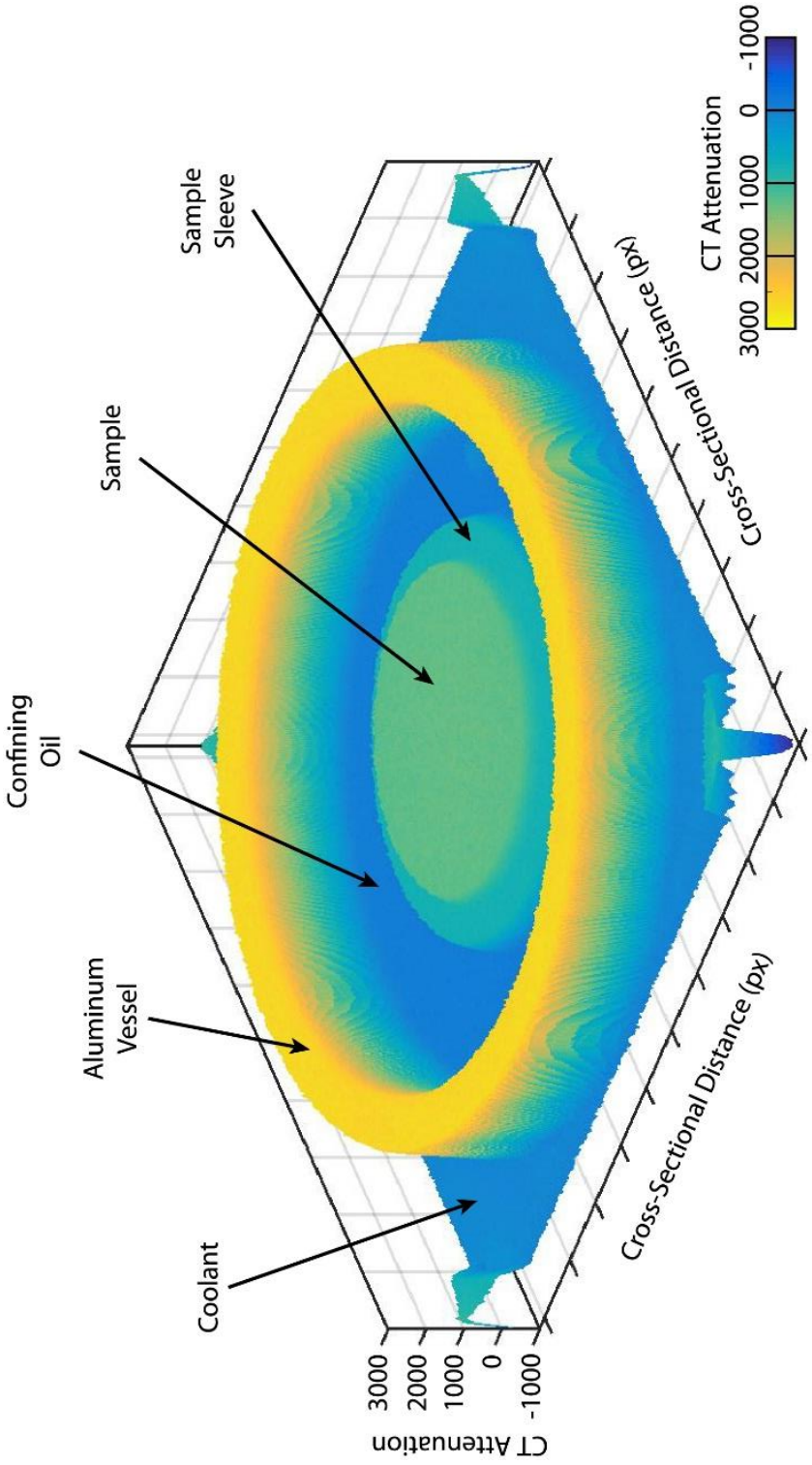

Figure B.1: Example of raw CT attenuations for unmasked slice.

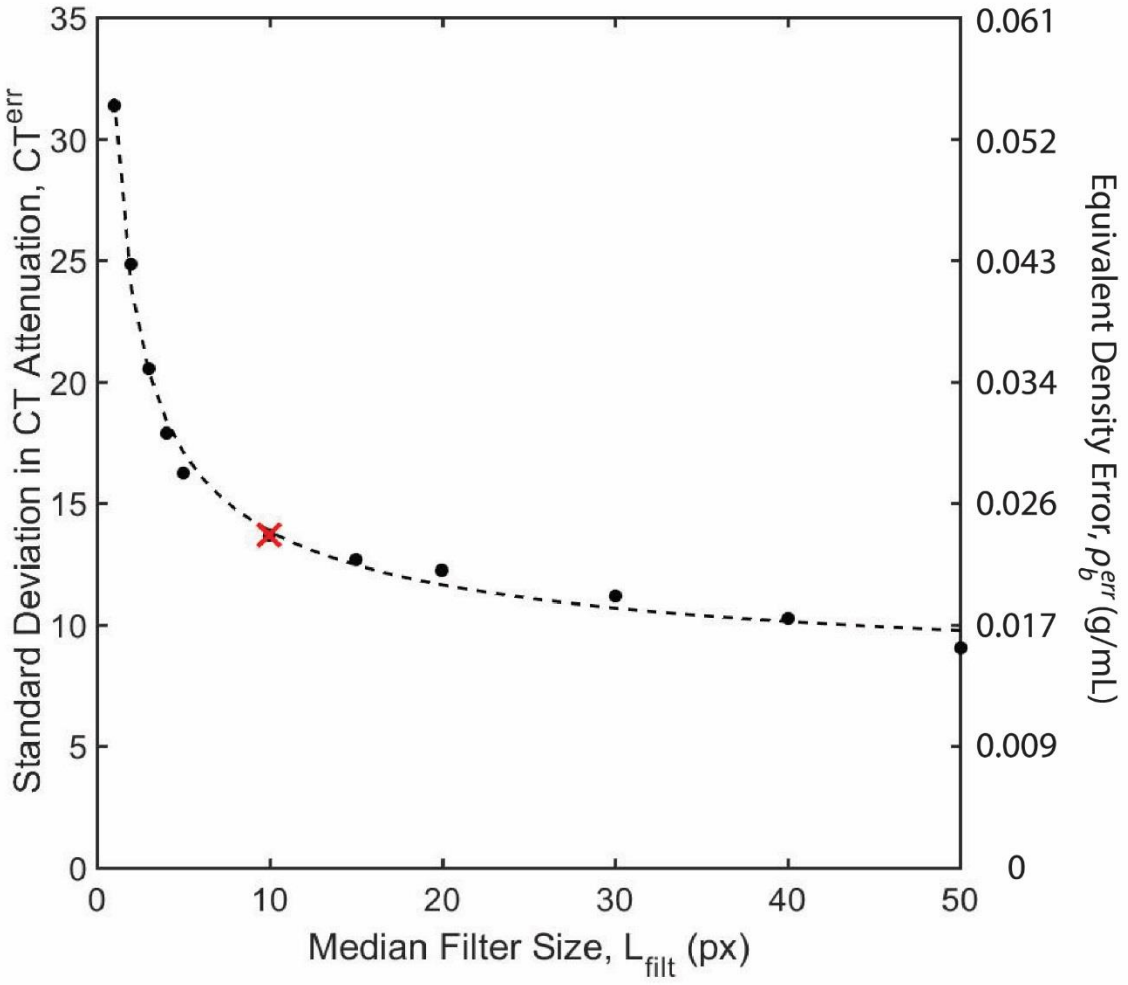

Figure B.2: CT measurement error at a range of median filter sizes.

Standard deviation of the confining fluid CT attenuation and equivalent density error at a range of median filter sizes (black dots). Dashed line indicates the power law fit of the data (Equation B.2) and red cross indicates the median filter size used during scan post-processing.

B.4 Sample Porosity and Bulk Density

CT attenuation is measured as the ratio of the number of X-ray received by the detector when measure with and without the sample between the source and detector. X-rays may be deflected by material between the tube and the detector. CT attenuation is typically assumed to be linearly related to the bulk density of the material being scanned, such that less dense material has lower attenuation and more dense material has high attenuation. With this assumption, I can calculate the porosity and bulk density in each voxel, which provided essential insight into the core-scale processes.

The bulk density of the saturated (ρ_b^{wet}) and unsaturated (ρ_b^{dry}) samples are functions of the bulk sample porosity (ϕ) and the solid grain (ρ_s), liquid brine (ρ_l), and methane gas (ρ_g) densities (Table D.1):

$$\rho_b^{wet} = \big((1 - \phi) \cdot \rho_s\big) + (\phi \cdot \rho_l) \text{ and} \tag{B.3}$$

$$\rho_b^{dry} = \big((1 - \phi) \cdot \rho_s\big) + \big(\phi \cdot \rho_g\big). \tag{B.4}$$

I calculate the change in bulk density between the saturated and unsaturated samples, assuming constant porosity, by subtracting Equations B.4 from B.3 and solving for the porosity:

$$\phi = \frac{\rho_b^{wet} - \rho_b^{dry}}{\rho_l - \rho_g}. \tag{B.5}$$

I solve for the CT-derived sample porosity (ϕ_{CT}) by assuming the CT attenuation of a material is linearly proportional to its density and rewriting Equation B.5 in terms of the saturated (CT^{wet}) and unsaturated (CT^{dry}) CT attenuations and the difference between the attenuations of pure brine and methane (CT^{l-g}):

$$\phi_{CT} = \frac{CT^{wet} - CT^{dry}}{CT^{l-g}}. \quad \text{(B.6)}$$

Since the CT attenuations of pure brine and methane are unknown, I determine CT^{l-g} using the gravimetrically-calculated bulk sample porosity (ϕ_{grav}; Section 2.2.2) and the average values for CT^{wet} and CT^{dry} across the sample:

$$CT^{l-g} = \frac{CT^{wet} - CT^{dry}}{\phi_{grav}}. \quad \text{(B.7)}$$

I calculate the bulk density in each voxel in the saturated (ρ_b^{wet}) and unsaturated (ρ_b^{dry}) scans using Equations B.3 and B.4 and the CT-derived porosities. I then linearly interpolated between these endpoints to determine the bulk density of each voxel in each experimental scan (ρ_b^{exp}):

$$\rho_b^{exp} = \left[\rho_b^{dry} + \left(\left(\rho_b^{wet} - \rho_b^{dry}\right) \cdot \left(\frac{\left(CT^{exp} - CT^{dry}\right)}{\left(CT^{wet} - CT^{dry}\right)}\right)\right)\right]. \quad \text{(B.8)}$$

B.5 MATLAB Implementation

I developed a standard, semi-autonomous MATLAB script that efficiently and consistently post-process the CT data I collected during my experiments. This script first processes the raw by having the user input initial parameters and pick the sample positions, importing all the data, and then masking (Section B.3.1) and filtering (Section B.3.2) the data. It then calculates the sample porosity and bulk density (Section B.4) on a voxel-by-voxel basis and determines the total affected volume for each scan. Finally, it records all the data into clear, preset data folders and outputs basic data visualization results. Portions of this script have been modified from code I received from Dr. David DiCarlo at the

University of Texas at Austin, Hildebrant Department of Petroleum and Geosystem Engineering (PGE).

I specifically designed this post-processing procedure to work with the output from the CT scanner in PGE and to output results that are important to my experiments. However, much of the procedure and calculations have the potential for application across a variety of experiment studies performed in CT scanners. Thus, I have stored my post-processing code, in its entirety, in an online code repository and can be accessed for free at GitHub under the project name CT_PostProc_Hydrate_Formation (https://github.com/meyerdw3/CT_PostProc_Hydrate_Formation). I have incorporated verbose comments into the code describing the purpose and execution of each section. I have also provided an example data set designed to work directly with this code. I hope that this will provide a good starting point of future experimental work both related and unrelated to hydrates.

APPENDIX C: DERIVATION OF BULK PHASE SATURATIONS AND MASS CONVERSION AND VOLUMETRIC PHASE RATIOS

C.1 Bulk Phase Saturations

I calculate the liquid brine (S_l), methane gas (S_g), and solid hydrate (S_h) bulk phase saturations within the affected volume using methane and water mass balance and assuming the sum of the phases is equal to one:

$$V_{aff}\rho_l S_l = V_{aff}\rho_l - V_l\rho_l - V_{aff}\frac{\rho_h N M_w}{M_h(1-C_i)}S_h, \tag{C.1}$$

$$V_{aff}\rho_g S_g = V_m\rho_g - V_{aff}\frac{\rho_h M_m}{M_h}S_h, \text{ and} \tag{C.2}$$

$$1 = S_g + S_h + S_l. \tag{C.3}$$

I measure the volumes of brine removed (V_l) and methane injected (V_m) by the change in volume on the syringe pumps. I determine affected volume (V_{aff}; Section 2.5) using the CT scans. The initial brine salinity (C_i), assumed densities of the liquid (ρ_l), gas (ρ_g), and hydrate (ρ_h) phases, molecular masses of water (M_w), methane (M_m), and hydrate (M_h), and hydration number of Structure I methane hydrate (N) are shown in Table D.1. I first rearrange Equations C.1 – C.2 to isolate the unknowns:

$$V_{aff}\rho_l - V_l\rho_l = V_{aff}\rho_l S_l + V_{aff}\frac{\rho_h N M_w}{M_h(1-C_i)}S_h \text{ and} \tag{C.4}$$

$$V_m\rho_g = V_{aff}\rho_g S_g + V_{aff}\frac{\rho_h M_m}{M_h}S_h. \tag{C.5}$$

I combine and simplify Equations C.4 and C.5 to remove S_h:

$$\frac{\rho_h\rho_l M_m}{M_h}\left(V_{aff} - V_l\right) - \frac{\rho_h\rho_g N M_w}{M_h(1-C_i)}V_m = \frac{\rho_h\rho_l M_m}{M_h}V_{aff}S_l - \frac{\rho_h\rho_g N M_w}{M_h(1-C_i)}V_{aff}S_g. \tag{C.6}$$

I combine and simplify Equations C.3 and C.5 to remove S_h:

$$\frac{\rho_h M_m}{M_h} V_{aff} - \rho_g V_m = \left(\frac{\rho_h M_m}{M_h} V_{aff} - \rho_g V_{aff}\right) S_g + \frac{\rho_h M_m}{M_h} V_{aff} S_l. \quad \text{(C.7)}$$

I combine Equations C.6 and C.7 to remove S_l and solve for the bulk gas saturation:

$$S_g = \frac{\frac{\rho_h}{M_h}\left(\frac{\rho_g M_w N V_m}{(1-C_i)} + \rho_l M_m V_l\right) - \rho_g \rho_l V_m}{V_{aff}\left(\frac{\rho_h}{M_h}\left(\frac{\rho_g M_w N}{(1-C_i)} + \rho_l M_m\right) - \rho_g \rho_l\right)}. \quad \text{(C.8)}$$

I solve Equation C.7 for the bulk brine saturation, using Equation C.8 to calculate S_g within that Equation C.9:

$$S_l = 1 - S_g + \frac{\rho_g M_h}{M_m \rho_h}\left(S_g - \frac{V_m}{V_{aff}}\right). \quad \text{(C.9)}$$

I then solve Equation C.3 for the bulk hydrate saturation:

$$S_h = 1 - \left(S_g + S_l\right). \quad \text{(C.10)}$$

C.2 Mass Conversion and Phase Ratios

I use mass balance to calculate the fraction of methane gas converted into hydrate and the amounts of hydrate and gas present in my sample over time. I can calculate the mass conservation ratio (X_{conv}) using:

$$X_{conv} = \frac{S_h V_{aff}}{V_m} \frac{M_m \rho_h}{\rho_g M_h} \text{ or} \quad \text{(C.11)}$$

$$X_{conv} = 1 - \left(\frac{S_g V_{aff}}{V_m}\right). \quad \text{(C.12)}$$

I solve the volumetric injection ratio (X_{inj}) for the volume of methane injected ($V_m = X_{inj} V_l$) and substitute it into Equations C.11 and C.12:

$$X_{conv} = \frac{S_h V_{aff}}{X_{inj} V_l} \frac{M_m \rho_h}{\rho_g M_h} \text{ and} \quad \text{(C.13)}$$

$$X_{conv} = 1 - \left(\frac{S_g V_{aff}}{X_{inj} V_l}\right). \quad \text{(C.14)}$$

I calculate the volumetric hydrate (X^h) and gas (X^g) phase ratios using:

$$X^h = \frac{S_h V_{aff}}{V_l} \text{ and} \tag{C.15}$$

$$X^g = \frac{S_g V_{aff}}{V_l}. \tag{C.16}$$

I substitute Equations C.15 and C.16 into Equations C.13 and C.14, respectively, and solve for the volumetric gas and hydrate phase ratios:

$$X^h = X_{conv} X_{inj} \frac{\rho_g M_h}{M_m \rho_h} \text{ and} \tag{C.17}$$

$$X^g = X_{inj}(1 - X_{conv}). \tag{C.18}$$

I calculate the bulk gas (S_g) and hydrate (S_h) saturations assuming $V_l = 1$ mL and $V_{aff} = 100$ mL at a range of injection ratios using Equations C.8 and C.10. I then use Equation C.13 to calculate the conversion ratio as a function of the injection ratio. Finally, I use Equations C.17 and C.18 to calculate the volumetric hydrate and gas phase ratios. This analysis indicates that, with no hydrate conversion ($X_{conv} = 0$), $X_{inj} = 1$, $X^g = 1$, and $X^h = 0$ and with total hydrate conversion ($X_{conv} = 1$), $X_{inj} = 5.34$, $X^g = 0$, and $X^h = 4.93$ (Figure 2.8).

APPENDIX D: DERIVATION OF HYDRATE SKIN GROWTH AND SALT DIFFUSION

D.1 Hydrate Skin Growth

I derive an analytical solution for the thickness of the hydrate skin (x) over time (t) using a simple, one-dimensional model for methane diffusion across the hydrate skin. I assume the following: 1) methane transport occurs by diffusion through the solid hydrate; 2) the methane concentration at the gas-hydrate interface equals the methane gas solubility in water (C_m^g); 3) the methane concentration at the brine-hydrate interface equals the hydrate solubility in water (C_m^h); and 4) the diffusion rate can be approximated by a linear methane concentration profile across the hydrate. All the methane diffused through the hydrate forms additional hydrate, such that:

$$D_m \frac{(C_m^g - C_m^h)}{x} dt = \frac{\rho_h}{M_h} dx. \tag{D.1}$$

Equation D.2 is integrated to solve for the hydrate skin thickness (x):

$$x = \sqrt{\frac{2D_m M_h (C_m^g - C_m^h)}{\rho_h}} \sqrt{t}. \tag{D.2}$$

D.2 Hydrate-Driven Salt Flux

I derive an analytical solution for the salt flux (q_{salt}) at the brine-hydrate interface due to additional hydrate formation at that boundary. As the hydrate skin thickness increases due to hydrate formation (Equation D.2), it excludes salt into the brine at the interface and could elevate the local salinity. I evaluate q_{salt} using:

$$q_{salt} = q_h \frac{N M_w C_i}{(1 - C_i) M_{salt}}. \tag{D.3}$$

I assume the water converted into hydrate comes from the brine near the brine-hydrate interface and that the salinity of that brine is equal to the initial salinity (C_i). I calculate the rate of hydrate formation (q_h) using:

$$q_h = \frac{dx}{dt}\frac{\rho_h}{M_h}, \tag{D.4}$$

where dx/dt is the derivative of the hydrate thickness (Equation D.2) with respect to time:

$$\frac{dx}{dt} = \sqrt{\frac{D_m M_h (C_m^g - C_m^h)}{2\rho_h}}\frac{1}{\sqrt{t}}. \tag{D.5}$$

I substitute Equation D.5 into Equation D.4, and get:

$$q_h = \sqrt{\frac{D_m \rho_h (C_m^g - C_m^h)}{2M_h}}\frac{1}{\sqrt{t}}. \tag{D.6}$$

I then substitute Equation D.6 into Equation D.3 to solve for the salt flux:

$$q_{salt} = \frac{NM_w C_i}{(1 - C_i)M_{salt}}\sqrt{\frac{D_m \rho_h (C_m^g - C_m^h)}{2M_h}}\frac{1}{\sqrt{t}}. \tag{D.7}$$

D.3 Salt Concentration Profile Over Time

I use the salt flux (q_{salt}; Equation D.7) as a salt source at the brine-hydrate interface and derive a solution for the salt concentration with distance from the hydrate boundary (x) and time (t). The salt concentration (C) in the brine domain starts at initial concentration (C_i):

$$C(t = 0) = C_i. \tag{D.8}$$

The governing equation for the change in salt concentration is:

$$\frac{\partial C}{\partial t} = D_c \frac{\partial^2 C}{\partial x^2}. \tag{D.9}$$

I impose a no transport boundary at the far edge of the brine domain:

$$\left.\frac{\partial C}{\partial x}\right|_{x=L_c} = 0. \tag{D.10}$$

The boundary condition at the brine-hydrate interface is:

$$-D_c \left.\frac{\partial C}{\partial x}\right|_{x=0} = q_{salt}, \tag{D.11}$$

I substitute C^* for C in Equations D.8 – D.11, where $C^* = C - C_i$, and apply a Laplace transform to yield:

$$\frac{d^2\overline{C^*}}{dL^2} - \overline{C^*}\frac{s}{D_c} = 0, \tag{D.12}$$

$$\left.\frac{d\overline{C^*}}{dx}\right|_{x=L_c} = 0, \text{ and} \tag{D.13}$$

$$\left.\frac{d\overline{C^*}}{dx}\right|_{x=0} = \frac{A\sqrt{\pi}}{\sqrt{s}}. \tag{D.14}$$

s is the Laplace transform parameter with respect to time and A is:

$$A = -\frac{NM_wC_i}{D_c(1-C_i)M_{salt}}\sqrt{\frac{D_m\rho_h(C_m^g - C_m^h)}{2M_h}}. \tag{D.15}$$

I find the solution to Equations D.12 – D.14:

$$\overline{C^*} = \frac{A\sqrt{\pi D_c}}{s}\left[\sinh\left(\sqrt{\frac{s}{D_c}}x\right) + \frac{\cosh\left(\sqrt{\frac{s}{D_c}}x\right)}{\tanh\left(\sqrt{\frac{s}{D_c}}L\right)}\right]. \tag{D.16}$$

I obtain the solution to the salt concentration in actual time domain by applying a numerical inverse Laplace transform to Equation D.15 (Hoog et al., 1982).

Symbol	Name	Value
C_i	initial salinity (kg kg^{-1})	0.07
C_{eq}	three-phase equilibrium salinity (kg kg^{-1})	0.2125
C_m^g	solubility of methane in water (mol m^{-3})	146.07
C_m^h	solubility of hydrate in water (mol m^{-3})	61.09
D_c	diffusion coefficient of salt in water (m s^{-2})[a]	10^{-9}
D_m	diffusion coefficient of methane in hydrate (m s^{-2})[b, c]	10^{-15}
M_h	Molecular mass of Structure I (SI) methane hydrate (g mol^{-1})	119.655
M_m	Molecular mass of methane (g mol^{-1})	16.04
M_{salt}	Sodium chloride molecular mass (kg mol^{-1})	0.0584
M_w	Molecular mass of water (g mol^{-1})	18.02
N	Hydration number for SI methane hydrate[d, e, f]	5.75
ρ_s	Solid grain density (kg m^{-3})	2650
ρ_g	Methane gas density (kg m^{-3})	112
ρ_l^m	Methane density in the liquid phase (kg m^{-3})	2.02
ρ_l	Liquid brine density (kg m^{-3})	1063
ρ_h	Solid hydrate density (kg m^{-3})	912
X_m^h	mass fraction of methane in hydrate (kg kg^{-1})	0.1341

Table D.1: Stoichiometric parameters at my experimental conditions.

[a]Davie and Buffett (2001). [b]Genov et al. (2004). [c]Kuhs et al. (2006). [d]Uchida et al. (1995). [e]Sloan and Fleyfel (1991). [f]Davidson et al. (1986).

APPENDIX E: HYDRATE FORMATION MODEL DERIVATION

E.1 Mass Conservation

The mass of methane injected (m_m; Equation E.1) during a particular time interval (dt) is equal to sum of the masses of methane in: 1) the gaseous phase (m_m^g; Equation E.2) and 2) the hydrate formed due to the diffusion of methane through the skin in each grid block ($[m_m^h]_{k,n}$; Equation E.3):

$$m_m = q_m \pi r_g^2 dt, \tag{E.1}$$

$$m_m^g = \nu_k dt \pi r_g^2 \rho_g, \tag{E.2}$$

$$[m_m^h]_{k,n} = \nu_k dt 2\pi r_g Q_{k,n} dt + \sum_{i=1}^{k-1} \nu_i dt 2\pi r_g Q_{i,n} dt. \tag{E.3}$$

I impose a constant gas flux (q_m) that changes proportionally to the volumetric methane flux (dV_m) observed in the experiments:

$$q_m = \frac{dV_m \rho_g r_g^2}{{r_{smpl}}^2 \phi S_g}. \tag{E.4}$$

The values for q_m used in this study are given in Table 4.1. I calculate the methane transport rate through the hydrate ($Q_{k,n}$) by assuming Fickian diffusion of methane through the hydrate skin:

$$Q_{k,n} = -D_m \frac{(C_m^g - C_m^h)}{(r_{k,n} - r_g)}. \tag{E.5}$$

The gas finger radius (r_g) is a calibrated model input (Table 1). The diffusion coefficient of methane through hydrate (D_m), the gas (ρ_g) and hydrate (ρ_h) phase densities, the mass fraction of methane in hydrate (X_m^h), and the assumed methane concentrations at the gas-hydrate (C_m^g) and brine-hydrate (C_m^h) interfaces are given in Table 4.1. The radii of each

gridblock at each time-step ($r_{k,n}$) and velocity of the gas at each gridblock (v_k) are calculated as a part of this derivation.

E.2 Hydrate Skin Thickness

The hydrate skin thickens over time as methane diffuses through the skin and forms hydrate at the brine-hydrate interface. The mass of methane diffused in a gridblock (k) at a particular time-step (n) is equivalent to the mass of methane in the additional hydrate formed in that gridblock since the previous time-step ($n-1$):

$$v_k dt 2\pi r_g Q_{k,n} dt = v_k dt \pi \left(r_{k,n}^2 - r_{k,n-1}^2\right) \rho_h X_m^h. \quad \text{(E.6)}$$

I approximate the volume of hydrate formed between time-steps by the change in the hydrate skin thickness multiplied by the surface area of the gas finger at the previous time-step, such that:

$$v_k dt \pi \left(r_{k,n}^2 - r_{k,n-1}^2\right) \approx v_k dt 2\pi r_{k,n-1} \left(r_{k,n} - r_{k,n-1}\right). \quad \text{(E.7)}$$

I substitute Equation E.7 into Equation E.6 and rearrange it:

$$r_{k,n}^2 - \left(r_g + r_{k,n-1}\right) r_{k,n} + r_g r_{k,n-1} - \frac{r_g D_m \left(C_m^w - C_h^w\right)}{r_{k,n-1} \rho_h X_m^h} dt = 0. \quad \text{(E.8)}$$

The only unknown in Equation E.8 is the hydrate skin radius of the current gridblock at the current time-step ($r_{k,n}$). I solve for $r_{k,n}$ using the quadratic equation and the coefficients in Equation E.8. Since the time interval is constant, I perform this calculation to determine the skin thickness for the first gridblock ($k = 1$) at the current time (n) and then update all other gridblocks with the thickness of the previous gridblock ($k - 1$) from the previous time-step ($n - 1$).

E.3 Finger Velocity

Any methane injected that does not form hydrate at the current time-step (n) forms a new gridblock and extends the gas finger. I substitute Equation E.6 into Equation E.3 and solve for the gas finger velocity of the current grid block (v_k):

$$v_k = \frac{q_m r_g^2 - \sum_{i=1}^{k-1} v_i (r_{i,n}^2 - r_{i,n-1}^2)\rho_h X_m^h}{r_g^2 \rho_g + (r_{k,n}^2 - r_{k,n-1}^2)\rho_h X_m^h}. \quad \text{(E.9)}$$

E.4 Conversion Ratio

I define the mass conversion ratio ($X_{conv} = m_m^h / m_m$) as the ratio of the mass of methane converted to hydrate (m_m^h) to the total mass of methane injected (m_m) over time. I determine m_m and m_m^h at each time elapsed (t) from the local gas flux, the volume of hydrate around the gas finger at each time-step ($V_{f,n}^h$), and the gas and hydrate stoichiometries (Table 1):

$$m_m = \frac{q_m \pi r_g^2 t}{\rho_g} \text{ and} \quad \text{(E.10)}$$

$$m_m^h = \frac{V_{f,n}^h \rho_h X_m^h}{\rho_g}. \quad \text{(E.11)}$$

I determine $V_{f,n}^h$ through the summation of the cross-sectional area of the hydrate skin and length of each gridblock:

$$V_{f,n}^h = \sum_{i=1}^{k} v_i dt \pi (r_{k,n}^2 - r_g^2). \quad \text{(E.12)}$$

E.5 Gas and Hydrate Saturation

I calculate the bulk gas (S_g) and hydrate (S_h) saturations within the characteristic volume ($V_{c,n} = A_c L_{f,n}$) around the finger at each time-step. The length of the gas finger at

each time-step ($L_{f,n}$) is calculated as a summation of the length of each gridblock:

$$L_{f,n} = \sum_{i=1}^{k} v_i dt. \quad \text{(E.13)}$$

The characteristic area (A_c) is calculated from the sample cross-section and the number of fingers (n_f):

$$A_c = \frac{\pi r_{smpl}^2}{n_f}. \quad \text{(E.14)}$$

I calculate n_f from the cross-sectional area of the sample where gas is present and the cross-sectional area of an individual gas finger:

$$n_f = \frac{r_{smpl}^2 \phi S_g}{r_g^2}. \quad \text{(E.15)}$$

I calculate $S_{h,n}$ and $S_{g,n}$ at each time-step from the total volumes of hydrate ($V_{f,n}^h$) and gas ($V_{f,n}^g$) around the finger at that time-step (Equation E.12):

$$S_{h,n} = \frac{V_{f,n}^h}{V_{c,n}} \text{ and} \quad \text{(E.16)}$$

$$S_{g,n} = \frac{V_{f,n}^g}{V_{c,n}}. \quad \text{(E.17)}$$

I calculate $V_{f,n}^g$ from the cross-sectional area and length of the gas finger:

$$V_{f,n}^g = \pi r_g^2 L_{f,n}. \quad \text{(E.18)}$$

APPENDIX F: DIFFUSION-LIMITED HYDRATE GROWTH MODEL

I demonstrated that, during gas injection into the hydrate stability zone, a hydrate skin forms at the gas-brine interface and limits hydrate formation to methane diffusion through the skin from the gas to the brine. As a result, the skin thickness (x) increases as a function of the square-root of time (Meyer et al., 2018):

$$x = \begin{Bmatrix} 0 & (t = 0) \\ \sqrt{\frac{2D_m(C_m^g - C_m^h)M_h}{\rho_h} t} & (t > 0) \end{Bmatrix}. \tag{F.1}$$

In this study, I envision that the gas fingers can be described as a bundle of cylindrical tubes with a characteristic finger density (A_C^{-1}; Equation E.14). In this case, the diffusion-limited reaction rate (r_{diff}^m) as either a function of time,

$$r_{diff}^m = A_{gw}\sqrt{\frac{D_m(C_m^g - C_m^h)\rho_h}{2M_h}} + A_{gw}\frac{D_m(C_m^g - C_m^h)}{r_g}, \tag{F.2}$$

or hydrate saturation (S_h),

$$r_{diff}^m = \begin{Bmatrix} 0 & (S_h = 0) \\ A_{gw}\frac{D_m(C_m^g - C_m^h)}{r_g}\left[\frac{1}{\sqrt{1 + \frac{2\phi S_h}{A_{gw} r_g} - 1}} + 1\right] & \left(0 < S_h < (1 - S_g)\right) \\ 0 & \left(S_h \geq (1 - S_g)\right) \end{Bmatrix}, \tag{F.3}$$

where S_h increases as a function of time,

$$S_h = \frac{A_{gw}}{\phi}\sqrt{\frac{2D_m(C_m^g - C_m^h)M_h}{\rho_h} t} + \frac{A_{gw}D_m(C_m^g - C_m^h)M_h}{\phi r_g \rho_h} t. \tag{F.4}$$

The gas-brine contact surface (A_{gw}) for my cylindrical model is calculated per unit volume from the finger density and the gas finger circumference:

$$A_{gw} = \frac{2r_g}{r_C^2}. \tag{F.5}$$

This solution is dependent upon my assumed finger geometry, and therefore can easily be transformed for any regular finger geometry (e.g. square, hexagonal).

I generalize this solution, however, for application with irregular geometries where only the average contact surface area per porous media volume is known. I assume that the skin thickness is negligible compared to the size of the gas fingers and simplify Equations F.2 and F.3 to:

$$r_{diff}^m = A_{gw}\sqrt{\frac{D_m(C_m^g - C_m^h)\rho_h}{2M_h}} \text{ and} \tag{F.6}$$

$$r_{diff}^m = \begin{Bmatrix} 0 & (S_h = 0) \\ \frac{A_{gw}^2 D_m(C_m^g - C_m^h)}{\phi S_h} & \left(0 < S_h < \left(1 - S_g\right)\right) \\ 0 & \left(S_h \geq \left(1 - S_g\right)\right) \end{Bmatrix} \tag{F.7}$$

where S_h increases as a function of time,

$$S_h = \frac{A_{gw}}{\phi}\sqrt{\frac{2D_m(C_m^g - C_m^h)M_h}{\rho_h}\,t}. \tag{F.8}$$

In this case, the gas-brine contact surface is likely provide by an empirical relationship determined for a similarly sized sand as those used in my experiments.

Bibliography

Archer, D., Martin, P., Buffett, B., Brovkin, V., Rahmstorf, S., and Ganopolski, A. (2004). The importance of ocean temperature to global biogeochemistry. *Earth and Planetary Science Letters, 222*(2), 333-348. doi: http://dx.doi.org/10.1016/j.epsl.2004.03.011

Ballard, A., Shoup, G., and Sloan, D. (2011). Chapter Seven - Industrial Operating Procedures for Hydrate Control *Natural Gas Hydrates in Flow Assurance* (pp. 145-162). Boston: Gulf Professional Publishing.

Beer, F. P., and Johnston, R. (1992). *Mechanics of Materials* (2nd ed.). New York City: McGraw-Hill Higher Education.

Boswell, R., and Collett, T. (2011). Current prospective on gas hydrate resources. *Energy & Environmental Science, 4*, 10.

Boswell, R., Collett, T. S., Frye, M., Shedd, W., McConnell, D. R., and Shelander, D. (2012a). Subsurface gas hydrate in the northern Gulf of Mexico. *Marine and Petroleum Geology, 34,* 27. doi: 10.1016/j.marpetgeo.2011.10.003

Boswell, R., Frye, M., Shelander, D., Shedd, W., McConnell, D. R., and Cook, A. (2012b). Architecture of gas-hydrate-bearing sands from Walker Ridge 313, Green Canyon 955, and Alaminos Canyon 21: Northern deepwater Gulf of Mexico. *Marine and Petroleum Geology, 34*(1), 134-149. doi: http://dx.doi.org/10.1016/j.marpetgeo.2011.08.010

Boswell, R., Shelander, D., Lee, M., Latham, T., Collett, T., Guerin, G., Moridis, G., Reagan, M., and Goldberg, D. (2009). Occurrence of gas hydrate in Oligocene Frio sand: Alaminos Canyon Block 818: Northern Gulf of Mexico. *Marine and Petroleum Geology, 26*(8), 1499-1512. doi: 10.1016/j.marpetgeo.2009.03.005

Boswell, R., Schoderbek, D., Collett, T. S., Ohtsuki, S., White, M., and Anderson, B. J. (2017). The Iġnik Sikumi Field Experiment, Alaska North Slope: Design, Operations, and Implications for CO2–CH4 Exchange in Gas Hydrate Reservoirs. *Energy & Fuels, 31*(1), 140-153. doi: 10.1021/acs.energyfuels.6b01909

Brewer, P. G., Orr Jr, F. M., Friederich, G., Kvenvolden, K. A., and Orange, D. L. (1998). Gas hydrate formation in the deep sea: In situ experiments with controlled release of methane, natural gas, and carbon dioxide. *Energy and Fuels, 12*(1), 183-188.

Brusseau, M. L., Peng, S., Schnaar, G., and Costanza-Robinson, M. S. (2006). Relationships among air-water interfacial area, capillary pressure, and water

saturation for a sandy porous medium. *Water Resources Research, 42*(3), n/a-n/a. doi: 10.1029/2005wr004058

Brusseau, M. L., Peng, S., Schnaar, G., and Murao, A. (2007). Measuring Air−Water Interfacial Areas with X-ray Microtomography and Interfacial Partitioning Tracer Tests. *Environmental Science & Technology, 41*(6), 1956-1961. doi: 10.1021/es061474m

Casey, B., Germaine, J. T., Flemings, P. B., Reece, J. S., Gao, B., and Betts, W. (2013). Liquid limit as a predictor of mudrock permeability. *Marine and Petroleum Geology, 44*, 256-263. doi: http://dx.doi.org/10.1016/j.marpetgeo.2013.04.008

Chun, J.-H., Ryu, B.-J., Son, B.-K., Kim, J.-H., Lee, J. Y., Bahk, J.-J., Kim, H.-J., Woo, K. S., and Nehza, O. (2011). Sediment mounds and other sedimentary features related to hydrate occurrences in a columnar seismic blanking zone of the Ulleung Basin, East Sea, Korea. *Marine and Petroleum Geology, 28*(10), 1787-1800. doi: https://doi.org/10.1016/j.marpetgeo.2011.06.006

Clarke, M., and Bishnoi, P. R. (2001). Determination of the activation energy and intrinsic rate constant of methane gas hydrate decomposition. *The Canadian Journal of Chemical Engineering, 79*(1), 143-147. doi: doi:10.1002/cjce.5450790122

Collett, T. S., Lee, M. W., Zyrinova, M. V., Mrozewski, S. A., Guerin, G., Cook, A. E., and Goldberg, D. S. (2012). Gulf of Mexico Gas Hydrate Joint Industry Project Leg II logging-while-drilling data acquisition and analysis. *Marine and Petroleum Geology, 34*, 21.

Cook, A. E., and Malinverno, A. (2013). Short migration of methane into a gas hydrate-bearing sand layer at Walker Ridge, Gulf of Mexico. *Geochemistry, Geophysics, Geosystems, 14*(2), 283-291. doi: 10.1002/ggge.20040

Crutchley, G. J., Fraser, D. R. A., Pecher, I. A., Gorman, A. R., Maslen, G., and Henrys, S. A. (2015). Gas migration into gas hydrate-bearing sediments on the southern Hikurangi margin of New Zealand. *Journal of Geophysical Research: Solid Earth, 120*(2), 725-743. doi: 10.1002/2014jb011503

Darnell, K. N., and Flemings, P. B. (2015). Transient seafloor venting on continental slopes from warming-induced methane hydrate dissociation. *Geophysical Research Letters, 42*(24), 10,765-710,772. doi: 10.1002/2015gl067012

Dash, J. G., Rempel, A. W., and Wettlaufer, J. S. (2006). The physics of premelted ice and its geophysical consequences. *Reviews of Modern Physics, 78*(3), 695-741.

Davidson, D. W., Handa, Y. P., Ratcliffe, C. I., Ripmeester, J. A., Tse, J. S., Dahn, J. R., Lee, F., and Calvert, L. D. (1986). Crystallographic Studies of Clathrate Hydrates. Part I. *Molecular Crystals and Liquid Crystals, 141*(1-2), 141-149. doi: 10.1080/00268948608080205

Davie, M. K., and Buffett, B. A. (2001). A numerical model for the formation of gas hydrate below the seafloor. *Journal of Geophysical Research: Solid Earth, 106*(B1), 497-514. doi: 10.1029/2000jb900363

Davie, M. K., and Buffett, B. A. (2003). A steady state model for marine hydrate formation: Constraints on methane supply from pore water sulfate profiles. *Journal of Geophysical Research: Solid Earth, 108*(B10), doi: 10.1029/2002jb002300

Davies, S. R., Sloan, E. D., Sum, A. K., and Koh, C. A. (2010). In Situ Studies of the Mass Transfer Mechanism across a Methane Hydrate Film Using High-Resolution Confocal Raman Spectroscopy. *The Journal of Physical Chemistry C, 114*(2), 1173-1180. doi: 10.1021/jp909416y

Davis, S. N., and DeWiest, R. J. M. (1967). *Hydrogeology*. New York, NY: John Wiley and Sons.

England, W. A., Mackenzie, A. S., Mann, D. M., and Quigley, T. M. (1987). The movement and entrapment of petroleum fluids in the subsurface. *Journal of the Geological Society, 144*(2), 327-347. doi: 10.1144/gsjgs.144.2.0327

Englezos, P., Kalogerakis, N., Dholabhai, P. D., and Bishnoi, P. R. (1987). Kinetics of formation of methane and ethane gas hydrates. *Chemical Engineering Science, 42*(11), 2647-2658. doi: http://dx.doi.org/10.1016/0009-2509(87)87015-X

Frederick, J. M., and Buffett, B. A. (2011). Topography- and fracture-driven fluid focusing in layered ocean sediments. *Geophysical Research Letters, 38*(L08614), doi: 10.1029/2010GL046027

Frye, M., Shedd, W., and Boswell, R. (2012). Gas hydrate resource potential in the Terrebonne Basin, Northern Gulf of Mexico. *Marine and Petroleum Geology, 34*(1), 150-168. doi: https://doi.org/10.1016/j.marpetgeo.2011.08.001

Fu, X., Cueto-Felgueroso, L., and Juanes, R. (2018). Nonequilibrium Thermodynamics of Hydrate Growth on a Gas-Liquid Interface. *Physical Review Letters, 120*(14), 144501. doi: 10.1103/PhysRevLett.120.144501

Genov, G., Kuhs, W. F., Staykova, D. K., Goreshnik, E., and Salamatin, A. N. (2004). Experimental studies on the formation of porous gas hydrates. *American Mineralogist, 89*(8-9), 1228-1239. doi: 10.2138/am-2004-8-910

Germaine, J. T., and Germaine, A. V. (2009). *Geotechnical Laboratory Measurements for Engineers*. Hoboken, NJ: John Wiley & Sons, Inc.

Ginsburg, G. D., and Soloviev, V. A. (1997). Methane migration within the submarine gas-hydrate stability zone under deep-water conditions. *Marine Geology, 137*(1–2), 49-57. doi: http://dx.doi.org/10.1016/S0025-3227(96)00078-3

Glover, P. W., and Walker, E. (2009). Grain-size to effective pore-size transformation derived from electrokinetic theory. *GEOPHYSICS, 74*(1), E17-E29. doi: 10.1190/1.3033217

Haeckel, M., Suess, E., Wallmann, K., and Rickert, D. (2004). Rising methane gas bubbles form massive hydrate layers at the seafloor. *Geochimica et Cosmochimica Acta, 68*(21), 4335-4345. doi: http://dx.doi.org/10.1016/j.gca.2004.01.018

Hassanzadeh, H., Pooladi-Darvish, M., Elsharkawy, A. M., Keith, D. W., and Leonenko, Y. (2008). Predicting PVT data for CO2–brine mixtures for black-oil simulation of CO2 geological storage. *International Journal of Greenhouse Gas Control, 2*(1), 65-77. doi: https://doi.org/10.1016/S1750-5836(07)00010-2

Henry, P., Thomas, M., and Clennell, M. B. (1999). Formation of natural gas hydrate in marine sediments 2. Thermodynamic calculations of stability conditions in porous sediments. *Journal of Geophysical Research, 104*(B10), 18.

Hesse, R., and Harrison, W. E. (1981). Gas hydrates (clathrates) causing pore-water freshening and oxygen isotope fractionation in deep-water sedimentary sections of terrigenous continental margins. *Earth and Planetary Science Letters, 55*(3), 453-462. doi: http://dx.doi.org/10.1016/0012-821X(81)90172-2

Hoog, F. R. d., Knight, J. H., and Stokes, A. N. (1982). An Improved Method for Numerical Inversion of Laplace Transforms. *SIAM Journal on Scientific and Statistical Computing, 3*(3), 357-366. doi: 10.1137/0903022

House, K. Z., Schrag, D. P., Harvey, C. F., and Lackner, K. S. (2006). Permanent carbon dioxide storage in deep-sea sediments. *Proceedings of the National Academy of Sciences, 103*(33), 12291-12295. doi: 10.1073/pnas.0605318103

Huo, Z., Hester, K., Sloan, E. D., and Miller, K. T. (2003). Methane hydrate nonstoichiometry and phase diagram. *AIChE Journal, 49*(5), 1300-1306. doi: 10.1002/aic.690490521

Jin, Y., Konno, Y., and Nagao, J. (2012). Growth of Methane Clathrate Hydrates in Porous Media. *Energy & Fuels, 26*(4), 2242-2247. doi: 10.1021/ef3001357

Katsuki, D., Ohmura, R., Ebinuma, T., and Narita, H. (2007). Methane hydrate crystal growth in a porous medium filled with methane-saturated liquid water. *Philosophical Magazine, 87*(7), 1057-1069. doi: 10.1080/14786430601021652

Kim, H. C., Bishnoi, P. R., Heidemann, R., and Rizvi, S. S. H. (1987). *Kinetics of Methane Hydrate Decomposition* (Vol. 42).

Kneafsey, T. J., Tomutsa, L., Moridis, G. J., Seol, Y., Freifeld, B. M., Taylor, C. E., and Gupta, A. (2007). Methane hydrate formation and dissociation in a partially saturated core-scale sand sample. *Journal of Petroleum Science and Engineering, 56*(1–3), 108-126. doi: http://dx.doi.org/10.1016/j.petrol.2006.02.002

Koh, D.-Y., Kang, H., Lee, J.-W., Park, Y., Kim, S.-J., Lee, J., Lee, J. Y., and Lee, H. (2016). Energy-efficient natural gas hydrate production using gas exchange. *Applied Energy, 162*(Supplement C), 114-130. doi: https://doi.org/10.1016/j.apenergy.2015.10.082

Konno, Y., Fujii, T., Sato, A., Akamine, K., Naiki, M., Masuda, Y., Yamamoto, K., and Nagao, J. (2017). Key Findings of the World's First Offshore Methane Hydrate Production Test off the Coast of Japan: Toward Future Commercial Production. *Energy & Fuels, 31*(3), 2607-2616. doi: 10.1021/acs.energyfuels.6b03143

Kuhs, W. F., Staykova, D. K., and Salamatin, A. N. (2006). Formation of Methane Hydrate from Polydisperse Ice Powders. *The Journal of Physical Chemistry B, 110*(26), 13283-13295. doi: 10.1021/jp061060f

Kuhs, W. F., Klapproth, A., Gotthardt, F., Techmer, K., and Heinrichs, T. (2000). The formation of meso- and macroporous gas hydrates. *Geophysical Research Letters, 27*(18), 2929-2932. doi: doi:10.1029/2000GL006112

Kuhs, W. F., Genov, G., Goreshnik, E., Zeller, A., Techmer, K. S., and Bohrmann, G. (2004). The Impact of Porous Microstructures of Gas Hydrates On Their Macroscopic Properties.

Kvenvolden, K. A. (1993). Gas hydrates—geological perspective and global change. *Reviews of Geophysics, 31*(2), 173-187. doi: 10.1029/93rg00268

Kvenvolden, K. A. (1988). Methane Hydrate: A Major Reservoir of Carbon in the Shallow Geosphere? *Chemical Geology, 71*, 11.

Kvenvolden, K. A., and McMenamin, M. A. (1980). Hydrates of natural gas; a review of their geologic occurrence. *Report Rep. 825*.

Lambe, T. W. (1969). *Soil Mechanics*. New York: John Wiley & Sons, Inc.

Liu, X., and Flemings, P. B. (2006). Passing gas through the hydrate stability zone at southern Hydrate Ridge, offshore Oregon. *Earth and Planetary Science Letters*(241), 16.

Liu, X., and Flemings, P. B. (2007). Dynamic multiphase flow model of hydrate formation in marine sediments. *Journal of Geophysical Research: Solid Earth, 112*(B3), B03101. doi: 10.1029/2005jb004227

Lüdmann, T., and Wong, H. K. (2003). Characteristics of gas hydrate occurrences associated with mud diapirism and gas escape structures in the northwestern Sea of Okhotsk. *Marine Geology, 201*(4), 269-286. doi: https://doi.org/10.1016/S0025-3227(03)00224-X

Malinverno, A. (2010). Marine gas hydrates in thin sand layers that soak up microbial methane. *Earth and Planetary Science Letters, 292*(3–4), 399-408. doi: http://dx.doi.org/10.1016/j.epsl.2010.02.008

Malinverno, A., and Goldberg, D. S. (2015). Testing short-range migration of microbial methane as a hydrate formation mechanism: Results from Andaman Sea and Kumano Basin drill sites and global implications. *Earth and Planetary Science Letters, 422*, 105-114. doi: http://dx.doi.org/10.1016/j.epsl.2015.04.019

Meyer, D. W., Flemings, P. B., DiCarlo, D. A., You, K., Phillips, S. C., and Kneafsey, T. (2018). Experimental investigation of gas flow and hydrate formation within the hydrate stability zone. *Journal of Geophysical Research: Solid Earth*. doi: 10.1029/2018JB015748

Mienert, J., Vanneste, M., Bünz, S., Andreassen, K., Haflidason, H., and Sejrup, H. P. (2005). Ocean warming and gas hydrate stability on the mid-Norwegian margin at the Storegga Slide. *Marine and Petroleum Geology, 22*(1–2), 233-244. doi: http://dx.doi.org/10.1016/j.marpetgeo.2004.10.018

Milkov, A. V. (2004). Global estimates of hydrate-bound gas in marine sediments: how much is really out there? *Earth-Science Reviews, 66*(3–4), 183-197. doi: http://dx.doi.org/10.1016/j.earscirev.2003.11.002

Moridis, G., Kowalsky, M. B., and Pruess, K. (2008). *TOUGH+HYDRATE v1.2 User's Manual: A Code for the Simulation of System Behavior in Hydrate-Bearing Geologic Media*: Lawrence Berkeley National Laboratory.

Moridis, G. J. (2008). Toward Production From Gas Hydrates: Current Status, Assessment of Resources, and Simulation-Based Evaluation of Technology and Potential.

Natarajan, V., Bishnoi, P. R., and Kalogerakis, N. (1994). Induction phenomena in gas hydrate nucleation. *Chemical Engineering Science, 49*(13), 2075-2087. doi: http://dx.doi.org/10.1016/0009-2509(94)E0026-M

Nelson, P. H. (2009). Pore-throat sizes in sandstones, tight sandstones, and shales. *AAPG Bulletin, 93*(3), 12.

Nixon, M. F., and Grozic, J. L. H. (2007). Submarine slope failure due to gas hydrate dissociation: a preliminary quantification. *Canadian Geotechnical Journal, 44*(3), 10. doi: 10.1139/T06-121

Nole, M., Daigle, H., Cook, A. E., and Malinverno, A. (2016). Short-range, overpressure-driven methane migration in coarse-grained gas hydrate reservoirs. *Geophysical Research Letters, 43*(18), 9500-9508. doi: 10.1002/2016gl070096

Olsen, H. W. (1966). Darcy's Law in Saturated Kaolinite. *Water Resources Research, 2*(2), 9.

Onur, E. M. (2014). *Predicting the Permeability of Sandy Soils from Grain Size Distribution.* Master of Science, Kent State University, Ohio.

Pini, R., Krevor, S. C. M., and Benson, S. M. (2012). Capillary pressure and heterogeneity for the CO2/water system in sandstone rocks at reservoir conditions. *Advances in Water Resources, 38*, 48-59. doi: http://dx.doi.org/10.1016/j.advwatres.2011.12.007

Pitzer, K. S. (1991). Ion interaction approach: Theory and data correlation. In K. S. Pitzer (Ed.), *Activity Coefficients in Electrolyte Solutions* (2nd ed., pp. 75-153). Boca Raton, FL: CRC Press.

Priegnitz, M., Thaler, J., Spangenberg, E., Rücker, C., and Schicks, J. M. (2013). A cylindrical electrical resistivity tomography array for three-dimensional monitoring of hydrate formation and dissociation. *Review of Scientific Instruments, 84*(10), 104502. doi: doi:http://dx.doi.org/10.1063/1.4825372

Reagan, M. T., and Moridis, G. J. (2008). Dynamic response of oceanic hydrate deposits to ocean temperature change. *Journal of Geophysical Research: Oceans, 113*(C12). doi: doi:10.1029/2008JC004938

Reagan, M. T., and Moridis, G. J. (2009). Large-scale simulation of methane hydrate dissociation along the West Spitsbergen Margin. *Geophysical Research Letters, 36*(23). doi: doi:10.1029/2009GL041332

Rees, E. V. L., Kneafsey, T., and Seol, Y. (2011). Methane Hydrate Distribution from Prolonged and Repeated Formation in Natural and Compacted Sand Samples: X-Ray CT Observations. *Journal of Geological Research, 2011*. doi: 10.1155/2011/791815

Rempel, A. W. (2011). A model for the diffusive growth of hydrate saturation anomalies in layered sediments. *Journal of Geophysical Research: Solid Earth, 116*(B10), n/a-n/a. doi: 10.1029/2011jb008484

Rempel, A. W., and Buffett, B. A. (1997). Formation and accumulation of gas hydrate in porous media. *Journal of Geophysical Research: Solid Earth, 102*(B5), 10151-10164. doi: 10.1029/97jb00392

Rempel, A. W., Wettlaufer, J. S., and Worster, M. G. (2004). Premelting dynamics in a continuum model of frost heave. *Journal of Fluid Mechanics, 498*, 227-244. doi: Doi: 10.1017/s0022112003006761

Riedel, M., Novosel, I., Spence, G. D., Hyndman, R. D., Chapman, R. N., Solem, R. C., and Lewis, T. (2006). Geophysical and geochemical signatures associated with gas hydrate–related venting in the northern Cascadia margin. *GSA Bulletin, 118*(1-2), 23-38. doi: 10.1130/b25720.1

Riestenberg, D., West, O., Lee, S., McCallum, S., and Phelps, T. J. (2003). Sediment surface effects on methane hydrate formation and dissociation. *Marine Geology, 198*(1–2), 181-190. doi: http://dx.doi.org/10.1016/S0025-3227(03)00100-2

Schowalter, T. T. (1979). Mechanics of Secondary Hydrocarbon Migration and Entrapment. *AAPG Bulletin, 63*(5), 37.

Seol, Y., and Kneafsey, T. J. (2009). X-ray computed-tomography observations of water flow through anisotropic methane hydrate-bearing sand. *Journal of Petroleum Science and Engineering, 66*(3–4), 121-132. doi: http://dx.doi.org/10.1016/j.petrol.2009.01.008

Shipley, T. H., Houston, M. H., Buffler, R. T., Shaub, J., McMillen, K. J., Ladd, J. W., and Worzel, J. L. (1979). Seismic Evidence for Widespread Possible Gas Hydrate

Horizons on Continental Slopes and Rises. *The American Association of Petroleum Geologists Bulletin, 63*(12), 10.

Skempton, A. W. (1954). The Pore-Pressure Coefficients A and B. *Géotechnique, 4*(4), 143-147. doi: 10.1680/geot.1954.4.4.143

Skovborg, P., Ng, H. J., Rasmussen, P., and Mohn, U. (1993). Measurement of induction times for the formation of methane and ethane gas hydrates. *Chemical Engineering Science, 48*(3), 445-453. doi: http://dx.doi.org/10.1016/0009-2509(93)80299-6

Sloan, E. D., and Fleyfel, F. (1991). A molecular mechanism for gas hydrate nucleation from ice. *AIChE Journal, 37*(9), 1281-1292. doi: 10.1002/aic.690370902

Sloan, E. D., and Koh, C. A. (2007). *Clathrate Hydrates of Natural Gases* (3nd ed.). Boca Raton, FL: CRC Press.

Spangenberg, E., Kulenkampff, J., Naumann, R., and Erzinger, J. (2005). Pore space hydrate formation in a glass bead sample from methane dissolved in water. *Geophysical Research Letters, 32*(24), n/a-n/a. doi: 10.1029/2005gl024107

Sun, X., and Mohanty, K. K. (2006). Kinetic simulation of methane hydrate formation and dissociation in porous media. *Chemical Engineering Science, 61*(11), 3476-3495. doi: https://doi.org/10.1016/j.ces.2005.12.017

Taylor, C. J., Miller, K. T., Koh, C. A., and Sloan, E. D. (2007). Macroscopic investigation of hydrate film growth at the hydrocarbon/water interface. *Chemical Engineering Science, 62*(23), 6524-6533. doi: http://dx.doi.org/10.1016/j.ces.2007.07.038

Tohidi, B., Anderson, R., Clennell, M. B., Burgass, R. W., and Biderkab, A. B. (2001). Visual observation of gas-hydrate formation and dissociation in synthetic porous media by means of glass micromodels. *Geology, 29*(9), 4.

Torres, M. E., Wallmann, K., Tréhu, A. M., Bohrmann, G., Borowski, W. S., and Tomaru, H. (2004). Gas hydrate growth, methane transport, and chloride enrichment at the southern summit of Hydrate Ridge, Cascadia margin off Oregon. *Earth and Planetary Science Letters, 226*(1–2), 225-241. doi: http://dx.doi.org/10.1016/j.epsl.2004.07.029

Torres, M. E., McManus, J., Hammond, D. E., de Angelis, M. A., Heeschen, K. U., Colbert, S. L., Tryon, M. D., Brown, K. M., and Suess, E. (2002). Fluid and chemical fluxes in and out of sediments hosting methane hydrate deposits on

Hydrate Ridge, OR, I: Hydrological provinces. *Earth and Planetary Science Letters, 201*(3), 525-540. doi: https://doi.org/10.1016/S0012-821X(02)00733-1

Tréhu, A. M., Flemings, P. B., Bangs, N. L., Chevallier, J., Gràcia, E., Johnson, J. E., Liu, C. S., Liu, X., Riedel, M., and Torres, M. E. (2004). Feeding methane vents and gas hydrate deposits at south Hydrate Ridge. *Geophysical Research Letters, 31*(23), L23310. doi: 10.1029/2004gl021286

Uchida, T., Takagi, A., Kawabata, J., Mae, S., and Hondoh, T. (1995). Raman spectroscopic analyses of the growth process of CO2 hydrates. *Energy Conversion and Management, 36*(6), 547-550. doi: https://doi.org/10.1016/0196-8904(95)00064-K

Ussler, W., and Paull, C. K. (2001). Ion Exclusion Associated with Marine Gas Hydrate Deposits *Natural Gas Hydrates: Occurrence, Distribution, and Detection* (pp. 41-51): American Geophysical Union.

West, T. R. (2010). *Geology Applied to Engineering*. Long Grove, IL: Waveland Press.

Wright, J. F., Dallimore, S. R., Nixon, F. M., and Duchesne, C. (2005). In situ stability of gas hydrate in reservoir sediments of the JAPEX/JNOC/GSC et al. Mallike 5L-38 gas hydrate production research well. In S. R. Dallimore, and Collett, T. S. (Ed.), *Scientific Results from the Mallik 2002 Gas Hydrate Production Research Well Program, Mackenzie Delta, Northwest Territories, Canada* (Vol. Bulletin 585, pp. 14): Geological Survey of Canada.

Xu, W., and Ruppel, C. (1999). Predicting the occurrence, distribution, and evolution of methane gas hydrate in porous marine sediments. *Journal of Geophysical Research: Solid Earth, 104*(B3), 5081-5095. doi: 10.1029/1998jb900092

Yamamoto, K., Terao, Y., Fujii, T., Ikawa, T., Seki, M., Matsuzawa, M., and Kanno, T. (2014). *Operational Overview of the First Offshore Production Test of Methane Hydrates in the Eastern Nankai Trough.* Presented at the Offshore Technology Conference, Houston, TX.

You, K., and Flemings, P. B. (2017). Methane hydrate formation in thick sand reservoirs: 1. Short-range methane diffusion. *Marine and Petroleum Geology*. doi: https://doi.org/10.1016/j.marpetgeo.2017.10.011

You, K., and Flemings, P. B. (in review). Methane Hydrate Formation in Thick Sand Reservoirs: 2. Long-Range Gas Transport. *Journal of Geophysical Research: Solid Earth*.

You, K., DiCarlo, D., and Flemings, P. B. (2015a). Quantifying hydrate solidification front advancing using method of characteristics. *Journal of Geophysical Research: Solid Earth, 120*(10), 6681-6697. doi: 10.1002/2015jb011985

You, K., Kneafsey, T. J., Flemings, P. B., Polito, P., and Bryant, S. L. (2015b). Salinity-buffered methane hydrate formation and dissociation in gas-rich systems. *Journal of Geophysical Research: Solid Earth, 120*(2), 643-661. doi: 10.1002/2014jb011190

Yousif, M. H., and Sloan, E. D. (1991). Experimental Investigation of Hydrate Formation and Dissociation in Consolidated Porous Media. doi: 10.2118/20172-pa

Zappoli, B., Beysens, D., and Garrabos, Y. (2014). *Heat Transfers and Related Effects in Supercritical Fluids* (Vol. 108): Springer Netherlands.